

**Bangor University**

## **DOCTOR OF PHILOSOPHY**

### **Developing coupled Reduced Order Models for Shielding and Reactor Physics applications**

Coombs, Edward

*Award date:*  
2022

*Awarding institution:*  
Bangor University

[Link to publication](#)

#### **General rights**

Copyright and moral rights for the publications made accessible in the public portal are retained by the authors and/or other copyright owners and it is a condition of accessing publications that users recognise and abide by the legal requirements associated with these rights.

- Users may download and print one copy of any publication from the public portal for the purpose of private study or research.
- You may not further distribute the material or use it for any profit-making activity or commercial gain
- You may freely distribute the URL identifying the publication in the public portal ?

#### **Take down policy**

If you believe that this document breaches copyright please contact us providing details, and we will remove access to the work immediately and investigate your claim.



PRIFYSGOL  
**BANGOR**  
UNIVERSITY

School of Computer Science and Electronic Engineering  
College of Environmental Sciences and Engineering

**Developing coupled Reduced Order  
Models for Shielding and Reactor  
Physics applications**

---


Edward Coombs

Submitted in partial satisfaction of the requirements for the  
Degree of Doctor of Philosophy  
in Engineering

*Supervisor* Prof Paul Spencer

June 2021

# Acknowledgements

 *To be trusted is a greater compliment than to be loved.*

— **George MacDonald (1824-1905)**

First off, I would like to express my sincere gratitude and appreciation to all my supervisors: Prof Paul Spencer, Prof Christopher Pain and Prof Paul Smith. The regular insight and encouragement of Paul Spencer has been an immense help, much of his time has been given over to make the project a reality. I would also express my thanks to Chris Pain whose work particularly in the field of reduced order modelling is prolific and inspiring in scope and impact.

My time at Imperial Collage has always been exciting and rich in ideas. Building on the work done by Dr Dunhui Xiao while he was under the supervision of Dr. Fangxin Fang, Prof. Christopher Pain and Dr. Andrew Buchan has been a privilege. I would also like to thank all the members of the AMCG group for their warm welcome and help at Imperial Collage, Dr Clair Heaney chief among them who from which I have learned a lot.

Without the funding from the KESS2 program operating with the support of the European Social Funds (ESF) through the Welsh Government and the company Jacobs I would not of been able to complete this work. Prof Paul Smith and Dr Brenden Tolit of Jacobs and their profound experience have kept this project in the right direction and I can not express how grateful I am for that. I would like to finally thank my friends, family and loves ones for their understanding.

**Statement of Originality**

The work presented in this thesis/dissertation is entirely from the studies of the individual student, except where otherwise stated. Where derivations are presented and the origin of the work is either wholly or in part from other sources, then full reference is given to the original author. This work has not been presented previously for any degree, nor is it at present under consideration by any other degree awarding body.

Student:

Edward Coombs

**Statement of Availability**

I hereby acknowledge the availability of any part of this thesis/dissertation for viewing, photocopying or incorporation into future studies, providing that full reference is given to the origins of any information contained herein. I further give permission for a copy of this work to be deposited with the Bangor University Institutional Digital Repository, the British Library ETHOS system, and/or in any other repository authorised for use by Bangor University and where necessary have gained the required permissions for the use of third party material. I acknowledge that Bangor University may make the title and a summary of this thesis/dissertation freely available.

Student:

Edward Coombs

Signature

*Ed Coombs*

I hereby declare that this thesis is the results of my own investigations, except where otherwise stated. All other sources are acknowledged by bibliographic references. This work has not previously been accepted in substance for any degree and is not being concurrently submitted in candidature for any degree unless, as agreed by the University, for approved dual awards.

Yr wyf drwy hyn yn datgan mai canlyniad fy ymchwil fy hun yw'r thesis hwn, ac eithrio lle nodir yn wahanol. Caiff ffynonellau eraill eu cydnabod gan droednodiadau yn rhoi cyfeiriadau eglur. Nid yw sylwedd y gwaith hwn wedi cael ei dderbyn o'r blaen ar gyfer unrhyw radd, ac nid yw'n cael ei gyflwyno ar yr un pryd mewn ymgeisiaeth am unrhyw radd oni bai ei fod, fel y cytunwyd gan y Brifysgol, am gymwysterau deuol cymeradwy.

# Abstract

Reduced order modelling (ROM) in engineering has rapidly become of great interest, yielding potential of speed up while maintaining high fidelity. Practical problems involving neutron diffusion, scattering and shielding have particularity complex multi-scale behaviour in energy and space making real-time, multi-query, design or data assimilation applications are beginning to benefit from ROM research. This is typically done via Proper Orthogonal Decomposition (POD), coupled with Galerkin projection. In this thesis we demonstrate multiple novel approaches to Non-intrusive reduced order modelling (NIROMs), building on the work done in [1]. We apply them to two research areas, shielding and neutron diffusion.

First a novel way of using reduced order models (ROMs) in a coupling scheme to model more complex material configurations from a library of individual material reduced order models (ROMs) is presented. Secondly this framework is generalised to n-group and validated with a 2-group shielding benchmark. Finally the lack of guaranteed conservative NIROM solutions is addressed and demonstrated with variants of the Advection-Diffusion equation, achieved through a novel Sub-Grid Scale ROM (SGS ROM) to add conservation and resolution to ROM solutions.

# List of Symbols and Abbreviations

This list describes most of the symbols and abbreviations that will be later used within the body of the thesis.

$\alpha$  ROM Coefficients

$\Delta t$  Change in  $t$

$\Delta x$  Change in  $x$

$\delta x$  Small change in  $x$

$\lambda_i$  Entries of Matrix  $\Sigma$  are the singular values

$\mathbb{P}/P/p$  Training Parameter

$\mathbb{R}$  Some Real number

$\mathbb{U}/U$  Left Reflection and Rotation Matrix in SVD

$\mathbb{X}$  Snapshot Matrix

$\Phi_S$  Abstract POD basis functions

$\psi$  Neutron Flux

$\psi_+, \psi_-$  Positive Flux, Negative Flux

$\Sigma$  Entries of Matrix  $\Sigma$  are the singular values

$\Sigma_c, \Sigma_s, \Sigma_f$  Macroscopic capture, scatter and fission cross-section

$eV$  Electron volts

$I$  The Identity matrix

$L$  Domain Length

$MeV$  Mega Electron volts

$n_{dof}/ny$  Number of degrees of Freedom

$N_{S_{nim}}$  Minimum number of snapshots

$N_S$  Number of snapshots

$T$  Generic Scalar Variable  $T(x, t)$

$t$  Time Variable

$u$  Advection Speed

$V^*$  Right Reflection and Rotation Matrix in SVD

$w_{i,j}$  NIROM Weights

$x$  Distance Variable

ASPIS Greek term for shield referring here to a series of shielding benchmarks

CUP Central processing uni

CV Control Volume

DEIM Discrete Empirical Interpolation

DOF Degrees of Freedom

GNAT Gauss-Newton with approximated tensors



NESTOR Neutron Source Thermal Reactor

NIROM Non-Intrusive Reduced Order Model

NVD Normalised Variable Diagram

ODE Ordinary Differential Equation

PDE Partial Differential Equation

POD Proper Orthogonal Decomposition

RBF Radial Basis Function

RMS Root Mean Square

ROM Reduced Order Model

SGS Sub-Grid Scale

SUPCV Super Control Volume

SVD Singular Value Decomposition

# Contents

<b>1</b>	<b>Introduction</b>	<b>2</b>
1.1	Motivation and Objectives . . . . .	4
1.2	Contributions . . . . .	7
1.3	An overview of current Reduced Order Modelling literature . . . . .	9
1.3.1	Intrusive Reduced Order Modelling literature . . . . .	10
1.3.2	Non-Intrusive Reduced Order Modelling literature . . . . .	12
<b>2</b>	<b>Background Theory</b>	<b>14</b>
2.1	Numerical methods . . . . .	14
2.2	Reduced order modelling . . . . .	20
2.2.1	Proper Orthogonal decomposition (POD) . . . . .	22
2.2.2	Radial basis interpolation . . . . .	25
2.3	Non-Intrusive Reduced Order Models . . . . .	29
2.3.1	The NIROM algorithm for steady state problems . . . . .	31
2.4	Reactor Physics and shielding . . . . .	32
2.5	The ASPIS benchmark . . . . .	38
<b>3</b>	<b>Preliminary Reduced Order Models</b>	<b>39</b>
3.1	A single parameter attenuation model of shielding . . . . .	42
3.1.1	A logarithmic pre-conditioner . . . . .	48
3.1.2	Error, stability, and convergence measures used in this work . . . . .	48
3.1.3	Time complexity and POD basis information capture . . . . .	51
3.1.4	Results and discussion for a ROM of simple exponential attenuation flux . . . . .	53
3.2	Two and three parameter attenuation models of shielding . . . . .	58
3.2.1	Results and discussion for two and three parameter attenuation models of shielding . . . . .	60
3.3	Four parameter attenuation models of shielding . . . . .	64
3.3.1	Results and discussion for four parameter attenuation models of shielding . . . . .	66
3.4	Coupling of ROM towards the ASPIS benchmark model . . . . .	70
3.4.1	Results . . . . .	73

<b>4</b>	<b>Coupled 1-Group Reduced Order Models for generic and ASPIS benchmark configurations of slabs</b>	<b>75</b>
4.1	Model with positive and negative scatter . . . . .	76
4.2	The coupling scheme . . . . .	81
<b>5</b>	<b>Coupled 2-Group Reduced Order Models for generic and ASPIS benchmark configurations of slabs</b>	<b>96</b>
5.1	Two-Group Analytic Solutions derivation . . . . .	98
5.1.1	Single Shield 2-group ROMs . . . . .	104
5.2	Coupled two group ASPIS Configuration Scheme and Results .	110
5.2.1	Two group ROM results and training . . . . .	115
5.2.2	Results and discussion of Coupled 2-Group ASPIS problem	117
<b>6</b>	<b>Derivation of a Sub-Grid Scale Full Order Method</b>	<b>120</b>
6.1	Sub-grid scale modelling . . . . .	123
6.2	Extending the sub-grid scale approach to model diffusion, source and absorption. . . . .	136
6.2.1	Diffusion in the sub-grid scale model . . . . .	136
6.2.2	Source and absorption in the sub-grid scale model . . .	139
6.3	1D Sub-Grid Scale Numerical Results . . . . .	145
6.3.1	Full Order Full Order Sub-Grid Scale Numerical Results .	146
6.3.2	Reduced Order Sub-Grid Scale Numerical Results . . . .	150
6.4	Extension of the Sub-Grid Scale model to 2D . . . . .	158
6.4.1	2D Full Order Sub-Grid Scale Numerical Results . . . . .	160
6.4.2	2D Reduced Order Sub-Grid Scale Numerical Results . .	162
<b>7</b>	<b>Conclusion and Future Work</b>	<b>169</b>
7.1	Conclusions . . . . .	169
7.2	Future Work . . . . .	172
7.2.1	Extending training and possible applications . . . . .	172
7.2.2	Additional directions . . . . .	173
7.3	Appendices . . . . .	174
7.3.1	Linear Algebra . . . . .	174
	Vector space and field axioms . . . . .	174
	Example . . . . .	175
	Vector Basis . . . . .	175
	Hilbert–Schmidt norm and Hilbert space . . . . .	176
7.3.2	The Error function . . . . .	177
7.3.3	Notes on coding languages and tools . . . . .	177
7.3.4	Odd and even functions . . . . .	178
7.3.5	Condition number . . . . .	178
7.3.6	Intrusive reduced order models . . . . .	180

# List of Figures

2.1	A schematic visualisation, called a <i>stencil</i> , showing how the Upwinding scheme propagates in time and space. . . . .	16
2.2	An overview of the reduced ordering modelling process. The full order model's state space dimension or number of degrees of freedom is reduced forming an approximation to the full order model, namely the reduced order model. . . . .	21
2.3	The singular value decomposition (SVD) can be visualised geometrically in three steps, a rotation or reflection $\mathbb{U}$ , a scaling $\Sigma$ and a further rotation or reflection $\mathbb{V}^*$ [2] . . . . .	24
2.4	The interpolation is good when the characteristic length is suitably chosen. However you can still see a Runge's phenomenon (or Gibb's phenomenon) at the far right of the domain. Here $\sigma = 0.1$ , the red curve is the original 36 data points and the blue curve is an attempted radial basis function interpolation for 113 points. .	27
2.5	The interpolation fails if the characteristic length is too small. The radial basis functions become narrow and the interpolation kernel matrix becomes close to the identity matrix. The solution will be close at the interpolation point and almost zero everywhere else. Here $\sigma = 0.001$ , the red curve is the original 36 data points and the blue curve is an attempted radial basis function interpolation for 113 points. We call this the bed-of-nails case. . . . .	27
2.6	The interpolation is noisy when the characteristic length is too large. The radial basis functions become too flat and give little information. Here $\sigma = 0.8$ , the red curve is the original 36 data points and the blue curve is an attempted radial basis function interpolation for 113 points. . . . .	28
2.7	The diffusion approximation offers a physical interpretation is similar to the fluxes of gases. Moving from high collision density to low collision density. There are more collisions per cubic centimetre on the left so the neutrons are on average scattered left to right, diffusing to the right. . . . .	37
2.8	The material configuration used in the coupled ROMs, chapter 3 and 4. This a modified version of the domina uised in the ASPIS benchmark. . . . .	38

3.1	Visualization of the snapshots stored as column vectors of the snapshot matrix. . . . .	44
3.2	Visualisation of the Offline stage of the NIROM. The principle input of the algorithm is the snapshot matrix $\mathbb{X}$ in which the training data is stored. The NIROM produces the POD basis and the weights needed to reconstruct any new solution in the Online stage. . . .	46
3.3	The spatial resolution here is a unit fixed with 6 spatial nodes while we investigate the effects of adding more training data though additional snapshots. . . . .	53
3.4	Here we see for the no-log snapshot matrix, at some points towards the end of the spatial domain values of the ROM solutions are negative in sign and far from the expected solution. This is eventually resolved by increasing the number of snapshots or immediately resolved by taking log of the snapshot matrix and exp of the ROM solutions. Note the x-axis is number added beyond the minimum which here was 3, so in this case the no log data becomes positive after 11 snapshots in total. Each line is the error at a spatial node with the error highest in nodes right to left. . .	54
3.5	The relative error plot for each spatial node shows the effectiveness of the logarithmic pre-conditioner from section 3.1.1 and the point at which adding more data yields diminishing returns. Each line is the error at a spatial node with the error highest in nodes right to left. . . . .	55
3.6	We see the order of convergence is not smooth due to oscillations but can be found to be bounded at about 0.8 for both runs. . . .	56
3.7	Singular values are quickly dropping off (a), instantly for the log data set, (b) the energy captured starts fairly high with just one basis function. reaching 98% after just 4 POD basis functions. The first few most dominant POD basis functions without the preconditioner (c) and with the preconditioner (d). We can see that the 1 <sup>st</sup> one in both instances hold much of the same shape information as the training data set, the set of exponentials from equation (3.2). . . . .	57
3.8	The spatial domain here is now modelling two or more individual shields. Both the effects of adding more training data through more snapshots and also now increasing the number of nodes and hence spatial resolution are explored. These example meshes show two shields one in blue and one in orange and the lowest resolution mesh with 6 node in each shield and a 30 node mesh with resolution being a range investigated from 6 nodes to 60 nodes.	60

3.9	Root mean squared error of ROM solutions drops off rapidly with addition of more snapshots and for this problem very genitally as the spatial degrees of freedom increase (a). With the preconditioner this is even more rapid (b). Maximum Relative error of ROM whole solution with the preconditioner applied drops more rapidly (c). At this smaller scale you begin to see the periodic oscillations as the number of snapshots increases (d) which was clear in the 1D log-log plots in the previous sections of results 3.6.	61
3.10	This plot shows ROM and exact solutions for the two parameter problem. A single POD basis function is not sufficient to capture all the information and we expect this from the cumulative energy. We see little difference between 4 and 12 POD basis functions. The problem mesh is a 60 node version of 3.8. . . . .	62
3.11	The energy capture with POD basis and shape of the first few the POD basis functions is shown. . . . .	62
3.12	This plot shows solutions for the three parameter problem. Similarly we see that a single POD basis function is not sufficient. Using 4 and 12 POD basis functions gives good results. The problem mesh is based on 3.8 with the addition of an extra shield.	63
3.13	The energy capture with POD basis and shape of the first few the POD basis functions is shown. . . . .	63
3.14	Root mean squared error of ROM solution drops rapidly with the addition of more snapshots and for this problem very genitally as the spatial degrees of freedoms increase (a). With the preconditioner we improve the solutions even more rapidly (b). Looking at the maximum relative error we see initial variation with only 6 spatial nodes and a low amount of snapshots. Adding more snapshots quickly eliminates this without (c) and with (d) the log preconditioner. . . . .	67
3.15	Here we have ROM solutions for the four parameter problem on linear (a) and log-linear (b) plots for $8^4$ snapshots and linear (c) and log-linear (d) plots for $2^4$ snapshots. We can see clearly that with more snapshots greatly improves the results. A selection of characteristic lengths are used. POD basis functions are chosen such that 95% energy is captured. We can see in the log-linear version of the plots that $(max - min)/mean$ gives the best results here. . . . .	68

3.16	This plot shows the flux profile of three ROMs coupled in one direction. The ROM is trained 20% either side of the ASPIS data for three regions, namely steel, air and steel. The unknown point the ROMs is finding is chosen to be far from the training data with out leaving the space and a value of 95% of the energy informed the number of POD basis functions used. . . . .	71
3.17	Here show multiple slabs coupled together coupled with physical properties, the attenuation factor, calculated from the Iron-88 benchmark but with the geometry of the ASPIS problem in linear (a) and log-linear (b) scales. . . . .	71
3.18	Here we have a comparison of coupled vs global NIROM for a test problem for attenuation of $[2.5, 10]$ (a). Here we see the error in the two methods (b)). Even though we only have two parameters, coupling gives an improvement. . . . .	72
3.19	For elementary functions made of exponential functions we see and error in the order of 0.1 or less even for this few snapshots, here 12 . . . . .	73
3.20	Highly erratic functions as expected need more snapshots to get similar errors. Here we have gone from 12 to 40 to get an error comparable to the first set of profiles. . . . .	74
4.1	The iterative coupling scheme is outlined. The boundary conditions at the start and end of the problem are fixed while the free boundary conditions are gradually improved as guesses yield flux profiles in the shields with can inform new, better guesses until the scheme converges. . . . .	83
4.2	The results for the 1-group coupling of two directional fluxes from the analytical model for the ASPIS configuration are shown. Here in we have the scalar flux, the total of the two directional fluxes, in log-linear (a) and linear scales (b) the error in the scalar flux in linear (c) and log-linear plots (d). The tolerance for continuity in the negative flux is chosen to be $1.0 - 10^{-6}$ and hence the continuity at all free boundaries of the negative flux at the material interfaces is bounded above by this tolerance value. . . . .	85
4.3	Here we have log-linear plots of the directional fluxes, the positive flux exact solutions coupled (e) and negative flux exact solutions coupled (f). . . . .	86
4.4	Here we have the absolute error in the scalar flux on linear plot with true sign of the error (g) and log-linear scale with just the size of the error (h). . . . .	87

4.5	The relative error at the interfaces (i) is shown along the RMS error. There is no difference at the interfaces with the void parts of the shield. There is not much structure beyond this but the variation is less than an order of magnitude within the RMS. The tolerance progresses towards the desired tolerance, in this case $10^{-6}$ . (j) . . . . .	87
4.6	Here we have the scalar flux from the ROM coupling in log-linear (a) and linear scales (b) the error in the scalar flux in linear (c) and log-linear plots (d). The tolerance is $1.0 - 10^{-2}$ in other words a maximum of a 1.0% error across the interfaces. . . . .	91
4.7	Here we have the error at the start and end of each slab and void model. (a) the value of the tolerance (b) the positive flux exact solutions coupled (c) and negative flux exact solutions coupled (d). The tolerance is $10^{-6}$ . The end point of the slab is omitted as it is not an interface. We can see the ROM produced a different value to represent zero then the reference solution. The interface values all have error less than 0.12 with most 2% to 4%. . . . .	92
4.8	Here we have the absolute error in the scalar flux on linear plot with true sign of the error and log-linear scale with just the size of the error. . . . .	94
5.1	This figure gives a general overview of the boundary conditions at the beginning and end of a shield. Later the coupled models will have extra boundary at interfaces. For now we are considering a single shield to build intuition of the physics of each material. Each of the material examples in figures 5.2,5.3,5.4 and 5.5 has a width chosen from table 5.1 and cross sections as table 5.2. . . .	105
5.2	Here for a thin, $0.5cm$ boral shield we have (a) the individual directional fluxes for the ROM and exact solutions (b) the relative error in scalar flux (c) the first 4 basis functions and (d) and the energy of the POD basis functions (d). . . . .	106
5.3	Here we have the individual directional fluxes in the ROM and exact solutions (a) the relative error 2 (b) the first 4 basis functions (c) and the energy plot (d) in a thick $5.08cm$ stainless steel shield. . . . .	107
5.4	Here we have the individual directional fluxes in the ROM and exact solutions (a) the relative error 2 (b) the first 4 basis functions (c) and the energy plot (d) in a thick $19.9cm$ water slab. . . . .	108
5.5	Here we have the individual directional fluxes in the ROM and exact solutions in log-linear plot for a $15.24cm$ concrete shield. . . . .	109
5.6	ROM iterative coupling scheme . . . . .	111



5.7	Domain for the ROM ASPIS configuration is made of 25 homogeneous shields with widths and cross sections show in tables 5.1 and 5.2 respectively. This figure gives an overview of the boundary conditions at the beginning and end of the whole shield. Two cases for the inlet are presented, a flux spectra split evenly and a case with all the inlet flux in the 1st group. . . . .	112
5.8	This figure is an example of how the boundary conditions at each interface are used to achieve continuity between a shield model for steel one for water at an interface point $L_I$ . Excluding the inlet and outlet boundary condition at the beginning and end of the whole shield and zooming in on one of the remaining free boundary conditions at each material interface of each material we see that the pairs of directional fluxes must match up to a tolerance condition for the coupling scheme to achieve continuity across the domain. . . . .	113
5.9	(a),(b) The results, on liner and log-linear scales, for exact slabs coupled together in the ASPIS configuration with input fluxes of (0.5, 0.5) for the left hand boundary conditions and (c),(d) The results for exact slabs coupled together in the ASPIS configuration with input fluxes of (1.0, 0.0) for the left hand boundary conditions in both linear and log-linear scales. The fluxes at the end of the shield remain similar in both cases. Even with no input thermal fluxes a sizable amount builds up from scatter. . . . .	114
5.10	(a),(b) The flux profiles in linear and log-linear scales, (c) (d) the relative error in linear and log-linear scales. We see low error in the coupled ROM solutions until the very end of the domain. This is due to the rapid drop in flux at the very end of the shield. . .	117
5.11	(a),(b) The absolute error in linear and log-linear scales. (c) The value of the tolerance at each iteration. The value of the characteristic length has been tuned to permit the smallest tolerance still stable. (d) The worst interface at each iteration. Interfaces 1 to 14 are group-1 and 15 to 28 are group-2. . . . .	118
6.1	The levels of the wavelet basis functions as well as the numbering of the wavelet basis functions. . . . .	125
6.2	The Wavelet basis showing the domain $\Omega_i$ it occupies and its boundaries on which we consider flux entering and leaving. . . .	127
6.3	(a) A fully coarse representation of the initial condition (b) a possible representation using on the sub-grid scale nodes. Throughout this work the initial conditions are representation as figure (a), that is fully coarse with initial sub-grid scale corrections of zero. . . . .	146

6.4	(a) Solutions without Sub-Grid Scale corrections and (b) with Sub-Grid Scale corrections (b). Increasing the number of wavelet levels improves the resolution of the solutions. Without the Sub-Grid Scale corrections numerical diffusion is present and distorts the solution. The solutions with more wavelet levels approach the true solution. . . . .	147
6.5	Coarse control volume solution with Sub-Grid Scale correction and uncorrected coarse solution with same reference. The Sub-Grid Scale corrections remove the numerical diffusion. . . . .	148
6.6	(a) Sub-Grid Scale solutions over a range of time steps with no diffusion $NUSP = 10, NW = 63, U = 1.0$ and (b) Sub-Grid Scale solutions over a range of time steps with no advection $NUSP = 9, NW = 7, D = 0.16$ . . . . .	149
6.7	Snapshots of Sub-Grid Scale Advection-Diffusion equation are taken at different time steps. We can see the wave front cross the domain and under goes diffusion as the flux leaves the domain. . . . .	150
6.8	(a) The NIROM and exact solution, (b) the relative error, (c) the information captured by the POD basis functions and (d) the shape of the POD basis functions. . . . .	151
6.9	(a) For 3 or more POD basis functions the ROM and the FOM are strongly correlated. and in (b) the use of 2 POD basis functions shows little correlation for early time steps with vague correlation later in time. A single POD basis function performs even worse at early time, showing inverse correlation from the ROM to the FOM in some parts of the time domain. . . . .	152
6.10	(a) Run times, in seconds (s), of the Reduced Order Model and its internal calculation phases, (b) The Reduced Order Model run time and the full order run time. You can see orders of magnitude of speed up. . . . .	153
6.11	(a) The NIROM and exact solution, (b) the relative error, (c) the information captured by the POD basis functions and (d) the shape of the POD basis functions for a logarithmic pre-conditioner of the NIROM. . . . .	154
6.12	(a) For 3 or more POD basis functions the ROM and the FOM are strongly correlated. and in (b) the use of 2 POD basis functions shows little correlation for early time steps with vague correlation later in time. A single POD basis function performs even worse at early time, showing inverse correlation from the ROM to the FOM in some parts of the time domain. There is some slight overall improvement with the logarithmic pre-conditioner . . . . .	155

6.13	(a) The NIROM and exact solution, (b) the relative error, (c) the information captured by the POD basis functions and (d) the shape of the POD basis functions with a deviation from the mean as a pre-conditioner. . . . .	156
6.14	(a) For 3 or more POD basis functions the ROM and the FOM are strongly correlated. and in (b) the use of 2 POD basis functions shows little correlation for early time steps with vague correlation later in time. A single POD basis function performs even worse at early time, showing inverse correlation from the ROM to the FOM in some parts of the time domain. . . . .	157
6.15	(a) The coarse control values in coloured contours and sub-grid scale control volumes in white inline contours at $t_5$ , (b) the coarse control values in coloured contours and sub-grid scale control volumes in white inline contours at sampled time step $t_8$ , (c) the coarse solution with the sub-grid scale correction at $t_5$ (d) the coarse solution with the sub-grid scale correction at sampled time step $t_5$ . . . . .	160
6.16	Size of corrections in Sub-Grid Scale as time evolves take from the 1D profile that forms the peak of the 2D solutions at 8 evenly sampled time steps. . . . .	161
6.17	(a) The reduced order model solution and (b) the exact solution of a 2D Gaussian profile undergoing advection to the right. The point the ROM is investigating is an untrained point as far from the training data as possible, the mean of the 160 <sup>th</sup> and 161 <sup>th</sup> time step. . . . .	163
6.18	(The POD basis functions. . . . .	163
6.19	The energy of the POD basis functions. Only the first 13 out of a possible 100 are shown. . . . .	164
6.20	The error in the ROM solution compared with the exact solution. The ROM uses just 24 POD out of a possible 400. . . . .	165
6.21	The RMS error of the ROM along with the maximum relative error both at each time step. The ROM uses just 24 POD out of a possible 400. . . . .	166
6.22	The value of the correlation coefficient between the ROM and FOM solutions at each time step. Convergence is demonstrated through using 8, 16 and 24 POD basis functions. . . . .	167

# List of Tables

1.1	In shielding and beyond, the choice of group classification represents the distribution of neutron energies within some medium. The main differences among reactor types are informed by this distribution, sometimes known as the neutron flux or energy spectra. Interactions within and between groups will be either neutron scattering or neutron attenuation through capture, with increased complexity in multi-group, multi-directional, materially inhomogeneous problems such as ASPIS. . . . .	3
4.1	1-Group Macroscopic Cross-sections in the 1-Group problem. These have been derived from the periodic table and confirmed by the code WIMS. . . . .	81
5.1	Material Geometry . . . . .	102
5.2	2-Group Material Cross-sections . . . . .	102
6.1	Run times (s) . . . . .	168



# Chapter 1

## Introduction

The aim of this thesis is to develop and apply new reduced order models (ROMs), techniques that increases computational efficiency while maintaining accuracy to problems relevant in nuclear energy. Two areas of application were outlined: Shielding and Reactor Physics.

**Shielding.** In operation and design, shielding is a key consideration. An operational reactor is a powerful source of radiation. Fission and the subsequent decays, produce neutrons and gamma rays, both very penetrating forms of radiation. The whole site must consider this to maintain the safety of personnel from possible exposure. This biological shielding is often made from various steels, void and water configurations and the problems studied here use a well known benchmark, ASPIS [3]. The calculations of the space-energy distribution of neutrons, necessary for operation and design, are known as multi-group methods in biological shielding [4]. In general free neutrons can be divided into many energy groups with 2-group, 3-group, 10-group examples presented in table 1.1 and mono-energetic all neutrons lumped into a single group while the cutting edge 47-group classification can be seen in [5]. Many applications do not require a fine division of neutron energies. The subdivision of energy regions into groups is a choice and is chosen to best reflect the application at hand. For example the Cadmium and Epicadmium distinction is a physical cut-off for absorption by cadmium. Chapters 4 and 5 solve real world shielding problems, first mono-energetic shielding and then 2-group shielding, building a generalisable framework for n-group applications. While chapters 1-3 provide background, motivation and introduce the necessary concepts to understand the reduced order models.

**Reactor Physics.** The other area of application in this thesis is reactor physics, with focus on radiation transport equations and, later, in chapter chapter 6, more general Advection-diffusion type problems. More elementary problems are used to develop the property of conservativeness in ROM solutions. The Advection-diffusion equations with source and absorption can cover a wide range of physical quantities in a system undergoing processes of diffusion, advection and absorption, heat transfer and thermal hydraulics being relevant in the study of nuclear reactors. Outside this, analysis of the Advection-diffusion equations provides insights into similar, formally identical or closely related equations in different contexts, the Fokker–Planck equation [6][7], the Black–Scholes equation [8], the Navier–Stokes equations [9] to name a few.

**Table 1.1:** In shielding and beyond, the choice of group classification represents the distribution of neutron energies within some medium. The main differences among reactor types are informed by this distribution, sometimes know as the neutron flux or energy spectra. Interactions within and between groups will be either neutron scattering or neutron attenuation through capture, with increased complexity in multi-group, multi-directional, materially inhomogeneous problems such as ASPIS.

n	2-group	3-group	10-group
1	Thermal neutrons group $0.025eV - 1keV$	Thermal neutrons $0.025eV - 1eV$	Cold Neutrons $0eV - 0.025eV$
2	Fast neutrons group $1keV - 10MeV$	Resonance neutrons $1eV - 1keV$	Thermal Neutrons $0.025eV$
3		Fast neutrons $1keV - 10MeV$	Epithermal Neutrons $0.025eV - 0.4eV$
4			Cadmium Neutrons $0.4eV - 0.5eV$
5			Epicadmium Neutrons $0.5eV - 1eV$
6			Slow Neutrons $1eV - 10eV$
7			Resonance Neutrons $10eV - 300eV$
8			Intermediate Neutrons $300eV - 1MeV$
9			Fast Neutrons $1MeV - 20MeV$
10			Relativistic Neutrons beyond $20MeV$

## 1.1 Motivation and Objectives

Numerical simulations are a key part of understanding many physical systems in various fields such as climatology, economics, biology and engineering. Simulations often involve a large number of partial differential equations (PDEs). Typical discretization techniques yield a system of  $n$  ordinary differential equations (ODEs). This can make the number of degrees of freedom large [10]. Whence a complicated enough problem will be prohibitively expensive to compute: both in storage and CPU cost. A diversified approach to energy generation is the only viable strategy to meet the increasingly complex needs of the globe. Nuclear Power provides a large carbon-free base load [11]. With developments in the design of next generation plants and fuels, comes the need for high fidelity computational modelling [12].

The application of Reduced Order Modelling (ROM) is fast becoming an established tool in many industries providing a speed up and computational cost reduction while maintaining desirable accuracy. This field has already been employed in many nuclear specific problems. For motivation we will briefly present a few triumphs from nuclear specific problems as well as problems in the wider engineering context.

**Transport** In Neutron and photon transport [13] demonstrated the first Reduced Order Model (ROM) that efficiently resolves the angular dimension of the time independent, Boltzmann Transport Equation, applying this discretisation to a 2D kinked duct shielding problem and an infinite pincell model noted for the complex angular flux profiles it generates [14]. Similarly an angular ROM has been applied to model radiative transfer in non grey media: specifically air/H<sub>2</sub>O mixture flowing in a square differentially heated cavity [15]. Impressively, the paper [16] produced fast predictions of reactivity and neutron distributions within reactor cores with temperature variation and control rod adjustments efficiently integrated into the model through ROMs. Additionally ROMs have been employed in the non-linear coupling between neutronics and heat transfer phenomena for sub-



channel models with geometric and physical quantities being used in ROM parameterisations [17].

**Design** Engineering design focused applications such as, rapid prototyping [18] [19], sensor placement [20] and experimental design [21] have all leveraged ROMs for better, more efficient techniques. In aerospace, shape optimisation ROMs [22] and [23] were used to design and optimise aircraft wings, reducing reliance on expensive wind tunnel experiments.

**Oceanography** In models of convective boussinesq flows, fluid flow models ignoring density differences except in terms multiplied the acceleration due to gravity, ROMs have been successfully used both in the abstract [24] [25] and in ocean modelling [26]. Successes have been found in more complex fluid flows. In large scale upper ocean circulation [10] uses a ROM technique to assimilate weather forecasting data in the context of an optimal control problem, oceanic general circulation that fits real observations in a fixed time interval.

**Geothermal/Petrochemical** ROMs have been used in the instrumentation systems for geotechnical investigation, environmental site assessment and mineral exploration. Specifically systems that transmits and receives electrical signals along different positions within a borehole. A borehole induction modelling ROM [27] reduced costs of the computation several orders of magnitude compared with established practices. In Reservoir management and optimisation, a 3D ROM for two-phase flow through porous media [28] made a five-fold speed up on standard approaches. In [29] standard approaches for maximising a field's potential recovery are adaptively refined with a ROM, a cost reduction 96% with only 1% difference in solution quality when compared with a new standard calculation.

**Optics** In the simulation and design of semiconductor electronics, specifically photonic crystal design [30] achieved a speed up while maintaining accuracy of a band gap optimization problem with nested grids coupling a state equation and evolution equation for the system. The paper [31] maximises

the energy output of mode-locked lasers through use of ROMs. Quantum eigenvalue problems involving the Schrödinger equation subjected to electric potential and energy band variations induced by electric fields, photons, molecular structures and defects have used ROMs for speed up of large scale problems, for example [32].

**Power grids** Computational complexity of large power system networks for example non-linear swing dynamics [33] and maximum power tracking pitch controller for grid connected wind turbines [34] have benefited from use of ROMs. Many of these applications being a combination of real-time, hugely complex, expensive and non-linear.

**Air pollution** Real time models of the build environment have yielded to ROMs. In [35] large eddy simulation to resolve turbulence elegantly handles the complexity of non-linear dynamics with a quadratic expansion method. Work for large regional scale pollution modelling tools have been completed using ROMs, the speed up providing a rapid response tool [36].

**Medicine** ROMs with fluid-structure interactions models can help us better understand response of aneurysms [37] and haemodynamics [38].

As such this is an active research topic with variants of ROM techniques being successfully applied in nuclear realm as well as a broad range of other fields. The contributions of this thesis build on this via addressing limitations of a specific and particularly versatile family of ROMs, Non-intrusive Reduced Order Models (NIROMs). With this in mind, the importance and potential in addressing coupling and conservation in shielding and neutron transport is now presented.

## 1.2 Contributions

This thesis explores novel ways of using Reduced Order Models in the analysis of Nuclear Reactors, neutral particle radiation transport, shielding and the Advection-Diffusion equation. The emphasis of the thesis is Non-intrusive Reduced Order Models (NIROMs), that is a type of ROM that avoids projection and solving expensive governing equations after the ROM training has been completed: first realised in [1]. Chapters 3,4 and 5 are exclusively working with NIROMs, where as chapter 6 can in principle be extend to more established intrusive, projection based ROMs. This is expanded in the appendices, with application left to future work.

Along side a review of the current literature and a comprehensive presentation of the background theory, chapter 2, including more elementary Non-intrusive Reduced Order Models (NIROMs), chapter 3, the novel contributions of the thesis are:

1. Novel coupling of NIROMs. Several models with absorption and 1-group scattering are employed to build a library of individual material reduced order models (ROMs), then using a non-intrusive ROM technique (NIROM) are coupled together to model more complex material configurations.
2. This novel ROM coupling is then applied in an easily to generalise way to 2-group scattering and absorption models and validated against a known benchmark: the ASPIS shield [3].
3. A novel conservative numerical method is derived, solving the Advection-Diffusion equation that increases resolution additively. This is further expanded becoming two-dimensional and including source and absorption terms.
4. This method is then applied to generate data for a NIROM. Now the conservative properties of the numerical method are conferred on to the NIROM solutions.

**Coupling** The coupling of simple models to model more complex configurations is a common technique, used across many numerical methods and applications but yet to be explored in Non-intrusive Reduced Order Models. The coupled models presented in chapters 4 and 5 are trained on analytical, closed form solutions providing a proof of principle for the coupling of NIROMs. This demonstrates that experimental data or more expensive models with the same parameterisation and boundary conditions, as informed by the scattering physics, can be successfully coupled and speed up. The preliminary work with NIROMs, chapter 3, experiments with interfaces as just another parameter of the NIROM with the limited scalability further justifying exploring ROM coupling as an alternative.

**Conservation** The other theme in these achievements, addressing conservation, is also highly desirable in numerical methods. Physical conservation laws are associated with a symmetry in the underlying physics with continuity equations and transport equations being prevalent in most engineering applications [39]. The way conservation has been addressed in this work is a strong form of conservation law in that: local conservation law (flow or flux in and out of a local volume is a conserved quantity) implies control over global conservation through a series of partial sums that also increases resolution. Previously ROMs have addressed conservation through intrusive projections with NIROMs not directly addressing conservation, instead sampling more parameters at boundaries through a Smolyak grid to get acceptable accuracy [40]. As such this thesis provides a novel contribution, addressing conservation for NIROMs as a mathematical certainty.

## 1.3 An overview of current Reduced Order Modelling literature

The specific concepts and methods needed to understand the contributions of the thesis will be expanded in chapter 2. For now we will briefly, survey the work that has already been done in the field of reduced order modelling.

A wealth of reduced order modelling (ROM) techniques exist with articles reviewing and surveying ROM techniques: system-theoretic approaches with their origins in control theory and single progressing have found success in electronics, reviewed in [41], [42], while projection-based, reduced basis approaches have been very suitable to problems with many complex PDEs such as fluid flow and multi-physics, surveyed in [43],[44], [45],[46], with machine learning neural networks also proving a promising ROM technique [47]. Amongst these approaches for constructing a ROM proper orthogonal decomposition (POD) [48],[49] is becoming increasingly prevalent for many disciplines with the work in this thesis being build on applications, variations and improvements of the POD method. This is an exciting method in reduced order modelling chiefly because the POD method captures of the greatest possible information of a system for a given dimensionality reduction.

The vast majority of POD based papers referenced here are accessible enough to provide an introduction however for current, accessible larger texts for reduced order modelling, a good place for introductory study is the book [50] and associated series of online open-source lectures. A more in depth text featuring a-priori analysis of convergence, stability and non-linearity with a sophisticated level of mathematical vigour applied to established projection based ROMs would be the book [51] or the online handbook [52].

Mathematically speaking when constructing a ROM we are finding a subspace to represent high dimensional data in a low dimensional sub-space. The first instance of a ROM in this sense has its origins in the work of Lawrence Sirovich [53], [54], [55], using ROM to research kinetic theory and its connection to supersonic flow, turbulence and the dynamics of coherent structures. The

underlining notion is that structures in high quality data for a set of problems, either through experiment or high fidelity simulations, can be used to recreate cheap solutions to the same problems for some new parameter or time instance from a low dimensional sub-space of the high quality data. We call the model used to obtain high fidelity training data for ROMs a full order model (FOM).

Broadly, to construct a ROM we have two stages: we must find a low dimensional sub-space of the training data obtained with the full order model (FOM), then find new reduced solutions for untrained parameterisations and time instances.

### **1.3.1 Intrusive Reduced Order Modelling literature**

The most prevalent ROM approach is the use of Proper Orthogonal Decomposition (POD) as a projection-based, intrusive method. Success with POD is not limited to the field of reduced order modelling. The resulting multitudes of confusing nomenclature and initialisms and should be cleared-up: the Karhounen–Loeve expansions in signal analysis and pattern recognition [56], principal component analysis (PCA) in statistics and some data science applications [57], empirical orthogonal functions (EOF) in geophysical fluid dynamics and meteorology [58] and the Singular Value Decomposition (SVD) in linear algebra [59]. From this point on the terminology we will use is POD when referencing reduced basis functions or specific POD-based methods with the SVD only be mentioned in reference to the decomposition of a specific matrix.

In reduced order modelling the POD method finds a basis that spans a low dimensional sub-space of the high fidelity training data and then uses Galerkin projection to get new, cheaper, "reduced" governing equations: solving them for untrained parameterisations and time instances [60]. Using the governing equations of the full order model maintains the properties and characteristics of the full order model; for example stability and conservation. We call methods reliant on projection in this sense "intrusive" as they refer to the original governing equations.

The two main issues with the convectonal approach are stability [61] and inefficiency in non-linear terms [62] with early work attempting to address both piece-wise [63]. With Galerkin projection POD based approaches there are some problems where spurious oscillations and Gibbs-like phenomena can degraded ROM solutions [64]. Concepts such as the Petrov–Galerkin method [65],[66], calibration, regularisation and Fourier expansion overcome many issued with stability.

There are stabilisation approaches that give good results but are very problem specific: [67] addresses the closure problem of the discarded POD basis functions in turbulence models for instance. Interesting work has been done on the sensitivity of POD methods and how close the attractors and phase space of ROMs match the FOMs in the context of fluid flow problems [68]. Control of the stability and asymptotics is been discussed [69],[70], avoiding erroneous states in ROM applications where long-time integration is necessary. Numerical stability is also dependant on the inner product used in the Galerkin projection with [71] addressing this using linear constraints on the projection [71]. Other stabilisation methods for the inner product of POD-Galerkin ROMs have been very problems specific [72],[73].

As we have seen with the many fluid-flow applications of POD, detailed features in high fidelity FOM data including non-linear behaviour is captured well with a POD basis. The problem lies in recovering the reduced solutions via projection. Without a strategy to separate and over-come the non-linear terms in the projection, POD is limited to linear and bi-linear problems [49],[74].

Fortunately inefficiency in non-linear terms can be overcome with techniques such discrete empirical interpolation method (DEIM) [75],[60], [74] where an interpolation of the non-linear quantities in a reduced domain includes only a small number of elements. Another approach handling non-linear terms in POD-Galerkin is to approximation the non-linear terms with quadratic expansion of the non-linear term [76]. The paper [77] convincingly demonstrates a hybrid approach of DEIM and quadratic expansion, providing significant improvements for fluid flow problems in comparison with either

approach alone. Gauss–Newton with approximated tensors method (GNAT) [78],[79] works well at the discrete level and is very suitable for parallel computing but may be inconvenient with changes at each time step meaning the ROM cannot generally be expressed as a low-dimensional ODE.

In stark contrast with intrusive ROMs, Non-Intrusive Reduced Order Model (NIROM) require no knowledge of the physical system and in fact are entirely data-driven: making use of experimental data or FOM data indiscriminately thus avoiding issues like stability or inefficiency in non-linear terms.

### **1.3.2 Non-Intrusive Reduced Order Modelling literature**

An alternative to intrusive ROMs is to use a Non-Intrusive Reduced Order Model (NIROM) [1]. The NIROM method is data driven, as such the NIROM does not require us to solve more governing equations. This is exciting as ROMs can be constructed straight from the full order models in state of the art commercial codes. Work with FOM legacy codes or software without access to the source code is an attractive reason to use a NIROM: avoiding difficult or impossible modifications, ports or APIs that may be needed to work with them and a projection based ROM.

The NIROM approach used in the rest of this thesis is based on Radical Basis Interpolation (RBF-interpolation) has been applied successfully in [40],[80],[81]. The RBF-interpolation is combined with the POD basis as a means of calculating POD coefficients, elegantly construing ROM solutions for new parameterisations or time instances. This is detailed in chapter 2.

This RBF-interpolation can be improved via renormalising the parameterisation [82],[83] and as such most of the ROMs in this work are on unit domains and normalised parameterisations: physical units re-mapped in post-processing steps. The paper [84] expands the family of interpolation based NIROMs, using Kriging interpolation in a way analogous to the RBF-interpolation method.



The paper [85] uses a meshless moving least-squares approach to solve a particularly challenging problem: incompressible magnetohydrodynamic flow. This method depends on high-order accuracy for integrals in variational weak form however. Other data-driven approaches include [86] which is based on a genetic algorithm and [87],[88] using deep neural networks. The disadvantage of the such methods is the intensive training time. Excitingly the paper [88] addresses the same problem as chapter 6: lack of guaranteed conservation in NIROM solutions. The paper does this using deep learning, whereas here we guarantee conservation for NIROM solutions with the more simple, quick to train RBF-interpolation approach to NIROM.

The RBF-interpolation NIROM technique has two distinct stages: a offline stage where a matrix kernel and training data are assembled and an rapid online stage that yields a solution for new untrained inputs. The online stage is rapid and thus suitable for developing a new coupling scheme. We therefore aim to develop and apply this new reduced order modelling techniques to well understood nuclear specific test problems.

# Chapter 2

## Background Theory

In this chapter we will briefly discuss terms and concepts need to understand the methods presented and developed in later chapters in this thesis. Firstly through reviewing a few common numerical methods and concepts of numerical analysis, then the background mathematics of reduced order modelling and finally reactor physics models needed in shielding and neutron transport.

Both the field of reduced order modelling in general and radial basis interpolation specifically used in our particular class of reduced order models are still emerging fields. As such there are many acronyms and multiple names and modes of understanding. Here we will endeavour to bring clarity through pairing the broad motivations and themes with examples. When concepts have multitude acronyms, this will be initially clarified and minimally referenced thereafter with preference to conventions from projection based POD reduced order models. Terminology is introduced in *italics*.

### 2.1 Numerical methods

In the most general sense, a *numerical scheme* or *numerical method* can be thought of as a recipe or algorithmic description which when successfully applied solves a mathematical problem via approximation. The study of numerical methods is called *numerical analysis*. The practical implementation of a numerical scheme is called a *solver* and is computed with software and code. This is done with provision for setting up, inputting the problem and outputting the solutions in a useful way.

Areas of study in numerical analysis include many sub-disciplines. Some examples featured in this work are:

- Solving eigenvalue or singular value problems, for example the singular value decomposition of a matrix.
- Systems of linear equations, for example solutions and approximations of the matrix equation  $Ax = b$  where  $A$  is an  $m \times n$  matrix,  $x$  is a column vector with  $n$  entries, and  $b$  is a column vector with  $m$  entries.
- Interpolation, extrapolation, and regression, for example using radial basis interpolation.
- Systems of ordinary (ODEs) and partial differential equations (PDEs).

Initially the most important area in numerical analysis for this thesis is the solution of ordinary (ODEs) and partial differential equation (PDEs). Such techniques being sometimes known as "numerical integration" as they "integrate" the differential equation in some sense. The physical problems in this thesis, shielding and neutron transports can all be posed as differential equations.

## Upwinding, an illustrative example

We will present an example numerical scheme called *Upwinding* to solve an important differential equation called the advection equation. A version of an Upwinding scheme is vital to the work in chapter 6.

Advection is the bulk motion or transport in 1-dimension and can be thought of as changes in density or field  $T$ . A small change in time  $\Delta t$  and space  $u\Delta t$  can be made:

$$T(x, t + \Delta t) = T(x - u\Delta t, t) \quad (2.1)$$

Although advection is a simple problem that can be solved analytically via the method of characteristics and for some initial condition  $T_0 = T_0(x, 0)$  there

is a unique solution:  $T = T_0(x - ut)$ , some problems do not have known analytical solutions, for example the Navier-Stokes equations which govern most practical fluid dynamics applications [89].

A Taylor series expansion of both sides yields a partial differential equation (PDE) which can be discretized:

$$\forall u, \quad \frac{\partial T}{\partial t} + \nabla \cdot (uT) = 0 \quad (\text{PDE: Continuous}) \quad (2.2)$$

$$u > 0 \quad \frac{\tilde{T}_i^{n+1} - \tilde{T}_i^n}{\Delta t} + u \frac{\tilde{T}_i^n - \tilde{T}_{i-1}^n}{\Delta x} = 0 \quad (\text{Upwinding scheme: Discrete}) \quad (2.3)$$

$$u < 0 \quad \frac{\tilde{T}_i^{n+1} - \tilde{T}_i^n}{\Delta t} + u \frac{\tilde{T}_i^n - \tilde{T}_{i+1}^n}{\Delta x} = 0 \quad (\text{Upwinding scheme: Discrete}) \quad (2.4)$$

where  $T$  is the field being advected,  $\tilde{T}$  is a discrete approximation of  $T$ ,  $t$  is time,  $\nabla$  is the gradient operator and  $u > 0$  is the velocity. This is shown in figure 2.1.

*Discretization* is the process of converting continuous mathematical equations into discrete equations. Analytical solutions are represented continuously in all space. Numerical solutions are represented on a discrete set of points called a mesh [90].

The discrete equation is solved on a mesh in time and space. A uniform mesh takes the form:

$$t_n = t_0 + n\Delta t \quad x_i = 1 + \Delta x \quad (2.5)$$

for some index  $n = 0, 1, \dots, T_{Final}$  and  $i = 0, 1, \dots, M$  on the domain  $[0, L]$  with  $\Delta x = \frac{L}{M}$ .

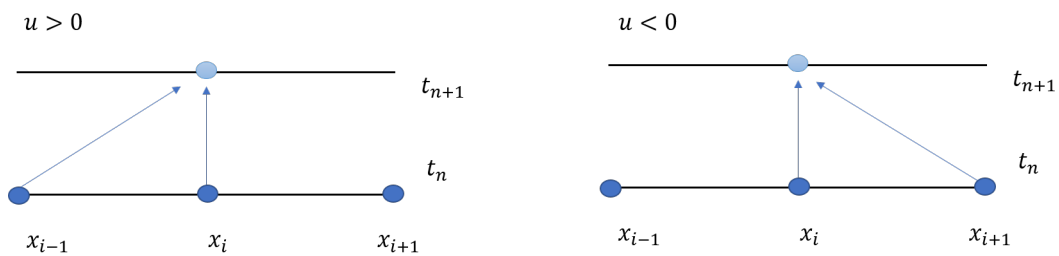


**Figure 2.1:** A schematic visualisation, called a *stencil*, showing how the Upwinding scheme propagates in time and space.

Upwinding has the following useful properties:

- *Conditionally stable*: errors are damped on the condition  $|\frac{u\Delta t}{\Delta x}| \leq 1$ , the Courant–Friedrichs–Lewy condition, but blow up outside this region.
- *First order*: First order derivative terms highest used, Specifically  $p = 1$  and the truncation error behaves as  $O(\Delta x^p)$  in big-O-notation .
- *Bounded*: the error is bounded.

In the derivation of the numerical scheme, the continuous terms of the advection equation can be replaced by discrete terms via inspection from a possible stencil. A more general approach to deriving numerical scheme is using Finite volume method. There both sides of the (PDE) are integrated and replaced with quadrature methods for approximating surface and volume integrals. This is the approach used in the derivation of the Sub-grid Scale model in chapter 6.

Other popular techniques for numerical integration include:

- Finite element methods: Dividing the domain into small pieces and finding local solutions that satisfy the differential equation within the boundary of this pieces [91].
- Finite volume methods: One differential equation is replaces be lots of small integrals that can be dealt with via quadrature [92].
- Monte Carlo methods: Other methods use a fixed grid. Here the integrand is evaluated at random points [93],[94],[95],[96].
- Meshless: There is no mesh, each point is tracks its interactions with its neighbours [97].

In this work we will mostly be using raw data or PDE solutions from finite volume methods as they are widely known and simple to work with. These solutions will be necessary to build the reduced order model and the

techniques for analysis of numerical methods are applicable to the ROM techniques in this thesis. Practical actions like parallelisation can improve most methods so that each processor can work in parallel. Some techniques can focus numerical efforts where they are most needed such as Domain decomposition methods breaking the problem down or Adaptive meshes which can add and removes detail where the problem necessitates [98],[99].

## Numerical analysis

We use an iterative approach in two distinct respects in this work: the reduced order models in chapters 4 and 5 are coupled (joined together) through an iterative scheme and also the methods in chapter 6 uses an iterative approach called successive over-relaxation [100]. Iterations index repeated steps of the algorithm and a numerical solver will typically provide better and better approximations to the solution in a step-wise manner or *iterate* a numerical scheme towards a solution.

The process of getting closer to the true solution is known as *convergence*. When the numerical scheme is approaching the correct solution then we see that the error between the true, exact solution and the solutions offered by the numerical scheme closes. If this change is bellow a certain value we call the *tolerance*  $\epsilon$  we consider the solution to be the correct. We say the solution has *converged*, whence  $|T_{exact} - T_{approximation}| < \epsilon$ . If this does not happen then we know the solution is not getting any better and we would need to investigate the methodology.

There are various desirable properties and ways to compare numerical schemes. If convergence is *fast* then processing time is saved and thus a solution is found more rapidly. Although speed is an important feature it is often more important to find a solution even when the initial guess is far from a good solution. We call this property *robust*. If the solver is not robust we may not achieve convergence at all. A scheme is *stable* if convergences steadily to a solution and dampens rather than magnifying approximation errors. When his does not happen it many get farther from the solution in which case we say the solutions has *diverged*. It many also stop at a point above the tolerance,

we say the scheme has not suitability converged. In some numerical methods stability can be precisely quantified via Von Neumann stability analysis where the numerical error decomposed through a Fourier series.

Numerical methods are approximations and as such understanding sources of inexactness is vital to obtain high levels of *accuracy*. While precise values of inaccuracy are specific to the application at hand, understanding how they are introduced is important to compare and develop numerical schemes. For example the use of a truncated series, ignoring higher order terms, will be a source of some inexactness referred to as *truncation error*. Many numerical schemes over estimate diffusion and this is called *numerical diffusion*. This can sometimes be desirable to avoid singularities where they might be unwanted. An other important point to note is the precision of the values stored by the computer. The floating-point values will be set in some byte size which will correspond to a rough number of decimal places as storage may often be not base ten. There will always be some trade-off between computing time and precision. The complexity and hence the number of operations a computer processor has to perform will vary considerably between different numerical schemes. Large operations such as populating large matrices or matrix inversions may only need to be done once in the whole calculation or multiple times in a single iteration. This must all be taken in to account when building a viable solver. The overall workload of the processor is called the *computational cost*. This may be measured in overall computing time, storage, number of iterations or time complexity. It is often helpful to understand the worst-case behaviour of a scheme and this is done through looking at the asymptotic behaviour of the complexity in terms of big-O notation or order. This is of particular importance in the field of reduced order modelling .

## 2.2 Reduced order modelling

As the emphasis of this thesis is to explore reduced order modelling in nuclear specific problems, we introduce some broad definitions and conceptualisations before getting in to the mathematics.

**Full order model:** A full order model is the mathematical model that undergoes reduction. The original model is often unfeasible, complex or expensive in particular if the application necessitates near real time solutions. Many computational fluid dynamics or neutronics applications have degrees of freedoms upwards of  $10^6$ . To generate the reduced order model it is often necessary to make limited and carefully chosen runs of the full order model.

**Reduced order model:** A reduced order model (ROM) sometimes know as a model order reduction is a technique for reducing the computational complexity of mathematical models in numerical methods. Complexity has many precise meanings in different scientific fields. For our purposes we consider a large number of dimensions or degrees of freedom, high non-linearity or resources required to run the model: importantly time and memory. Reduced order modelling aims to address this and in order to fulfil this reduced order models must:

- Have a small approximation error compared to the full order model
- Maintain the desired properties of the full order model such as stability
- Be computationally efficient and robust.
- The reduced order model should have the same capabilities as the full order model.

The ROM can then be thought of as a black box meeting these characteristics, see figure 2.2. The models should share input variables, boundary conditions and parameterization for example, but should be much quicker or cheaper



than a new run of the full order model for the same initial problem set-up. Although the scope of reduced order models can be more sophisticated, a helpful conceptualisation is the language a simple control theory problem. Numerical models will have an associated state-space dimension or number of degrees of freedom with a successful reduced order modelling technique reducing one or both of these while being a good approximation to the original model.

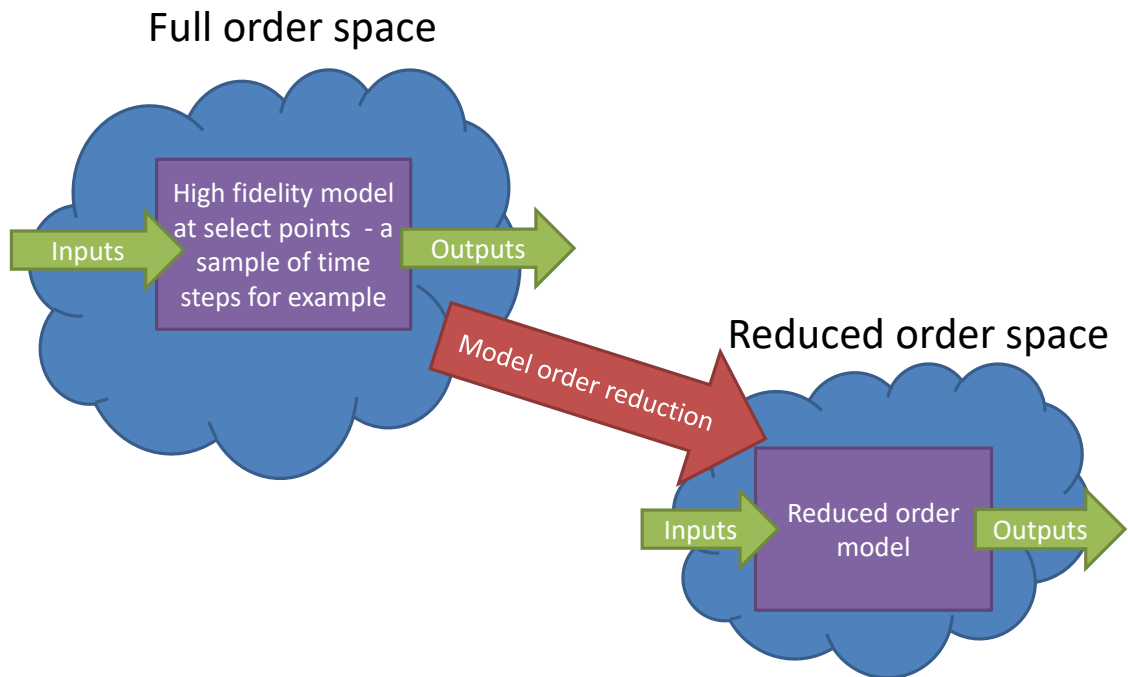


**Figure 2.2:** An overview of the reduced ordering modelling process. The full order model's state space dimension or number of degrees of freedom is reduced forming an approximation to the full order model, namely the reduced order model.

The solutions from the full order model that are used in the construction of a reduced order model must be pre-calculated and stored. We structure these solutions in the *snapshot matrix*. The data from the full order model can be collected and stored in a snapshot matrix. Each column is called a snapshot and contains the high fidelity, full order model solutions. This is typically organised such that for some snapshot matrix with entries  $i, j$ , the same variable or multiple variables are stored in  $i$ th row position. If the ROM is testing for time as its ROM parameter for example, the columns (each

individual snapshot) would be full order solutions at different time steps. The purpose of the ROM would then be a black box model that takes new times unknown by the snapshots but in between their corresponding times, will call the parameter the ROM tests  $\hat{p}$ , and returns a new, reduced solution that rapidly approximates what a full order model would recover for the time step  $\hat{p}$ . The choice of which data is included in the snapshot matrix is called the model training. You can only extrapolate outside the area which the model was trained so far. All choices of parameter inside the training space should be viable for the application at hand.

Offline and Online stage: The reduced order model process is divided into two sections, a longer and expensive offline stage where the data from the full order model is collected in the snapshot matrix and an online stage where new ROM solutions are rapidly generated from a chosen ROM technique [101].

Intrusive and non-intrusive: Intrusive reduced order models are projection-based reductions. A basis in which new solutions can exist is found and the coefficients to reconstitute this basis are then obtained through projection of this basis onto the original physics of the full order model. A non-intrusive reduced order model (NIROM) does not require this projection, it can be a data driven way to combine the reduced basis for new solutions.

The specific ROM techniques in this thesis use a non-intrusive reduced order model (NIROM). To understand how this method is implemented we must take an aside to look at two concepts in depth: POD basis functions and radial basis interpolations.

### **2.2.1 Proper Orthogonal decomposition (POD)**

Reduced order models find solutions in a reduced space that is closest, in a least squares sense, to the space described by the training data in the snapshot matrix [102]. These are vector spaces and thus is spanned by a

basis. The mathematical task at hand in developing ROM techniques is to find coefficients to reconstruct new solutions from this basis.

We introduce proper orthogonal decomposition (POD) [103]. The POD basis functions are obtained by first forming a snapshot matrix  $\mathbb{X}$  where each column is the solution of the model equations at each time step.

The goal of POD is to find a set of orthogonal basis functions  $\{\Phi_s\} \in \{1, 2, \dots, N_S\}$ , such that;

$$\frac{1}{S} \sum_{s=1}^{N_S} |\langle \mathbb{U}, \Phi_s \rangle_{L^2}|^2, \quad (2.6)$$

is maximised subject to

$$\sum_{s=1}^{N_S} |\langle \Phi_s, \Phi_s \rangle_{L^2}|^2 = 1, \quad (2.7)$$

where  $\langle \cdot, \cdot \rangle$  is the inner product associated with the  $L_2$  norm. As introduced in [55] the singular value decomposition (SVD) can be used to find a solution for this optimisation problem [104],[105].

**Theorem.** *Singular Value Decomposition - SVD*

Every matrix  $A \in \mathbb{C}^{m \times n}$  has a singular value decomposition,  $\mathbb{U} = U \Sigma V^*$ . Where,

- $U, \Sigma, V^*$  are unique.  $V^*$  is Hermitian transpose of  $V$ .
- $U^*U = I, V^*V = I$  that is,  $U, V$  are unitary. If  $U \in \mathbb{R}^{n \times n}, V^* \in \mathbb{R}^{m \times m}$  entries are orthonormal columns.
- $\Sigma \in \mathbb{R}^{n \times m}$  is diagonal.

Singular value decomposition is a generalisation of spectral decomposition of a positive-semi-definite matrix. Intuitively,  $\mathbb{U} = M$  represents a linear transformation between for vector spaces. We see in figure 2.3 the SVD does this transformation in three steps, a rotation or reflection, a scaling and a further rotation or reflection.

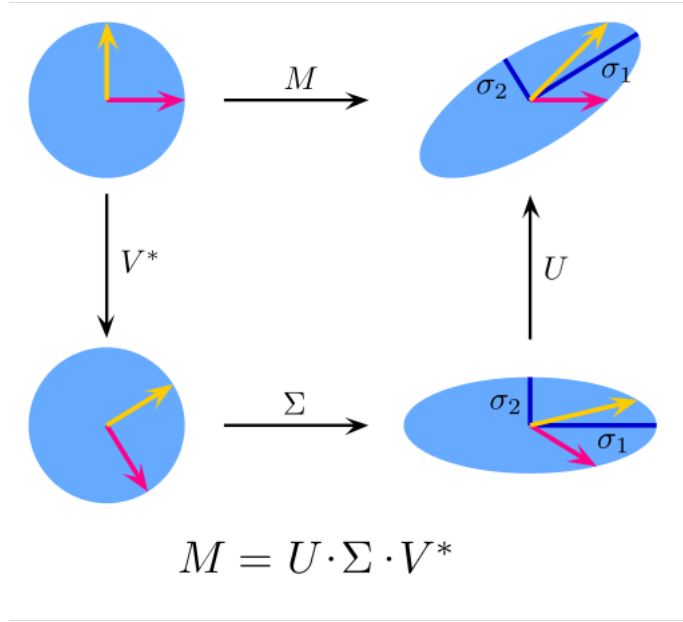


**Figure 2.3:** The singular value decomposition (SVD) can be visualised geometrically in three steps, a rotation or reflection  $U$ , a scaling  $\Sigma$  and a further rotation or reflection  $V^*$  [2]

The POD basis vectors are the column vectors of the matrix  $V$ ,

$$\Phi_s = \frac{1}{\sqrt{\lambda_s}} U V_{:,s}, \quad (2.8)$$

where  $\lambda_s$  are the non zero entries of the singular value matrix  $\Sigma$  and form a monotone decreasing sequence. Thus an optimal basis of size  $P$  is the first  $P$  columns of  $U$ . We are optimal in the sense the basis the closest to  $U$  for size  $P$  in the Hilbert-Schmidt norm. The information captured by POD basis functions can be quantified the normalised cumulative sum of the singular values:

$$I_{Energy} = \frac{\sum_{i=1}^t \lambda_i^2}{\sum_{i=1}^{N_S} \lambda_i^2}, \quad (2.9)$$

which approaches 1 as  $t$  is increased. This is often called the energy of the POD basis. The reduced solution variables  $y$  for some test parameter that the ROM is investigating  $\hat{p}$  can be expressed through POD by:

$$y(x, \hat{p}) = \sum_{i=1}^{t < n_{dof}} \alpha_i(\hat{p}) \Phi_i(x), \quad (2.10)$$

where  $\alpha_j$  are coefficients arising from a ROM technique and  $n_{dof}$  is the size of a snapshot vector, the columns of  $\mathbb{X}$ . The coefficients in this work will be obtained through Radial basis interpolation.

### 2.2.2 Radial basis interpolation

Radial basis function and Radial basis interpolations: A radial basis function is a real valued function that only depends on the distance between the input and some fixed distance  $c$ . That is:  $\phi(\mathbf{r}) = \phi(\|\mathbf{x} - \mathbf{c}\|)$ . The weighted sum of these functions can be used to approximate other functions [106]. In the context of this work we approximate the coefficients of the reduced basis. The functions used as radial basis functions are sometimes called characteristic functions and can be any real valued smooth function of a distance, called centres in some literature. Common functions include:

- Gaussian curve:

$$\phi_{RBF}(r; \sigma) = e^{-\frac{r^2}{\sigma^2}} \quad (2.11)$$

- Inverse quadratic curve:

$$\phi_{RBF}(r; \sigma) = \frac{1}{r^2 + \sigma^2} \quad (2.12)$$

- Multiquadratic curve:

$$\phi_{RBF}(r; \sigma) = \sqrt{r^2 + \sigma^2} \quad (2.13)$$

- Inverse multiquadratic curve:

$$\phi_{RBF}(r; \sigma) = \frac{1}{\sqrt{r^2 + \sigma^2}} \quad (2.14)$$

- Polyharmonic spline:

$$\phi_{RBF}(r) = r^m, \quad m = 1, 3, \dots \quad (2.15)$$

$$\phi_{RBF}(r) = r^m \ln(r), \quad m = 2, 4, \dots \quad (2.16)$$

The parameter  $\sigma$  is the characteristic length [107]. With Gaussian characteristic function this is a shape parameter that tunes the shape of the function so that it can smoothly change from a flat curve to a thin spike [108]. The functions are chosen such that the interpolate exists and is unique. This uniqueness acts as a classifier and is a very simple form of neural network. Series expansions: The ROM solutions are in most techniques reconstructed through a series expansion. The series expansion is a sum of two parts: a basis vectors are formed by the reduced basis  $\phi(x)$  that spans the space the reduced order model solutions  $y(x)$  must be members of and the ROM coefficients  $\alpha$  which are unknown until the Online stage of the ROM and specific to the ROM technique used.

$$y(x_i) = \sum_i \alpha(x_i, p) \phi(x_i) \quad (2.17)$$

where the number of terms in the series is less than the degrees of freedom of the full order model.

We will briefly look at an example of how to use radial basis functions to interpolate an elementary function.

Let  $f(x) = \frac{\sin^2(3\pi\|x\|)}{\|x\|-1}$  and also let  $x_i = \frac{i}{35}, i = 0, 1, \dots, 35$  be 36 equally spaced points on the unit interval. The approximation for the elementary function  $f(x)$  is then:

$$f(x) \approx \widehat{f(x)} = \sum_{i=0}^{35} w_i \phi(\|x - x_i\|) \quad (2.18)$$

where  $\phi$  is a choice of radial basis function and the weights  $w_i$  are chosen by forming the radial basis kernel and solving the inversion of the matrix equation:

$$\begin{pmatrix} \phi(\|x_0 - x_0\|) & \phi(\|x_1 - x_0\|) & \cdots & \phi(\|x_{35} - x_0\|) \\ \phi(\|x_0 - x_1\|) & \phi(\|x_1 - x_1\|) & \cdots & \phi(\|x_{35} - x_1\|) \\ \vdots & \vdots & \ddots & \vdots \\ \phi(\|x_0 - x_{35}\|) & \phi(\|x_1 - x_{35}\|) & \cdots & \phi(\|x_{35} - x_{35}\|) \end{pmatrix} \begin{pmatrix} w_1 \\ w_2 \\ \vdots \\ w_{35} \end{pmatrix} = \begin{pmatrix} f(x_1) \\ f(x_2) \\ \vdots \\ f(x_{35}) \end{pmatrix} \quad (2.19)$$

The solving this matrix equation is equivalent to setting the approximation equal to the function  $f(x_i)$  for all  $i$  and solving for the weights. Note that the approximation  $\widehat{f(x)}$  is a function of  $x$  not  $x_i$  and is thus a mesh-free method of interpolation. The nodes need not be equally spaced or even structured and the interpolation works well for large numbers of degrees of freedom or high dimensions. Radial basis interpolation has been used to interpolate differential operators to solve PDEs such as the Navier-stokes equations. In the figures 2.4,2.5,2.6 we show the interpolation of  $f$  with best and worse cases of characteristic length. A Gaussian characteristic function is used.

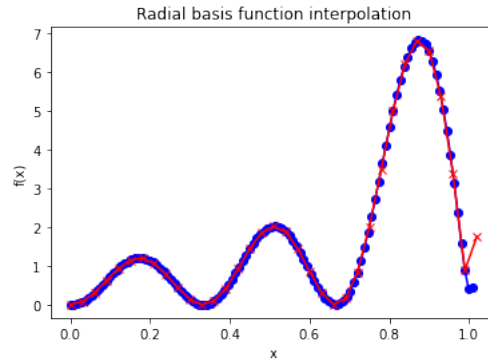


**Figure 2.4:** The interpolation is good when the characteristic length is suitably chosen. However you can still see a Runge's phenomenon (or Gibb's phenomenon) at the far right of the domain. Here  $\sigma = 0.1$ , the red curve is the original 36 data points and the blue curve is an attempted radial basis function interpolation for 113 points.

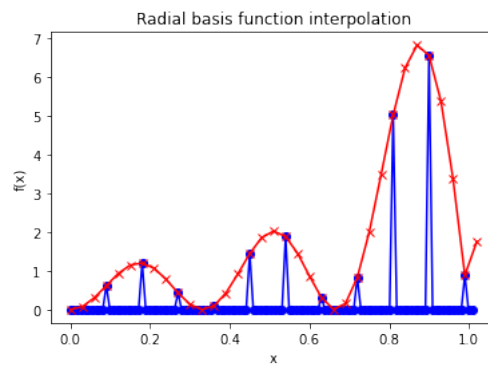


**Figure 2.5:** The interpolation fails if the characteristic length is too small. The radial basis functions become narrow and the interpolation kernel matrix becomes close to the identity matrix. The solution will be close at the interpolation point and almost zero everywhere else. Here  $\sigma = 0.001$ , the red curve is the original 36 data points and the blue curve is an attempted radial basis function interpolation for 113 points. We call this the bed-of-nails case.

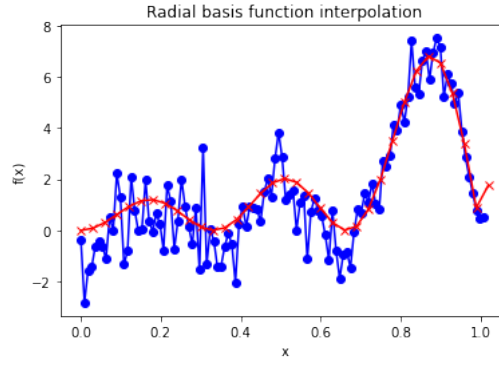


**Figure 2.6:** The interpolation is noisy when the characteristic length is too large. The radial basis functions become too flat and give little information. Here  $\sigma = 0.8$ , the red curve is the original 36 data points and the blue curve is an attempted radial basis function interpolation for 113 points.

You can see that the choice of characteristic length in radial basis interpolation can yield very varied results. Practically the choice should be such that the matrix equation formed in interpolation is close to being ill-conditioned so as to avoid the bed-of-nails case but not so ill-conditioned as to make the matrix equation uncomputable or the interpolation noisy and featureless. This can be heuristically managed by choosing a length of physical significance to the problems scale or keeping the condition close but a few orders of magnitude above the machine precision. This is often tracked as part of matrix solvers. It is important to note that in some literature the characteristic length is written as reciprocal to the presented framework in equations (2.11) through to (2.16) and the phenomena in figures 2.4, 2.5, 2.6 would then need different characteristic lengths to be reproduced. In this work the NIROM makes use of radial basis interpolation to find ROM coefficients  $\alpha$  for corresponding POD basis functions.



## 2.3 Non-Intrusive Reduced Order Models

Non-Intrusive Reduced Order Model (NIROM) approach for a single parameter is presented. Here radial basis (RBF) interpolation is used to find POD basis coefficients. This is done without loss of generality as the single parameter can be a vector of parameters and possible time-stepping applications may be considered as just another parameter. We therefore present the algorithm in general, in "steady state" with specific worked examples and visualisation of the NIROM algorithm presented later in chapter 3.

Recall from our discussion of POD basis functions, equation 2.10. A reduced ROM solution  $y$  for some test parameter  $\hat{p}$  will take the form of the linear combination:

$$y(x, \hat{p}) = \sum_{i=1}^{t < n_{dof}} \alpha_i(\hat{p}) \Phi_i(x), \quad (2.20)$$

The training data is a collection of snapshots from a model or data set with each snapshot depending on some variable  $x$  and a different parameter from a vector of parameters  $p$ . Multiple variables can be handled in the NIROM via concatenation into a single variable: this is expanded on later in chapter 3 and used through the rest of the work. Consider an example snapshot:

$$\psi(x; P) \approx \phi(x; p) \quad (2.21)$$

where  $\psi$  and  $\phi(x; p)$  are snapshots that are either known solutions/data or the result of high fidelity numerical models respectively. We use a range of parameters to cover the domain of interest for the problem at hand:

$$p \in (p_{min}, \dots, p_{max}) \quad (2.22)$$

with the a ROM being able to investigate new test parameters in this range with confidence and over the training snapshots if investigated at the same point as one of them with very close to the same fidelity in spite of the dimension reduction.

We thus take our snapshot matrix  $X$  to be a collection of snapshots:

$$\mathbb{X} = \left( \phi(x; p_1), \dots, \phi(x; p_{N_S}) \right) \quad (2.23)$$

This matrix is our training data along with the parameter the ROM has to investigate are the principle inputs of the NIROM algorithm. Characteristic length and function are the ways we can tune the NIROM output and behave just like the radial basis interpolations in figures 2.4, 2.5 and 2.6. With the right training, smooth and accurate ROM solutions are obtainable with the NIROM algorithm that offer a real speed-up for large classes of numerical problems.

The full NIROM algorithm is now presented, however the key take-away for the reader at this stage is:

- Large **Offline** stage is slow but **need only be done once** - data collection, POD basis, weights calculations happen here.
- Rapid **Online** stage is very fast and can be done for **any new test parameter**  $\hat{p}$  in the training range .

For an overview of the steps we:

First high fidelity training data is collected to best cover the parameter ranges of interest → a POD basis that best captures the information needed and thus physics for possible new solutions in the range of parameters is computed → a set of ROM coefficients  $\alpha_{known}$ , RBF kernel and weights  $w_{i,j}$  is found and completes the offline stage → finally for the online stage, a new, more simple RBF kernel using the test parameter is calculated and a linear combination of ROM coefficients and POD basis functions is formed.

### 2.3.1 The NIROM algorithm for steady state problems

We outline a way of getting the ROM coefficients  $\alpha_i$ . The Non-Intrusive Reduced Order Model (NIROM) algorithm used here takes the form:

---

**Algorithm 1** Offline stage - Construct the ROM

---

- 1: **procedure 1:** POD basis construction
- 2:   Generate snapshots over the parameter space  $p$  by running full order model for the ; ▷ Store in snapshot matrix  $\mathbb{X}$ .
- 3:   Obtain POD basis functions  $\Phi_i$  by performing an SVD of the snapshot matrix  $\mathbb{X}$ ; ▷ At this point the user can wish to analyze the energy/information captured by the POD basis functions.
- 4: **procedure 2:** Obtaining known  $\alpha$  and weights
- 5:   Obtain the ROM coefficients  $\alpha$  for the known solutions in the snapshot matrix by taking the dot product of the snap matrix dot product of POD basis functions with solutions. That becomes:

$$\alpha_{known} = \langle \phi, \Phi^T \rangle \quad (2.24)$$

▷

- 6:   Calculate weights by solving for the known  $\alpha$ :

$$\alpha = \sum_{i=1}^{N_S} w_{i,j} f(\|\mathbf{p}_i - \mathbf{p}_j\|), \quad p_i \in p. \quad (2.25)$$

The function  $f$  is taken to be a Gaussian with characteristic length scale taken as the  $\min(p)$ . The matrix  $F$  can be pre-computed and inverted.

$$F_{i,j} = f(\|\mathbf{p}_i - \mathbf{p}_j\|), \quad p_i \in p. \quad (2.26)$$

In Einstein notation the weights calculation becomes:

$$\alpha_{i,j} F_{j,\beta}^{-1} = w_{j,\alpha} F_{\alpha,j} F_{j,\beta}^{-1} = w_{i,\alpha} \delta_{\alpha,\beta} = w_{i,\beta} \quad (2.27)$$

- ▷ Set aside the POD basis function and weights for Online stage
-

---

**Algorithm 2** Online stage - Evaluate the ROM

---

- 1: **procedure** 3: New ROM coefficients for parameter  $\hat{p}$
- 2:     Evaluate the ROM coefficients for new  $\hat{p}$

$$\alpha_{\hat{p}} = \sum_{i=1}^t w_{i,j} f(\|\mathbf{p}_i - \hat{\mathbf{p}}\|), \quad p_i \in p. \quad (2.28)$$

- 3: The solution is reconstructed:

$$\phi(x; \hat{p}) = \sum_{i=1}^t \alpha_i(\hat{p}) \Phi_i(x) \quad (2.29)$$

---

## 2.4 Reactor Physics and shielding

The reactor is a source of highly penetrating radiation. Neutron radiation without suitable shielding can travel macroscopic distances in the order of 100s of meters. Free from charge, neutrons travel in straight lines until interaction and only are an indirect source of ionising radiation. Some will eventually decay via beta decay with a half-life of about 15 minutes. Others will deviate from their straight paths to collide with a nucleus, subsequently scattered in a new direction or absorbed and will thus produce further sources radiation. The wear and tear of structures such as the shielding is called the embrittlement and can only be combated through replacement and annealing. There are therefore sizeable economic and safety considerations in the engineering of shielding.

### Neutron transport equation

Neutron transport or neutronics is a type of radiative transport with its origins in the Boltzmann transport equation [109]. Even after the advent of high performance computing it is a very computationally taxing problem being a fully 3D, time dependant problem with variables of energy span several orders of magnitude from fractions of meV to several MeV. The Boltzmann transport equation conserves neutrons with each term representing a loss

or gain of neutrons. In neutron transport we can interpret the Boltzmann transport equation as:

Rate of change in neutron flux + Loss via free streaming

=

Loss of neutron to all reactions

+

Gain of neutrons from scattering from other angles or energies

+

Gain of neutrons via fission reactions (2.30)

We represent the neutrons with a variable  $\psi(\mathbf{r}, \Omega, E, t)$  the neutron flux, a measure of the number of neutrons passing through a volume element divided by its cross section area and by the time interval. The typical  $\text{cm}^{-2}\text{s}^{-1}$ , units are neutrons per centimetre squared per second. It is a function of energy  $E$ , angle  $\Omega$ , time  $t$  and direction  $\mathbf{r}$ . Typically in real world engineering problems neutron flux will be function of angle. In chapters 4 and 5 we integrate the angle over hemispheres so that we only have two "angles" - left and right. The preliminary works in chapter 3 consider a scalar flux which can be thought of as the number of neutrons crossing through some arbitrary cross-sectional unit area in all directions per unit time. This is the same as the sum or integration of all angular fluxes.

The neutron cross-section defines the likelihood of certain interactions and will be very important throughout this thesis. The cross-sections  $\Sigma_s, \Sigma_a, \Sigma_t$  etc, denotes the probability that a nuclear reaction will occur in a given area, for scatter, absorption, total and so on. These will determine the capture and scattering behaviours, linking the various models to real world materials and physics.

In the rest of this chapter we will survey a few standard formulations for neutron transport and introduce a very simple model shielding that we can use to investigate the reduced order modelling techniques.

The full neutron transport equation with time-dependence is given by:

$$\begin{aligned} & \left( \frac{1}{v(E)} \frac{\partial}{\partial t} + \hat{\Omega} \cdot \nabla \psi(\mathbf{r}, \hat{\Omega}, E, t) + \Sigma_t(\mathbf{r}, E, t) \right) \psi(\mathbf{r}, \hat{\Omega}, E, t) = \\ & \int_{\hat{\Omega}'} \int_{E'} \Sigma_s(\mathbf{r}, \hat{\Omega}' \rightarrow \hat{\Omega}, E' \rightarrow E, t) \psi(\mathbf{r}, \hat{\Omega}', E', t) dE' d\hat{\Omega}' \\ & + \lambda \frac{\chi(E)}{4\pi} \int_{E'} \nu \Sigma_f(\mathbf{r}, E') \int_{\hat{\Omega}'} \psi(\mathbf{r}, \hat{\Omega}', E', t) dE' d\hat{\Omega}' \end{aligned} \quad (2.31)$$

The angular neutron flux  $\psi(\mathbf{r}, \hat{\Omega}, E, t)$  is a function of space  $\mathbf{r}$ , angle  $\hat{\Omega}$ , energy,  $E$  and time  $t$ . The neutron velocity vector is given by  $v$ , the average number of neutrons emitted per fission  $\nu$ , the cross-sections  $\Sigma_t, \Sigma_s, \Sigma_f$  representing total, scattering and fission respectively. The fission energy spectrum is given by  $\chi$ . The eigenvalue  $\lambda$  is related to the neutron multiplication factor  $k_{eff} = \frac{1}{\lambda}$ : this dictates if the reactor is "critical" - the neutron density remains unchanged  $k_{eff} = 1$ , "sub-critical" - the neutron density is decreasing as time passes  $k_{eff} < 1$ , "super-critical" - the neutron density is increasing with time  $k_{eff} > 1$ .

For shielding the calculations are "fixed-source" that is, the source is known and treated as a boundary condition and we will be interested in finding the neutron distribution throughout the problem. We will consider  $k_{eff} = 1$  and be mostly considering steady-state problems.

The steady-state version of the transport equation is given by:

$$\begin{aligned} \hat{\Omega} \cdot \nabla \psi(\mathbf{r}, \hat{\Omega}, E) + \Sigma_t(\mathbf{r}, E) \psi(\mathbf{r}, \hat{\Omega}, E) &= \int_{\hat{\Omega}'} \int_{E'} \Sigma_s(\mathbf{r}, \hat{\Omega}' \rightarrow \hat{\Omega}, E' \rightarrow E) \psi(\mathbf{r}, \hat{\Omega}', E) dE' d\hat{\Omega}' \\ &+ \lambda \frac{\chi(E)}{4\pi} \int_{E'} \nu \Sigma_f(\mathbf{r}, E') \int_{\hat{\Omega}'} \psi(\mathbf{r}, \hat{\Omega}', E') dE' d\hat{\Omega}' \end{aligned} \quad (2.32)$$

The angular neutron flux  $\psi(\mathbf{r}, \hat{\Omega}, E)$  is now only a function of space  $\mathbf{r}$ , angle  $\hat{\Omega}$  and energy,  $E$ .

The standard discretisation for energy breaks down energy with multi-group methods where each energy represents a band. For more details see the book [110]. For many problems where thermal neutrons are the only consideration, 2-group is sufficient i.e  $g = 2$ . The multi-group transport equation is therefore given by:

$$\begin{aligned} \hat{\Omega} \cdot \nabla \psi_g(\mathbf{r}, \hat{\Omega}) + \Sigma_{t,g}(\mathbf{r}) \psi_g(\mathbf{r}, \hat{\Omega}, E) &= \int_{\hat{\Omega}'} \sum_{g'=1}^G \Sigma_{s \rightarrow g'}(\mathbf{r}, \hat{\Omega}' \rightarrow \hat{\Omega}) \psi_{g'}(\mathbf{r}, \hat{\Omega}) d\hat{\Omega}' \\ &+ \lambda \frac{\chi_g}{4\pi} \sum_{g'=1}^G \nu \Sigma_{f,g'}(\mathbf{r}) \int_{\hat{\Omega}'} \psi_{g'}(\mathbf{r}, \hat{\Omega}') d\hat{\Omega}' \quad \forall g \in (1, 2, \dots, G). \end{aligned} \quad (2.33)$$

where  $g$  is an index representing the energy group. Note each energy group will have sets of fluxes for each angular discretisation considered and will have separate sets of cross-sections.

All shielding models in this work should be considered with this equation in mind as this is the standard way of thinking about transport in both criticality and shielding problems. For solution, time, when considered, and space are straightforward to discretize however angular discretization may take the form of functional expansion of spherical harmonics, namely  $P_N$  methods, or the quadrature of  $S_N$  methods. Hopefully the reader can appreciate the Neutron transport equations are straightforward to derive but solution, deterministic or stochastic, is involved.

A simpler proxy for these governing equations is to use the multi-group and mono-group diffusion equations. These equations can be derived from the Neutron transport equations or derived from Fick's law [111],[112]. In our context the law states: The neutron current density  $J$  is directly proportional to the negative gradient of the neutron flux  $\psi$ . That is:

$$J \propto -\nabla\psi \quad (2.34)$$

In one spatial dimension:

$$J = -D \frac{\partial\psi}{\partial x} \quad (2.35)$$

where the diffusion coefficient  $D$  can be related to the mean free path, the mean cosine angle scattered in a medium or transport and absorption cross-sections.

This derivation from Fick's Law is the single step of substitution into the continuity equation:

$$\frac{\partial\psi}{\partial t} = S - \Sigma_a\psi - \nabla J \quad (2.36)$$

meaning,

$$\text{Rate of change in neutron flux} = \text{production rate} - \text{absorption rate} - \text{leakage rate} \quad (2.37)$$

This is the same neutron balance principle in the full Neutron transport equations. The mono-energetic neutron transport equation takes the form:

$$\frac{1}{\nu} \frac{\partial\psi}{\partial t} + \Sigma_a\psi + \nabla \cdot (\psi) - \nabla \cdot (D\nabla\psi) = S. \quad (2.38)$$

where  $\psi$  the neutron flux density,  $\nu$  is the average neutron speed of a thermal neutron,  $D$  is the diffusion coefficient,  $\Sigma_a$  is the macroscopic absorption cross-section and  $S$  is the source term. This is an equation of continuity and very important to reactor physics [113]. Figure 2.7 gives a physical interpretation of diffusion theory. Diffusion theory can be used in multiplying systems, where fissile material is present  $\Sigma_f \neq 0$  in other words  $S \neq 0$ .



In non-multiplying systems such as shielding a simple analytical model can arise by considering a infinite plane source in the  $y - z$  plane with the mono-energetic neutron transport being then only as function of  $x$ . The only possible solutions must take the form:

$$\psi(x) = c_1 e^{-px} + c_2 e^{px} \quad (2.39)$$

where  $p$  is some attenuation parameter with units one over length. The only physical part of this equation is:

$$\psi(x) = c_1 e^{-px} \quad (2.40)$$

as finite flux is a necessary condition along with  $x > 0$ . In chapter 3 we will take this equation as a toy model of shielding to investigate boundary conditions, interfaces and reduced order models.

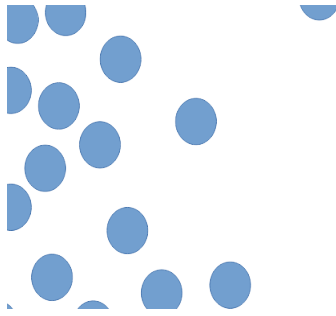


**Figure 2.7:** The diffusion approximation offers a physical interpretation is similar to the fluxes of gases. Moving from high collision density to low collision density. There are more collisions per cubic centimetre on the left so the neutrons are on average scattered left to right, diffusing to the right.

This equation has its origins in Fick's law, key assumptions in deriving this law are widely known with figure 2.7 giving an overview and the validity of those assumptions to this physical situation must be considered: infinite medium, sources, isotropic scattering, slowly varying flux and time-dependent flux [114].

These assumptions can be weakened considerably if a) we are a few mean free paths away from extremities and b)  $S \gg \Sigma$ . Anisotropic scattering can be corrected for using transport theory. Nevertheless models based on Fick's law gives a reasonable approximation.

## 2.5 The ASPIS benchmark

The ASPIS experiments were a series of benchmarks taken at the United Kingdom Winfrith Atomic Energy Authority site [3]. The shielding facility installed at the site shared the same name. Winfrith housed several experimental reactors over its lifetime. The ASPIS benchmarks made use of the experimental reactor NESTOR, a source of large amount of neutrons, primarily developed as a useful tool for investigating the design of power-producing reactors and carrying out sub-critical experiments on core assemblies.

In this work we use a configuration of a shield array, figure 2.8, from one of these experiments as a recognisable problem to compare accuracy of results. The experiments show up to a full 47-group result. To consider 1D scattering with pairs of positive-negative directional fluxes for 1-group and 2-group models respectively angular components of the neutron flux are integrated over hemispheres. The only components of the total scalar flux that remain are the fluxes travelling in the left (negative) or right (negative) direction.

The exact solutions used to evaluate the ASPIS benchmark ROMs performance in chapters 4 and 5 come from the code WIMs [5], where a 47-group model with the angular dimension of the problem represented potentially in full 3D is integrated over two hemispheres with the energy groups condensed to give appropriate solutions for comparison with the 1D ASPIS benchmarks in 1-group and 2-group classifications.



Material configuration [Key: Void Boral Mild steel 1 Mild steel 2 Water Concrete]

**Figure 2.8:** The material configuration used in the coupled ROMs, chapter 3 and 4. This is a modified version of the domain used in the ASPIS benchmark.

# Chapter 3

## Preliminary Reduced Order Models

### Overview

This chapter presents a toy-ROM using an analytical model to generate training data and investigates a few different ROM paramterisations, starting with a single attenuation parameter  $p = \Sigma_t$  that could be thought of a total cross-section and later examples using width or interface position also having  $p = p(\Sigma_t, l)$  where  $l$  is the width or interface position.

There is emphasis in building an intuition of the factors effecting the ROM: How many snapshots are needed?, What number of spatial nodes should be employed?, Which paramterisations of the training space make sense? Exploring the logarithmic pre-conditioner? Should interfaces in NIROMs be approached as multiple coupled ROMs or just different paramterisations or a single ROMs? A few metrics and conventions are presented which will be useful in the analysis of ROMs in later chapters such as error metrics, investigating unseen-points in the training space of the ROM farthest from the sen-points, normalised boundary conditions, uniform meshing and uniform sampling in training regimes, singular values presented as a cumulative energy sum, Gaussian radical basis functions as the default choice. Insight from this chapter are employed in chapters 4 and 5 to the ASPIS ROMs.

## Introduction

In the previous chapter we introduced the mathematical background needed to understand the Non-intrusive reduced order model NIROM technique and the basic definitions and concepts used in numerical methods and shielding. In this chapter we make use of some preliminary analytical models for shielding as well as some more abstract elementary functions as we build an understating of the Non-intrusive reduced order model NIROM technique. The exponential function, formulated as equations 3.2 or 2.40, is used frequently in these models as it is safe to assume a dominant behaviour in shielding models will be attenuation.

Recall while numerical methods such as finite difference approximate solutions of the governing equations of a model, reduced order modelling (ROM techniques) reduces computational complexity of high fidelity models generating a rapid approximation to similar models. ROM is in this sense a meta-technique: traditional numerical methods model a real world phenomena with certain levels of abstraction whereas ROMs start with a model or data set as an input and add a further level of abstraction to highlight or improve upon properties of the model itself.

We will investigate how the NIROM performs as we vary a few key model parameters that make up the input models or data of the ROM, the parameters that govern the training in the Offline stage of the ROM and the choice of characteristic length in the Online stage of the ROM:

- **Model parameters:** The most important and universal consideration here is the size of the model, quantified as the number of degrees of freedom, being the number of parameters of the system that may vary independently. In models with a state space representation this would be the dimension of the model state space
- **Offline Training parameters:** The Offline stage is outlined in the NIROM algorithm in figure 3.2 and consists obtaining the data used as snapshots and building the ROM from them. In the Offline line stage the number of snapshots, logarithmic spacing, concatenation for multi-variable problems, vectorised input parameters all will determine the ROMs effectiveness.
- **Online parameters:** Here choice of characteristic length has a large effect on whether radial basis function interpolation of the ROM coefficients is sufficient.

The number of degrees of freedom will add more detail to the snapshots used as training data but increase the size of the problem. Accessing how this trade-off functions will let us understand whether more snapshots or degrees of freedom within individual snapshots is the best choice to improve the NIROM. The actual shape and range of the training space is important to consider: the training across different orders of magnitude can be enhanced with logarithmic spacing in the training stage. The training should include the maximum and minimum parameterization of any desired ROM solution. The shape of the training space is formed as each parameter for training is assigned an axis and together taken as a whole these axis form a hyper-cube. As the offline stage of the ROM is constructed we have to index our way through this space in some arbitrary manor and you could choose to

sample just some of the points. In this work we limit ourselves to a brute-force approach using all points in the hyper-cube but we may apply logarithmic spacing to the axis first.

An investigation into all the considerations mentioned above with simpler preliminary models will enable us to build the broad intuition needed to apply the NIROM to complex, larger scale problems in shielding. We aim in later chapters to consider the ASPIS problem, a materially inhomogeneous problem. As such another factor we investigate using preliminary models how the position of material interfaces as a ROM parameter behaves. We will see variable preliminary results in this approach and demonstrate that a more promising approach is to build a library of homogeneous ROMs and couple them together.

### **3.1 A single parameter attenuation model of shielding**

This first simple model serves as a test case to develop and understand the NIROM approach for a single parameter.

For this analytical test case a set of exponential functions are used to approximate solution to the Boltzmann Transport Equation (2.38) for neutrons. A general solution to the neutron transport equation takes the form  $\psi(x, \Omega, E, ; P)$  and depends on  $x$  some position,  $\Omega$  direction of motion,  $E$  energy, nuclear cross-sections and is not in steady state. In this model we assume we have a single energy group, a one dimensional spatial domain, and steady state solutions. In the later chapters we break down attenuation into multiple parameters to model more complex scattering behaviours with the total attenuation  $p = \Sigma_t$ . In this chapter we will use the model of an attenuation parameter simplifying and modelling material and geometric properties by using just a single attenuation parameter, namely  $p$  the probably of neutron capture per unit length and ignoring anymore complex behaviour such as scatter. In the later chapter we will work towards models of full

neutron transport, for now the governing equation of the attenuation model takes the form of an attenuation equation:

$$-\frac{\partial \phi}{\partial x} = p \quad (3.1)$$

When solved with unit bound condition at the start of the shield and zero at the end applied gives us a closed form solution for to use as the model. We have:

$$\psi(x, \Omega, E, ; P) \approx \phi(x; p) = e^{-px} \quad (3.2)$$

with the choice of parameter in the range:

$$p \in (10^1, \dots, 10^5) \quad (3.3)$$

with the set the divided with logarithmic spacing. This forces the solution  $\phi(x = 1)$  at the last point on the unit domain to be  $\phi(x = 1) = 10^n$  for some  $n$  corresponding to a snapshot solution. When multiple shields are modelled the input of the next shield is the output of the previous. This analytical model allows us to construct toy-ROMs in order to show the general considerations needed when using the NIROM, explore different parameterisations and investigate a logarithmic pre-conditioner of the snapshot matrix.

To begin the Offline stage of the ROM we store all the solutions from our model as columns of a matrix of snapshots and so we take this snapshot matrix  $X$  to be:

$$\mathbb{X} = \left( \phi(x; p_1), \dots, \phi(x; p_{N_S}) \right) \quad (3.4)$$

or visually:

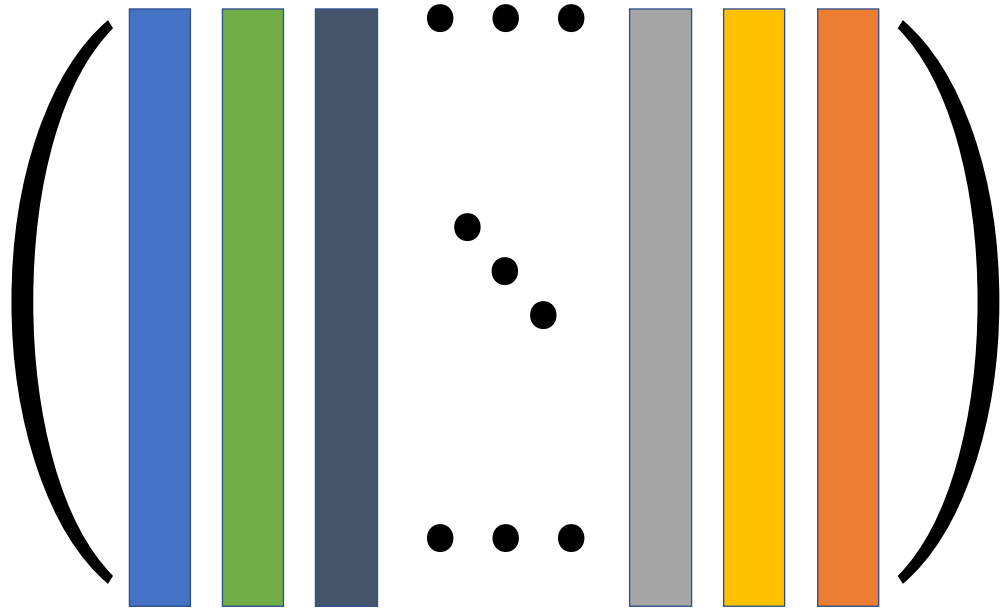


**Figure 3.1:** Visualization of the snapshots stored as column vectors of the snapshot matrix.

In the previous chapter we presented a general version of the NIROM algorithm that can be thought of as a the general approach. Here the NIROM algorithm is specific to this application only in the sense that it is steady state. A time dependant problem would be very similar in that it would have the time stepping through as just another parameter whereas here we only have attenuation parameter  $p$ .

### **The NIROM algorithm for steady state problems**

We recall the way of getting the ROM coefficients  $\alpha_i$  in the Offline stage of the algorithm and then a specific solution in the Online stage. The NIROM technique is thus:



---

**Algorithm 3** Offline stage - Construct the ROM

---

- 1: **procedure 1:** POD basis construction
- 2:   Generate snapshots over the parameter space  $p$  by running full order model for the ; ▷ Store in snapshot matrix  $\mathbb{X}$ .
- 3:   Obtain POD basis functions  $\Phi_i$  by performing an SVD of the snapshot matrix  $\mathbb{X}$ ; ▷ At this point the user can wish to analyze the energy/information captured by the POD basis functions.
- 4: **procedure 2:** Obtaining known  $\alpha$  and weights
- 5:   Obtain the ROM coefficients  $\alpha$  for the known solutions in the snapshot matrix by taking the dot product of the snap matrix dot product of POD basis functions with solutions. That becomes:

$$\alpha_{known} = \langle \phi, \Phi^T \rangle \quad (3.5)$$

▷

- 6:   Calculate weights by solving for the known  $\alpha$ :

$$\alpha = \sum_{i=1}^{N_S} w_{i,j} f(\|\mathbf{p}_i - \mathbf{p}_j\|), \quad p_i \in p. \quad (3.6)$$

The function  $f$  is taken to be a Gaussian with characteristic length scale taken as the  $\min(p)$ . The matrix  $F$  can be pre-computed and inverted.

$$F_{i,j} = f(\|\mathbf{p}_i - \mathbf{p}_j\|), \quad p_i \in p. \quad (3.7)$$

In Einstein notation the weights calculation becomes:

$$\alpha_{i,j} F_{j,\beta}^{-1} = w_{j,\alpha} F_{\alpha,j} F_{j,\beta}^{-1} = w_{i,\alpha} \delta_{\alpha,\beta} = w_{i,\beta} \quad (3.8)$$

- ▷ Set aside the POD basis function and weights for Online stage
- 

---

**Algorithm 4** Online stage - Evaluate the ROM

---

- 1: **procedure 3:** New ROM coefficients for parameter  $\hat{p}$
- 2:   Evaluate the ROM coefficients for new  $\hat{p}$

$$\alpha_{\hat{p}} = \sum_{i=1}^t w_{i,j} f(\|\mathbf{p}_i - \hat{\mathbf{p}}\|), \quad p_i \in p. \quad (3.9)$$

- 3: The solution is reconstructed:

$$\phi(x; \hat{p}) = \sum_{i=1}^t \alpha_i(\hat{p}) \Phi_i(x) \quad (3.10)$$

---

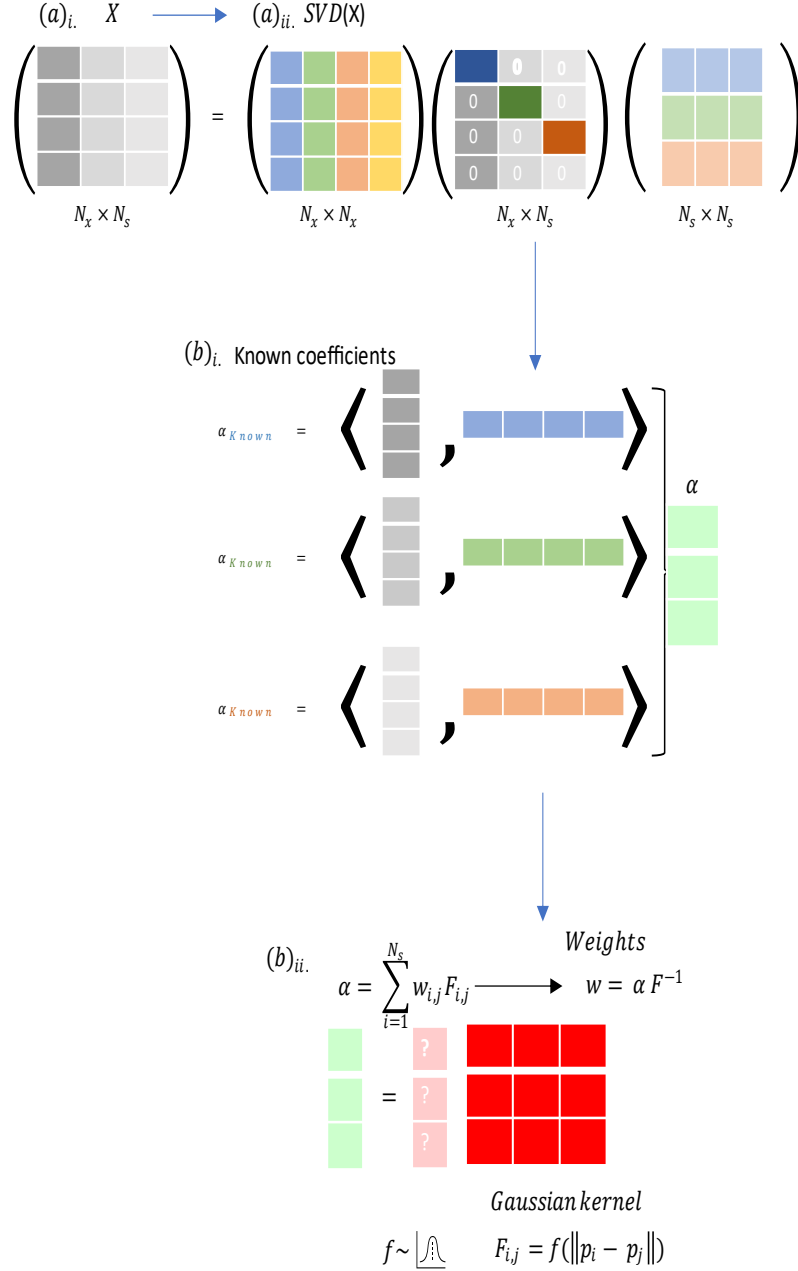


**Figure 3.2:** Visualisation of the Offline stage of the NIROM. The principle input of the algorithm is the snapshot matrix  $\mathbb{X}$  in which the training data is stored. The NIROM produces the POD basis and the weights needed to reconstruct any new solution in the Online stage.

In figure 3.2 we visualise the steps of the Offline stage to the NIROM algorithm. In the first step  $(a)_i$  the data is collected in the snapshot matrix. Each column is associated with a training parameter vector  $p$  in a way that will let us

reconstruct any new solution for a new value of  $p = \hat{p}$  in the Online stage. Recall from the background in the previous chapter, the SVD of the snapshot matrix in step  $(a)_{ii}$ . gives the POD basis functions. The columns of the first matrix are the basis functions sorted in order of the information they confer when used in the Online stage. The size of the singular values in the middle matrix quantify this information capture. The step  $(b)_i$ . takes the dot product of the individual snapshots, giving a set of ROM coefficients for the known solutions. The final step of the Offline stage  $(b)_{ii}$ . calculates the weights needed for a radial basis interpolation of these known coefficients.

In the Online stage these weights enable radial basis interpolation to approximate any ROM coefficient for any new training parameter. The solutions are finally reconstructed from linear combinations of ROM coefficients and POD basis functions.

### 3.1.1 A logarithmic pre-conditioner

Sometimes an extra step in the NIROM process is used in this work. Qualitatively, the idea that a logarithmic pre-conditioner could improve ROMs where the applications have are dominated by exponential decay is worth considering. The pre-conditioner used in this work takes the logarithm of the snapshot matrix, performs the ROM calculations and takes the exponential of the final ROM solution as:

---

**Algorithm 5** Logarithmic pre-conditioner

---

- 1: training data for each parameter under investigating is collected in the snapshot matrix
  - 2: the logarithm of this snapshot matrix is taken to be the new snapshot matrix
  - 3: the NIROM algorithm is then employed
  - 4: During post-processing, the ROM solution is recovered via taking the exponential of the NIROM output solutions.
- 

### 3.1.2 Error, stability, and convergence measures used in this work

Throughout this work we are interested in systematically understanding error, stability and convergence hence validity of the method in question. Error is considered with respect to some reference value taken from an accepted source such as a benchmark experiment or theoretical exact value etc. Stability of the method evaluates how the error propagates through the algorithm. Measures of convergence typically give an idea of how many iterations are needed in an iterative method. Different quantitative and qualitative insights can be gained from different error measures with a consistent collection building up a more complete picture for direct comparisons.

The error measures used throughout this work are:

- The root mean squared error:

$$RMS = \sqrt{\frac{\sum_i (\psi_{ROM}(x_i) - \psi_{exact}(x_i))^2}{n_{dof}}} = \sqrt{\frac{1}{n_{dof}} \|\psi_{ROM} - \psi_{exact}\|_{L_2}^2} \quad (3.11)$$

aggregates the distribution of the error around their average into a single number. The distance between the value predicated by the ROM and the reference value  $\psi_{ROM}(x) - \psi_{exact}(x)$  is called the residual (or absolute error). The sign of the residual qualifies whether there is an under or over estimation of the actual value. The RMS gives an overall value of the error.

- The relative error:

$$e_{relative} = \frac{|\psi_{ROM}(x) - \psi_{exact}(x)|}{|\psi_{exact}(x)|} \quad (3.12)$$

shows discrepancy between the ROM and the reference solution at each choice of spatial node  $x$ . The absolute value is sometimes omitted when under or over estimation is not clear from the absolute error. However absolute relative error is the default measure used in this work unless otherwise stated.

- The percentage error:

$$e_{percentage} = 100 \times e_{relative} \quad (3.13)$$

- An error bound: is the maximum error.

- The  $L_2$  error:

$$e_{relative} = \frac{\|\psi_{ROM} - \psi_{exact}\|_{L_2}}{\|\psi_{exact}\|_{L_2}} \quad (3.14)$$

The relative error can undergo the  $L_2$  norm as shown in the formula to give a single overall measure. This is useful when looking a convergence with respect to different model parameters.

- Relative error at last point:

$$e_{relative}(x = 1) = \frac{\|\psi_{ROM}(x = 1) - \psi_{exact}(x = 1)\|}{\|\psi_{exact}(x = 1)\|} \quad (3.15)$$

is useful for understanding error at and across the boundaries of the domains. This is particularly important in shielding problems and in the coupling of one system to another.

By convergence we mean making improvements to the solutions from one run or iteration to the next. The iterations can be steps in an algorithm or in some contexts just a run of the method with a different model parameter if investigating sensitivity of error to that given parameter. An example would be finding out how the model improves with more spatial nodes. Convergence behaviour can be extrapolated with the order of convergence, the slope of the line of best fit in plots of  $L_2$  error against the property under investigation for convergence behaviour of a log-log scale.

Stability is particularly a consideration in time-dependant problems and we will need this in the final chapters. A helpful tool for understanding stability is Von Neumann stability analysis in which particularly suitable for numerical schemes in PDEs. A scheme is stable if errors made at one time step or spatial node do not magnify as the scheme propagates to the next time step or spatial node. A well known example would be the Courant–Friedrichs–Lewy condition,  $|\frac{u\Delta t}{\Delta x}| < \frac{1}{2}$ , arising from numerical schemes with explicit time integration of the advection equation with speed  $u$ . A good text for detailed explanation of deriving conditions for numerical is [115]. Broadly a derivation of a stability condition for some specific scheme would be as follows: Consider numerical round-off error, the difference in numerical and analytical solutions for the same finite-precision. As the exact solution must satisfy the discretisation of the problem, the error must also satisfy discretisation of the problem. Showing this fact demonstrates the scheme has the same growth or decay in error with respect to time. You can then perform a Fourier decomposition of the error  $\epsilon(x, t)$  as a function of space giving a series in which the amplification factor  $G(t)$  can be identified and is a function of time and set this factor to

be bounded such that  $|G| \leq 1$ . This gives a condition for how and if error propagates as you step in time and space.

Throughout the rest of this work we will make use of these measures. Specifically the next section will use of some of these measures to investigate how a simple ROM of a model shield with a single attenuation factor behaves as we go from a very small amount of training data to a larger number of snapshots. First however we will introduce the concept of time complexity which can be used to understand limitations in scale of numerical methods.

### 3.1.3 Time complexity and POD basis information capture

Scalability of algorithms is an important consideration. In principle ROMs enable us to solve bigger problems than a fresh direct numerical simulation making use of existing training data. In practice this is a great tool for prototyping, design and digital twins. Time complexity of generating training data, number of future runs desired and the information of the ROM will inform when this technique the best choice.

We expect that using more snapshots or more degrees of freedom will take longer to compute. An a priori measure of time complexity comes from considering asymptotics of the operations in the NIROM algorithm is big-O notation [116]. This estimate and notation is very important as we can quickly distinguish between an algorithm that just needs better implementation or an algorithm that will always be too slow for a large enough input. To see this we introduce the following definition.

For operations represented by functions on the integers  $f(n)$  we have that:

$$f(n) = O(g(n)) \text{ if there exists } M \text{ such that } f(n) \leq Mg(n) \quad (3.16)$$

for some sufficiently large  $n$ . For example the function:  $f(x) = x^2 + x + 1$  can be written  $f(x) = O(x^2)$  for  $x \rightarrow \infty$ . Which fulfills the definition as  $|f(x)| \leq Mx^2$  for suitable  $x > x_0$  and  $M$ .

We expect a dominant operation in the NIROM to be the matrix inversion which using Gauss–Jordan elimination is order  $O(n^3)$ . Similarly the SVD is an operation of order  $O(nm^2)$ . Consequently the NRIOM should take about  $2^3$  times longer to run if the number of degrees of freedom doubles and  $2^2$  times longer when the number of snapshots is doubled.

Recall from the background theory in the previous chapter, a measure specific to the POD based ROM techniques is the information captured by POD basis sometimes called energy and is defined in the previous chapter. We use this to inform how many POD basis functions are needed to construct ROM solutions and when combined with the plots of the POD basis functions give an indication of when a basis function is just representing noise.



### 3.1.4 Results and discussion for a ROM of simple exponential attenuation flux

This first investigation fixes most of the model parameters, only varying the amount of training data in the form of the number of snapshots. A simple toy model helps check the code used to implement the NIROM is robust and develops some expectations we can use to ensure robustness going into more complicated applications, how much data to use initially for example. Here we will apply the simple model presented at the start of this chapter, the single attenuation parameter model as shown in equation (3.2) on a highly idealised shield of unit length, figure 3.3, with the setup with the following parameters:

- Number of snapshots at most:  $N_S = 60$
- Minimum number of snapshots:  $N_{S_{min}} = 3$
- Spatial nodes,  $ny = 6$ ,
- Pre-conditioned training with and without logarithmic spacing as section 3.1.1
- All basis functions used, initially no truncation of the POD basis

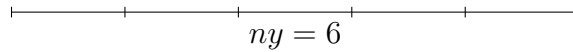


**Figure 3.3:** The spatial resolution here is a unit fixed with 6 spatial nodes while we investigate the effects of adding more training data though additional snapshots.

The values of spatial nodes in this first example is fixed at 6 so it is clear if the ROM can handle a low number of spatial nodes and also is fixed so we can investigate the number of snapshots. Starting at 3 snapshots we expect to see poor results as the range of parameters the model was trained on  $p$  spans orders of magnitude. It is mathematically not possible to have less than 2 and 3 was chosen so as to have a middle value. By using a fixed percentage of basis functions of 100% we don't have to worry about the reduction as a

source of error in this initial investigation. Later on we will pick the number of basis functions based on understanding this information capture.

As the training took place with attenuation factors that span 5 orders of magnitudes,  $10^1, \dots, 10^5$  and the snapshots themselves are exponentially shaped we expected to see some large variation in error across the domain initially using the minimum number of snapshots. In figures 3.4 and 3.5 we look at the error at each spatial node as the number on snapshots is increased, the first as a ratio of ROM to exact solutions to show the point at which the error is constantly positive and the second to show the solution reaches constancy with the osculations diminishing. We see that in figure 3.4 a model can yield acceptable results after 11 or more snapshots for training. Before this we see the ROM is incapable of resolving the smallest points satisfactorily. In contrast we see that the addition of a pre-conditioner from section 3.1.1 for logarithmically spaced training gives acceptable results in this case with very little training. The line correspond to the 6 spatial nodes. The highest error is for the point at at the end of the shield and the lowest is for the point at the initial boundary.

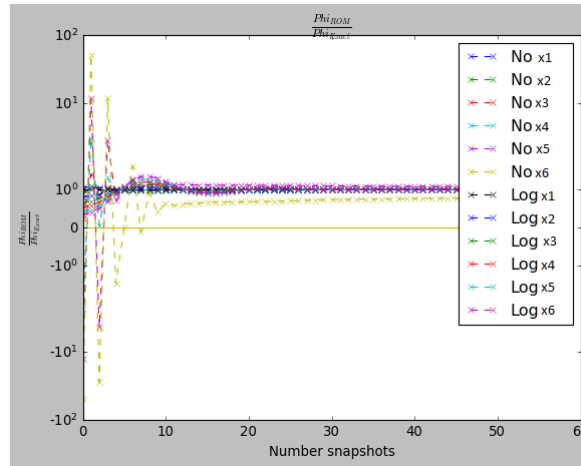


**Figure 3.4:** Here we see for the no-log snapshot matrix, at some points towards the end of the spatial domain values of the ROM solutions are negative in sign and far from the expected solution. This is eventually resolved by increasing the number of snapshots or immediately resolved by taking log of the snapshot matrix and exp of the ROM solutions. Note the x-axis is number added beyond the minimum which here was 3, so in this case the no log data becomes positive after 11 snapshots in total. Each line is the error at a spatial node with the error highest in nodes right to left.

The true values of the relative error are more clear in figure 3.5 however it is does not show the sign of the error.

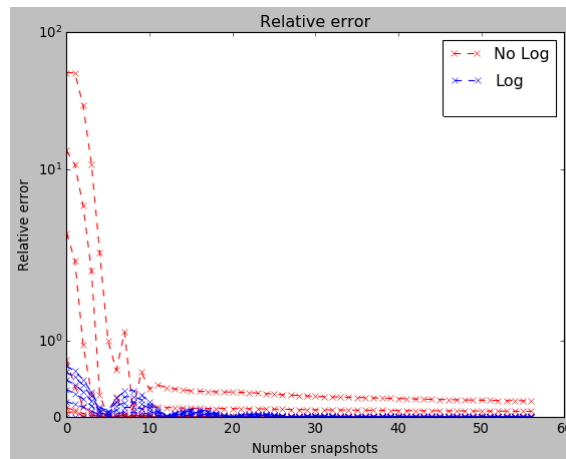


**Figure 3.5:** The relative error plot for each spatial node shows the effectiveness of the logarithmic pre-conditioner from section 3.1.1 and the point at which adding more data yields diminishing returns. Each line is the error at a spatial node with the error highest in nodes right to left.

Figure 3.6 shows the  $L_2$ -error, an average of all the spatial nodes. The slope of the best fit line of this plot is an estimate for the order of convergence. We see it can be bounded by a straight line with a negative slope on the log-linear scale, meaning the  $L_2$  error is inversely proportional to the log of the number of snapshots ie)  $y(x) = y_{intercept} + m_{slope} \log(x)$ .

We see periodicity which could be explained as a result of the points the ROM is resolving being fixed. In general a function  $f$  is periodic if  $f(x + P) = f(x)$  for some  $P \neq 0$ . We suggest that  $P = \log(\hat{p})$ , the point in the parameter space the ROM is resolving and that  $x \approx k \log(\Delta x)$  is the distance to the nearest neighbour in the training space when plotted on a log-log plot for some  $k > 0$ .

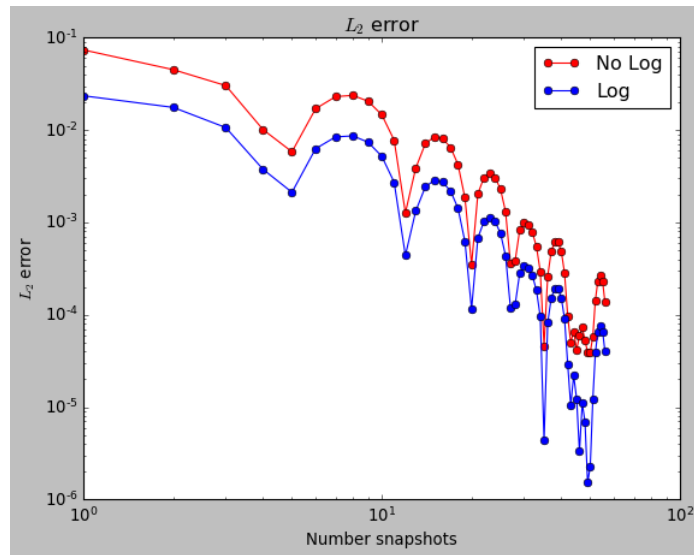


**Figure 3.6:** We see the order of convergence is not smooth due to oscillations but can be found to be bounded at about 0.8 for both runs.

In figures 3.7 (a) and (b) we show the singular values from two of the runs, with and without the logarithmic preconditioner. The singular values show us the energy or information gained by additional POD basis functions. This method of analysis will guide our choice of the number of POD basis functions and in this preliminary problem we need just a single basis function with the preconditioner and very few without the preconditioner. The POD basis functions in (3.7) (c) and (d) hold shape information that enables us to build the ROM solutions. The first few hold the most and eventually the last basis function just represent noise.

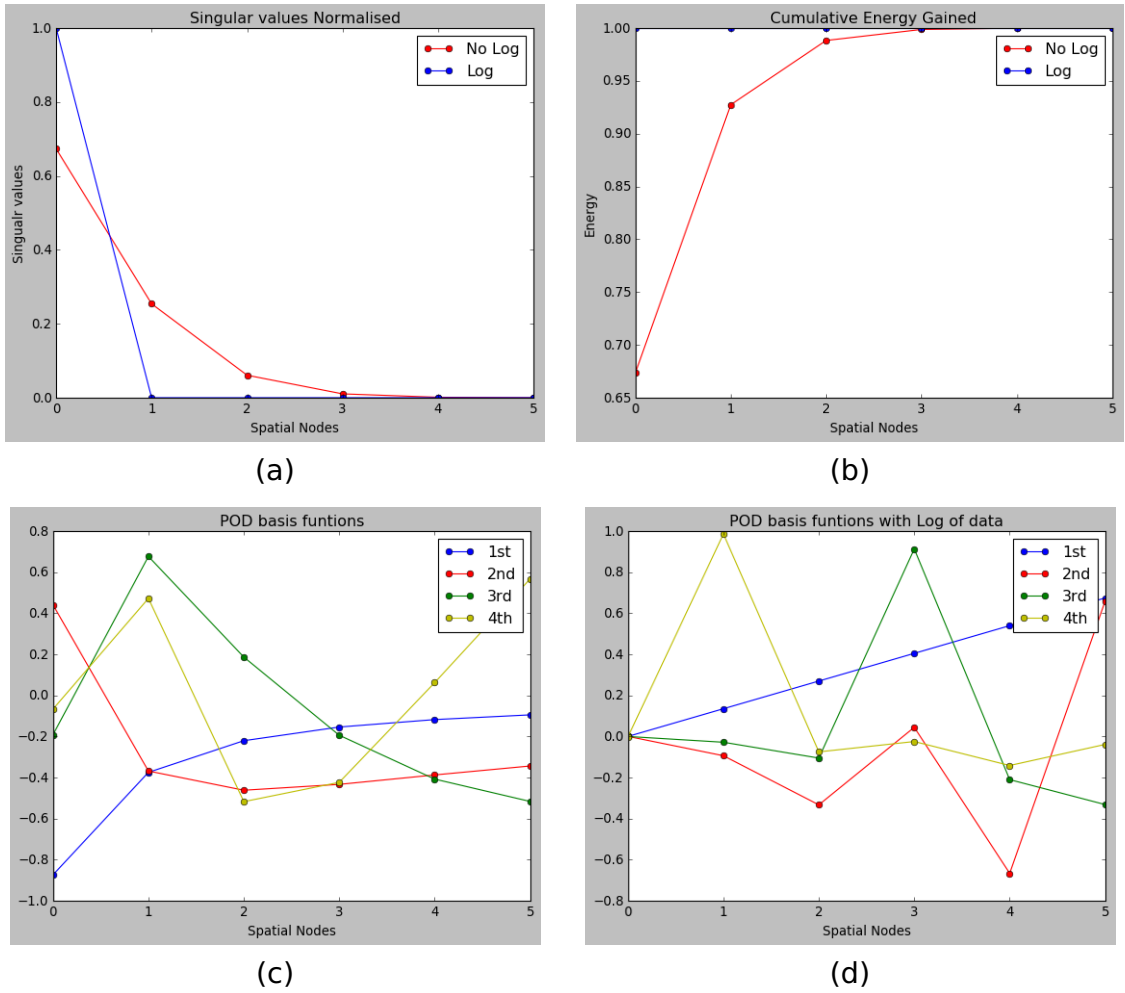


**Figure 3.7:** Singular values are quickly dropping off (a), instantly for the log data set, (b) the energy captured starts fairly high with just one basis function. reaching 98% after just 4 POD basis functions. The first few most dominant POD basis functions without the preconditioner (c) and with the preconditioner (d). We can see that the 1<sup>st</sup> one in both instances hold much of the same shape information as the training data set, the set of exponentials from equation (3.2).

Looking at the NIROM of these preliminary model we see how the size of the potential dimensionality reduction can be understood from the singular values. We also highlight the importance of the ROMs training, both in number of snapshots and shape of the training space, and note that positivity is not guaranteed at the boundaries. However we see promising results from only 6 spatial nodes.

## 3.2 Two and three parameter attenuation models of shielding

This second simple model serves as a test case to develop and understand the NIROM approach for more than a single parameter. Here inhomogeneous materials are modelled piecewise with fixed lengths of each material. Each material now has its own attenuation coefficient. Later in this chapter we investigate making the length, and hence interface, a ROM parameter.

For this analytical test case a set of piecewise exponential functions are used to approximate solutions to the Boltzmann Transport Equation for neutrons. We assume we have a single energy group, a one dimensional spatial domain, and steady state solutions. Now however we model material and geometric properties by use of a different attenuation parameter in each section of the domain; namely  $p_1$ ,  $p_2$  and  $p_3$  probability of neutron capture per unit length in the 1st and 2nd or possibly 3rd section of the unit interval.

For two parameters with unit domain split evenly in half we have that:

$$\psi(x, \Omega, E, ; P) \approx \phi(x; p) = \begin{cases} C_1 e^{-p_1 x}, & \text{for } 0 \leq x \leq \frac{1}{2} \\ C_2 e^{-p_2 x}, & \text{for } \frac{1}{2} \leq x \leq 1 \end{cases} \quad (3.17)$$

where  $C_1 = 1$  and  $C_2 = e^{-\frac{p_2}{2}}$ . For three parameters with unit domain split evenly into thirds we have that:

$$\psi(x, \Omega, E, ; P) \approx \phi(x; p) = \begin{cases} e^{-p_1 x}, & \text{for } 0 \leq x \leq \frac{1}{3} \\ C_1 e^{-p_2 x}, & \text{for } \frac{1}{3} \leq x \leq \frac{2}{3} \\ C_2 e^{-p_3 x}, & \text{for } \frac{2}{3} \leq x \leq 1 \end{cases} \quad (3.18)$$

where  $C_1 = 1$ ,  $C_2 = e^{-\frac{p_2}{3}}$  and  $C_3 = e^{-\frac{2p_3}{3}}$ .

For each parameter we use a choice of parameter domain with range  $\log(p)$ :

$$p \in (10^1, \dots, 10^5) \quad (3.19)$$

with the set the divided with logarithmic spacing such that:

$$\mathbb{P} = (p_1, p_2, p_3) \quad (3.20)$$

where  $p_1 = p_2 = p_3 = p$  and  $\mathbb{P}$  matrix of the parameters for some ordering such that every snapshot vector has a corresponding point in this space of parameters formed by treating  $p_1, p_2$  and  $p_3$  as axes. Note the solutions are still forced to have  $\phi(x = 1)$  at the last point on the unit domain to be  $\phi(x = 1) = 10^n$  for some  $n$  corresponding to a snapshot solution.

We take our snapshot matrix  $X$  to be:

$$\mathbb{X} = \left( \phi(x; \mathbb{P}_1), \dots, \phi(x; \mathbb{P}_{N_S}) \right) \quad (3.21)$$

for some order of parameter coordinates  $\mathbb{P} = (p_1, p_2, p_3)$ .

### 3.2.1 Results and discussion for two and three parameter attenuation models of shielding

The following results and discussion show the RMS error as spatial degrees of freedom and number of snapshots is varied as surface plots. This confirms our assumptions that convergence will be improved by adding more data both in the form of more snapshots and more spatial nodes. We would also like to see if the log preconditioner offers improvements when using a data set that is now only piecewise logarithmic. The model was setup with:

- Maximum number of snapshots:  $N_{S_{max}} = 30$
- Minimum number of snapshots:  $N_{S_{min}} = 3$
- Number of spatial nodes,  $ny = 60$ .

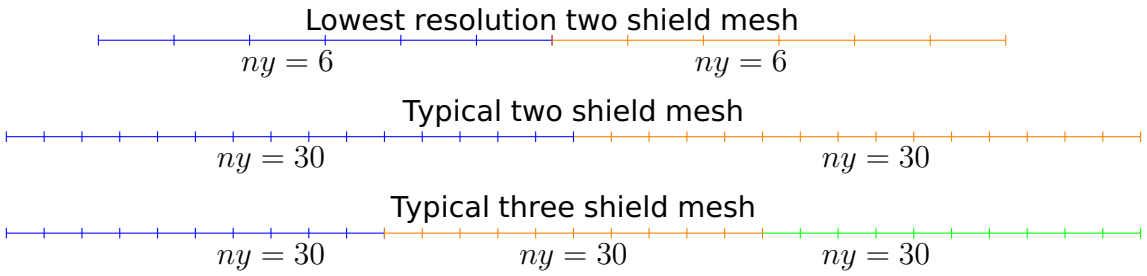


**Figure 3.8:** The spatial domain here is now modelling two or more individual shields. Both the effects of adding more training data through more snapshots and also now increasing the number of nodes and hence spatial resolution are explored. These example meshes show two shields one in blue and one in orange and the lowest resolution mesh with 6 node in each shield and a 30 node mesh with resolution being a range investigated from 6 nodes to 60 nodes.

In the set of figures 3.9 we just look a slice the two parameter ROMs coordinate space. This is done to more simply compare with the previous on parameter ROM. Plots (a) and (b) are taken from the first section of the two parameter ROM and (c) and (d) are taken from the second section. The ROM solutions are at an unseen point in the training space, furthest from the seen-points, and the exact solutions are the analytical solution at the ROM parameter in question.



We see that in figures 3.9 (a) and (b) from looking at the Root mean squared error, RMS error, as we increase spatial nodes and number of snapshots used the log preconditioner still improves NIROMs for shielding for inhomogeneous materials. As the models are made more complex and depart from constituting single exponential we expect to see this improvement somewhat diminished. We will see that in later chapters this preconditioner still can give some improvement. In figures 3.9 (c) and (d) we look at the maximum relative error as we increase spatial nodes and number of snapshots used. We see more clearly the effects of increasing spatial degrees of freedom.

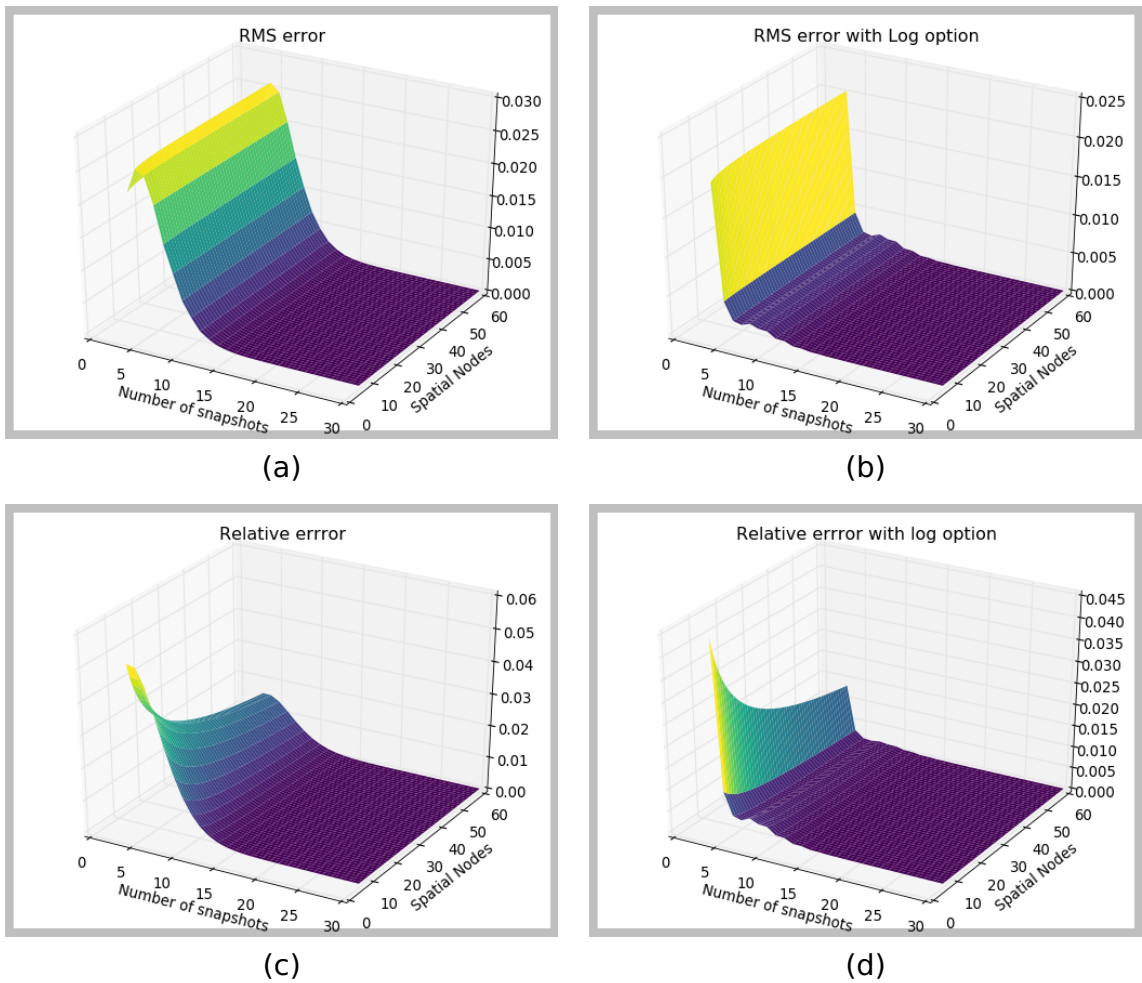


**Figure 3.9:** Root mean squared error of ROM solutions drops off rapidly with addition of more snapshots and for this problem very genitally as the spatial degrees of freedom increase (a). With the preconditioner this is even more rapid (b). Maximum Relative error of ROM whole solution with the preconditioner applied drops more rapidly (c). At this smaller scale you begin to see the periodic oscillations as the number of snapshots increases (d) which was clear in the 1D log-log plots in the previous sections of results 3.6.

We show in figure 3.10 results across the whole domain for the ROM model and exact solution with the two parameter case using  $p = [2.5, 10]$ . We expect that we will need fewer than all 24 of the POD basis function to obtain good results. The energy in 3.11 shows the information captured by using more POD basis functions and thus informs our choice of the number of POD basis functions.

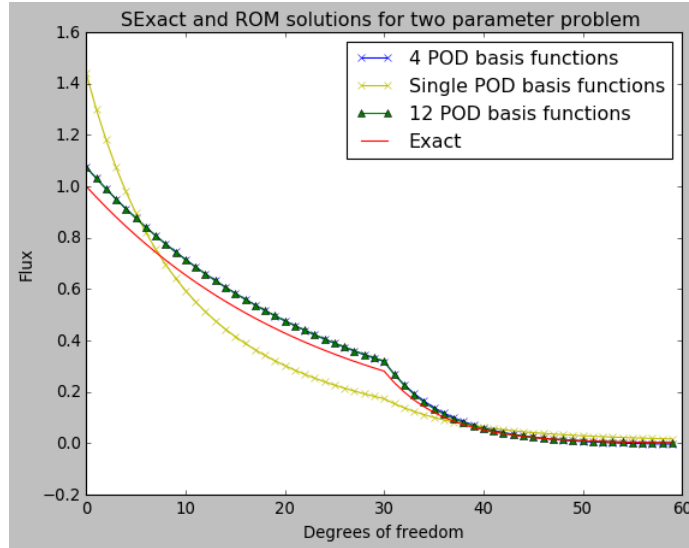


**Figure 3.10:** This plot shows ROM and exact solutions for the two parameter problem. A single POD basis function is not sufficient to capture all the information and we expect this from the cumulative energy. We see little difference between 4 and 12 POD basis functions. The problem mesh is a 60 node version of 3.8.

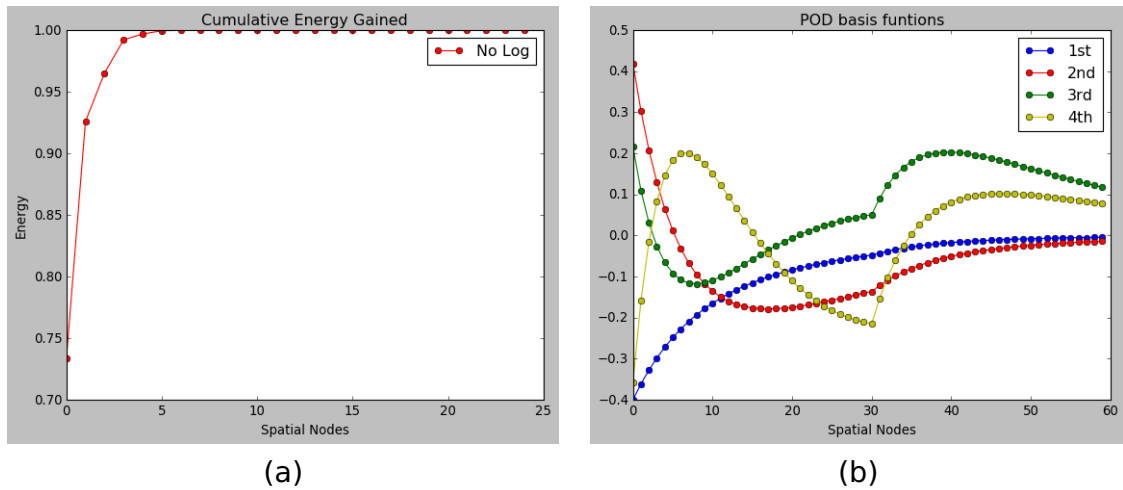


**Figure 3.11:** The energy capture with POD basis and shape of the first few the POD basis functions is shown.

In figure 3.12 we see the results across the whole domain for the ROM model and exact solution of the three parameter case with  $p = [3, 5, 8]$ . We see that the case with three parameters still has good agreement. In general we see

that for sufficient numbers of POD basis functions ROMs will have good feature recognition and that adding more interfaces poses little trouble. The energy in 3.13 shows the information captured by using more POD basis functions. We can also see features such as the position of the three interfaces captured in the POD basis functions.

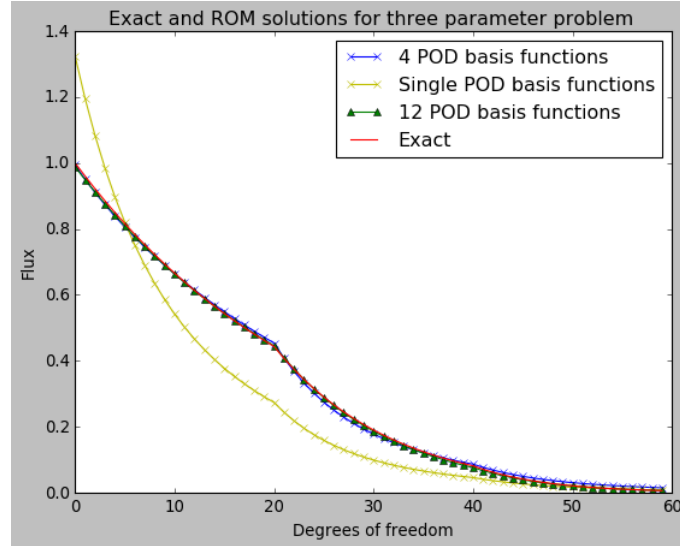


**Figure 3.12:** This plot shows solutions for the three parameter problem. Similarly we see that a single POD basis function is not sufficient. Using 4 and 12 POD basis functions gives good results. The problem mesh is based on 3.8 with the addition of an extra shield.

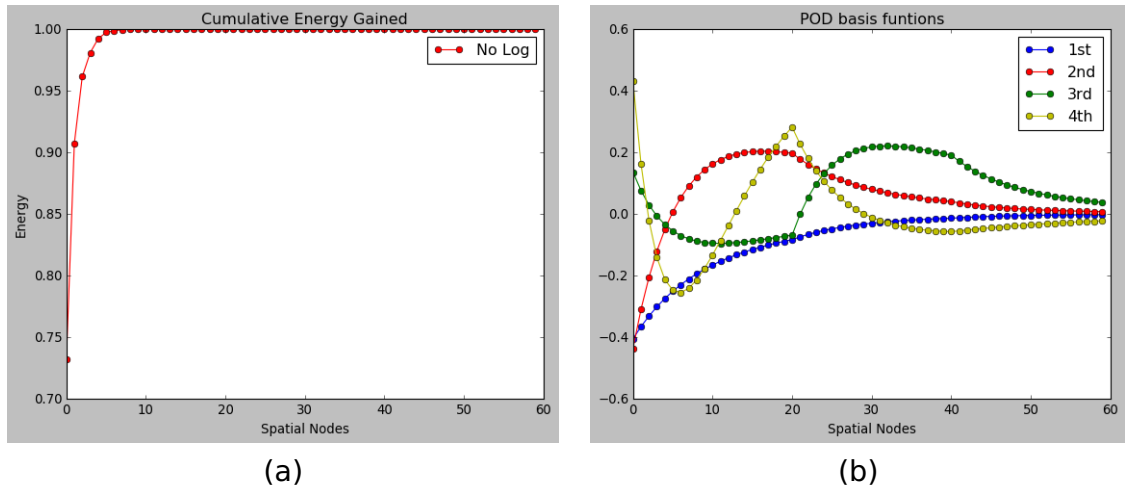


**Figure 3.13:** The energy capture with POD basis and shape of the first few the POD basis functions is shown.

### 3.3 Four parameter attenuation models of shielding

This third model uses the same analytical test problem for a global NIROM for a two domain shield. The thickness of the domains and respective attenuation factors are used as the four NIROM parameters.

For this analytical test case a set of piecewise exponential functions are used to approximate solution to the Boltzmann Transport Equation for neutrons. We assume we have a single energy group, a one dimensional spacial domain, and steady state solutions. Now however we model material and geometric properties by using a different attenuation parameter in each section of the domain; namely  $p_1$ ,  $p_2$  and  $p_3$  probability of neutron capture per unit length in the 1st and 2nd or possibly 3rd section of the interval. The new parameters introduced are the proportion of the interval that the fist shield occupies  $l_1 \in (0, 1)$  and the total length of the interval two shields combined occupy  $l_2 \in (0.5, 1.5)$ . The exact solution used to generate the snapshots is now:

$$\psi(x, \Omega, E, ; P) \approx \phi(x; p) = \begin{cases} C_1 e^{-p_1 x}, & \text{for } 0 \leq x \leq l_1 \\ C_2 e^{-p_2 x}, & \text{for } l_1 \leq x \leq l_2 \end{cases} \quad (3.22)$$

where  $C_1 = 1$  and  $C_2 = e^{-l_1 p_1}$ . We sample  $l_1$  and  $l_2$  evenly from  $l_1 \in (0, 1)$  and  $l_2 \in (0.5, 1.5)$ . For each attenuation parameter we use a choice of parameter domain with range  $\log(p)$ :

$$p \in (10^1, \dots, 10^5) \quad (3.23)$$

with the sets  $p_1$  and  $p_2$  divided with logarithmic spacing and  $l_1, l_2$  evenly spaced such that:

$$\mathbb{P} = (p_1, p_2, l_1, l_2) \quad (3.24)$$

where  $p_1 = p_2 = p$  and  $\mathbb{P}$  matrix of the parameters for some ordering such that every snapshot vector has a corresponding point in this space of parameters

formed by treating  $p_1, p_2, l_1$  and  $l_2$  as axis.

We take our snapshot matrix  $X$  to be:

$$\mathbb{X} = \left( \phi(x; \mathbb{P}_1), \dots, \phi(x; \mathbb{P}_{N_S}) \right) \quad (3.25)$$

for some order of parameter coordinates  $\mathbb{P} = (p_1, p_2, l_1, l_2)$ .

### 3.3.1 Results and discussion for four parameter attenuation models of shielding

This third preliminary model shows the convergence results for spatial degrees of freedom and number of snapshots as surface plots for the four parameter model. With more training parameters the training data is more dense in some sense and thus the convergence as more data is added is very rapid. The effect of characteristic length is also investigated to develop some heuristics, informed by [117], we can use as a first choice in later work.

The model was setup with:  $\mathbb{P} = [5, 8, 0.65, 0.7]$  all untrained points in the parameter space,  $N_S \in (2^4, 6^4)$ , Spatial nodes,  $n_y \in (6, 30)$ . As with the previous model we look at convergence of the ROM solutions as we increase the training data using both more spatial nodes and snapshots.

In figure 3.14 (a) and (b) we see rapid improvement from 6 to 10 snapshots and little gain thereafter and very gentle improvement from adding spatial nodes. With a more complex model we see the difference with and without the preconditioner is somewhat lessened but still deliver an improvement none the less. In (c) and (d) we see the maximum relative error. With little data the preconditioner is actually worse for the first time. After an increase from 6 to 10 snapshots we see the preconditioner improves the results.

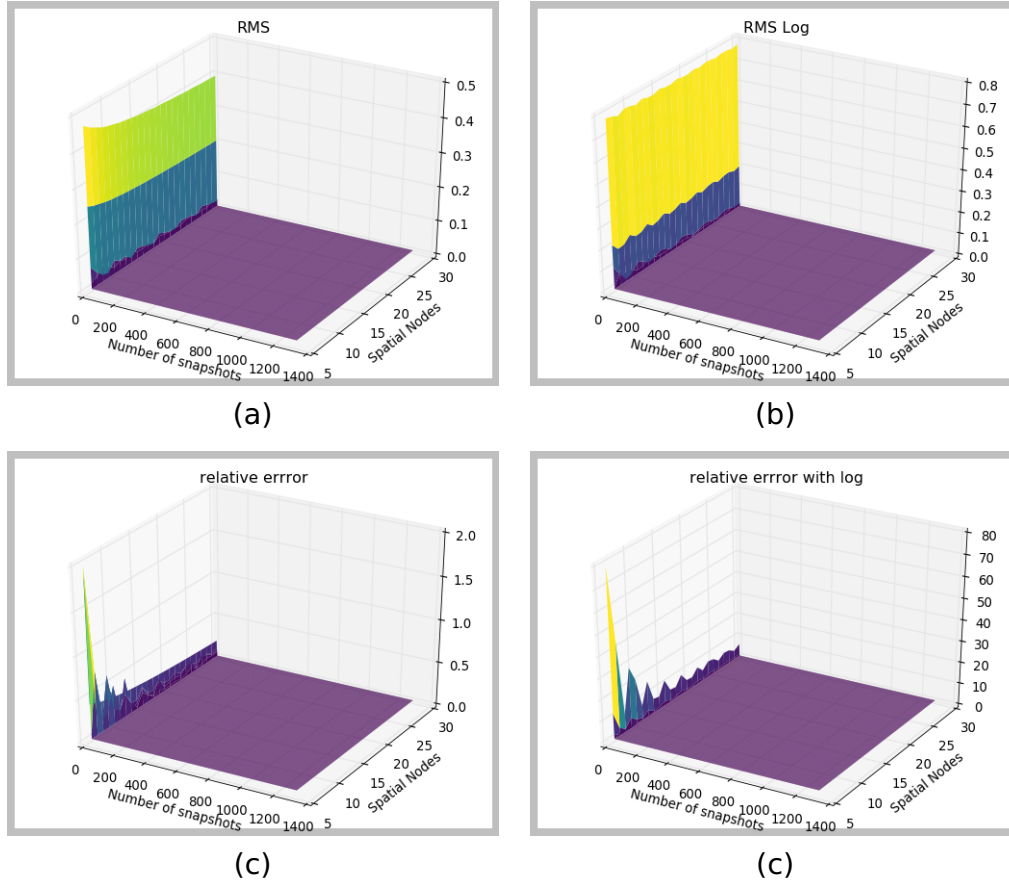


**Figure 3.14:** Root mean squared error of ROM solution drops rapidly with the addition of more snapshots and for this problem very genitally as the spatial degrees of freedoms increase (a). With the preconditioner we improve the solutions even more rapidly (b). Looking at the maximum relative error we see initial variation with only 6 spatial nodes and a low amount of snapshots. Adding more snapshots quickly eliminates this without (c) and with (d) the log preconditioner.

Here in figure 3.15 we see ROM results for the four parameter case with  $p = [2.5, 10, 0.5, 1]$  an untrained point with parameter space of size  $8^4$  and also  $2^4$ . More training data improves the results. We can see a lot of variation in the results for different characteristic lengths. The best results would come from the choice of characteristic length that makes kernel matrix of the radial basis interpolation on the edge of being ill-conditioned. Its is not practical to find this point for every run of the ROM as we try a few heuristics. The rational behind them is that we seek to characterise the shape of the parameter space with a singe number. The most robust choice we found in this investigation was the difference in maximum and minimum values in the parameter space, normalised by dividing through by the mean number of snapshots in a parameter axis. The other choices came from thinking of

the training as a space and trying measure that characterise spaces such as volume.

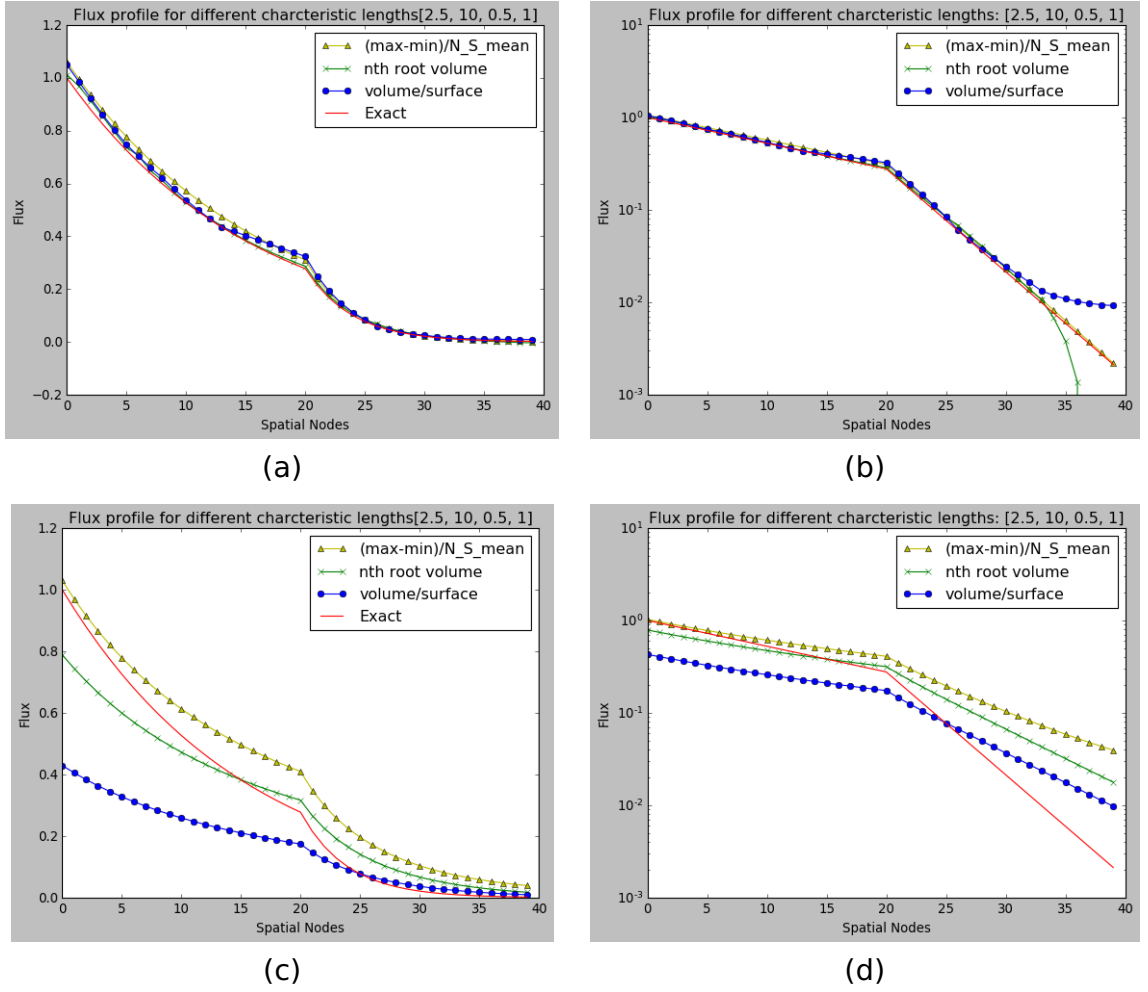


**Figure 3.15:** Here we have ROM solutions for the four parameter problem on linear (a) and log-linear (b) plots for  $8^4$  snapshots and linear (c) and log-linear (d) plots for  $2^4$  snapshots. We can see clearly that with more snapshots greatly improves the results. A selection of characteristic lengths are used. POD basis functions are chosen such that 95% energy is captured. We can see in the log-linear version of the plots that  $(\max - \min)/\text{mean}$  gives the best results here.

In this section we make few important realisations:

1. choice of characteristic length is extremely important.
2. adding more parameters scales geometrically in terms of snapshots.

Noting some characteristic lengths performed better in different sections of the domain, we see that going forward to a more complex problem where each section will represent different materials, consistency between each



material will be important and difficult to obtain with one global ROM for all materials. This will be compounded as more complex shielding problems will have fluxes spanning more orders of magnitude. We also see that a limit to how many materials we can model is imposed by the scalability of the ROM. A novel way to overcome this is to couple ROM solutions together. By this we mean that solutions at the boundary of one ROM for one material inform the solutions of next ROM for the next material.

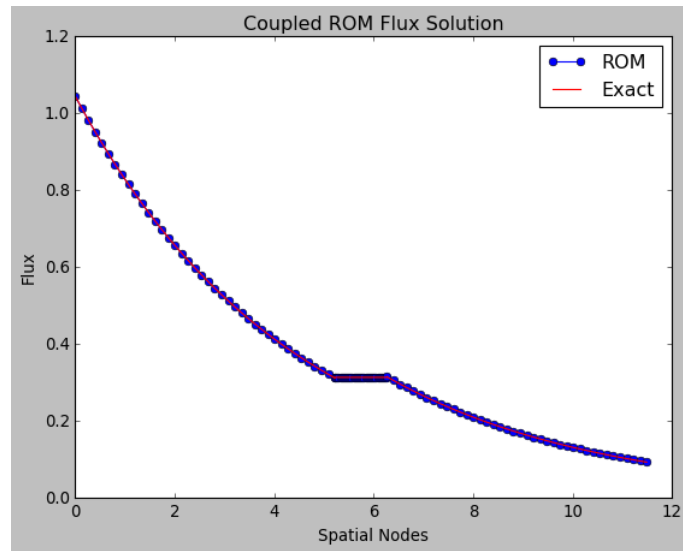
### **3.4 Coupling of ROM towards the ASPIS benchmark model**

In the previous section we suggested that for more complex problems involving more materials would benefit from breaking down a global ROM into a library of different ROMs for each material and joining them together through a coupling scheme. In this section we make a preliminary investigation into coupling ROMs and compare with the global ROMs from the previous section. This lays the ground work for building a more detailed ROMs for each material in the ASPIS benchmark our target application in later chapters. With a single parameter and flux we can only couple in one direction, forwards or backwards. In later work we use models with directional and inter energy group scattering as well as attenuation and will need a scheme to couple these fluxes successfully. In this preliminary work we will couple a single flux in the forward direction.

#### **Results and discussion of preliminary coupling**

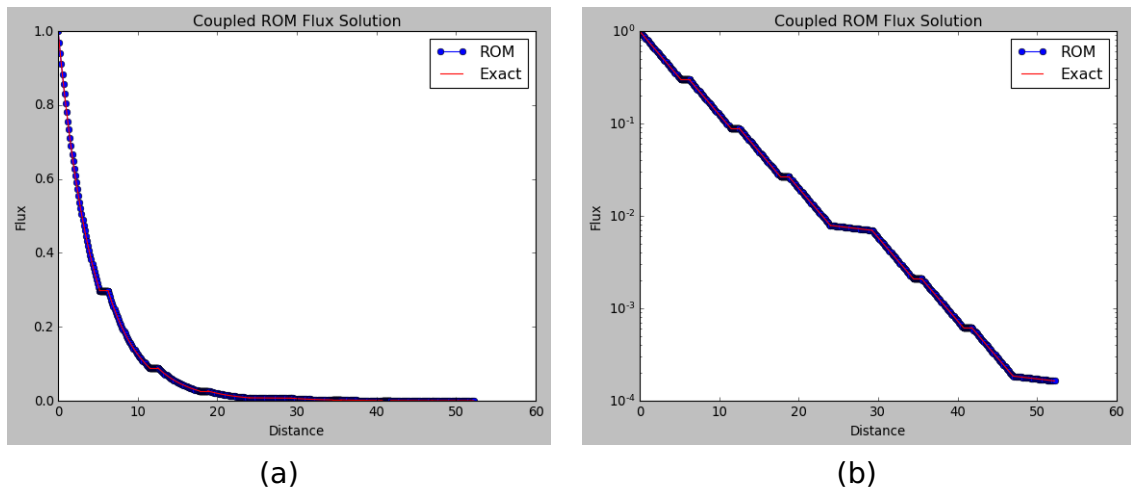
The same model as in the previous sections is used for a single parameter, the attenuation factor. The coupling used the value at the end of the first shield as the input boundary condition for the second and so on across the whole domain. This model simply couples the flux is coupled in one direction only. We also add a model for shielding of air that just returns the input flux though the region where the material is air. This model of air will be sufficient through this work. In Figure 4.6 we see two single attenuation factor ROM models for steel coupled together with a small section of air between. The ROMs were trained with data chosen 20% either side of the attenuation factor representing steel.

Figure 3.17 shows the same simple coupling as the previous figure but for a larger selection of materials, air, stainless and mild steels. The properties come from the Iron-88 benchmark and the order is inspired by the ASPIS problem. On the log-linear scale we can see upon coupling several materials we begin to span more and more orders of magnitude in flux. Each ROM is



**Figure 3.16:** This plot shows the flux profile of three ROMs coupled in one direction. The ROM is trained 20% either side of the ASPIS data for three regions, namely steel, air and steel. The unknown point the ROMs are finding is chosen to be far from the training data without leaving the space and a value of 95% of the energy informed the number of POD basis functions used.

simple however coupling allows a more complex overall model to emerge. In later work when we add more complex coupling scheme due to scatter being modelling we will see shields effecting both forward and reverse neighbours. A clear advantage of coupling is that we can add detail where needed and remove when unnecessary. Each shield ROM could in principle have different training, degrees of freedom and snapshots etc.



**Figure 3.17:** Here show multiple slabs coupled together coupled with physical properties, the attenuation factor, calculated from the Iron-88 benchmark but with the geometry of the ASPIS problem in linear (a) and log-linear (b) scales.

In figure 3.18 we see that when the training is set up with the same total number of snapshots the coupled ROM performs better than the global ROM.

The preliminary model used has a fixed interface and is a two parameter, the attenuation factors in each material, model. Note the coupled ROM out performs the global ROM with effectively half the number of snapshots as the two methods have the same total number of snapshots but in the coupled ROM these are split evenly in each material.

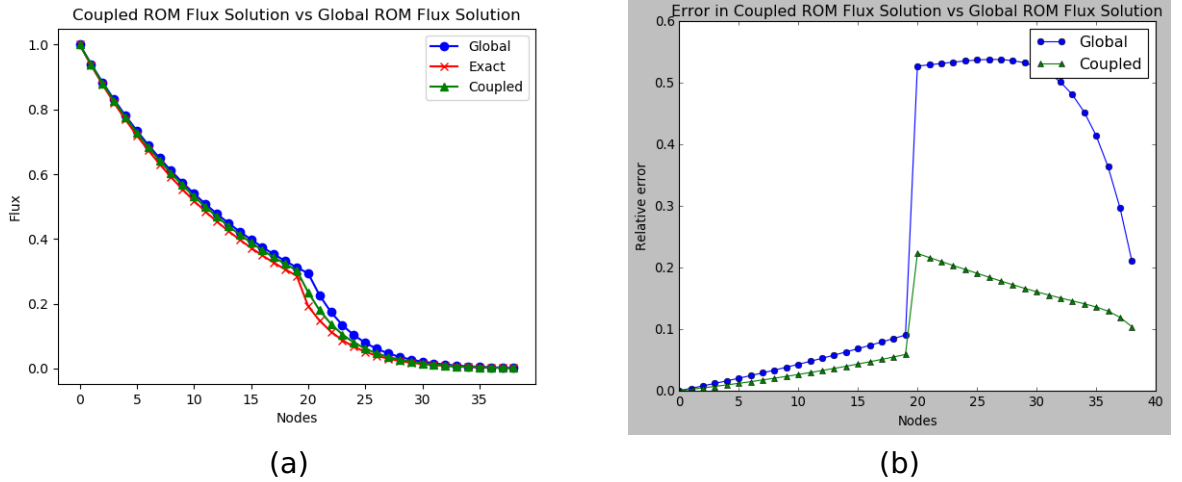


**Figure 3.18:** Here we have a comparison of coupled vs global NIROM for a test problem for attenuation of  $[2.5, 10]$  (a). Here we see the error in the two methods (b)). Even though we only have two parameters, coupling gives an improvement.

Going forward we will need to develop ROMs scheme that can handle multiple variables and we demonstrate how this can be done in the next section using concatenation of snapshot data. The conceptual leap is that the columns of the snapshot matrix need not have direct physical meaning as long as the variables can be recovered in post-processing. We will also need to develop more complex coupling for realistic physical problems.

## Using elementary functions to investigate multiple variable ROM

In this section we investigate how to handle multiple variables with our ROM technique. A way to approach this is to concatenate multiple variables into a single snapshot vector. The ROM now reproduces a profile that contains several variables. The individual variables can be recovered in a post-processing step.

### 3.4.1 Results

In figure 3.19 we see that the ROM trained on concatenated data can reproduce the concatenated ROM solutions. Each of the two variable was represented by two sets of single exponential profiles concatenated in a way that each snapshot is just one profile from the first variable followed by one from the second. The individual variables can be recovered after the ROM.

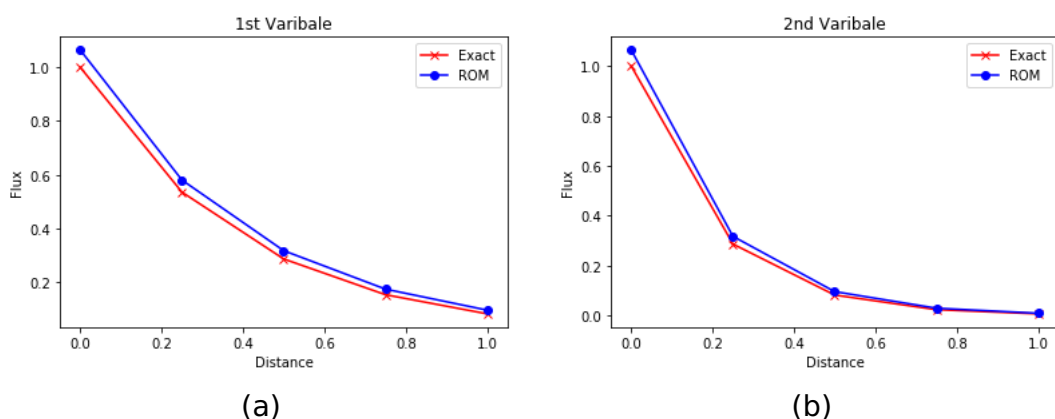


**Figure 3.19:** For elementary functions made of exponential functions we see an error in the order of 0.1 or less even for this few snapshots, here 12

In figure 3.20 we use a pair of functions that are no longer smooth: a two sine curve with increasing amounts of random noise and shift across the domain left-to-right  $f(x) = \sin(px) + W$ , where  $p$  is varied to get a snapshot matrix and  $W$  is a random number. This is done to briefly show that the ROM can capture noisy training data. We see that we need more snapshots to get comparable results. This is still a small number for an erratic function and shows that the ROM is very capable of feature recognition.

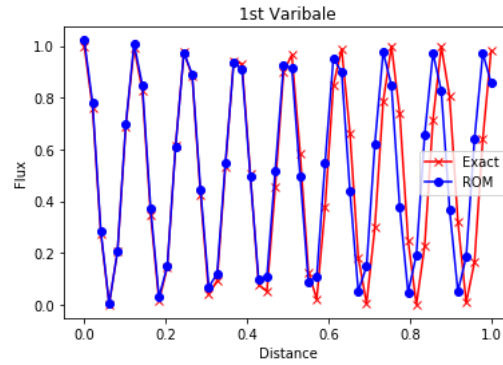


**Figure 3.20:** Highly erratic functions as expected need more snapshots to get similar errors. Here we have gone from 12 to 40 to get an error comparable to the first set of profiles.

In this chapter we have prepared all the tools we need to develop and apply the ROM to the ASPIS benchmark problem. We can see that coupling provides a way to add more materials without scalability issues. We also saw the potential in a logarithmic preconditioner and a method for ROMs with multiple variables.

## Conclusion

These preliminary investigations demonstrate a few concepts. First, the validity of the logarithmic pre-conditioner with decay dominated training data. Second, that coupling ROM domains is worth investigation and could offer an improvement over interface position as a ROM parameter with multiple parameters being modelled. Third, that multiple variables can be treated as a concatenated variable making up a single snapshot. We also learn that characteristic length is extremely important. These insights will all be useful going forward.

# Chapter 4

## Coupled 1-Group Reduced Order Models for generic and ASPIS benchmark configurations of slabs

### **Overview**

This chapter presents a bi-directional analytical scattering model of shielding for a single energy group. This is applied to an inhomogeneous material domain with the configurations of materials based on the ASPIS benchmark experiments. A coupling scheme is introduced to join homogeneous material models to form the larger inhomogeneous models. This coupling is first understood with analytical solutions. Following this a coupled ROM is developed testing the widths as the main ROM parameter and testing boundary conditions as a ROM parameter that facilitates the coupling. We demonstrate that the online component of the NIROM is rapid enough to be used in the iteration loop of the coupling scheme. A multi-group version of this scattering model of shielding is later developed in chapter 5.

# Introduction

The following numerical examples in this chapter are intended to demonstrate the concept of coupling single slab reduced order models (ROMs). Generic configurations of different material slabs are first coupled to show to how the coupling scheme works. Ultimately the full configuration of the ASPIS benchmark are coupled. The analytical model used here has scattering in two directions in and out of the slabs and hence the coupling scheme is 1-dimensional. Beyond 1D, angular discretization is the standard [118]. Although this model was chosen as a stepping stone to enable the development of a multi-dimensional coupling scheme for N-group problems, 1-group models have quantitative applications in very fast or very thermal reactors with appropriate choice of cross-sections. Neutron transport is still an area of active development in research and industry. Problems can be highly challenging as they often necessitates a full 3 spatial plus a time dimension and possibly meV to MeV ranges of energy spectra. Even though the full order models used here are analytical, hence not costly to evaluate, and can be coupled to solve the problem for the whole configuration, the work done here is indented to be a proof concept. The novel concept here is a methodology for coupling ROM solutions and the library built from these analytical single slab solutions could in the future be replaced with real life data or a most sophisticated model for a single slab.

## 4.1 Model with positive and negative scatter

We derive the model for a 1-group shield with positive and negative scatter. The model gives us neutron flux, a scalar measure of the number of neutrons in an arbitrary cross-sectional unit area in all directions per unit time, as a function of distance, the material properties: macroscopic capture, scatter and fission cross-sections  $\Sigma_c, \Sigma_s, \Sigma_f$  and domain length  $L$ . This model comes from the mono-energetic neutron transport equations for a reactor shield however here we will derive it from first principles.

Let the component of the neutron flux in the positive direction be  $\psi_+(x)$  and



the negative direction  $\psi_-(x)$ . We can represent the potential affects on the neutron flux of all possible scatterings in a matrix operator  $\hat{S}$ :

$$\hat{S} \cdot \hat{\psi} = \begin{pmatrix} \Sigma_{++} & \Sigma_{+-} \\ \Sigma_{-+} & \Sigma_{--} \end{pmatrix} \begin{pmatrix} \psi_+ \\ \psi_- \end{pmatrix} \quad (4.1)$$

where  $\Sigma_{++}$  is the cross-section for scattering from the positive x-direction to the x-direction, which in the 1-group, mono-energetic problem has no effect on the flux. By symmetry of the 1-dimensional domain  $\Sigma_{++} = \Sigma_{--}$  and the flux scattering from positive x-direction to the negative x-direction or, vice versa by symmetry,  $\Sigma_{+-} = \Sigma_{-+}$ . Hence the scattering can be represented by two numbers,  $\Sigma_S$  a total scattering and  $\alpha$  the probability that the scatter changes the direction of the particle. Thus

$$\hat{S} \cdot \hat{\psi} = \begin{pmatrix} (1-\alpha)\Sigma_S & \alpha\Sigma_S \\ \alpha\Sigma_S & (1-\alpha)\Sigma_S \end{pmatrix} \begin{pmatrix} \psi_+ \\ \psi_- \end{pmatrix} = \Sigma_S \begin{pmatrix} (1-\alpha) & \alpha \\ \alpha & (1-\alpha) \end{pmatrix} \begin{pmatrix} \psi_+ \\ \psi_- \end{pmatrix} \quad (4.2)$$

For isotropic scattering  $\alpha = \frac{1}{2}$ .

Suppose a small change  $\delta x$  is made. The first term is just any unchanged positive flux  $\psi_+(x)$ . There will be losses and gains in flux due to the interactions represented by the cross-sections to account for. The first few terms are some positive flux  $\psi_+(x)$  lost due to capture, fission or a change in direction from scattering positive to the negative. However some positive flux  $\psi_+(x)$  is also gained from scatter in the opposite direction from negative to positive. The last term is the flux gained from fission of both directions. Therefore we can form a particle balance equation:

$$\psi_+(x+\delta x) = \psi_+ - (\Sigma_c + \alpha\Sigma_s + \Sigma_f)\psi_+\delta x + \alpha\Sigma_s\psi_-\delta x + \frac{1}{2}\lambda\nu\Sigma_f(\psi_+ + \psi_-)\delta x \quad (4.3)$$

and thus a corresponding particle balance for the negative flux  $\psi_-(x)$  can be formed:

$$\psi_-(x+\delta x) = -\psi_- + (\Sigma_c + \alpha\Sigma_s + \Sigma_f)\psi_-\delta x - \alpha\Sigma_s\psi_+\delta x - \frac{1}{2}\lambda\nu\Sigma_f(\psi_+ + \psi_-)\delta x \quad (4.4)$$

where  $\nu$  is the neutron speed and  $\lambda$  is the fundamental eigenvalue. To make the flux distribution time-independent, that is to say the chain reaction in the source is materials is in a steady-state. We call this state reactor criticality and is represented by  $\lambda = 1$ .

Taking the limit as  $\delta x$  approaches zero yields a pair of differential equations:

$$\frac{d\psi_+}{dx} + (\Sigma_c + \alpha\Sigma_s + \Sigma_f)\psi_+ = \alpha\Sigma_s\psi_- + \frac{1}{2}\lambda\nu\Sigma_f(\psi_+ + \psi_-) \quad (4.5)$$

$$-\frac{d\psi_-}{dx} + (\Sigma_c + \alpha\Sigma_s + \Sigma_f)\psi_- = \alpha\Sigma_s\psi_+ + \frac{1}{2}\lambda\nu\Sigma_f(\psi_+ + \psi_-) \quad (4.6)$$

The scalar flux given by:

$$\psi(x) = \psi_+(x) + \psi_-(x) \quad (4.7)$$

gives the total flux of neutrons in all directions and the current is given by:

$$J(x) = \psi_+(x) - \psi_-(x) \quad (4.8)$$

gives the net flux of neutrons in the positive direction. We can take the sum and the difference of the pair of differential equations to get a pair for the scalar flux and the current instead:

$$\frac{d\psi}{dx} = \Sigma_t J = 0 \quad (4.9)$$

$$\frac{dJ}{dx} = \Sigma_e \psi = 0 \quad (4.10)$$

where  $\Sigma_t = \Sigma_c + 2\alpha\Sigma_s + \Sigma_f$  is the total cross-section and  $\Sigma_e = \Sigma_c - (\lambda\nu - 1)\Sigma_f$  is the emission cross-section. The first of which can be differentiated and the gradient of the current can be substituted from the second to yield:

$$\frac{d^2\psi}{dx^2} - \omega^2\psi = 0 \quad (4.11)$$

where  $\omega = \sqrt{\Sigma_t\Sigma_e}$ . Now  $\Sigma_t > 0$  so the general form of the solution depends exclusively on the sign  $\Sigma_e$ . In the case of our shielding problem we have no

fissile material and so  $\Sigma_f = 0$  hence:  $\Sigma_t = \Sigma_c + 2\alpha_A\Sigma_s$  and  $\Sigma_e = \Sigma_c$  and takes the general form:

$$\psi_+(x) = \frac{(1 - \beta)Ae^{\bar{\omega}x} + (1 + \beta)Be^{-\bar{\omega}x}}{2} \quad (4.12)$$

$$\psi_-(x) = \frac{(1 + \beta)Ae^{\bar{\omega}x} + (1 - \beta)Be^{-\bar{\omega}x}}{2} \quad (4.13)$$

where  $\Sigma_c, \Sigma_s, \Sigma_f$  and the capture, scatter and fission cross-sections respectively. For isotropic scattering we have that  $\alpha_A = \frac{1}{2}$ . we also fix  $\lambda = 1.0$  and  $\nu = 1.0$ . We have the constants:  $\omega = \sqrt{\Sigma_e\Sigma_t}$  and  $\beta = \frac{\bar{\omega}}{\Sigma_t}$

The first model will be on a single slab with flux at the start  $\Psi^+(0) = 1$  and  $\psi^-(L) = R$ . The purpose of setting the right hand boundary to be arbitrary is to build a model of multiple slabs using ROM to couple them together.

Applying the boundary conditions we get:

$$2 = A(1 - \beta) + B(1 + \beta) \quad (4.14)$$

$$2R = A(1 + \beta)e^{\bar{\omega}L} + B(1 - \beta)e^{-\bar{\omega}L} \quad (4.15)$$

for  $\psi_+$  and  $\psi_-$  respectively. These form a pair of linear simultaneous equations. Multiply the first equation by  $(1 + \beta)e^{\bar{\omega}L}$  and the second equation by  $(1 - \beta)$  to eliminate the  $A$  terms:

$$2(1 + \beta)e^{\bar{\omega}L} = A(1 - \beta)(1 + \beta)e^{\bar{\omega}L} + B(1 + \beta)(1 + \beta)e^{\bar{\omega}L} \quad (4.16)$$

$$2R(1 - \beta) = A(1 + \beta)(1 - \beta)e^{\bar{\omega}L} + B(1 - \beta)(1 - \beta)e^{-\bar{\omega}L} \quad (4.17)$$

We subtract the second equation from the first and collect the terms:

$$2[R(1 - \beta) - (1 + \beta)e^{\bar{\omega}L}] = B[(1 - \beta)^2e^{-\bar{\omega}L} - (1 + \beta)^2e^{\bar{\omega}L}] \quad (4.18)$$

Therefore we have that:

$$B = 2 \frac{(1 + \beta)e^{\bar{\omega}L} - R(1 - \beta)}{[(1 + \beta)^2e^{\bar{\omega}L} - (1 - \beta)^2e^{-\bar{\omega}L}]} \quad (4.19)$$

Similarly, eliminating the  $B$  terms in the first simultaneous equations we have that,

$$A = 2 \frac{(1 + \beta)R - e^{\bar{\omega}L}(1 - \beta)}{[(1 + \beta)^2 e^{\bar{\omega}L} - (1 - \beta)^2 e^{-\bar{\omega}L}]} \quad (4.20)$$

Now we have an analytical solutions for the flux:

$$\psi_+ = \frac{(1 + \beta)(1 - \beta)R - e^{\bar{\omega}L}(1 - \beta)^2}{[(1 + \beta)^2 e^{\bar{\omega}L} - (1 - \beta)^2 e^{-\bar{\omega}L}]} e^{\omega x} + \frac{(1 + \beta)^2 e^{\bar{\omega}L} - R(1 + \beta)(1 - \beta)}{[(1 + \beta)^2 e^{\bar{\omega}L} - (1 - \beta)^2 e^{-\bar{\omega}L}]} e^{-\omega x} \quad (4.21)$$

$$\psi_- = \frac{(1 + \beta)^2 R - e^{\bar{\omega}L}(1 - \beta)(1 + \beta)}{[(1 + \beta)^2 e^{\bar{\omega}L} - (1 - \beta)^2 e^{-\bar{\omega}L}]} e^{\omega x} + \frac{(1 + \beta)(1 - \beta)e^{\bar{\omega}L} - R(1 - \beta)^2}{[(1 + \beta)^2 e^{\bar{\omega}L} - (1 - \beta)^2 e^{-\bar{\omega}L}]} e^{-\omega x} \quad (4.22)$$

The total flux is:

$$\psi(x) = \psi_+(x) + \psi_-(x) \quad (4.23)$$

and the net current is:

$$J(x) = \psi_+(x) - \psi_-(x). \quad (4.24)$$

setting  $\psi_-(L) = R = 0$ , a zero flux boundary, will yield a model with the whole domain acting as a large single slab.

The cross-sections show the probability that a nuclear reaction occurs: shown in table 4.1. Microscopic cross-sections are typically measured experimentally and corresponds to the target area on the scale of the individual nucleus, measured in Barns or  $cm^2$ . One Barn in SI units is  $10^{-28}m^2$  and has its origins in the secrecy of the Manhattan project a coded reference to the US idiom: "couldn't hit the broad side of a barn" meaning poor aim. The Macroscopic cross-section is the probability of interaction in the target area of all nuclei in a given volume. It is important to note we use the Macroscopic cross-sections and that they are denoted with capital  $\Sigma_I$  where  $I$  is a label for the interaction of interest. For a capture interaction for example we have:

$$\Sigma_c = \sigma_c N \quad (4.25)$$

where  $N$  is the atomic number density and  $\sigma_c$  is the microscopic cross-section. The void is modelled to have transmission of flux only are therefore no interactions occur. The model just returns the boundary conditions when  $\omega = 0.0$  and  $\beta = 0.5$ .

**Table 4.1:** 1-Group Macroscopic Cross-sections in the 1-Group problem. These have been derived from the periodic table and confirmed by the code WIMS.

Material	$\Sigma_c (cm^{-1})$	$\Sigma_s (cm^{-1})$
Boral	$6.913127 \times 10^{-1}$	$2.099684 \times 10^{-1}$
Mild Steel 1	$9.715767 \times 10^{-3}$	$5.21055 \times 10^{-1}$
Stainless Steel	$1.192884 \times 10^{-2}$	$5.43487 \times 10^{-1}$
Water	$1.828413 \times 10^{-3}$	$8.640224 \times 10^{-1}$
Mild Steel 2	$9.485925 \times 10^{-3}$	$5.136567 \times 10^{-1}$
Concrete	$2.802773 \times 10^{-3}$	$3.549348 \times 10^{-1}$
	$\omega (cm^{-1})$	$\beta$ (Dimensionless)
Void	0.0	0.5

## 4.2 The coupling scheme

It is often useful to break down problems in numerical methods into smaller sub-domains. This can aid in parallel computation when the sub-domains are independent. Tools such as Domain decomposition methods split boundary value problems down in to smaller parts for example. In this work we break down problems into different homogeneous materials in particular, shielding on the ASPIS configuration for each material.

We now introduce the coupling scheme used to join the individual single shield models derived in the last section. The two directional fluxes are given by the equations 4.21 and 4.22. The equations are parameterised by the boundary conditions of the model. As such, the coupling scheme for the configuration of single shield models can be formulated naturally in accordance with the structure of the boundary conditions. In this problem if we were interested in the coupling of two shields with fluxes  $\Psi_1^+, \Psi_1^-$  in the first shield and  $\Psi_2^+, \Psi_2^-$  the in the second, then they would both have Dirichlet boundary conditions in following the forms:

$$\begin{aligned}\psi_1^+(0) &= 1 \\ \psi_2^-(L_2) &= 0\end{aligned}\tag{4.26}$$

two being fixed at the start 0 and end  $L_2$  of the configuration of shields. The rest of the boundary conditions are free boundary conditions an used to gain

continuity across the interfaces. For two shields we would have one interface at  $L_1$  and thus free boundary conditions:

$$\begin{aligned}\psi_1^+(L_1) &= \psi_2^+(L_1) \\ \psi_1^-(L_1) &= \psi_2^-(L_1)\end{aligned}\tag{4.27}$$

This leads to a system of boundary conditions where a set of guesses can first be made for the values of the free boundary conditions and the fixed boundary conditions remain fixed. The values of the neutron fluxes at the free boundaries after the initial set of guesses are applied can then be used as a new set of guesses. This can be repeated until the fluxes across the interfaces of the free boundaries have continuity up to some pre-set tolerance  $\epsilon$ .

$$\frac{\psi_2^-(L_1) - \psi_1^-(L_1)}{\psi_2^-(L_1)} < \epsilon\tag{4.28}$$

At this point we have an approximate solution for the whole domain and say the slabs have been coupled. We only need to check continuity in the negative fluxes across the interfaces as the analytical model for both directional fluxes they are both a function of the boundary condition in the negative flux. More generally for the case with  $n > 2$  shields, we have a set of free boundary conditions than can be dealt with with a set of corresponding pre-set tolerances or a single tolerance that bounds above the relative differences across the interfaces:

$$\max\left(\frac{\psi_2^-(L_1) - \psi_1^-(L_1)}{\psi_2^-(L_1)}, \dots, \frac{\psi_n^-(L_{n-1}) - \psi_{n-1}^-(L_{n-1})}{\psi_n^-(L_{n-1})}\right) < \epsilon\tag{4.29}$$

where  $L_0$  is the the start of the shield,  $L_n$  is the end of the shield and  $L_1, \dots, L_{n-1}$  are the interfaces the lie between.

The models that are used in this coupled scheme could be obtained from either ROMs or analytical models. The work is is a proof of concept and these models could be replaced by any model with the same structure of boundary conditions. Although the model used here is simple the online stage of the ROM technique is rapid compared to most more sophisticated calculation.

Here the coupling scheme is outlined in the following algorithm:

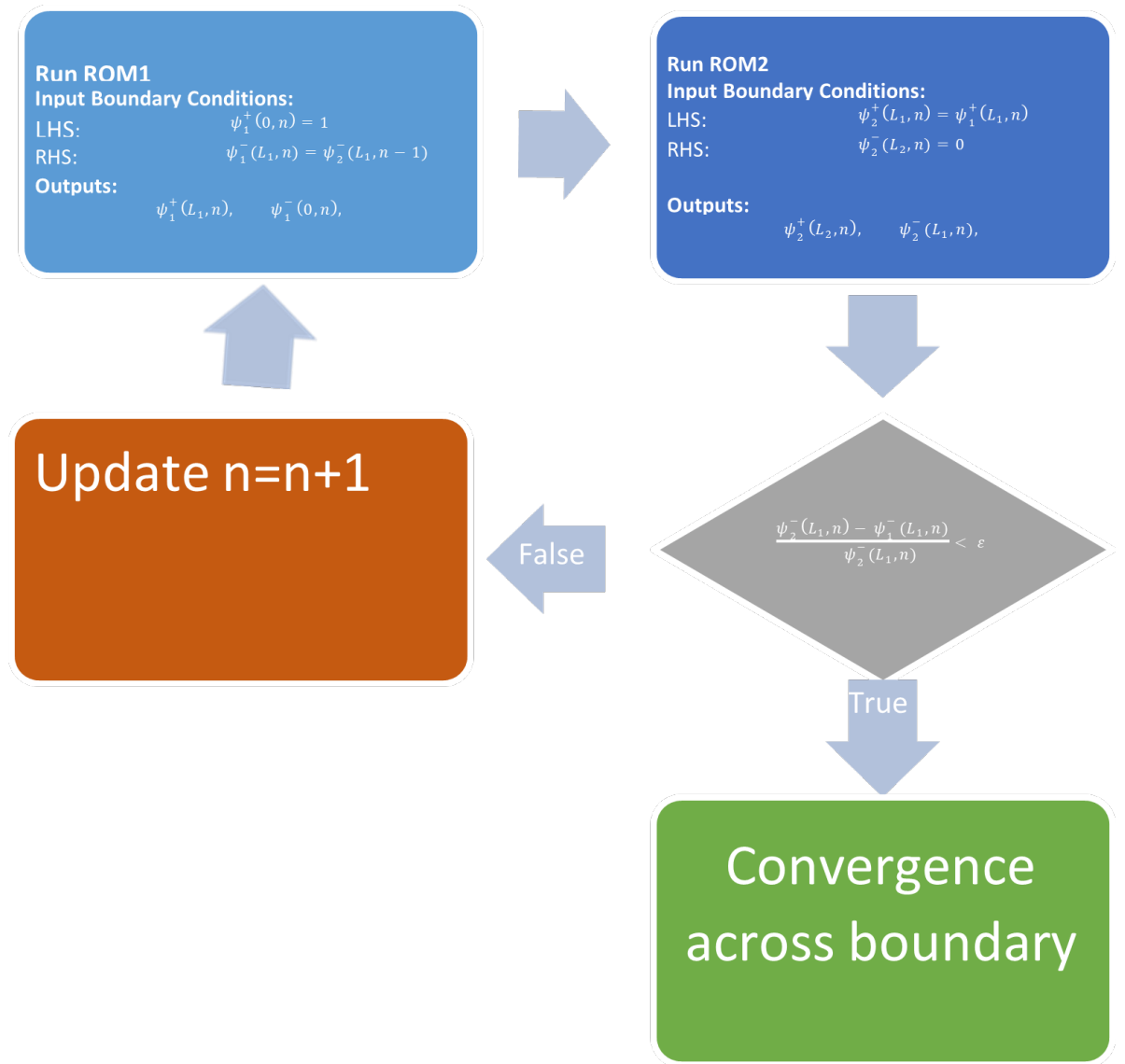


**Figure 4.1:** The iterative coupling scheme is outlined. The boundary conditions at the start and end of the problem are fixed while the free boundary conditions are gradually improved as guesses yield flux profiles in the shields with can inform new, better guesses until the scheme converges.

To increase the stability of the coupling when ROM solutions are used, instead of updating the next iteration with the interface fluxes from the free boundaries as the guess, we implement a new guess in a manner similar to successive over-relaxation: using the guesses from the previous iteration as well. This slows but stabilises the convergence behaviour of the scheme. This may be due to the relaxation potentially reducing the conditioning number of the problem. Recall the choice of characteristic length in the radial basis functions is heuristically thought to be best chosen when the problem is on the edge of being ill-conditioned. This conditioning number is not known at the outset of the problem so the use of successive over-relaxation like guessing gives us more control over the scheme should results or convergence not be suitable on first choice of characteristic length and relaxation factor.

To illustrate this, consider a generic iteration scheme  $f$ :

$$x_{n+1} = f(x_n) \quad (4.30)$$

then the successive over-relaxation inspired modification of the scheme would be:

$$x_{n+1}^{SOR} = \omega(1 - x_n^{SOR}) + \omega f(x_n^{SOR}) \quad (4.31)$$

where  $\omega > 1$  will typically speed up convergence and  $\omega < 1$  will help to improve convergence where a scheme may otherwise diverge or overshoot [100].



## Coupled Exact Solutions

Here the analytical solutions can be used to help build understanding and develop the method, particularly convergence properties. During the development of the solver for the coupling scheme, the coupled analytical solutions are here checked against known solutions from analytical solutions for n-slabs on the configuration 2.8. These exact solutions come from the state of the art code WIMS, with the full 47-group model collapsed down to a 1-group model [5]. Here the results of the coupled exact solutions with the set-up of the ASPSIS benchmark are constructed for later use as a comparison with the ROM coupling. The exact and coupled exact are plotted on there own meshes. The RMS error of the scalar flux is: 0.0182. In figure

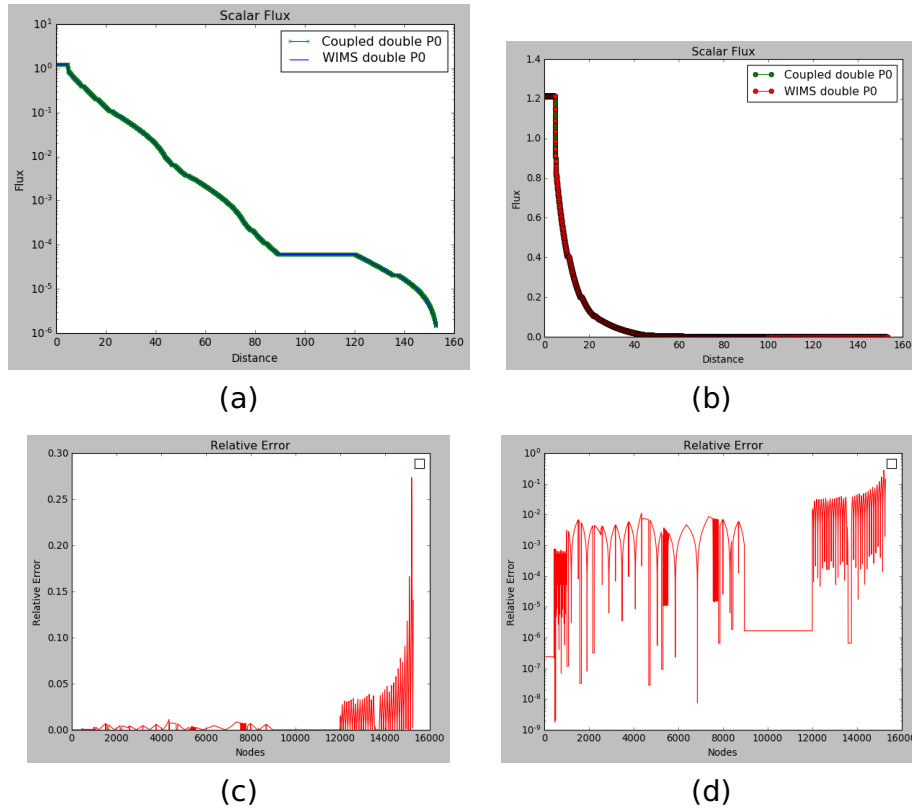


**Figure 4.2:** The results for the 1-group coupling of two directional fluxes from the analytical model for the ASPIS configuration are shown. Here in we have the scalar flux, the total of the two directional fluxes, in log-linear (a) and linear scales (b) the error in the scalar flux in linear (c) and log-linear plots (d). The tolerance for continuity in the negative flux is chosen to be  $1.0 - 10^{-6}$  and hence the continuity at all free boundaries of the negative flux at the material interfaces is bounded above by this tolerance value.

4.2 we can that there is a large variation in the flux profiles even when the boundary conditions are fixed to be a unit flux. In general, for later models

with 2-group scatter or more the boundary conditions sum to a unit flux. The use of log-linear scales make the dominate behaviours in the different materials more clear. The first 10% of the shield is effective, capturing 95% of the scalar flux from the boundary condition however  $\frac{1}{6}$ th of the scalar flux at the start of the shield is now from scatter, an increase from the fixed boundary condition. You can see the many narrow void slabs have only transmission of flux thorough the shield hence the flux in both directions remains constant where the voids occur. This can be modelled by setting  $\beta = 0.5$  and  $\omega = 0.0$  in the analytical model. The capture is higher in the boron and stainless steel slabs and the scatter is highest in the water shields. The plots of the individual directional fluxes show scattering back to the start of the shield. In the boron we see this scatter causing negative flux values higher than the unit boundary condition. In figure 4.3 we can see that although most flux is captured or scattered by the shield, flux of the order  $10^{-6}$  still reaches the end of the shield. At the start of the shield you can see an increase beyond the original boundary condition for scattering from the rest of the shield. The profile of the fluxes becomes more similar as we progress across the shield. This is in line with the 2-group and n-group models where the most interesting behaviours occur at the start of the shield.

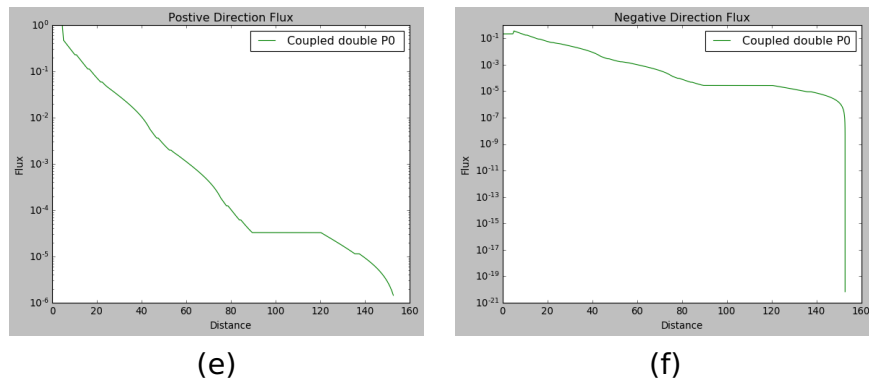


**Figure 4.3:** Here we have log-linear plots of the directional fluxes, the positive flux exact solutions coupled (e) and negative flux exact solutions coupled (f).

The relative error shown in figures 4.2(c) and (d) is fairly similar across the domain until the very end portion where it is higher towards as the size of the

fluxes involved are considerably smaller. The oscillation may be from small interpolation errors.

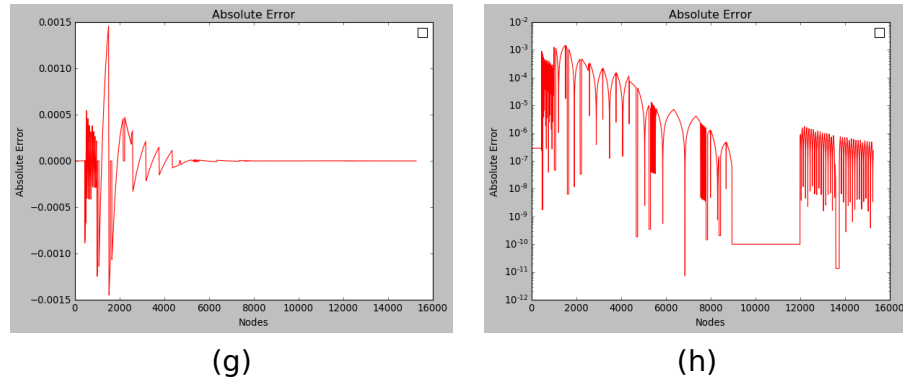


**Figure 4.4:** Here we have the absolute error in the scalar flux on linear plot with true sign of the error (g) and log-linear scale with just the size of the error (h).

In figure 4.4 you can see the absolute error is constantly a few orders of magnitude less than the value of the fluxes. The sign of the error, hence over or under estimation is not systemic. The absolute error is however bounded by the RMS error.

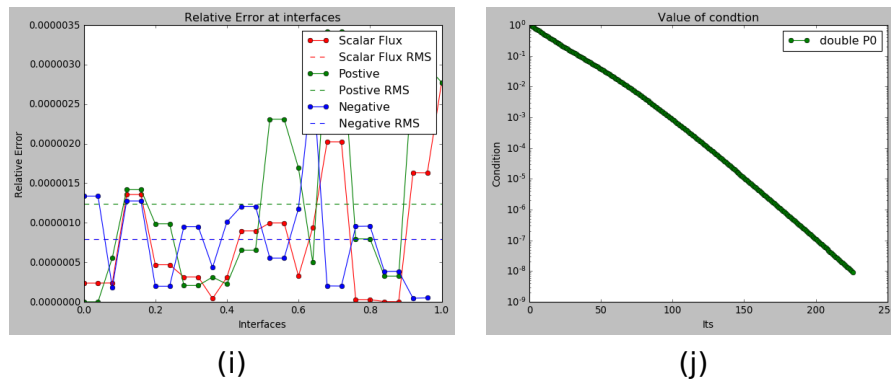


**Figure 4.5:** The relative error at the interfaces (i) is shown along the RMS error. There is no difference at the interfaces with the void parts of the shield. There is not much structure beyond this but the variation is less than an order of magnitude within the RMS. The tolerance progresses towards the desired tolerance, in this case  $10e-6$ . (j)

The condition used to check the tolerance of the iteration scheme is the maximum relative difference across the interfaces in the free boundary of the negative flux: the maximum of the values in figure 4.5(i) for each interface.

In the case of the analytical models in this section we can see in figure 4.5(j) it as the scheme iterates it is smooth and an order of convergence can be inferred from the plot.

## Coupled ROM Results

Here we couple ROM solutions with the set-up of the ASPIS benchmark. Recall the shield in the set-up contains several materials and voids of different specifications however then are spread thought out the domain and hence orders of magnitude variation in flux will be observed. The training of the ROM will thus contain ranges of points in respect to this.

We will see in the ROMs only the first two POD basis functions are required to capture all the dynamics as they capture 71% and 29% respectfully. The rest being only noise in this instance suggesting the underlying physics an be represented with only two modes.

### Training

The training of the ROMs is on logarithmically spaced intervals for the boundary condition fluxes and evenly spaced interval 20% either side for the slab widths. The logarithmically spaced intervals always include the end points  $R = 1.0$  and  $L = 1.0$  and the other end points are scaled to estimate their order of magnitude via a crude exponential decay fit.

- The boral is trained on  $3^3$  snapshots with the boundary condition fluxes  $R$  and  $L$  trained on  $[0.1, 0.31622777, 1. ]$ .
- The sets of steel slabs are both trained on  $7^3$  snapshots with the boundary condition fluxes  $R$  and  $L$  trained on  $[1.0 \times 10^{-7}, 1.46779927 \times 10^{-6}, 2.15443469 \times 10^{-5}, 3.16227766 \times 10^{-4}, 4.64158883 \times 10^{-03}, 6.81292069 \times 10^{-2}, 1.0]$
- The water is trained on  $4^3$  snapshots with boundary conditions fluxes  $R$  and  $L$  trained on  $[1.0 \times 10^{-5}, 4.64158883e \times 10^{-4}, 2.15443469 \times 10^{-2}, 1.0]$ .
- The concrete is trained on  $5^3$  snapshots with boundary conditions fluxes  $R$  and  $L$  trained on  $[1.0 \times 10^{-7}, 1.0 \times 10^{-6}, 1.0 \times 10^{-5}, 1.0 \times 10^{-4}, 1.0 \times 10^{-3}]$ .

- The stainless steel is trained on  $4^3$  snapshots with the boundary condition fluxes  $R$  and  $L$  trained on  $[1.0 \times 10^{-7}, 3.16227766 \times 10^{-4}, 1.0]$ .

Ranges close to 0 – 1 were chosen to cover all possible boundary conditions. This is prudent to give the user a full choice of problem set-up and also to accommodate large possible fluctuations on the way to convergences. Although in the analytical case the tolerance is approached monotonically decreasing, this is no longer guaranteed with ROM solutions. This is possibly due to factors such as Gibbs like phenomenon in the radial basis interpolation.

It is important to note that this training regime is a brute force approach that works well here with few,  $< 7$ , points in each axis of parameters. Even so for  $2 + 1$  parameters, the boundary conditions and the width,  $7^3$  points to train on is a large number and presents difficulties scaling as we will see in the 2-group model. Future work would be to sample this space of possible training regimes in some way to get best results, a Smolyak grid of points or a Monte Carlo approach may be viable for models with more parameters. It is also important to note how well the model performs with limited points in the parameter axis.

The first set of figures 4.6 show that the ROM results closely mirror the coupled exact results, displaying the same underlying physics. The scalar flux is rapidly absorbed across the shield and the voids show transmission only. Importantly, the scalar flux at the end of the shield is in the same order of magnitude as the coupled exact results and the increase due to scatter at the start of the shield is within 0.1% of the coupled exact flux. We can see the RMS error in the scalar flux ROM solutions is: 0.0483 with the first half of the shield having error less than 5%, typical errors being less than 10%, until the end of the shield where higher error is introduced by values close very close to zero but still different order so magnitude. The drop in flux from the start of the shield is rapid to the extent that a lot of the behaviour is only clear on a log-linear plots.

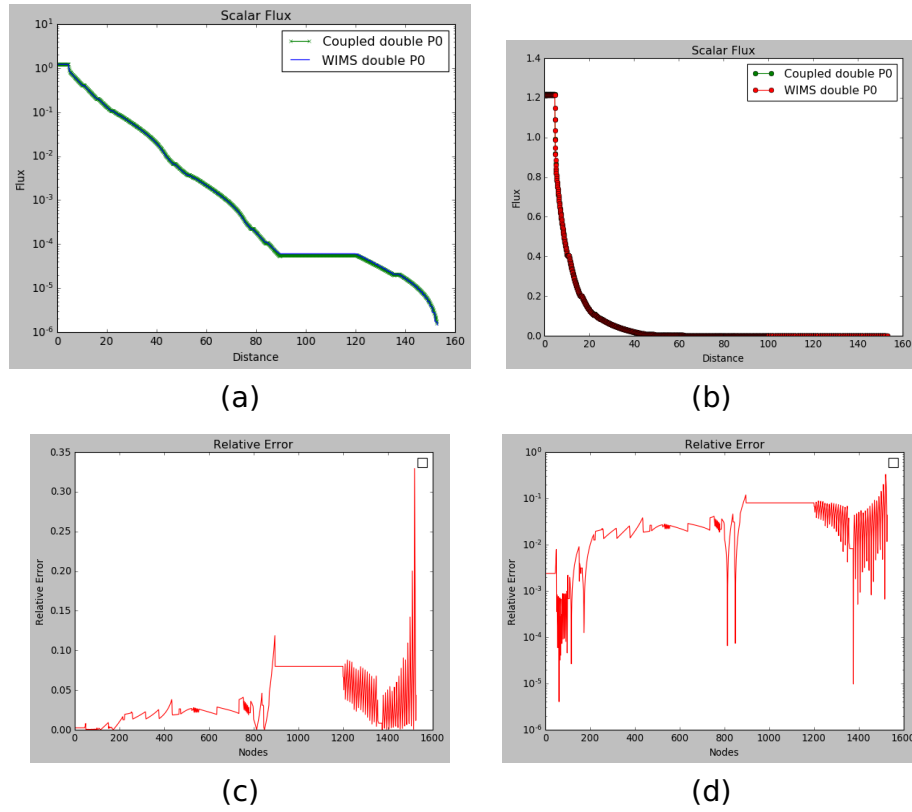


**Figure 4.6:** Here we have the scalar flux from the ROM coupling in log-linear (a) and linear scales (b) the error in the scalar flux in linear (c) and log-linear plots (d). The tolerance is  $1.0 - 10^{-2}$  in other words a maximum of a 1.0% error across the interfaces.

In figure 4.6 we have strong agreement until the end of the shield even though the model is only trained on  $< 7$  points in a range spanning 7 orders of magnitude. Many materials occur though out this range with few or no training points in the ultimate solution's range, however the modes provided by the POD basis capture the structure within each ROM, giving the best basis for the ROM for a given dimensionality in an L-2 sense. For each ROM, the mean number of training points is 5.71, with standard deviation of 1.55 points. The ROMs training means half the individual ROM models are trained on 7 points and the other half on 5 or fewer. The materials that span fewer orders of magnitude require less points to train.

The run times for the different steps of the scheme are:

- Total time: 1272.6 Coupling scheme time: 1256.8 Offline time: 15.9 plot time: 11.5 Total its: 136.0
- The total run time here is about 21mins.

The run times here are a worst case scenario as the starting guesses used are zeros. With some prior knowledge of the solution better guesses can significantly reduce the run time.

For a more complicated problem possessing the same structure of boundary conditions, this work shows that the coupling of ROM solutions may be viable as a way of breaking problems down or speed-up. With guesses 5% of the true values a run time of 31.6s is possible.

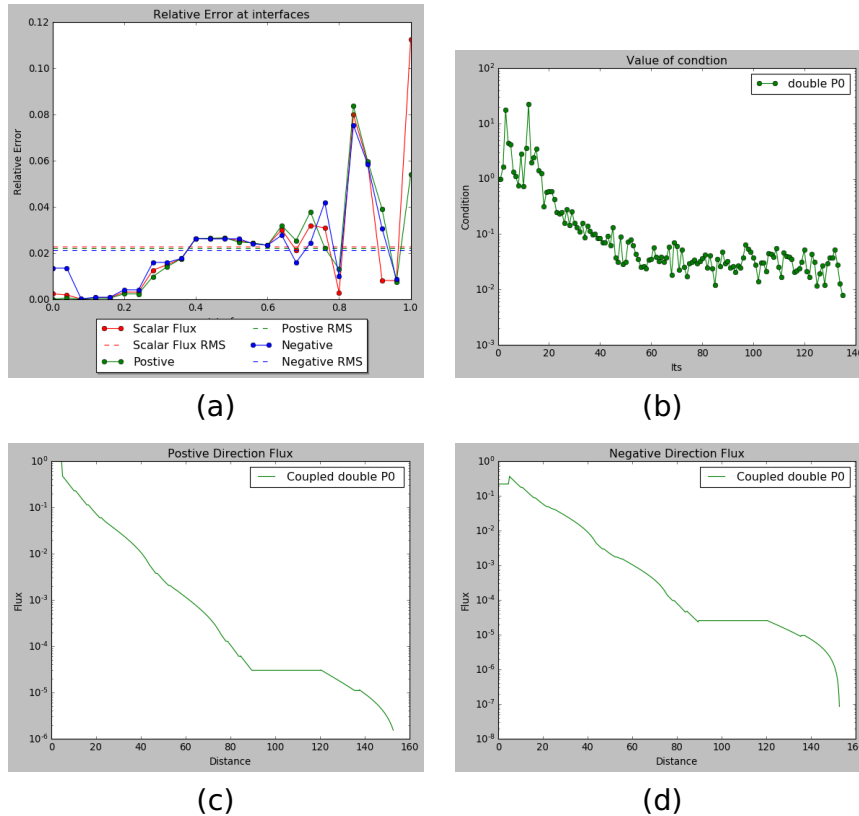


**Figure 4.7:** Here we have the error at the start and end of each slab and void model. (a) the value of the tolerance (b) the positive flux exact solutions coupled (c) and negative flux exact solutions coupled (d). The tolerance is  $10^{-6}$ . The end point of the slab is omitted as it is not an interface. We can see the ROM produced a different value to represent zero then the reference solution. The interface values all have error less than 0.12 with most 2% to 4%.





We can see in figure 4.7 (b) the condition, maximum error across the different shield interfaces as it tend towards the tolerance. Overall it improves but is no longer smooth as in the analytical case shown in figure 4.5. The convergence is no longer monotonic and now appears noisy or oscillating. Its is hard to tell if beyond the set tolerance is it osculating or just converging really slowly.

The directional fluxes are also faithful to the reference solutions having the same physical features. In the figure 4.8 you can in absolute terms the error

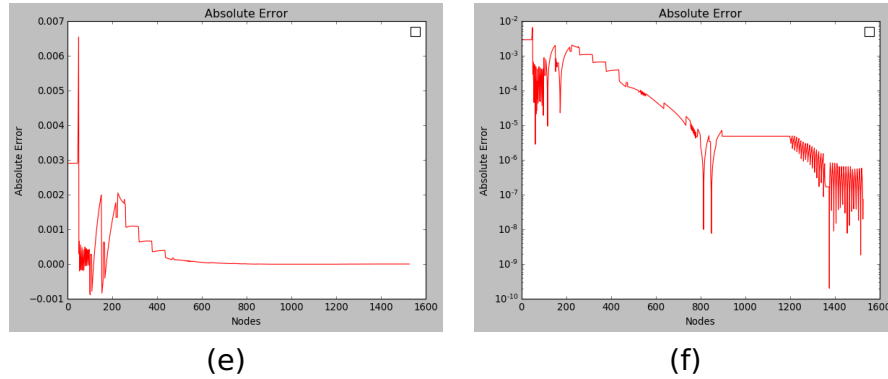


**Figure 4.8:** Here we have the absolute error in the scalar flux on linear plot with true sign of the error and log-linear scale with just the size of the error.

changed sign with more over estimate than underestimate.

## Conclusion

From this work we can conclude that the coupling of ROMs for a 1-group shielding problem is a viable tool, even with a very small number of training points, producing strong results in agreement with both the coupled analytic model and the solution from the double P0 model. Another implication of this work is that experimental data from a set-up with various different fluxes at the start and end of shields could be assimilated to replace the similar analytical model within each shield. The few training points, less than 7 in fact, required would also mean fewer experiments needed to assimilate an experimental model of the flux. This capability could enable modelling in real time.

Recall the two flux variables are recognized by the ROM is the form of a concatenated flux profile. The detailed feature in this profile describes the unprescribed boundaries at the shield. The ROMs gives strong feature recognition even at low number of POD basis functions as evident from the low error at the shield interfaces. This would suggest that a more feature rich model would still be viable. In the next chapter this work is developed to model coupled 2-group ROMs for shielding.

# Chapter 5

## Coupled 2-Group Reduced Order Models for generic and ASPIS benchmark configurations of slabs

### **Overview**

This chapter presents a bi-directional analytical scattering model of shielding for a 2-group formulation. The physics have more depth in this chapter and so the initial results build a library of individual material homogeneous shield models before going on to couple inhomogeneous material domains with the configuration of materials based on the ASPIS benchmark experiments. Again, the ROM is testing boundary conditions as a ROM parameter that facilitates the coupling. We demonstrate that the online component of the NIROM is rapid enough to be used in the iteration loop of the coupling scheme for a multi-group problem.

## Introduction

For applications covering more than just the fast or just the thermal range of energies, multi-group models are essential. From a 2-group model we can build a basis to understand and generalise to multi-group ROM models and more sophisticated coupled ROMs.

In this chapter, similarly to the 1-group chapter, an analytical two group model for homogeneous single slabs is derived. We make the following assumptions: with 2-groups the fast neutrons only have the option to leave the region via streaming, scattering out to the thermal group or absorbed. The thermal neutrons can only be absorbed or streamed out. For each scatter interaction there is given a direction in 1D. This gives a wide range of outcomes and with more groups we see increasingly more complicated interactions.

This model is parameterised in terms of four boundary conditions, as apposed to the two in the previous chapter, which is made use of to couple the homogeneous single slabs to form more complicated configurations of slabs. At the end of the configuration of slabs these boundaries can be fixed and the remaining interfaces between slabs can be free boundary conditions and thus used to iterate towards the model for the full configuration. The models for homogeneous singles can be replaced by reduced order models. A library of different homogeneous single shields is built up to train a reduced order model capable of modelling complicated configurations of slabs. This demonstrates the principle that reduced order models can be coupled for a complicated multi-group problem.

## 5.1 Two-Group Analytic Solutions derivation

Here a derivation of a 2-Group model for a single shield is presented. The model is parameterised in terms of the boundary conditions and width, later enabling the development of a new coupling scheme to model multiple materials at once. Starting from modified two-group diffusion theory, with groups 1, 2 representing the fast and thermal respectively. The cutoff energy for the thermal group is chosen such that upscattering from the thermal group can be ignored. This choice is problem specific to the reactor setup, typically  $0.5\text{eV} - 3\text{eV}$  and tend to be higher in gas-cooled reactors and lower in water-moderated reactors.

Let the capture cross-sections in groups 1 and 2 be  $\Sigma_{c1}$  and  $\Sigma_{c2}$ , respectively. The scatter cross-sections from group 1 to group 2 takes the from  $\Sigma_{s1,2}$  and scatter from group 2 to group 1  $\Sigma_{s2,1}$  with directional indices read similarly left-to-right, for example  $\Sigma_{s1+,2-}$  is the scatter from group 1 to 2 and from positive-x direction (right) to negative-x direction (left). Finally the in-group scatter denoted by  $\Sigma_{s1-,1+} = \Sigma_{s1+,1-}$  and  $\Sigma_{s2+,2-} = \Sigma_{s2-,2+}$ .

Conservation with the removal of up-scatter can then be written in the form of:

$$\frac{\Psi_{1+}}{dx} + (\Sigma_{c1} + \Sigma_{s1+,1-} + \Sigma_{s1+,2+} + \Sigma_{s1+,2-})\Psi_{1+} = \Sigma_{s1+,1-}\Psi_{1-}, \quad (5.1)$$

$$-\frac{\Psi_{1-}}{dx} + (\Sigma_{c1} + \Sigma_{s1-,1+} + \Sigma_{s1-,2+} + \Sigma_{s1-,2-})\Psi_{1-} = \Sigma_{s1-,1+}\Psi_{1+}, \quad (5.2)$$

$$\frac{\Psi_{2+}}{dx} + (\Sigma_{c2} + \Sigma_{s2+,2-})\Psi_{2+} = \Sigma_{s1+,2+}\Psi_{1+} + \Sigma_{s1-,2+}\Psi_{1-} + \Sigma_{s2-,2+}\Psi_{2-}, \quad (5.3)$$

$$-\frac{\Psi_{2-}}{dx} + (\Sigma_{c2} + \Sigma_{s2-,2+})\Psi_{2-} = \Sigma_{s1+,2-}\Psi_{1+} + \Sigma_{s1-,2-}\Psi_{1-} + \Sigma_{s2+,2-}\Psi_{2+}. \quad (5.4)$$

Let the Scalar Flux and Net Current in each group be:

$$\phi_1 = \psi_{1+} + \psi_{1-}, \quad J_1 = \psi_{1+} - \psi_{1-} \quad (5.5)$$

$$\phi_2 = \psi_{2+} + \psi_{2-}, \quad J_2 = \psi_{2+} - \psi_{2-}. \quad (5.6)$$

This simplifies the PDEs to the form:

$$\frac{\phi_1}{dx} + \Sigma_{t1} J_1 = 0 \quad (5.7)$$

$$\frac{J_1}{dx} + \Sigma_{e1} \phi_1 = 0 \quad (5.8)$$

$$\frac{\phi_2}{dx} + \Sigma_{t2} J_2 = \Sigma_{s12p} J_1 \quad (5.9)$$

$$\frac{J_2}{dx} + \Sigma_{e2} \phi_2 = \Sigma_{s12m} \phi_1. \quad (5.10)$$

where the total in-group cross-sections and emission cross section are:

$$\Sigma_{t1} = \Sigma_{c1} + 2\Sigma_{s1+,1-} + \Sigma_{s1+,2+} + \Sigma_{s1+,2-}, \quad (5.11)$$

$$\Sigma_{e1} = \Sigma_{c1} + \Sigma_{s1+s2} + \Sigma_{s1+,2-}, \quad (5.12)$$

$$\Sigma_{t1} = \Sigma_{c2} + 2\Sigma_{s1+,2-}, \quad (5.13)$$

$$\Sigma_{e2} = \Sigma_{c2}, \quad (5.14)$$

$$\Sigma_{s12p} = \Sigma_{s1+,2+} + \Sigma_{s1+,2-}, \quad (5.15)$$

$$\Sigma_{s12m} = \Sigma_{s1+,2+} - \Sigma_{s1+,2-}. \quad (5.16)$$

and we make use of the following symmetries:

$$\Sigma_{s1+,1-} = \Sigma_{s1-,1+}, \quad (5.17)$$

$$\Sigma_{s1-,1-} = \Sigma_{s1+,2+}, \quad (5.18)$$

$$\Sigma_{s1-,2+} = \Sigma_{s1+,2-}, \quad (5.19)$$

$$\Sigma_{s2-,2+} = \Sigma_{s2+,2-}. \quad (5.20)$$

The group one equations are independent from the group 2 and thus can be solved:

$$\phi_1(x) = A_1 e^{\omega_1 x} + B_1 e^{-\omega_1 x}, \quad (5.21)$$

$$J_1(x) = -\beta_1 (A_1 e^{\omega_1 x} - B_1 e^{-\omega_1 x}). \quad (5.22)$$

These can be substituted in to the group 2 PDEs and solved via characteristics:

$$\phi_2(x) = A_2 e^{\omega_2 x} + B_2 e^{-\omega_2 x} + \alpha_1 (A_1 e^{\omega_1 x} + B_1 e^{-\omega_1 x}), \quad (5.23)$$

$$J_2(x) = -\beta_2 (A_2 e^{\omega_2 x} - B_2 e^{-\omega_2 x}) - \alpha_2 (A_1 e^{\omega_1 x} - B_1 e^{-\omega_1 x}). \quad (5.24)$$

where:

$$\omega_1 = \sqrt{\Sigma_{t1} \Sigma_{e1}}, \quad \omega_2 = \sqrt{\Sigma_{t2} \Sigma_{e2}}, \quad (5.25)$$

$$\beta_1 = \sqrt{\frac{\Sigma_{e1}}{\Sigma_{t1}}}, \quad \beta_2 = \sqrt{\frac{\Sigma_{e2}}{\Sigma_{t2}}}, \quad (5.26)$$

$$\alpha_1 = \frac{\Sigma_{t2} \Sigma_{s12p} + \Sigma_{e2} \Sigma_{s12m}}{\omega_2^2 - \omega_1^2}, \quad \alpha_2 = \beta_1 (\alpha_1 \frac{\Sigma_{t1}}{\Sigma_{t2}} + \frac{\Sigma_{s12m}}{\Sigma_{t2}}). \quad (5.27)$$

Whence we have that:

$$\psi_{1+}(x) = \frac{A_1(1 - \beta_1)e^{\omega_1 x} + B_1(1 + \beta_1)e^{-\omega_1 x}}{2} \quad (5.28)$$

$$\psi_{1-}(x) = \frac{A_1(1 + \beta_1)e^{\omega_1 x} + B_1(1 - \beta_1)e^{-\omega_1 x}}{2} \quad (5.29)$$

$$\begin{aligned} \psi_{2+}(x) = & \frac{A_2(1 - \beta_2)e^{\omega_2 x} + B_2(1 + \beta_2)e^{-\omega_2 x}}{2} \\ & + \frac{A_1(\alpha_1 - \alpha_2)e^{\omega_1 x} + B_1(\alpha_1 + \alpha_2)e^{-\omega_1 x}}{2} \end{aligned} \quad (5.30)$$

$$\begin{aligned} \psi_{2-}(x) = & \frac{A_2(1 + \beta_2)e^{\omega_2 x} + B_2(1 - \beta_2)e^{-\omega_2 x}}{2} \\ & + \frac{A_1(\alpha_1 + \alpha_2)e^{\omega_1 x} + B_1(\alpha_1 - \alpha_2)e^{-\omega_1 x}}{2} \end{aligned} \quad (5.31)$$

The values of  $A$  and  $B$  are determined from the boundary conditions for the four fluxes. Hence:

$$L_1 = \psi_{1+}(x_1), \quad L_2 = \psi_{2+}(x_2), \quad (5.32)$$

$$R_1 = \psi_{1-}(x_1), \quad R_2 = \psi_{2-}(x_2). \quad (5.33)$$

So the 1-group boundary conditions at  $x_1$  and  $x_2$ :

$$2L_1 = A_1(1 - \beta_1)e^{\omega_2 x_1} + B_1(1 + \beta_1)e^{-\omega_2 x_1}, \quad (5.34)$$

$$2R_1 = A_1(1 + \beta_1)e^{\omega_2 x_2} + B_1(1 - \beta_1)e^{-\omega_2 x_2}. \quad (5.35)$$



Hence:

$$A_1 = 2 \frac{(1 + \beta_1)e^{-\omega_1 x_1} R_1 - (1 - \beta_1)e^{-\omega_1 x_2} L_1}{\Delta_1}, \quad (5.36)$$

$$B_1 = 2 \frac{(1 + \beta_1)e^{\omega_1 x_2} L_1 - (1 - \beta_1)e^{\omega_1 x_1} R_1}{\Delta_1}, \quad (5.37)$$

$$\Delta_1 = (1 + \beta_1)^2 e^{\omega_1(x_2 - x_1)} - (1 - \beta_1)^2 e^{-\omega_1(x_2 - x_1)} \quad (5.38)$$

Having determined  $A_1$  and  $B_1$ , we can determine  $A_2$  and  $B_2$ :

$$2\psi_{2+}(x_1) = A_2(1 - \beta_2)e^{\omega_2 x_1} + B_2(1 + \beta_2)e^{-\omega_2 x_1} \quad (5.39)$$

$$+ A_1(\alpha_1 - \alpha_2)e^{\omega_1 x_1} + B_1(\alpha_1 + \alpha_2)e^{-\omega_1 x_1} \quad (5.40)$$

we re-arrange and let:

$$2\tilde{L}_2 = 2L_2 - A_1(\alpha_1 - \alpha_2)e^{\omega_1 x_1} + B_1(\alpha_1 + \alpha_2)e^{-\omega_1 x_1} \quad (5.41)$$

$$= A_2(1 + \beta_2)e^{\omega_2 x_1} + B_2(1 - \beta_2)e^{-\omega_2 x_1} \quad (5.42)$$

Similarly

$$2\tilde{R}_2 = 2R_2 - A_1(\alpha_1 + \alpha_2)e^{\omega_1 x_2} + B_1(\alpha_1 - \alpha_2)e^{-\omega_1 x_2} \quad (5.43)$$

$$= A_2(1 + \beta_2)e^{\omega_2 x_2} + B_2(1 - \beta_2)e^{-\omega_2 x_2} \quad (5.44)$$

Finally:

$$A_2 = 2 \frac{(1 + \beta_2)e^{-\omega_2 x_1} \tilde{R}_1 - (1 - \beta_2)e^{-\omega_2 x_2} \tilde{L}_1}{\Delta_2}, \quad (5.45)$$

$$B_2 = 2 \frac{(1 + \beta_2)e^{\omega_2 x_2} \tilde{L}_1 - (1 - \beta_2)e^{\omega_2 x_1} \tilde{R}_1}{\Delta_2}, \quad (5.46)$$

$$\Delta_2 = (1 + \beta_2)^2 e^{\omega_2(x_2 - x_1)} - (1 - \beta_2)^2 e^{-\omega_2(x_2 - x_1)}. \quad (5.47)$$

This gives a complete 2-group model for a positive and negative directional scatter parameterized by the input and output fluxes for each energy group  $R_1, R_2$  and  $L_1, L_2$ . These parameterized boundary conditions will be used to coupled the individual shield ROMs together.

In a multi-group problem the input and output fluxes form a spectra. The boundary conditions are, in total, a unit positive flux input at the left hand

boundary, situated at the start of the slab. In these examples the flux is distributed evenly between the two energy groups, thus an input flux of 0.5 for the fast energy group (group 1) and also 0.5 for the thermal energy group (group 2). Thus there is unit scalar flux input at  $x = 0$ ; however, the scalar flux at  $x = 0$  will be greater than 1 due to the fluxes in the negative x-direction produced by scattering. A free boundary condition (no incoming flux) is assumed at the right hand boundary.

## The ASPIS configuration form 2-group problems

The material specification in terms of typical ROM training ranges of the ASPIS 1986 configuration are used as table 5.2: Two-group Cross-Sections here

**Table 5.1:** Material Geometry

Material	Training Range (cm)	Comments
Boral	0.4-0.6	Only one boral plate.
Mild steel 1	4.1-6.1	All plates have the same thickness.
Mild steel 2	2.0-3.0	Only one mild steel 2 plate.
Stainless steel	2.4-3.6	Plates of two different thicknesses.
Water	15.8-23.8	Two water slabs of similar thickness.
Concrete	12.2-18.3	Two slabs of same thickness.
Void	N/A.	Just checking that fluxes remain constant through the gap.

are formed by the code WIMS flux volume condensing 47 group data driven solutions [5]. The macroscopic cross-sections for the capture in and scatter in and between the 2 groups is presented in table 5.2. The values are given in the units ( $cm^{-1}$ ).

**Table 5.2:** 2-Group Material Cross-sections

Material	$\Sigma_{c1}$	$\Sigma_{c2}$	$\Sigma_{s1+,1-}$	$\Sigma_{s1,2}$	$\Sigma_{s2+,2-}$
Boral	0.003618	2.98814	0.114572	5.28E-07	0.092136
Mild Steel 1	0.000858	0.069514	0.164661	4.23E-05	0.480411
Mild Steel 2	0.002718	0.144996	0.249934	0.000533	0.477519
Stainless Steel	0.002476	0.173454	0.266546	0.000297	0.436575
Water	0.000302	0.019251	0.543568	0.038501	1.59705
Concrete	0.000239	0.00816	0.219499	0.008912	0.427796
Void	0	0	0	0	0

The table 5.2 summaries and quantifies the following properties:

- All materials have low capture in the fast group,
- Water and concrete have lower fast capture than boral or steel,
- Boral has much higher capture in the thermal group,
- Water and concrete have lower thermal capture than the steels,
- Boral and steels have very little down-scatter,
- Water has much higher within-group scatter than the other materials.
- Void has transmission only.

As with the 1-group model the we build a library of single shield ROMs. In the next section we will illustrate the effects of the various cross-sections shown in the previous table. This has two distinct purposes: to build understanding of the underlining physics, informing us of what to look for as the coupling scheme attempts to converge and also to understand how well the concatenated ROM profile for all fluxes is represented by the ROM. This will inform the number of POD basis functions needed in the coupling scheme and give insight into training regimes and characteristics length choice.

### 5.1.1 Single Shield 2-group ROMs

For the individual ROMs the training is initially done with the same set-up for all materials. The individual shields for all the materials involved with the ASPIS problem are trained with boundary conditions for thermal and fast fluxes on the LHS being sampled from the ranges  $0.5 - 1.00495$  and for the RHS fluxes  $\epsilon - 1.00495$ . Here  $\epsilon$  is just a positive number very close to zero. This is done as using zero as a point in the training when the coupling scheme iterates can lead to two problems: singular matrices in the construction of the offline stage of the ROM and also divergence into regions where fluxes that are negative and non-physical. This range of training points is chosen to in practice cover the range 0.0 to 1.0 and thus maintaining a normalised versions of the problem. The widths used for ROM parameterisation sampled from points ranging 20% either side of widths for a give shield, for example a shield of width of 0.5cm has a training range  $0.4 - 0.6$ cm.

In testing the individual ROMs a challenging test point is used. The values of the 5 ROM parameters (shield widths, and the two pairs of inlet and outlet boundary conditions) are chosen to be as far from the training points as possible. The use of 4 basis functions gives 0.999% of the energy in all materials. This is to be expected as the have similar underlining physics. The total amount of training data used is  $3^5$  points; three points from each parameter the shield width, and the two pairs of inlet and outlet boundary conditions are permutated as the ROM is trained. The total degrees of freedom in the concatenated ROM is 160. Figure 5.1 shows the boundary conditions used for the specific results in this section.

<b>Direction:</b> Inlet →	Inlet: →
<b>Boundary condition:</b> Fixed	Free
$\psi_{1+} = 0.5$	$\psi_{1+} = 0.0$
$\psi_{2+} = 0.5$	$\psi_{2+} = 0.0$
<b>Direction:</b> Outlet ←	Outlet: ←
$\psi_{1-} = 0.0$	$\psi_{1-} = 0.0$
$\psi_{2-} = 0.0$	$\psi_{2-} = 0.0$
<b>Boundary condition:</b> Free	Fixed

**Figure 5.1:** This figure gives a general overview of the boundary conditions at the beginning and end of a shield. Later the coupled models will have extra boundary at interfaces. For now we are considering a single shield to build intuition of the physics of each material. Each of the material examples in figures 5.2,5.3,5.4 and 5.5 has a width chosen from table 5.1 and cross sections as table 5.2.

Here a selection of single slab reduced order models is presented along side the exact solution, the first few POD basis functions and their energy. The two directional fluxes in the two groups are concatenated to form a single 1-dimensional snapshot from the four total fluxes. The different fluxes span a few orders of magnitude however the reduced order model is still capable of representing the features of all the directional group fluxes. In figure 5.2 (a) we can see the ROM is close to the exact solution. We can also see in (d) that only four POD basis functions are need, POD basis functions beyond this are only noise. We can see variation in the size of the different flux profiles. The higher capture in the thermal group reduces the thermal flux down to  $0.02\text{cm}^{-2}$  by the end of a thin  $0.5\text{cm}$  shield of boral. The small within-group scatter cross-section results in the production of only small amounts of negative flux. In figure 5.3 (a), the stainless steel shield, we see the best agreement with the exact solution out of the selection of the different single material shield ROMs in the set of figures: figure 5.2 a  $0.5\text{cm}$  shield of boral, figure 5.3 a  $5.08\text{cm}$  shield of stainless steel, figure 5.4 a  $19.9\text{cm}$  shield of water and figure 5.5 a  $15.24\text{cm}$  shield of concrete.

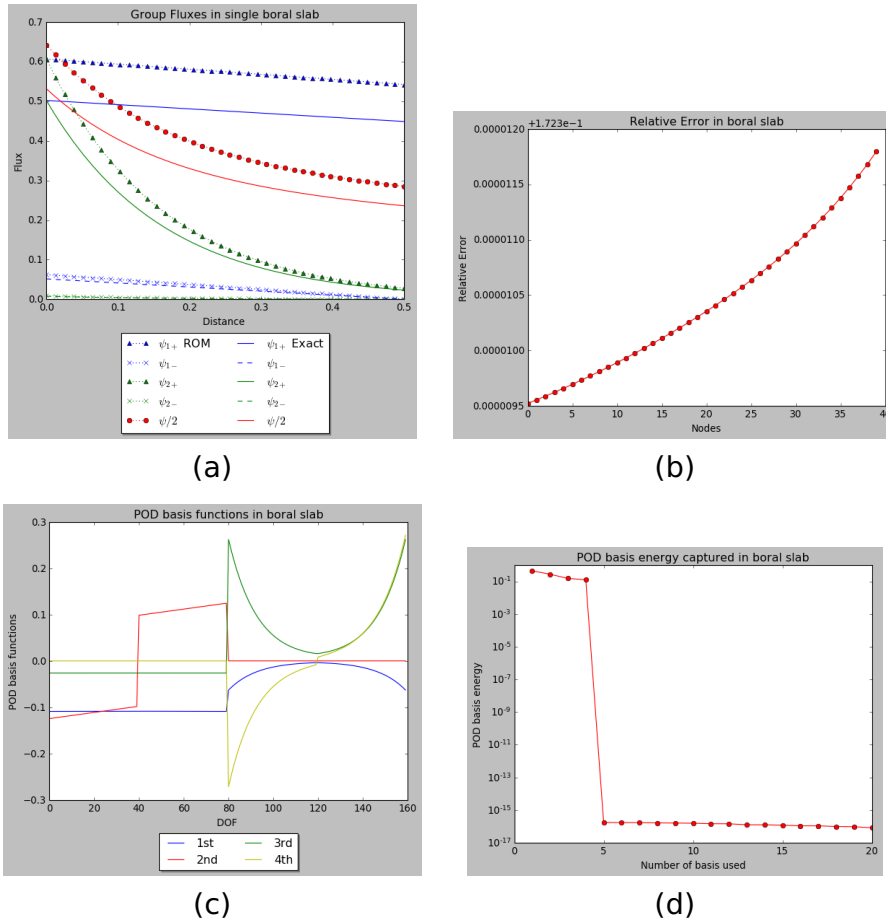


**Figure 5.2:** Here for a thin,  $0.5\text{cm}$  boron shield we have (a) the individual directional fluxes for the ROM and exact solutions (b) the relative error in scalar flux (c) the first 4 basis functions and (d) and the energy of the POD basis functions (d).

We continue to see only four POD basis functions are need. We can also see more capture. We see the thermal flux is reduced to near zero by the end of the shield and the fast group is also significantly attenuated. Part of this is due to being ten times thicker than the boron plate. The greater transit time allows the within-group scatter to be more prominent, generating more negative fluxes.

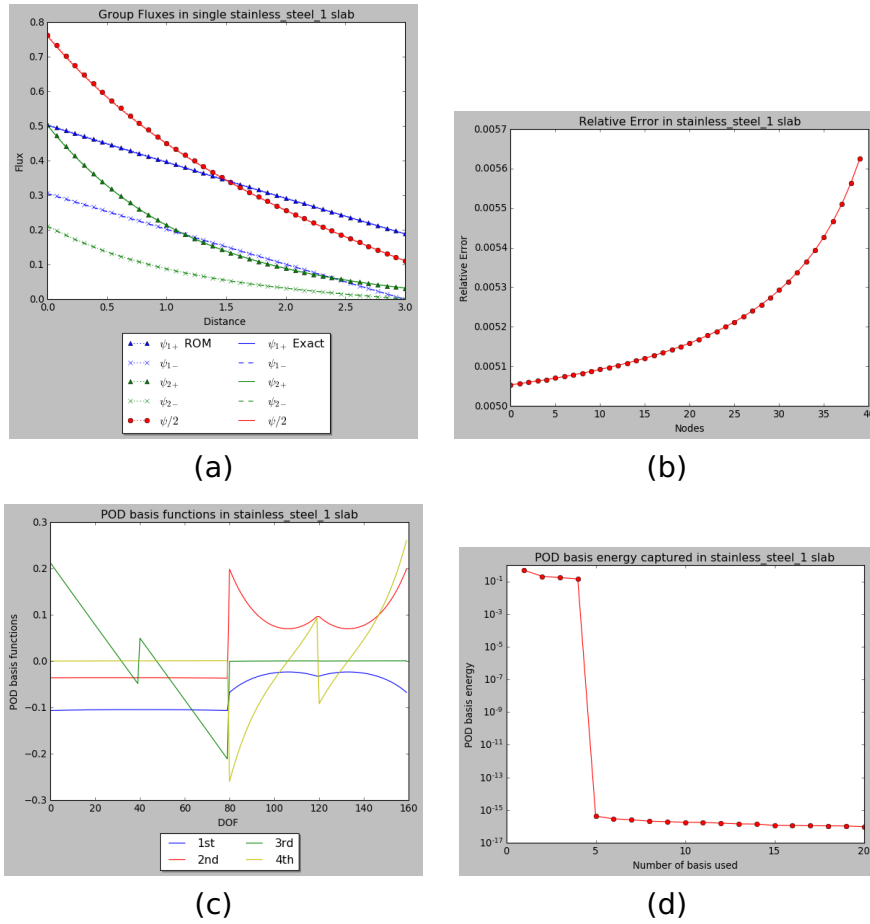


**Figure 5.3:** Here we have the individual directional fluxes in the ROM and exact solutions (a) the relative error 2 (b) the first 4 basis functions (c) and the energy plot (d) in a thick  $5.08\text{cm}$  stainless steel shield.

In 5.4 we see strong agreement for most of the shield with higher error only at the end portion. All fluxes are reduced to near zero by about half way through the slab. Again only four POD basis functions are needed. We can see that the shape of the POD basis function varies significantly between materials. In all cases however you can see how the POD basis functions resemble the concatenated ROM profiles.

In figure 5.5 we expect to see very similar, but less exaggerated, results to the water slab: concrete having a high water content. By half way through the flux is close to zero. The log-scale makes it more clear that the exponential fall off continues until the very end of the shield. We see much steeper gradients at the end of the shield. The thickness and high within-group scatter enables the negative fluxes to be considerable.

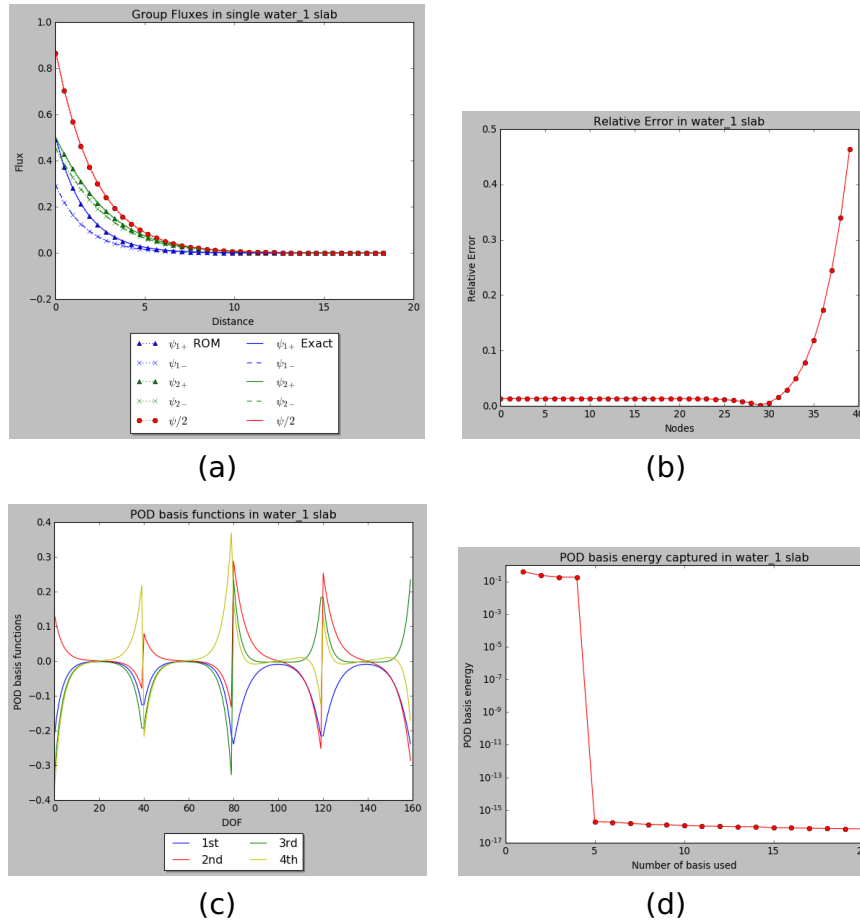
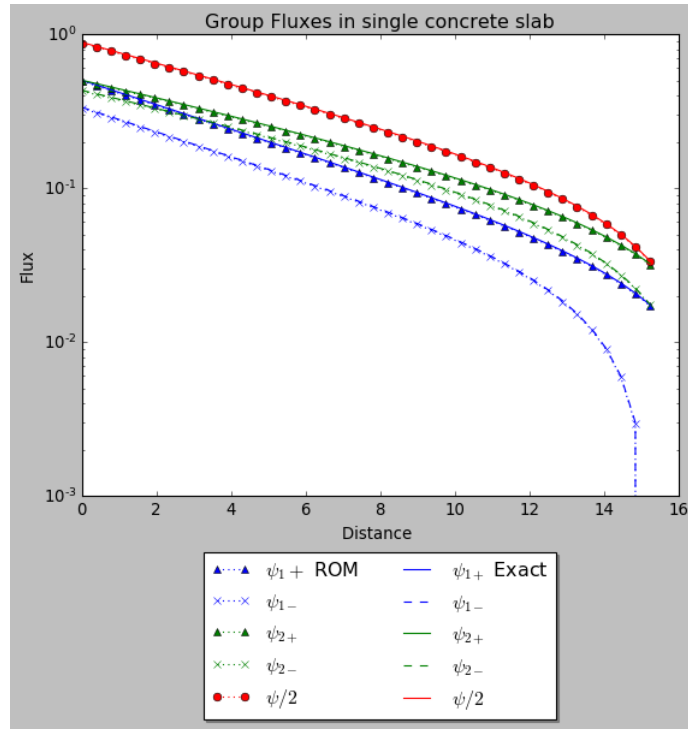


**Figure 5.4:** Here we have the individual directional fluxes in the ROM and exact solutions (a) the relative error 2 (b) the first 4 basis functions (c) and the energy plot (d) in a thick  $19.9cm$  water slab.

From looking at each individual material we gain a few insights that we can take on board for the coupling of multiple ROMs for the whole ASPIS configuration. The concrete and water, being highly scattering and thick, have profiles that will range several orders of magnitude just within a single shield. In the coupling scheme the training will have to reflect this by having more data in these materials. The error in the flux at the start and end of each material ROM will be very important in getting good results in the coupling scheme, particularly in these materials. The mild steel will also need more data as it occurs often throughout the ASPIS configuration and thus will span many orders of magnitude but the error at the boundaries is less of a concern. The other metals can get away with less training, being very similar to mild steel. We can also confirm that 4 POD basis functions is sufficient for all ROMs of this problem and gain insight into a good characteristic length for each





(e)

**Figure 5.5:** Here we have the individual directional fluxes in the ROM and exact solutions in log-linear plot for a  $15.24\text{cm}$  concrete shield.

material ROM. We expected the range of order of magnitude of flux in the coupled problem to be much greater in the 2-group case.

## 5.2 Coupled two group ASPIS Configuration Scheme and Results

The 2-group model for the ASPIS configuration, 2.8, will combine a boarder range of physical behaviours than the 1-group model. Also the input can now be a spectrum of fast and thermal boundary flux at the start of the shield and as such will require more training to reproduce results for all input values. We will also need to consider how to couple the 2-group solutions.

We can now apply what we have learned in the coupling of the 1-group shields and in the individual 2-group material ROMs to couple 2-group ROMs. First the coupling scheme for 1-group ROMs can be adapted to cope with two groups. This is done in much the same way as the 1-group coupling where we check continuity across each material boundary in the negative flux and update boundary conditions from one adjacent materials to the next. This is now done twice, one set of conditions on the boundaries in the fast group and one set in the thermal. Both must be less that a total tolerance for the scheme to have continuity and thus be a 2-group coupled model.

### Coupling scheme for two group problems

Here the iteration scheme for coupling the single slabs is presented. The coupling scheme joins the individual models of the slabs together. This is done by passing the fluxes from one slab to the next to ensure continuity within a certain tolerance. The incoming flux from one slab is the outgoing flux from the previous slab or the relevant total assembly boundary condition if the slab is the first or last. The overall assembly of slabs has boundary conditions fixed at each end, in this instance 1.0 at start and 0.0 at the end, figure 5.7. The parameters  $\psi_+(L_0) = p_1$  and  $\psi_-(L_1) = p_2$  are the inputs and outputs for the coupling scheme as figure 5.8.

Here the coupling scheme is outlined:

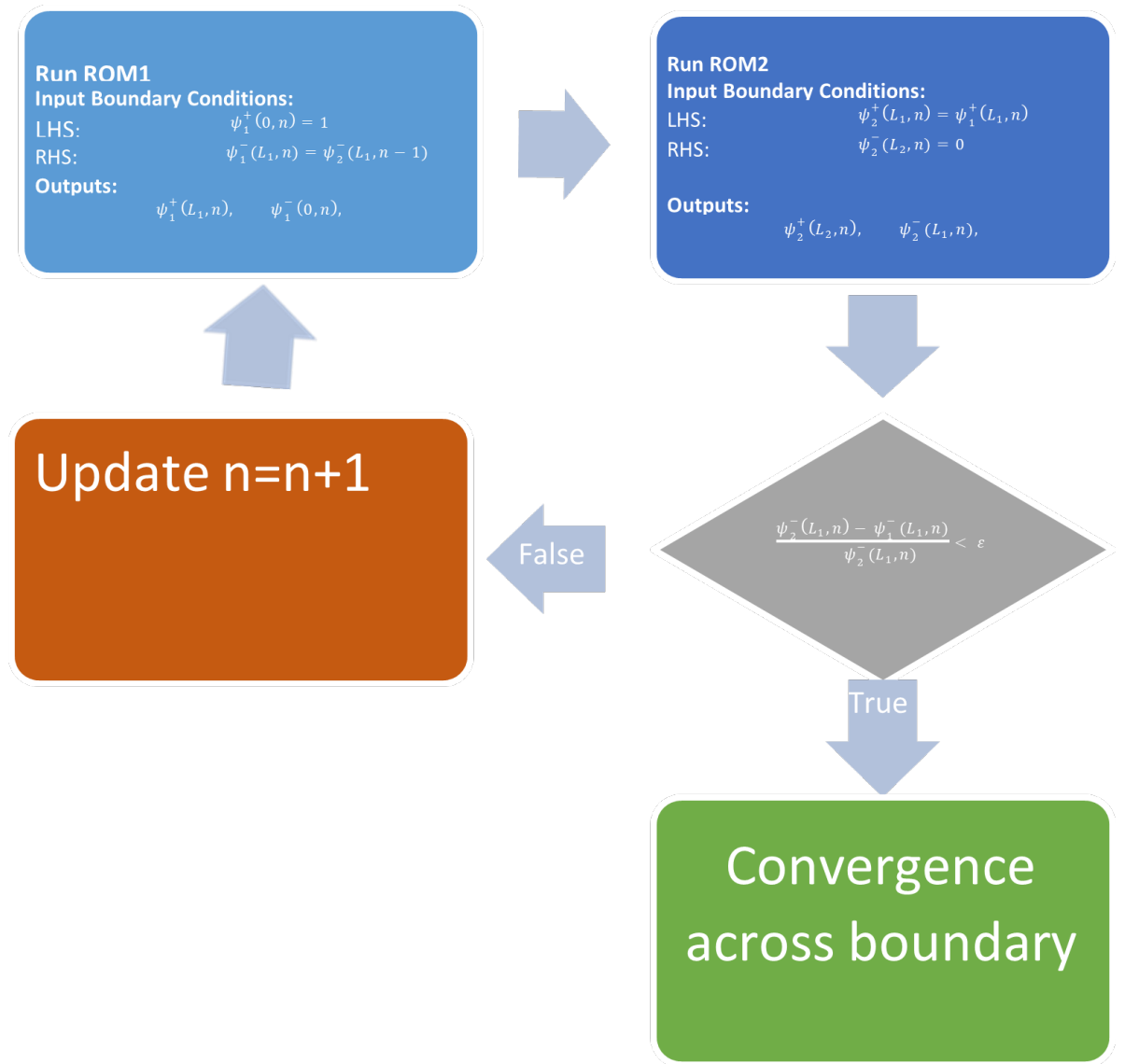


**Figure 5.6:** ROM iterative coupling scheme

**Direction:** Inlet →  
**Boundary condition:** Fixed  
 $\psi_{1+} = 0.5, 1.0$   
 $\psi_{2+} = 0.5, 0.0$   
**Direction:** Outlet ←  
 $\psi_{1-} = 0.0$   
 $\psi_{2-} = 0.0$   
**Boundary condition:** Free

Inlet: →  
**Free**  
 $\psi_{1+} = 0.0$   
 $\psi_{2+} = 0.0$   
**Outlet:** ←  
 $\psi_{1-} = 0.0$   
 $\psi_{2-} = 0.0$   
**Fixed**

**Figure 5.7:** Domain for the ROM ASPIS configuration is made of 25 homogeneous shields with widths and cross sections show in tables 5.1 and 5.2 respectively. This figure gives an overview of the boundary conditions at the beginning and end of the whole shield. Two cases for the inlet are presented, a flux spectra split evenly and a case with all the inlet flux in the 1st group.

For  $n$  individual shields we have a set of free boundary conditions and a tolerance that bounds above the relative differences across the interfaces:

$$\max\left(\frac{\psi_2^{1-}(L_1) - \psi_1^{1-}(L_1)}{\psi_2^{1-}(L_1)}, \dots, \frac{\psi_n^{1-}(L_{n-1}) - \psi_{n-1}^{1-}(L_{n-1})}{\psi_n^{1-}(L_{n-1})}\right) < \epsilon_1 \quad (5.48)$$

in the fast group and

$$\max\left(\frac{\psi_2^{2-}(L_1) - \psi_1^{2-}(L_1)}{\psi_2^{2-}(L_1)}, \dots, \frac{\psi_n^{2-}(L_{n-1}) - \psi_{n-1}^{2-}(L_{n-1})}{\psi_n^{2-}(L_{n-1})}\right) < \epsilon_2 \quad (5.49)$$

where  $L_0$  is the the start of the shield,  $L_n$  is the end of the shield and  $L_1, \dots, L_{n-1}$  are the interfaces the lie between.

Now in the 2-group coupling scheme both  $\epsilon_1$  and  $\epsilon_2$  must be less than the tolerance  $\epsilon$ . That is:

$$\max(\epsilon_1, \epsilon_2) < \epsilon \quad (5.50)$$

This means that the coupling can still be done in a way very similar to the 1-group problem. Namely in a single if loop with one tolerance  $\epsilon$ . This suggest that generalising to n-group would work in the same way with:

$$\max(\epsilon_1, \dots, \epsilon_n) < \epsilon \quad (5.51)$$

where  $n$  is the number of total groups.

**Boundary condition:** Free at 1st iteration,  
continuity condition placed on the fluxes thereafter.

$$\psi_{steel}^{1-}(L_I) - \psi_{water}^{1-}(L_I) < tol$$

$$\psi_{steel}^{2-}(L_I) - \psi_{water}^{2-}(L_I) < tol$$

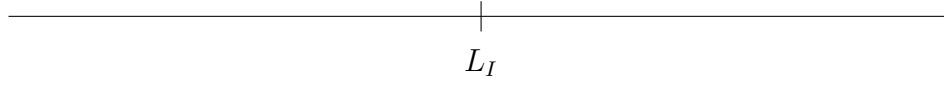


**Figure 5.8:** This figure is an example of how the boundary conditions at each interface are used to achieve continuity between a shield model for steel one for water at an interface point  $L_I$ . Excluding the inlet and outlet boundary condition at the beginning and end of the whole shield and zooming in on one of the remaining free boundary conditions at each material interface of each material we see that the pairs of directional fluxes must match up to a tolerance condition for the coupling scheme to achieve continuity across the domain.

Now in figure 5.9 we test the coupling scheme with the exact solutions. This gives us an idea of what the ROM solutions should look like. Two sets of solutions are coupled, first with the input spectrum split evenly between fast and thermal flux and the with all flux in the fast group only. In the total scalar flux we can see that the input spectra makes little difference and that some of the features are similar to the 1-group model. The biggest difference is that the 2-group model covers more order of magnitude. Comparing the two sets of figures we can see that the thermal flux strongly attenuated by the boron slab and then build back up due to mostly scatter. By  $16cm$  we see fluxes become very similar.

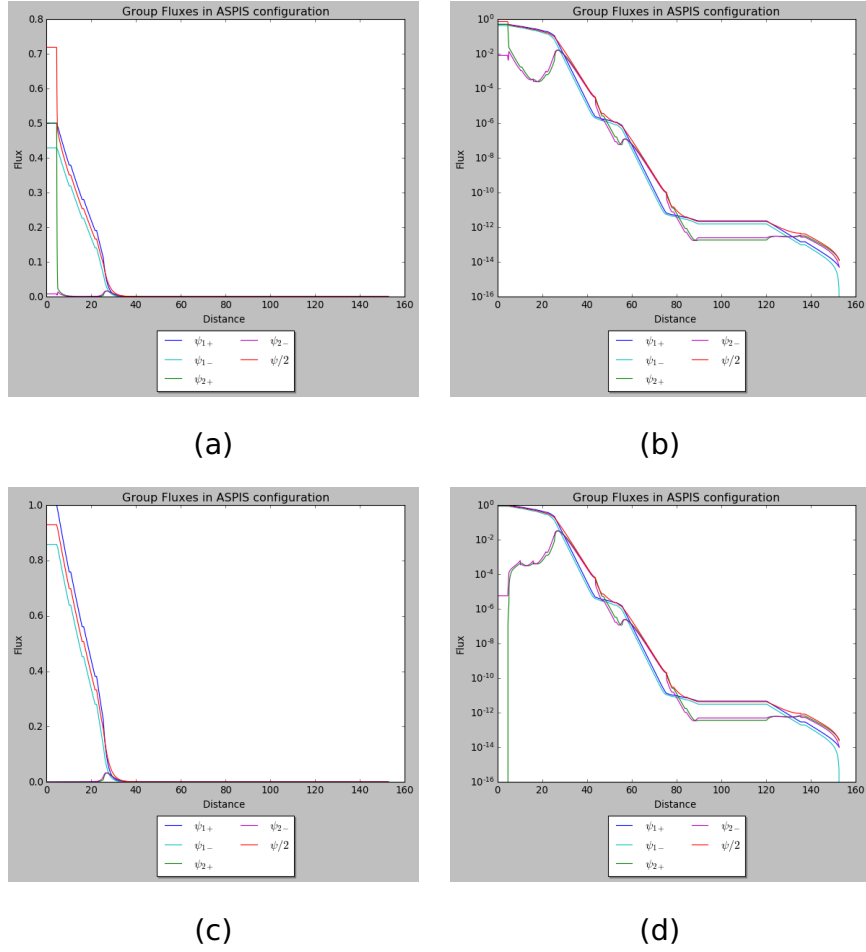


**Figure 5.9:** (a),(b) The results, on liner and log-linear scales, for exact slabs coupled together in the ASPIS configuration with input fluxes of  $(0.5, 0.5)$  for the left hand boundary conditions and (c),(d) The results for exact slabs coupled together in the ASPIS configuration with input fluxes of  $(1.0, 0.0)$  for the left hand boundary conditions in both linear and log-linear scales. The fluxes at the end of the shield remain similar in both cases. Even with no input thermal fluxes a sizable amount builds up from scatter.

### 5.2.1 Two group ROM results and training

The results for the 2-group coupled ROM for the ASPIS configuration are presented. Interestingly we can get good results with just two training points in the boundary conditions parameter axis. We therefore use  $2^5$  sets of parameters training on an lattice of  $5D$  inputs made of the 4 boundary condition fluxes and 1 axis for the width of the shields. With 5 parameters we see that a uniform lattice of training points formed from all permutations of a parameters is beginning to not scale strongly. While this sampling of the training points for 1-group and 2-group problems shows it is possible to get good agreement with exact solutions. The limitations in the scalability of sampling training points on a lattice indicated a more effective sampling of training points would be a desirable avenue of inquiry in further works. Extra training point could be added near the boundary conditions and interfaces using a Smolyak sparse grid as [77]. We will now explain the uniform lattice training regime and show that even with simple assumptions on implementation of a coupled ROM we can get very convincing results for the 2-group problem and valuable insight into how to further develop the techniques.

#### Training regime

Here the ROM is using  $2^5$  snapshots, each boundary condition is trained with 2 data points at  $10^{-18}$  and 0.6 and the width is trained from 0.95 the shield width to 1.1 of the shield width. What might not be obvious is that more training data in this problem does not necessarily give better results. Using  $3^5$  yields worst results and takes longer to converge. Using  $5^5$  data points gives very similar results to  $2^5$  data points however takes much longer to converge. The range of training parameters covers a range of possible flux spectra, the desired spectra for this problem is taken as  $(0.5, 0.5)$  between the fast and thermal group as to show an extreme case of the physical problem. An upper flux boundary condition training Of 1.0 was initially tested in the development of these results as to cover all possible input spectra and is a valid method but a more narrow range, specific to the test case gives faster convergence. The value  $10^{-18}$  was chosen to be close to zero and much smaller than any a

priori assumptions of the end flux, the 1-group flux was in the order  $10^{-6}$  at the exist, but also large enough to keep matrices used with in the method, such as the kernel matrices of the RBF interpolation, from becoming singular and thus not invertable.

Maintaining the width as a training parameter and also a full range of flux spectra demonstrates that this framework could be used with experimental data varying in the same parameters. With suitable convergence from a well chosen relaxation factor and characteristic lengths, real time calculations are a possibility. This indicates that coupled ROMs can be valid tool for rapid prototyping of shielding.

Recall from the individual ROMs that with the choice of just 4 POD basis functions, we get close to 100% of the information. The choice of characteristic length is made heuristically taking the best values from looking at how the library of interval material ROMs behaves with variation in characteristic length. An extreme choice of characteristic length makes the RFB kernel matrix almost singular, and the computation of its inverse prone to large numerical error. If this is managed however the RBF interpolation will have the best fit, that is the heuristic choice must make the problem close to this point but not stray to instability or unnecessarily long convergence.



## 5.2.2 Results and discussion of Coupled 2-Group ASPIS problem

The coupled 2-group ROM gives results very close to the coupled exact solution until the very end of the configuration. In the set of figures 5.10 we see the error for most of the domain is less than 0.05. The error begins to rise at the very end of the domain this is firstly due to a very rapid drop in flux this close to the end of the shield. Secondly, concerning the the very last point is largely a numerical artifact, representing zero with inconstant close to machine precision level numbers. The physics reproduced are therefore the same as in the coupled exact solutions and the details of this are clear on the log-linear scale.

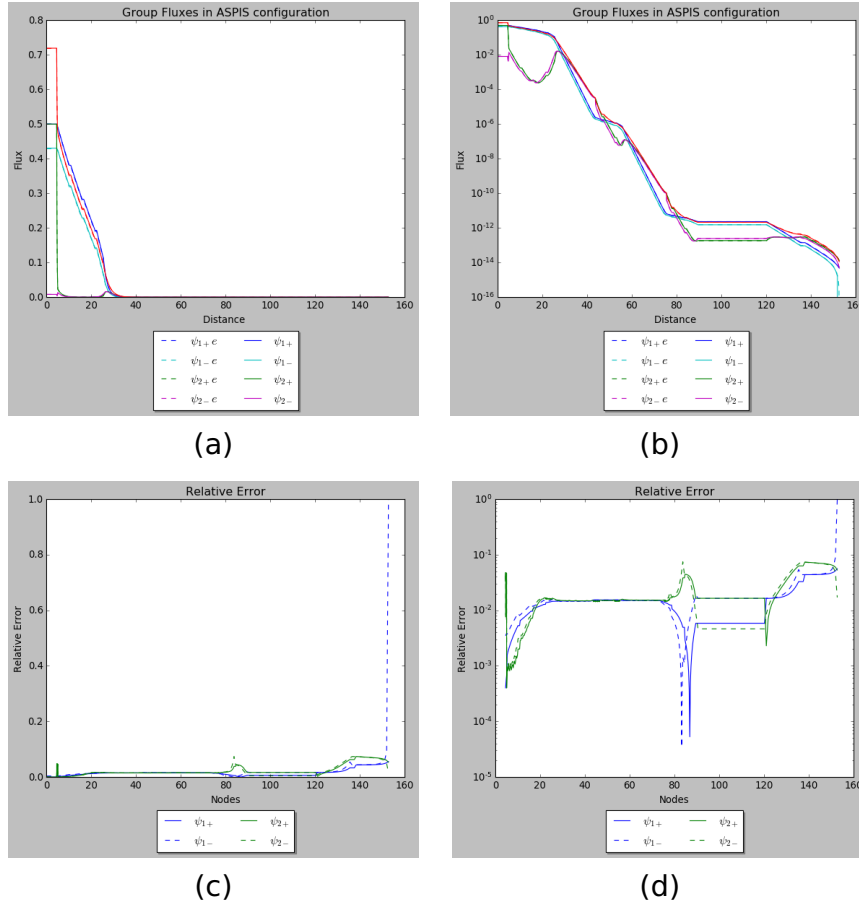


**Figure 5.10:** (a),(b) The flux profiles in linear and log-linear scales, (c) (d) the relative error in linear and log-linear scales. We see low error in the coupled ROM solutions until the very end of the domain. This is due to the rapid drop in flux at the very end of the shield.

In figure 5.11 we see where the model under or over estimates the solutions as indicated by the sign of the absolute error. The interface that the maximum tolerance is associated with is tracked as to show whether the ROM can converge any further. The first 14 are the fast group interfaces and the rest are the thermal group interfaces. We see that the scheme converges smoothly initially until pushing the tolerance beyond  $\epsilon = 0.995$ . After this point a more haphazard convergence follows.

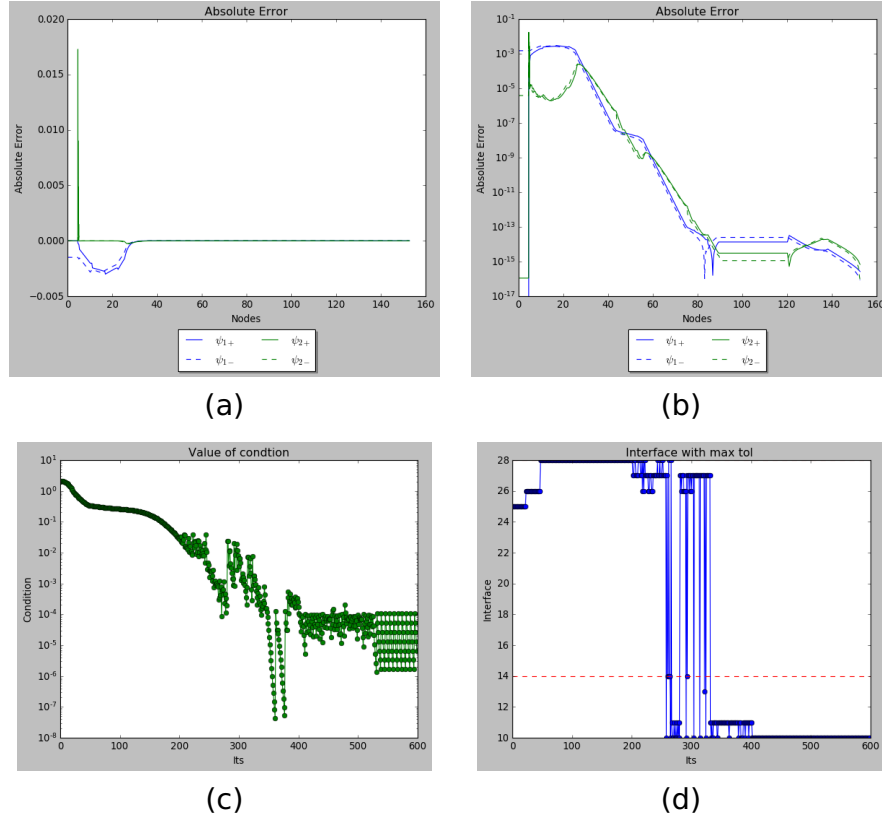


**Figure 5.11:** (a),(b) The absolute error in linear and log-linear scales. (c) The value of the tolerance at each iteration. The value of the characteristic length has been tuned to permit the smallest tolerance still stable. (d) The worst interface at each iteration. Interfaces 1 to 14 are group-1 and 15 to 28 are group-2.

The work in this chapter shows coupled ROMs are a viable approach to 2-Group problems on relevant inhomogeneous materials. High information is possible from just 4 POD basis functions to build a POD basis in which reduced, hence cheaper, solutions exist. The non-intrusive online interpolation ROM stage, with basic training and an informed characteristic length choice yields very low errors near 0.05 and good continuity across the boundaries of at least

$\epsilon = 0.995$ . Little further convergence was possible under the current training regime.

The loss of smoothness in convergence may be due the error introduced in numerical matrix inversion and its limitations. The area of convergence is one that could be further investigated as RBF interpolation is an emerging technique. As this is informed by the values at boundaries, efforts to reduced Gibb's (or Runge's) phenomena would be beneficial with clustering of data near boundaries [119]. Radial basis function interpolation is very suited to sparse and scattered data and as such another very important future piece of work the would be to refine the training as to not be on an evenly spaced lattice. This is dues to scalability as moving a 3-group model for example would require at least  $2^7$  data points in this current lattice taring regime. A Latin hyper cube has been used to sample possible training points and thus reduced the number required [120]. This would make sense as a sampling technique as it produces near random sampling that is very representative of the variability in a sample. Direct random sampling is not viable as the snapshots must be indexed for the ROM algorithm to be implemented. The is a promising area of research using neural networks in place of RBF interpolation which could also be perused.

## Conclusion

A limitation of the ROM scheme presented in this work is that there is no guarantee the ROM solutions are physically conservative. Conservation laws are not necessarily preserved: in our current application this one mean the total number of neutrons is the property that is not conserved. In the last chapter of this thesis a Sub-grid scale full order method is developed to addressed this problem. Understanding this method may help to build a non-intrusive ROM with this property.

# Chapter 6

## Derivation of a Sub-Grid Scale Full Order Method

### **Overview**

This chapter derives a novel sub-grid scale NIROM for 1D and 2D advection-diffusion type problems that can give conservatism to the ROM solution additively. The discretisation process is shown in depth with increasingly complex terms added to the governing equations, starting with just advection and building towards advection, diffusion, absorption and source. The NIROMS are tested on unseen time steps with the results at the end of the chapter show a speed up over the conventional finite volume approach with the NIROM guaranteeing conservation laws are obeyed in the ROM solutions.

# Introduction

In the previous chapter we saw coupling was a very viable tool for problems with an inhomogeneous material domain, with errors typically 0.05 for a problem spanning 14 orders of magnitude, however we identified three key limitations:

1. Training time: Scalability of a brute force lattice sampling training.
2. Heuristic choices: Reliance on the modellers time and experience with choice of characteristic length.
3. Conservation laws: Lack of control over whether ROM solutions obey conservation laws of properties conserved in the training data or models.

For limitation (1) there has been work done, partially in the area of fluid modelling that uses more sophisticated sampling and training regimes. An impressive result using the Latin Hyper cube to build complex ROMs of known fluid dynamics benchmark problems can be seen in [1]. For (2) the choice of characteristic length can be refined through understanding the condition numbers involved in the ROM calculation, physically based characteristic lengths such as wet diameter in a fluid dynamic context for example or employing a neural network to improve heuristics. This would be an exciting piece of further work in the context of coupled ROMs. This chapter explores (3) namely conservation laws.

There has already been great interest in adding conservation in other kinds of data-driven approaches. Work in Gaussian process regression based hidden physics models [121] and physics-informed neural networks [88] are promising and data-efficient areas. To outline the need for conservative ROM solutions we change from steady-state to problems involving time stepping. We must depart from directly solving problems in the field of shielding to more abstract mathematical formulations that start with very simple behaviours and add complexity to cover behaviour of interest, starting with advection

of a flux profile to diffusion absorption and source terms. In many numerical methods we can see problems from loss of conservation in the form of either numerical diffusion, where excess of diffusive behaviours is a numerical artefact or in the language of Hamiltonian mechanics we might think of loss of conservation as an energy drift [122]. We might be interested in what time scales this drift happens or the artificial diffusion appears.

In this work we look at homogeneous materials as we have demonstrated they can be coupled to model inhomogeneous cases. This is also a more simple problem to start from. Advection of a scalar field in 1D was chosen as the starting point as numerical diffusion is partially clear in a case with no physical diffusion present. A square initial profile will make clear any changes as we would expect to see the shape unchanged in the analytical solution to such a problem. How we begin to address the loss of conservation in ROM solutions is to develop a numerical scheme that solves this problem on two length scales. A careful choice of sub-grid scale representation with Haar wavelets enables us to gain conservative solutions. This numerical scheme forms a basis that could be used in a projection based intrusive ROM and thus solve the problem of conservative ROM solutions. A Non-intrusive (NIROM) approach is later presented, demonstrating the control over conservation.

Here we present the derivation of a numerical method that solves the differential equation on both the super and sub-grid scales. We will later show that the sub-grid scale model can be expanded to cover diffusion and absorption processes, generalised to 2D and be applied to non-intrusive reduced order modelling.

## 6.1 Sub-grid scale modelling

We develop a two-scale numerical model, in the form of a finite volume scheme tested at the two scales, and apply this to a series of equations of increasing complexity so as to model advection, then diffusion, sources and absorption. This will be done for an arbitrary scalar field that we will refer to as a temperature.

Starting with the advection equation for an arbitrary scalar field temperature:

$$\frac{\partial \tilde{T}}{\partial t} + \nabla \cdot (u \tilde{T}) = 0 \quad (6.1)$$

where  $\tilde{T}$  is the scalar field undergoing advection,  $t$  is time,  $\nabla$  is the gradient operator and  $u$  is the velocity [123]. We use a Dirichlet boundary condition of zero.

We approximate the analytical solution  $\tilde{T}$  with  $T$  and decompose the solution into a two-scale form of a coarse scale solution  $T_C$  and a fine sub-grid scale solution  $T_{SGS}$ .

$$\tilde{T} \approx T = T_C + T_{SGS} \quad (6.2)$$

As 2D case will be expanded upon later in this chapter we will focus on the 1D case. Without loss of generality we can consider the 1D problem

$$\frac{\partial \tilde{T}}{\partial t} + \frac{\partial (u \tilde{T})}{\partial x} = 0 \quad (6.3)$$

where  $u$  is now treated as a scalar advection speed. We partition the spatial domain into  $i$  control volumes  $\Omega_i$ . The control volume shape functions (or basis functions),  $M_i(x)$ , are given by

$$M_i(x) = \begin{cases} 1 & \text{for } x \in \Omega_i \\ 0 & \text{elsewhere} \end{cases} \quad (6.4)$$

which act as indicator functions, showing whether a value of  $x$  is in control volume  $\Omega_i$  and we expand  $T_C$  with time dependent coefficients  $T_{C_i}(t)$  as follows

$$T_C(x, t) = \sum_i T_{C_i}(t) M_i(x). \quad (6.5)$$

Within each control volume  $\Omega_i$  is a sub-grid scale solution  $T_{SGS_i}(x, t)$  expanded in Haar wavelets  $H_{i,j}(x)$  so the sub-grid solution for control volume  $i$  is given by

$$T_{SGS_i}(x, t) = \sum_j T_{SGS_{i,j}}(t) H_{i,j}(x), \quad (6.6)$$

where  $H_{i,j}(x)$  corresponds to the  $j$ th Haar wavelet in the  $i$ th control volume. The dependence of the basis functions  $M_i(x)$  and  $H_{i,j}(x)$  on  $x$  and the coefficients  $T_{C_i}(t)$  and  $T_{SGS_{i,j}}(t)$  on  $t$  is assumed from this point onwards and no longer written out explicitly.

The first few wavelet basis functions can be seen in figure 6.1 super imposed. The Haar wavelets form an orthonormal basis on the unit interval. The Haar wavelet basis does not contain a constant function as this is already contained in the control volume basis, ie.  $M_i$  is constant over the  $i$ th control volume. They look like a sequence of scaled rectangles and are defined as follows:

The mother wavelet on the unit interval defines the basic shape

$$H(x) = \begin{cases} 1 & \text{for } x \in [1, \frac{1}{2}), \\ -1 & \text{for } x \in [\frac{1}{2}, 1], \\ 0 & \text{elsewhere} \end{cases} \quad (6.7)$$

and basis of daughter wavelets are generated as

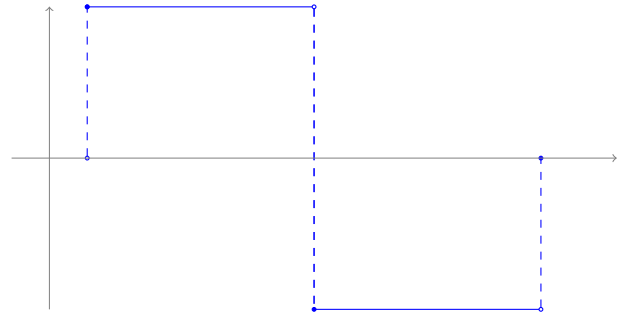
$$H_{i,j}(x) = H(2^i x - j) \quad (6.8)$$

for  $i > 0$  integer  $0 \leq j \leq 2^i - 1$  [124]. Although there are other families of wavelets used in numerical methods, [125],[126], we choose the haar wavelet for a few key reasons: they are the simplest wavelet basis and they are odd functions which integrate to zero over a symmetric domain. We will important make use of this later.



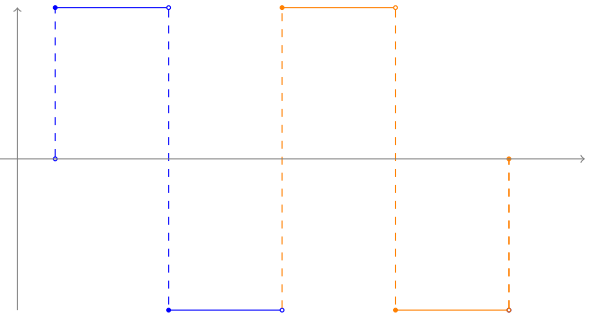
Wavelet level:  $l = 1$ ,

each wavelet now indexed:  $j = 1$ .



Wavelet level:  $l = 2$ ,

each wavelet now indexed:  $j = 2, 3$ .



Wavelet level:  $l = 3$ ,

wavelets now indexed:  $j = 4, 5, 6, 7$ .

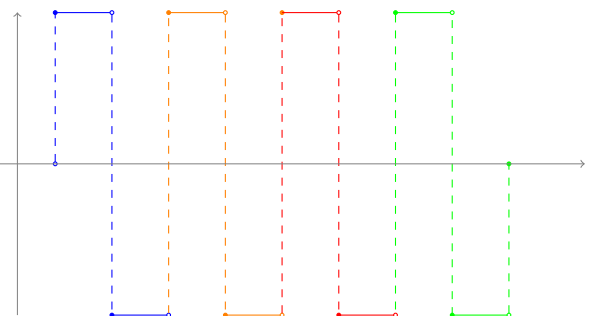


**Figure 6.1:** The levels of the wavelet basis functions as well as the numbering of the wavelet basis functions.

The derivation will take the form of a finite volume scheme in which volume integrals of divergence terms are converted to surface integrals which can be considered as discrete boundary fluxes. An other example of this process is in [127]. Finite volume is in reference to the volume surrounding each point on the mesh. In this method we will have coarse finite volumes and a number of sub-grid scale finite volumes associated with each coarse volume.

Returning to the derivation we now test the governing equation (6.3) over each of the two scales with the shape functions to give a Galerkin projection, integrate this over the problem domain and then set the result to equal zero

$$\int_{\Omega} M_i \left( \frac{\partial T}{\partial t} + \frac{\partial(uT)}{\partial x} \right) dx = 0 \quad \forall i \quad (6.9)$$

$$\int_{\Omega} H_{i,j} \left( \frac{\partial T}{\partial t} + \frac{\partial(uT)}{\partial x} \right) dx = 0 \quad \forall i, j, \quad (6.10)$$

where  $\Omega$  is the domain of interest, here a 1D line, which satisfies  $\Omega = \cup_i \Omega_i$ .

Galerkin projection as a method of numerical solution lends itself to this problem as the integrals can be evaluated on domains of arbitrary shape. Both control volume basis functions and wavelet basis functions contain discontinuities and in order to integrate the wavelet equation we split the domain of the integral in equation (6.10) into two parts,

$$\int_{\Omega_{i,j}^+} H_{i,j} \left( \frac{\partial T}{\partial t} + \frac{\partial(uT)}{\partial x} \right) dx + \int_{\Omega_{i,j}^-} H_{i,j} \left( \frac{\partial T}{\partial t} + \frac{\partial(uT)}{\partial x} \right) dx = 0 \quad \forall i, j, \quad (6.11)$$

where  $\Omega_{i,j}^+$  is associated with the positive wavelet values and  $\Omega_{i,j}^-$  negative wavelet values as shown in figure 6.2.

This is now a form where we can apply the divergence theorem to transform volume integrals into surface integrals. These terms can then be evaluated as fluxes at the surfaces of each control volume. This is done as because the flux entering a given volume is identical to the flux that leaves the adjacent volume we will have a two-scale conservative method.

We now apply the divergence theorem to equations (6.9) and (6.10) resulting in:

$$\int_{\Omega} M_i \frac{\partial T}{\partial t} dx + \int_{\Gamma_i} u T n_x d\Gamma = 0 \quad \forall i \quad (6.12)$$

$$\int_{\Omega} H_{i,j} \frac{\partial T}{\partial t} dx + \int_{\Gamma_{i,j}^+} H_{i,j} u T n_x d\Gamma + \int_{\Gamma_{i,j}^-} H_{i,j} u T n_x d\Gamma = 0 \quad \forall i, j, \quad (6.13)$$

where  $\Gamma_i$  is the surface of control volume  $\Omega_i$ ,  $\Gamma_{i,j}^+$  is surface associated with the region where the  $j$ th wavelet of the  $i$ th control volume is positive, and  $\Gamma_{i,j}^-$  is surface associated with the region where the  $j$ th wavelet of the  $i$ th control volume is negative.

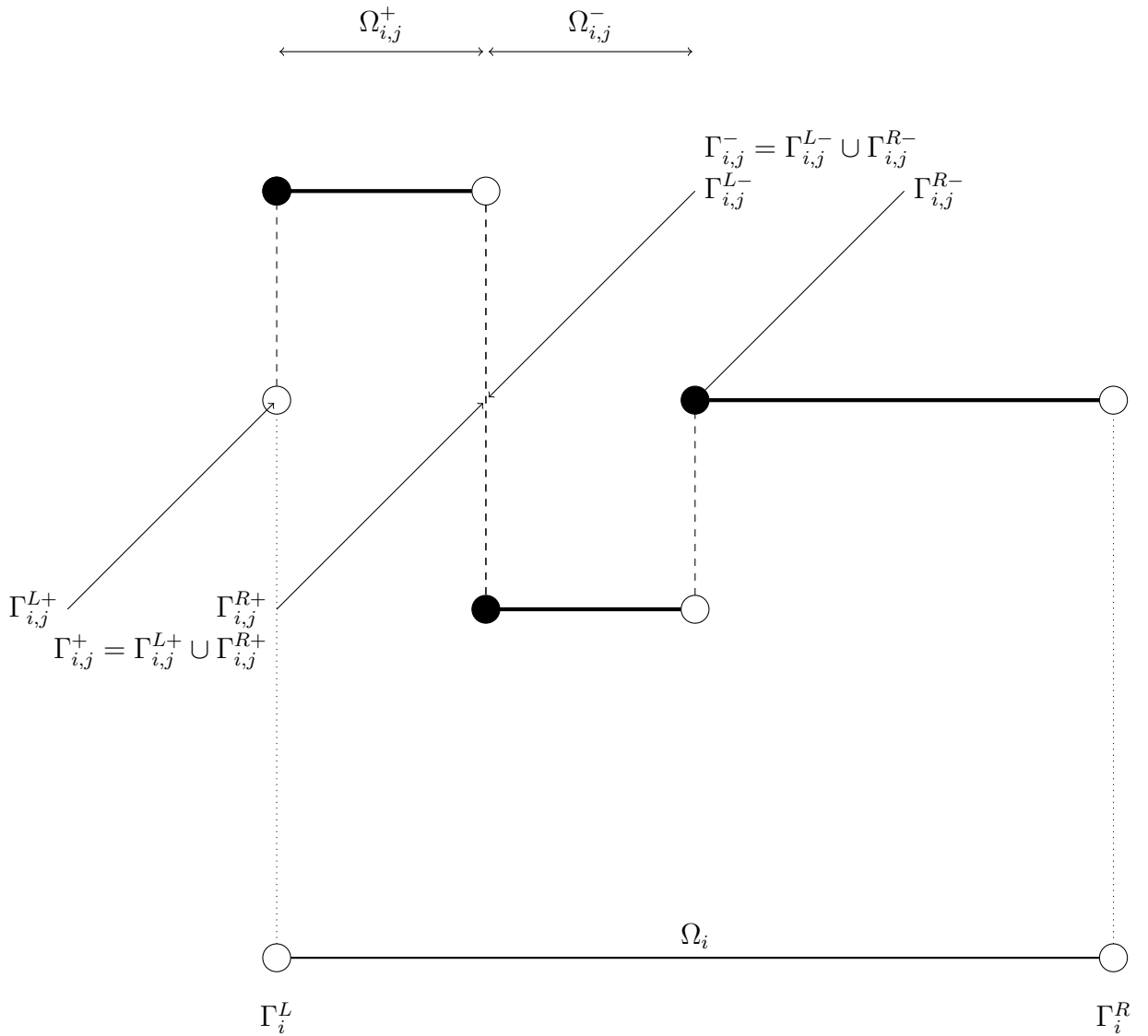


**Figure 6.2:** The Wavelet basis showing the domain  $\Omega_i$  it occupies and its boundaries on which we consider flux entering and leaving.

Noting that an even function times an odd function is odd and odd functions on symmetric domain integrate to identically zero [128]. We have that  $H_{i,j}$  is odd and  $M_i$  is even. ie.

$$\int_{\Omega} M_i H_{i,j} dx = 0 \quad \forall i, j, \quad (6.14)$$

thus we have that

$$\int_{\Omega} M_i \frac{\partial T_{SGS_i}}{\partial t} dx = 0 \quad \text{and} \quad \int_{\Omega} H_{i,j} \frac{\partial T_{C_i}}{\partial t} dx = 0. \quad (6.15)$$

We can therefore simplify the time derivative in equation (6.12) as follows

$$\int_{\Omega} M_i \left( \frac{\partial T_{C_i}}{\partial t} \right) dx + \int_{\Gamma_i} u T n_x d\Gamma = 0 \quad \forall i \quad (6.16)$$

$$\int_{\Omega} H_{i,j} \left( \frac{\partial T_{SGS_i}}{\partial t} \right) dx + \int_{\Gamma_{i,j}^+} H_{i,j} u T n_x d\Gamma + \int_{\Gamma_{i,j}^-} H_{i,j} u T n_x d\Gamma = 0 \quad \forall i, j. \quad (6.17)$$

Evaluating the surface integrals gives

$$\int_{\Omega} M_i \left( \frac{\partial T_{C_i}}{\partial t} \right) dx - (uT) \Big|_{x_i^L} + (uT) \Big|_{x_i^R} = 0 \quad \forall i \quad (6.18)$$

$$\int_{\Omega} H_{i,j} \left( \frac{\partial T_{SGS_i}}{\partial t} \right) dx - (uT) \Big|_{x_{i,j}^{+L}} + (uT) \Big|_{x_{i,j}^{+R}} - (uT) \Big|_{x_{i,j}^{-L}} + (uT) \Big|_{x_{i,j}^{-R}} = 0 \quad \forall i, j. \quad (6.19)$$

where  $x_i^L$  and  $x_i^R$  are the leftmost and rightmost points of the control volume  $\Omega_i$ ,  $x_{i,j}^{+L}$  and  $x_{i,j}^{+R}$  are the leftmost and rightmost points of surface  $\Gamma_{i,j}^+$  (the surface associated with the positive values of the  $j$ th Haar wavelet of the  $i$ th control volume), and  $x_{i,j}^{-L}$  and  $x_{i,j}^{-R}$  are the leftmost and rightmost points of surface  $\Gamma_{i,j}^-$ .

Discretising in time using the  $\theta$ -method and evaluating the volume integrals:

$$\int_{\Omega} M_i \left( \frac{T_{C_i}^{n+1} - T_{C_i}^n}{\Delta t} \right) dx - (uT) \Big|_{x_i^L}^{n+\theta} + (uT) \Big|_{x_i^R}^{n+\theta} = 0 \quad \forall i \quad (6.20)$$

$$\begin{aligned} \int_{\Omega} H_{i,j} \left( \frac{T_{SGS_i}^{n+1} - T_{SGS_i}^n}{\Delta t} \right) dx - (uT) \Big|_{x_{i,j}^+L}^{n+\theta} + (uT) \Big|_{x_{i,j}^+R}^{n+\theta} \\ + (uT) \Big|_{x_{i,j}^-L}^{n+\theta} - (uT) \Big|_{x_{i,j}^-R}^{n+\theta} = 0 \quad \forall i, j. \end{aligned} \quad (6.21)$$

in which  $\theta = 0$  gives an explicit, Forward Euler scheme,  $\theta = 1$  gives an implicit, Backward Euler scheme and  $\theta = 0.5$  gives a Crank-Nicholson scheme. Now evaluating the volume integrals on the left and using the orthogonal properties of the wavelets:

$$\Delta x_i \left( \frac{T_{C_i}^{n+1} - T_{C_i}^n}{\Delta t} \right) - (uT) \Big|_{x_i^L}^{n+\theta} + (uT) \Big|_{x_i^R}^{n+\theta} = 0 \quad \forall i \quad (6.22)$$

$$\Delta x_{i,j} \left( \frac{T_{SGS_{i,j}}^{n+1} - T_{SGS_{i,j}}^n}{\Delta t} \right) - (uT) \Big|_{x_{i,j}^+L}^{n+\theta} + (uT) \Big|_{x_{i,j}^+R}^{n+\theta} + (uT) \Big|_{x_{i,j}^-L}^{n+\theta} - (uT) \Big|_{x_{i,j}^-R}^{n+\theta} = 0 \quad \forall i, j. \quad (6.23)$$

in which  $\Delta x_i$  is the width of the  $i$ th control volume and  $\Delta x_{i,j}$  is the width of the interval in which  $H_{i,j}$  is non-zero. To improve stability or accuracy one can solve equation (6.22) for  $T_{C_i}^{n+1}$  and then update the value of  $T_{C_i}$  at the endpoints  $\Gamma_{i,j}^{+/-}$  in equation (6.23). Considering the fluxes above, they need to be evaluated at points where the basis functions are discontinuous. Several options are available which include the upwind value could be used (common, low accuracy, stable), the downwind value could be used (not used as information cannot propagate in the direction of  $u$ ), the average of the upwind and downwind values could be taken (2nd order accurate but unstable), a nonlinear combination of the average and upwind values depending on whether oscillations are detected (based on Normalised Variable Diagram (NVD) or Sweby diagram approaches) [129]. Here we choose upwinding for simplicity and stability.

Assuming an explicit discretisation in time ( $\theta = 0$ ), equations (6.22) and (6.23) become

$$T_{C_i}^{n+1} = T_{C_i}^n + \frac{\Delta t}{\Delta x_i} \left( (uT) \Big|_{x_i^L}^n - (uT) \Big|_{x_i^R}^n \right) \quad \forall i \quad (6.24)$$

$$T_{SGS_{i,j}}^{n+1} = T_{SGS_{i,j}}^n + \frac{\Delta t}{\Delta x_{i,j}} \left( (uT) \Big|_{x_{i,j}^{+L}}^n - (uT) \Big|_{x_{i,j}^{+R}}^n - (uT) \Big|_{x_{i,j}^{-L}}^n + (uT) \Big|_{x_{i,j}^{-R}}^n \right) \quad \forall i, j. \quad (6.25)$$

in which  $\Delta x_{i,j}$  is the width of the wavelet (over which it is non-zero)  $j$  within super-cell  $i$ .

It will be convenient to map between wavelet basis  $H_{i,j}$  and a **new** control volume discretisation  $T_{CV}$ :

$$\int_{\Omega} M_{CV_{i,k}} (T_{CV}^n - T^n) dV = 0 \quad (6.26)$$

in which  $k$  is a sub-CV discretisation index for super-control volume  $i$  and  $M_{CV_{i,k}}$  a CV basis function. Thus we can write:

$$T_{CV_{i,k}}^n = T_{C_i}^n + \sum_{l=1}^{\mathcal{L}} s_w(k, l) T_{SGS_{i,j_w(k,l)}}^n, \quad (6.27)$$

where  $\mathcal{L}$  is the number of levels of Haar wavelets and  $l$  is the level of Haar wavelet and in which

$$j_w(k, l) = \left\lfloor \frac{k-1}{2^{\mathcal{L}-l+1}} + 1 \right\rfloor + Pr(l-1), \quad (6.28)$$

and

$$s_w(k, l) = 2 \left( 2(j_w(k, l) - Pr(l-1)) - \left\lfloor \frac{k-1}{2^{\mathcal{L}-l}} + 1 \right\rfloor \right) - 1 \quad (6.29)$$

or

$$s_w(k, l) = 2 \left( 2 \left\lfloor \frac{k-1}{2^{\mathcal{L}-l+1}} + 1 \right\rfloor - \left\lfloor \frac{k-1}{2^{\mathcal{L}-l}} + 1 \right\rfloor \right) - 1 \quad (6.30)$$

and

$$\Delta x_{i,j} = \Delta x_i / 2^{(h_w(j)-1)}. \quad (6.31)$$

In addition, the wavelet level associated with wavelet  $j$  is:

$$h_w(j) = \text{maximum } l \text{ s.t. } j - Pr(l-1) > 0. \quad (6.32)$$

Also the product function is

$$Pr(l) = \sum_{k=1}^l 2^{k-1} \text{ with } Pr(0) = 0. \quad (6.33)$$

Thus equation (6.27) becomes:

$$\mathbf{T}_{CV} = \mathbf{M}_{CV2CW} \mathbf{T} = (\mathbf{M}_{CV2C} \quad \mathbf{M}_{CV2W}) \begin{pmatrix} \mathbf{T}_C \\ \mathbf{T}_{SGS} \end{pmatrix}. \quad (6.34)$$

There is also a way of mapping from a CV space to wavlets space:

$$AT_{SGS} = b \quad (6.35)$$

$$A_{i,j} = \Delta x_i / 2^{(h_w(j)-1)}, \quad (6.36)$$

with

$$A_{i,j} = 0, \quad (6.37)$$

for  $i \neq j$ .

$$b_{j_w(k,l)} = \sum_k^{N_{SUBCV}-1} \sum_{l=1}^{\mathcal{L}} s_w(k, l) (T_{CV_k} - T_c), \quad (6.38)$$

$$T_c = \frac{1}{N_{CV}} \sum_{i_1=1}^{N_1} T_{CV}. \quad (6.39)$$

Since  $A$  is diagonal we have that,

$$T_{SGS} = A^{-1}b, \quad (6.40)$$

where

$$A^{-1} = \frac{2^{(h_w(j)-1)}}{\Delta x_i}, \quad (6.41)$$

with

$$A^{-1} = 0, \quad (6.42)$$

for  $i \neq j$ .

We return to the derivation. Now that we have  $\mathbf{T}_{CV}$  and assuming  $u$  is constant, equations 6.24,6.25 simplify to:

$$T_{C_i}^{n+1} = T_{C_i}^n + u \frac{\Delta t}{\Delta x_i} \left( (T_{C_{i-1}}^n - T_{C_i}^n) + \sum_{l=1}^{\mathcal{L}} (-T_{SGS_{i-1,2^l-1}}^n - T_{SGS_{i,2^l-1}}^n) \right) \quad \forall i, \quad (6.43)$$

$$T_{SGS_{i,j}}^{n+1} = T_{SGS_{i,j}}^n + u \frac{\Delta t}{\Delta x_{i,j}} \left( T \Big|_{x_{i,j}^{+L}}^n - T \Big|_{x_{i,j}^{+R}}^n - T \Big|_{x_{i,j}^{-L}}^n + T \Big|_{x_{i,j}^{-R}}^n \right) \quad \forall i, j. \quad (6.44)$$



Expanding the right hand side of these equations in terms of CV basis functions then:

$$T_{C_i}^{n+1} = T_{C_i}^n + u \frac{\Delta t}{\Delta x_i} (T_{CV_{i-1, \mathcal{N}_{CV}}}^n - T_{CV_{i, \mathcal{N}_{CV}}}^n) \quad \forall i, \quad (6.45)$$

$$T_{SGS_{i,j}}^{n+1} = T_{SGS_{i,j}}^n + u \frac{\Delta t}{\Delta x_{i,j}} \left( T_{CV_{v(i,j), m_L^+(j)}}^n - T_{CV_{i, m_R^+(j)}}^n - T_{CV_{i, m_L^-(j)}}^n + T_{CV_{i, m_R^-(j)}}^n \right) \quad \forall i, j. \quad (6.46)$$

in which the functions  $m$  return the CV number associated with wavelet  $j$  and in which  $\mathcal{N}_w = Pr(\mathcal{L}) = \mathcal{N}_{SUBCV} - 1$  is the number of wavelet basis functions and  $\mathcal{N}_{SUBCV}$  is the number of CV basis functions within supercell  $i$  (or super control volume) and there will be  $\mathcal{N}_{SUPCV}$  supercells.

The other fluxes are (for the left or positive  $+$  part of the wavelet on the last level) expressed in terms of  $m$ :

$$\tilde{m}_L^+(j) = \left( \frac{2(j - Pr(h_w(j) - 1)) - 2}{2^{h_w(j)}} \right) \mathcal{N}_{SUBCV}, \quad (6.47)$$

$$m_R^+(j) = \left( \frac{2(j - Pr(h_w(j) - 1)) - 1}{2^{h_w(j)}} \right) \mathcal{N}_{SUBCV}, \quad (6.48)$$

$$m_R^-(j) = \left( \frac{2(j - Pr(h_w(j) - 1)) + 0}{2^{h_w(j)}} \right) \mathcal{N}_{SUBCV}. \quad (6.49)$$

The following expressions are also needed to find the fluxes and are defined in terms of  $\tilde{m}_L^+(j)$ :

$$v(i, j) = \begin{cases} i - 1 & \text{for } \tilde{m}_L^+(j) = 0, \\ i & \text{otherwise} \end{cases} \quad (6.50)$$

$$m_L^+(j) = \begin{cases} \mathcal{N}_{SUBCV} & \text{for } \tilde{m}_L^+(j) = 0, \\ \tilde{m}_L^+(j) & \text{otherwise} \end{cases} \quad (6.51)$$

and

$$m_L^-(j) = m_R^+(j). \quad (6.52)$$

The pair of equations (6.46) are the results of this discretization and form a numerical scheme for the coarse scale and the sub-grid scale. We can combine the two scales and get the numerical solution to the advection problem:

$$\tilde{T}(x, t) \approx T_{C_i}^n + T_{SGS_{ij}}^n \quad \forall \quad i, j, n. \quad (6.53)$$

The mapping to the CV basis finally allows all the control volume fluxes to be understood in terms of the indices  $i$  the coarse control volume and  $j$  the individual wavelet. This gives a conservative numerical scheme with more detail being added by increasing both the number of coarse control volumes or the number of wavelet levels. The coarse level scheme takes the familiar form of a 1st order upwind scheme, all be it with this new basis. The sub-grid level of the scheme can be conceptualised as a correction to existing coarse schemes with minimal bespoke changes, Lax-Wendroff for example [130].

Some key properties of this discretisation include:

- Demonstration of how to approximate surface integral terms mapped onto the wavelets for a finite volume scheme.
- Upwinding is proven stable, a positive scheme ( $T \geq 0$ ) with no gibbs oscillations, already accounts for the flow direction
- Conservative numerical scheme

Recall during the derivation, terms with a mix of the two types of wavelets, the Haar wavelets  $H_{i,j}$  and the Indicator functions  $M_i$  cancelled to zero when integrated of the control volumes (6.15). This demonstrates that the space  $\{M_i, H_{i,j}\}$  has linear sub-spaces  $M_i$  and  $H_{i,j}$  allowing the additive correction to the coarse scale scheme to be made. This logic holds as more new terms are added to our original PDE.

We will go on to suggest how this scheme could be used to yield conservative ROM solutions in intrusive ROMs in the appendices. The rest of this section shows how the SGS technique can be extended to apply beyond advection. This is done by deriving the full order sub-grid scale scheme for a diffusion approximation to the scalar transport equation with an added advection term, that is with diffusion, source and absorption terms. This is the extend to 2D. We will conclude with examples applying these numerical schemes to FOM results and NIROM results.

## 6.2 Extending the sub-grid scale approach to model diffusion, source and absorption.

In this section we will add diffusion, sources and absorption into the discretization of the sub-grid scale model. A governing equation that builds on the advection equation, equation (6.3), through adding extra terms takes the form of the diffusion approximation of transport:

$$\frac{\partial \tilde{T}}{\partial t} + \sigma \tilde{T} + \nabla \cdot (\mathbf{u} \tilde{T}) - \nabla \cdot (k \nabla \tilde{T}) = \tilde{S}. \quad (6.54)$$

If we were to consider diffusion theory of some scalar  $\tilde{T}$  as the application the,  $\sigma$  governs absorption,  $\kappa$  is the diffusion coefficient,  $S$  is a source or driving term and  $u$  advection speed. This equation looks like diffusion approximation of neutron transport with the addition of an artificial advection term [113],[131].

### 6.2.1 Diffusion in the sub-grid scale model

To develop a discrete sub-grid scale model for the diffusion term the of the diffusion approximation of the transport equation we go through a similar process as the derivation of the sub-grid scale advection scheme.

- The two test functions, the coarse indicator function  $M_i$  and the haar wavelet  $H_{i,j}$  are used.
- We integrate the diffusion approximation of the transport equation over these test functions to start deriving a finite volume scheme as in the derivation of 6.45 and 6.46.
- Recall this works as volume integrals in a partial differential equation that contain a divergence term are converted to surface integrals. Fluxes can then be found at the boundary of each discrete volume element.

The additional term  $-\nabla \cdot (k \nabla \tilde{T})$  captures the diffusion. When introduced in the sub-grid scale approach, through discretization by finite volumes, the

flux across the interfaces of the wavelets has an associated directions. This comes from thinking about the flux at some small distance left or right of a boundary of the positive or negative part of the wavelet to interpolate the fluxes involved in the diffusion term.

Now we end up with a pair of equations for the two scales, the coarse scale:

$$\begin{aligned}
T_{C_i}^{n+1} = & T_{C_i}^n + v_n u \frac{\Delta t}{\Delta x_i} (T_{CV_{i-1}, \mathcal{N}_{CV}}^n - T_{CV_{i, \mathcal{N}_{CV}}}^n) \\
& - v_n \frac{\Delta t}{\Delta x_i} k_{left} \left( \frac{T_{CV_{i,1}}^{n+1} - T_{CV_{i-1}, \mathcal{N}_{CV}}^{n+1}}{\Delta x_{left}} \right) \\
& + v_n \frac{\Delta t}{\Delta x_i} k_{right} \left( \frac{T_{CV_{i+1,1}}^{n+1} - T_{CV_{i, \mathcal{N}_{CV}}}^{n+1}}{\Delta x_{right}} \right) \\
& + v_n \Delta t \sigma T_{C_i}^{n+1} + v_n \Delta t S_{C_i}^{n+1} \quad \forall i, \tag{6.55}
\end{aligned}$$

with

$$\Delta x_{left} = \frac{1}{2}(\Delta x_{i,1} + \Delta x_{i-1, \mathcal{N}_{CV}}), \quad \Delta x_{right} = \frac{1}{2}(\Delta x_{i+1,1} + \Delta x_{i, \mathcal{N}_{CV}}), \tag{6.56}$$

$$k_{left} = \frac{1}{2}(k_{i,1} + k_{i-1, \mathcal{N}_{CV}}), \quad k_{right} = \frac{1}{2}(k_{i+1,1} + k_{i, \mathcal{N}_{CV}}), \tag{6.57}$$

and the sub-grid-scale equations:

$$\begin{aligned}
T_{SGS_{i,j}}^{n+1} = & T_{SGS_{i,j}}^n + v_n u \frac{\Delta t}{\Delta x_{i,j}} \left( T_{CV_{v(i,j),m_L^+(j)}}^n - T_{CV_{i,m_R^+(j)}}^n - v_n T_{CV_{i,m_L^-(j)}}^n + T_{CV_{i,m_R^-(j)}}^n \right) \\
& - v_n \frac{\Delta t}{\Delta x_i} k_{left}^+ \left( \frac{T_{CV_{i,u^-(m_L^+(j)+1)}^{n+1}} - T_{CV_{v(i,j),m_L^+(j)}}^{n+1}}{\Delta x_{left}^+} \right) \\
& + v_n \frac{\Delta t}{\Delta x_i} k_{right}^+ \left( \frac{T_{CV_{i,m_R^+(j)+1}^{n+1}} - T_{CV_{i,m_R^+(j)}}^{n+1}}{\Delta x_{right}^+} \right) \\
& + v_n \frac{\Delta t}{\Delta x_i} k_{left}^- \left( \frac{T_{CV_{i,m_L^-(j)+1}^{n+1}} - T_{CV_{i,m_L^-(j)}}^{n+1}}{\Delta x_{left}^-} \right) \\
& - v_n \frac{\Delta t}{\Delta x_i} k_{right}^- \left( \frac{T_{CV_{w^-(i,m_R^-(j)+1),u^-(m_R^-(j)+1)}^{n+1}} - T_{CV_{i,m_R^-(j)}}^{n+1}}{\Delta x_{right}^-} \right) \\
& + v_n \Delta t \sigma T_{SGS_{i,j}}^{n+1} \frac{\Delta t}{2} \\
& + v_n \Delta t S_{SGS_{i,j}}^{n+1} \quad \forall i, j.
\end{aligned} \tag{6.58}$$

with

$$\Delta x_{left}^+ = \frac{1}{2} \left( \Delta x_{i,u^-(m_L^+(j)+1)} + \Delta x_{v(i,j),m_L^+(j)} \right), \tag{6.59}$$

$$\Delta x_{right}^+ = \frac{1}{2} \left( \Delta x_{i,m_R^+(j)+1} + \Delta x_{i,m_R^+(j)} \right), \tag{6.60}$$

$$\Delta x_{left}^- = \frac{1}{2} \left( \Delta x_{i,m_R^+(j)+1} + \Delta x_{i,m_L^-(j)} \right), \tag{6.61}$$

$$\Delta x_{right}^- = \frac{1}{2} \left( \Delta x_{w^-(i,m_R^-(j)+1),u^-(m_R^-(j)+1)} + \Delta x_{i,m_R^-(j)} \right), \tag{6.62}$$

and

$$k_{left}^+ = \frac{1}{2} (k_{i,u^-(m_L^+(j)+1)} + k_{v(i,j),m_L^+(j)}), \tag{6.63}$$

$$k_{right}^+ = \frac{1}{2} (k_{i,m_R^+(j)+1} + k_{i,m_R^+(j)}), \tag{6.64}$$

$$k_{left}^- = \frac{1}{2}(k_{i,m_R^+(j)+1} + k_{i,m_L^-(j)}), \quad (6.65)$$

$$k_{right}^- = \frac{1}{2}(k_{w^-(i,m_R^-(j)+1),u^-(m_R^-(j)+1)} + k_{i,m_R^-(j)}). \quad (6.66)$$

The extra fluxes introduced by the discretization of the diffusion term are expressed by the mappings  $u^-$  and  $w^-$ :

$$u^-(k) = \begin{cases} 1 & \text{for } k = \mathcal{N}_{SUBCV} + 1, \\ k & \end{cases} \quad (6.67)$$

$$w^-(i, k) = \begin{cases} i + 1 & \text{for } k = \mathcal{N}_{SUBCV} + 1, \\ i & \text{otherwise.} \end{cases} \quad (6.68)$$

with the other mappings  $m^+, v, w, k, \Delta x$  defined in the previous section (6.51). The source and absorption terms are carried through this stage of the derivation without mapping to the CV basis. This will be done in the next section. For use at this stage the corresponding the source and absorption terms must be set to zero.

### 6.2.2 Source and absorption in the sub-grid scale model

The absorption,  $\sigma T$ , and source  $S(T)$  are both functions of  $T$  and therefore can be discretized in a similar manner. We will start with the source to derive the CV representations. This mapping will let us find the discretized source and absorption written in terms of a CV source or absorption which can then be slotted into the existing sub-grid scale discrete upwind equations (6.85) and (6.86).

Analogous to equation 6.27 the source  $S$  can be mapped from wavelets to control volumes as follows:

$$S_{CV,i,k}^n = S_{C,i}^n + \sum_{l=1}^{\mathcal{L}} s_w(k, l) S_{SGS,i,j_w(k,l)}^n, \quad (6.69)$$

This mapping let the source terms be re-written in matrix form:

$$\underline{S_{CV}}^n = G \begin{pmatrix} \underline{S_C}^n \\ \underline{S_{SGS}}^n \end{pmatrix}. \quad (6.70)$$

Premultiplying this equation by  $G^T$  results in an equation that can be used to form the reverse mapping, that is:

$$\begin{pmatrix} \underline{S_C}^n \\ \underline{S_{SGS}}^n \end{pmatrix} = D^{-1} G^T \underline{S_{CV}}^n, \quad (6.71)$$

which uses the wavelet orogonality property:

$$G^T G = D. \quad (6.72)$$

Thus taking the transpose of equation 6.69:

$$S_{C_i}^n = 0, \quad S_{SGS_{i,j}}^n = 0, \quad \forall i, j, \quad (6.73)$$

$$S_{C_i}^n \rightarrow S_{C_i}^n + S_{CV_{i,k}}^n, \quad \forall i, k \quad (6.74)$$

$$S_{SGS_{i,j_w}(k,l)}^n \rightarrow S_{SGS_{i,j_w}(k,l)}^n + \sum_{l=1}^{\mathcal{L}} s_w(k, l) S_{CV_{i,k}}^n, \quad \forall i, k \quad (6.75)$$

We now have a CV representation for the source terms

The absorpion term discretised is:

$$\int_{\Omega} M_{CV_i}(\sigma T) dV, \quad (6.76)$$

$$\int_{\Omega} H_{i,j}(\sigma T) dV. \quad (6.77)$$

Thus treating the  $\sigma T$  product like a source one can get, in matrix form, the result of equations 6.76, 6.77:

$$G^T D^{-1} \underline{\underline{\sigma}} G \begin{pmatrix} \underline{T_C}^n \\ \underline{T_{SGS}}^n \end{pmatrix}, \quad (6.78)$$

in which  $\underline{\underline{\sigma}}$  is the diagonal matrix containing the CV values of  $\sigma$ .



The discretized source can also be written in terms of CV sources (equations 6.76, 6.77): For the course grid scale (multiplying by  $v_n \frac{\Delta t}{\Delta x_i}$  to the discretization fits directly into equations 6.55, 6.55):

$$v_n \frac{\Delta t}{\Delta x_i} \sum_{k=1}^{\mathcal{N}_{CV}} \Delta x_{CVi,k} S_{CVi,k}^{n+1}, \quad (6.79)$$

and for the SGS source:

$$v_n \frac{\Delta t}{\Delta x_{i,j}} \left( \sum_{k=u^-(m_L^+(j)+1)}^{m_R^+(j)} \Delta x_{CVi,k} S_{CVi,k} + \sum_{k=m_L^-(j)+1}^{m_R^-(j)} \Delta x_{CVi,k} S_{CVi,k} \right). \quad (6.80)$$

Similarly for the discretization of sigma:

$$v_n \frac{\Delta t}{\Delta x_i} \sum_{k=1}^{\mathcal{N}_{CV}} \Delta x_{CVi,k} \sigma_{CVi,k} T_{CVi,k}^{n+1}, \quad (6.81)$$

and for the SGS  $\sigma T$  discretized term:

$$v_n \frac{\Delta t}{\Delta x_{i,j}} \left( \sum_{k=u^-(m_L^+(j)+1)}^{m_R^+(j)} \Delta x_{CVi,k} \sigma_{CVi,k} T_{CVi,k}^{n+1} + \sum_{k=m_L^-(j)+1}^{m_R^-(j)} \Delta x_{CVi,k} \sigma_{CVi,k} T_{CVi,k}^{n+1} \right). \quad (6.82)$$

For purposes of solving the equations it will be useful to define a course grid and SGS  $\sigma$ :

$$\widetilde{\sigma}_{Ci} = \frac{1}{\Delta x_i} \sum_{k=1}^{\mathcal{N}_{CV}} \Delta x_{CVi,k} \sigma_{CVi,k} + \frac{1}{\Delta x_i} \left( \frac{k_{left}}{\Delta x_{left}} + \frac{k_{right}}{\Delta x_{right}} \right), \quad (6.83)$$

$$\begin{aligned} \widetilde{\sigma}_{SGSi,j} = \frac{1}{\Delta x_{i,j}} & \left( \sum_{k=u^-(m_L^+(j)+1)}^{m_R^+(j)} \Delta x_{CVi,k} \sigma_{CVi,k} + \sum_{k=m_L^-(j)+1}^{m_R^-(j)} \Delta x_{CVi,k} \sigma_{CVi,k} \right) \\ & + \frac{1}{\Delta x_{i,j}} \left( \frac{k_{left}^+}{\Delta x_{left}^+} + \frac{k_{right}^+}{\Delta x_{right}^+} + \frac{k_{left}^-}{\Delta x_{left}^-} + \frac{k_{right}^-}{\Delta x_{right}^-} \right). \end{aligned} \quad (6.84)$$

Notice that in addition the the physically significant adoption term on the CV basis we have added another absorption term, a pseudo-absorption term, on both sides of the equations. This has been combined the the physical diffusion

terms and these pseudo-absorption terms used for the solution relaxation [132]. This is possible as the differential operator can be rewritten as the sum of two complementary operators, sometimes called a splitting method. Such methods are suitable for large, sparse non-linear problems and least-squares linear problems. In the previous chapter we used a similar approach called Successive Over-Relaxation, equation (4.31). These relaxations will speed up convergence and stabilise the scheme with appropriate choices step size and number of iterations.

Using these values of  $\sigma$ , equations (6.83), (6.84), to help with an iterative process, in which the left hand side of the equations are treated implicitly and the right hand side explicitly, then equations (6.55), (6.58) become for the course grid:

$$\begin{aligned}
\left( \frac{\Delta x_i}{\Delta t} + \Delta x_i \widetilde{\sigma}_{C_i} \right) T_{C_i}^{n+1} &= \Delta x_i \widetilde{\sigma}_{C_i} T_{C_i}^{n+1} + \frac{\Delta x_i}{\Delta t} T_{C_i}^n + u \left( T_{CV_{i-1}, \mathcal{N}_{CV}}^n - T_{CV_{i, \mathcal{N}_{CV}}}^n \right) \\
&\quad - k_{left} \left( \frac{T_{CV_{i,1}}^{n+1} - T_{CV_{i-1}, \mathcal{N}_{CV}}^{n+1}}{\Delta x_{left}} \right) \\
&\quad + k_{right} \left( \frac{T_{CV_{i+1,1}}^{n+1} - T_{CV_{i, \mathcal{N}_{CV}}}^{n+1}}{\Delta x_{right}} \right) \\
&\quad + \sum_{k=1}^{\mathcal{N}_{CV}} \Delta x_{CV_{i,k}} \sigma_{CV_{i,k}} T_{CV_{i,k}}^{n+1} \\
&\quad + \sum_{k=1}^{\mathcal{N}_{CV}} \Delta x_{CV_{i,k}} S_{CV_{i,k}}, \quad \forall i, \tag{6.85}
\end{aligned}$$

and for the sub-grid-scale:

$$\begin{aligned}
& \left( \frac{\Delta x_{i,j}}{\Delta t} + \widetilde{\sigma_{SGS_{i,j}}} \right) T_{SGS_{i,j}}^{n+1} = \Delta x_{i,j} \widetilde{\sigma_{SGS_{i,j}}} T_{SGS_{i,j}}^{n+1} + \frac{\Delta x_{i,j}}{\Delta t} T_{SGS_{i,j}}^n \\
& + u \left( T_{CV_{v(i,j),m_L^+(j)}}^n - T_{CV_{i,m_R^+(j)}}^n - T_{CV_{i,m_L^-(j)}}^n + T_{CV_{i,m_R^-(j)}}^n \right) \\
& - k_{left}^+ \left( \frac{T_{CV_{i,u^-(m_L^+(j)+1)}}^{n+1} - T_{CV_{v(i,j),m_L^+(j)}}^{n+1}}{\Delta x_{left}^+} \right) \\
& + k_{right}^+ \left( \frac{T_{CV_{i,m_R^+(j)+1}}^{n+1} - T_{CV_{i,m_R^+(j)}}^{n+1}}{\Delta x_{right}^+} \right) \\
& + k_{left}^- \left( \frac{T_{CV_{i,m_L^-(j)+1}}^{n+1} - T_{CV_{i,m_L^-(j)}}^{n+1}}{\Delta x_{left}^-} \right) \\
& - k_{right}^- \left( \frac{T_{CV_{w^-(i,m_R^-(j)+1),u^-(m_R^-(j)+1)}}^{n+1} - T_{CV_{i,m_R^-(j)}}^{n+1}}{\Delta x_{right}^-} \right) \\
& + \sum_{k=u^-(m_L^+(j)+1)}^{m_R^+(j)} \Delta x_{CV_{i,k}} \sigma_{CV_{i,k}} T_{CV_{i,k}}^{n+1} - \sum_{k=m_L^-(j)+1}^{m_R^-(j)} \Delta x_{CV_{i,k}} \sigma_{CV_{i,k}} T_{CV_{i,k}}^{n+1} \\
& + \sum_{k=u^-(m_L^+(j)+1)}^{m_R^+(j)} \Delta x_{CV_{i,k}} S_{CV_{i,k}} - \sum_{k=m_L^-(j)+1}^{m_R^-(j)} \Delta x_{CV_{i,k}} S_{CV_{i,k}}, \quad \forall i, j. \quad (6.86)
\end{aligned}$$

We now have a scheme for the sub-grid scale model of the diffusion approximation of the scalar transport equation. This demonstrates the approach can be performed for increasingly more complex PDEs and here we have many of the building blocks of Navier-stokes like PDEs. The source term being mathematically a generic function of  $T$  adds a lot of scope for

complexity or control applications, this is an area of increasing interest [133]. Higher order derivatives would follow a similar approach as the addition of the diffusion term. The addition of pseudo-absorption and move to implicit time stepping is a particularly desirable feature of numerical methods for PDEs due to the stability of the scheme being increasingly hard to guarantee as more terms are added.

## 6.3 1D Sub-Grid Scale Numerical Results

In this section we show numerical results for the Sub-Grid Scale Model derived earlier in the chapter:

1. A Full Order Model - to demonstrate the added conservation and resolution from the Sub-Grid Scale Model,
2. A Non-Intrusive Reduced Order Model (NIROM) - to show how time stepping can be just another ROM parameter as [81].

The results are based on the Sub-Grid Scale Model taking the form of the pair of equations (6.85) and (6.86) for the two respective length scales.

### Note on different control volumes

There are constraints on some of the choices regarding control volumes and wavelet levels. Recall we use:

- $\mathcal{N}_{SUPCV}$  or  $NSUP$  for the number of coarse or super-control volumes - this is indexed  $i$ ,
- $\mathcal{N}_{SUBCV}$  or  $NSUB$  for the number of fine control volumes per super-control volume - this is indexed  $j$ ,
- $\mathcal{N}_w$  or  $NW$  for the number of wavelets for each coarse grid node  $i$ .

Valid choices for  $\mathcal{N}_w$  for a sub-grid scale model obey  $\mathcal{N}_w = 2^n - 1$  for  $n \geq 1$ . With total number of nodes being:  $N_{Total} = (\mathcal{N}_w + 1)\mathcal{N}_{SUPCV}$ .

For example if a mesh is desired with 20 total nodes it could be constructed two ways:  $N_{total} = 20 = 5(3+1)$  or  $N_{total} = 20 = 10(1+1)$ , with  $\mathcal{N}_w = 3, \mathcal{N}_{SUPCV} = 5$  or  $\mathcal{N}_w = 1, \mathcal{N}_{SUPCV} = 10$ .

We can also check that a choice of  $\mathcal{N}_w = 0$  will return a model that only has coarse contributions:  $N_{total} = \mathcal{N}_{SUPCV}(0+1) = \mathcal{N}_{SUPCV}$ .

### 6.3.1 Full Order Full Order Sub-Grid Scale Numerical Results

The model is implemented with implicit time-stepping, an advection speed of  $u = 2.0$  and a small amount of diffusion  $D = 0.012$ . The domain is always the unit interval with a selection of different combinations of coarse and sub-grid scale control volumes considered. In 1D this is the same as nodes.

Fixed zero boundary conditions at the end of the domain are used. The source and absorption are not present for ease of communicating the benefits of the Sub-Grid Scale approach. Initial profile of unit step function centred at 0.2 in the domain. This is always represented with coarse control volumes only occupying a width  $\frac{1}{5}th$  of the whole unit interval shown in figure 6.3.

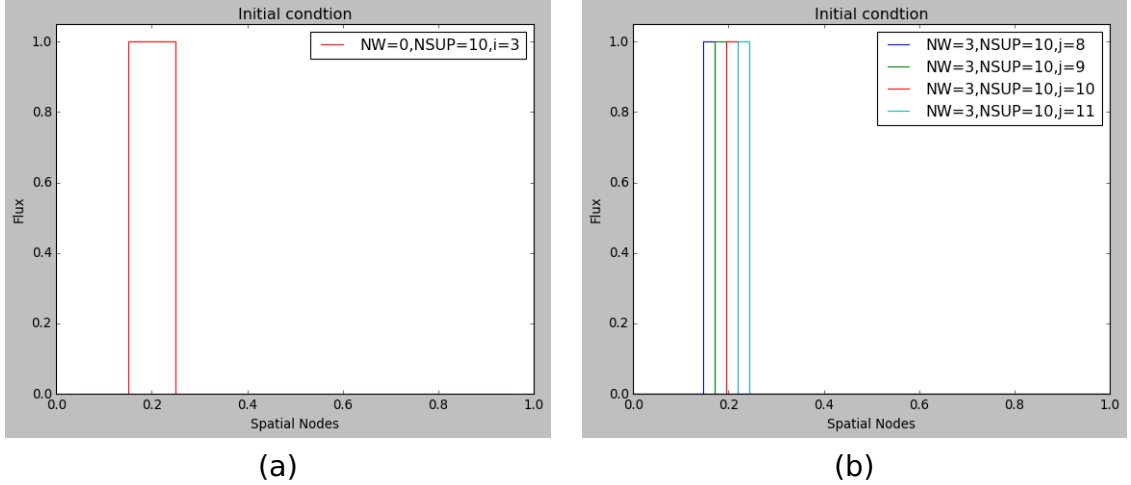


**Figure 6.3:** (a) A fully coarse representation of the initial condition (b) a possible representation using on the sub-grid scale nodes. Throughout this work the initial conditions are representation as figure (a), that is fully coarse with initial sub-grid scale corrections of zero.

Figures 6.4 and 6.5 show the power of the Sub-Grid Scale approach: an additive Sub-Grid Scale correction to a coarse numerical solution can add resolution and bring in control of conservation. In figure 6.4 (a) the solutions are with no Sub-grid scale corrections  $\mathcal{N}_w = 0$ . We have increasing total numbers of control volumes  $N_{total} = \mathcal{N}_{SUPCV} = 20, 40$  and 80 respectively. It is vital to note that this does not improve the solution as it worsens the numerical diffusion.

This is partially egregious as the majority of the diffusion is therefore a numerical artefact with  $D = 0.012$  being small and  $u = 2.0$  large we expect the advection of the wave to dominant.

With the Sub-grid scale corrections in 6.4 (b) we see a more greatly improved representation of the true diffusion. The control volumes shown in the results in (b) from lowest to highest total are:  $\{N_{total}, \mathcal{N}_w, \mathcal{N}_{SUPCV}, \mathcal{N}_{SUBCV}\}$  being,  $\{10, 1, 5, 2\}, \{40, 3, 10, 4\}, \{40, 7, 10, 4\}$ , and  $\{160, 15, 10, 16\}$  respectively. For any of these total numbers of control volumes numerical diffusion is increasingly close to being eliminated. In all cases we can see the outlet side of the domain where the wave front has not reached has a flux of zero. The crest of the wave is much larger as a result of the reduction in numerical diffusion. We can see that the increase in wavelets shows a convergence of partial sums, each correction adding to a solution that more closely obeys the conservation laws contained within the governing equations.

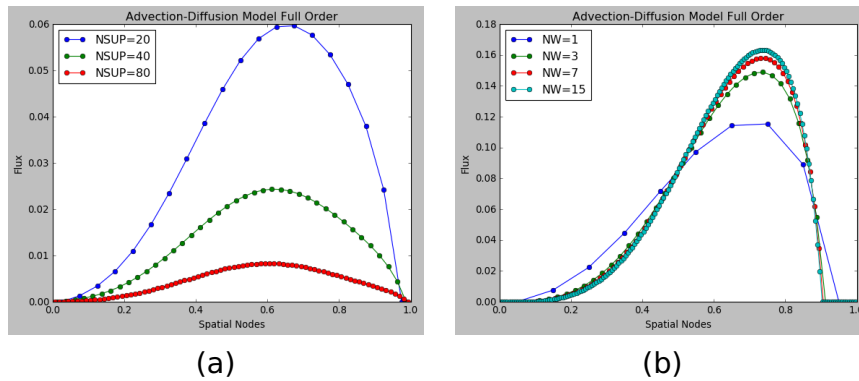


**Figure 6.4:** (a) Solutions without Sub-Grid Scale corrections and (b) with Sub-Grid Scale corrections (b). Increasing the number of wavelet levels improves the resolution of the solutions. Without the Sub-Grid Scale corrections numerical diffusion is present and distorts the solution. The solutions with more wavelet levels approach the true solution.

Figure 6.5 contrasts the two approaches with a solution of the same resolution. Here the number of wavelet levels is denoted by  $NW = 7$  gives the same number of total nodes as 80. We can see with the addition of the Sub-Grid Scale correction there is no flux in the part of the domain that the wave front has not yet reached as the desired diffusion is small. The coarse solution shows how much of a problem numerical diffusion can be as much of the shape and flux is lost.

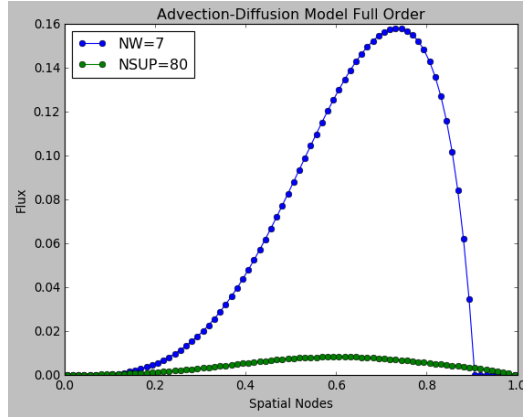


**Figure 6.5:** Coarse control volume solution with Sub-Grid Scale correction and uncorrected coarse solution with same reference. The Sub-Grid Scale corrections remove the numerical diffusion.

Figure 6.6 shows the shape of solutions with just advection and just diffusion present with true shape thank to wavelets. The zero boundary condition control volumes on the sides of the domain are clear and free of flux. The advection-diffusion equations takes the form of Fick's law of diffusion when only diffusion terms are non-zero.

We can see the exact solution for diffusion only reference in [38] taking the form:

$$f(x, t) = \frac{c}{2} \operatorname{erf}\left(\frac{a-x}{2\sqrt{dt}}\right) + \operatorname{erf}\left(\frac{b+x}{2\sqrt{dt}}\right) \quad (6.87)$$

where  $a, b, c, d$  are real number that will result from application of boundary conditions.

For advection only we have:

$$f(x, t) = F(x - ut) \quad (6.88)$$

where  $u$  is the wave speed and  $F$  is some arbitrary function from the initial and boundary conditions.



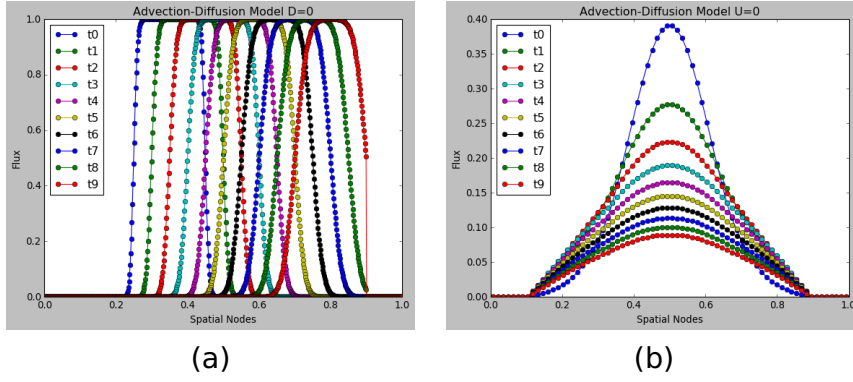


**Figure 6.6:** (a) Sub-Grid Scale solutions over a range of time steps with no diffusion  $NUSP = 10, NW = 63, U = 1.0$  and (b) Sub-Grid Scale solutions over a range of time steps with no advection  $NUSP = 9, NW = 7, D = 0.16$ .

Understanding the basic shapes of the solutions and their behaviours helps give convince in the successful implementation of the numeral scheme. If we consider the asymptotics of both only advection and only diffusion terms we see in the former, solutions full propagates out of the domain and in the latter diffuse to zero. The asymptotic expansion of the error function as a function of  $dt$  gives:

$$erf(x, t) \sim \exp\left(-\frac{x^2}{4dt}\right) \quad (6.89)$$

as shown in [134]. Thus we can expect to see a more Gaussian shape as we undergo diffusion.

We define the correlation coefficient as:

$$r(T_{ROM}, T_{FOM}) = \frac{cov(T_{ROM}, T_{FOM})}{\sigma(T_{ROM})\sigma(T_{FOM})} \quad (6.90)$$

where  $T_{ROM}$  and  $T_{FOM}$  are the solutions to the ROM and FOM respectively.  $\sigma$  is the standard deviation of the solutions and  $cov$  is the covariance defined as:

$$cov(T_{ROM}, T_{FOM}) = \mathbb{E}[(T_{ROM} - \sigma(T_{ROM}))(T_{FOM} - \sigma(T_{FOM}))] \quad (6.91)$$

with  $\mathbb{E}$  being the expected value. We will use this in the next section of results to compare the ROM with the FOM for different numbers of POD basis functions .

### 6.3.2 Reduced Order Sub-Grid Scale Numerical Results

In this section we demonstrate a single parameter NIROM trained on data from the Sub-Grid Scale model. The problem is set up similar to the last section now with  $u = 0.5$  and  $D = 0.3$ . The model now uses a total of  $N_{total} = 20$  spatial nodes with a single level of Sub-grid scale corrections,  $NW = 1$ . The NIROM is parameterized in time. As such the snapshots for the training data are taken for a selection of time steps as the solution progresses across the domain and undergoes diffusion.

Figure 6.7 shows the training data used. Here we can see that the flux initially at the origin only shows a wave-like motion and with time its peak travels across and out, through the zero boundary condition of the domain. The lengths involved and size of initial flux have been normalised to clearly present the results.

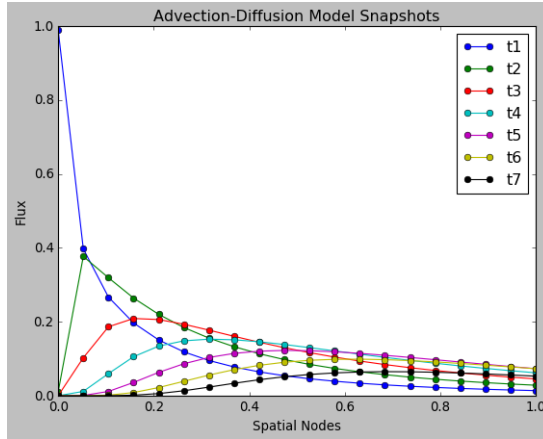


**Figure 6.7:** Snapshots of Sub-Grid Scale Advection-Diffusion equation are taken at different time steps. We can see the wave front cross the domain and under goes diffusion as the flux leaves the domain.

The NIROM is trained on 7 snapshots sampled as the solution evolves over time. This small number of snapshots still shows the NIROM approach working at any test point in the time domain. The initial flux is at the start of the domain only. With the initial condition being a single node of flux 1 and zero elsewhere, the flux initially drops very rapidly and later slows as the front progresses over the domain. The large variation in shape makes this a more challenging problem for the NIROM to handle.

**NIROM result: no pre-conditioner** We see in figures 6.8 (a) and (b) that about 10% error is achievable with only 7 snapshots. The parameter the NIROM is evaluating is the time the farthest from the training points within the training data set to further emphasis the strength of the NIROM approach. The first 3 POD basis functions were used capturing about 90% of the information with a Gaussian RBF employed of characteristic length 0.15 . If we were to used more training data we would see steeper information gain. The shape information presented by the POD basis functions gives an indication of which details are likely to be picked-up by the NIROM. We can see in figure 6.8 (d) a selection curves started with an exponential-like shape, various wave-forms taking shape and by 5 POD basis function we begin to see noise creeping in. The choice by the user can eliminate any noise with some insight as to what shape the solution is going to take verses what is noise. This model runs in seconds while the training data takes minutes to generate demonstrating with this simple problem the NIROM offers a speed-up.

Here figure 6.8 shows the results of the NIROM:

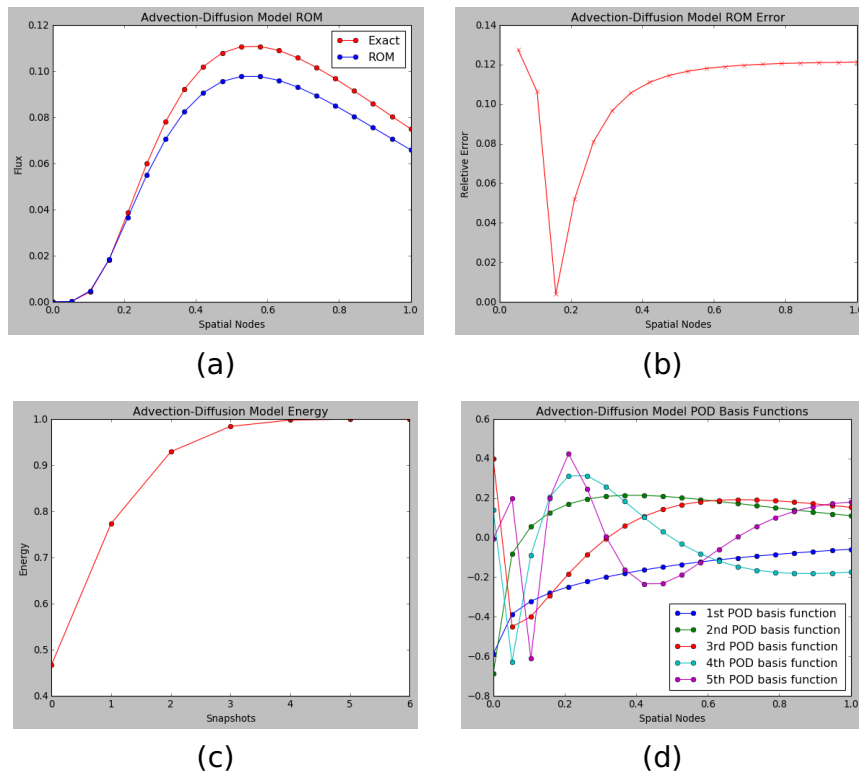


**Figure 6.8:** (a) The NIROM and exact solution, (b) the relative error, (c) the information captured by the POD basis functions and (d) the shape of the POD basis functions.

By way of convergence analysis figure 6.9 gives us the correlations between ROM and FOM solutions tested at each known time snapshot with (a) showing correlations in viable ROMs and (b) showing the correlation when not enough POD basis functions are used. When viewed in contrast with the information/energy eigenvalues in figure 6.8 (c) we can see correlation gives a more complete metric for evaluating a ROMs performance. The eigenvalues however are known from the offline stage of the ROM whereas the correlation requires multiple enquires of the online stage. Looking for the point when the shape of the POD basis functions in figure 6.8 (b) becomes noisy is the first and fastest available heuristic to build a good ROM. Taking all figures gives a more complete picture.

In figure 6.9 (b) the case using 2 POD basis functions shows a marginal choice of POD basis functions. Although starting poorly, there is some improved correlation at the later time steps, more in line with the 3 POD basis function case. When considering the training data in figure 6.7 this makes sense as there is larger variation in the earlier time steps in contrast with the later ones. This is due to the initial condition of a flux of 1 at node 0 and with values of zero elsewhere giving varied set of shapes for the POD basis function to capture.

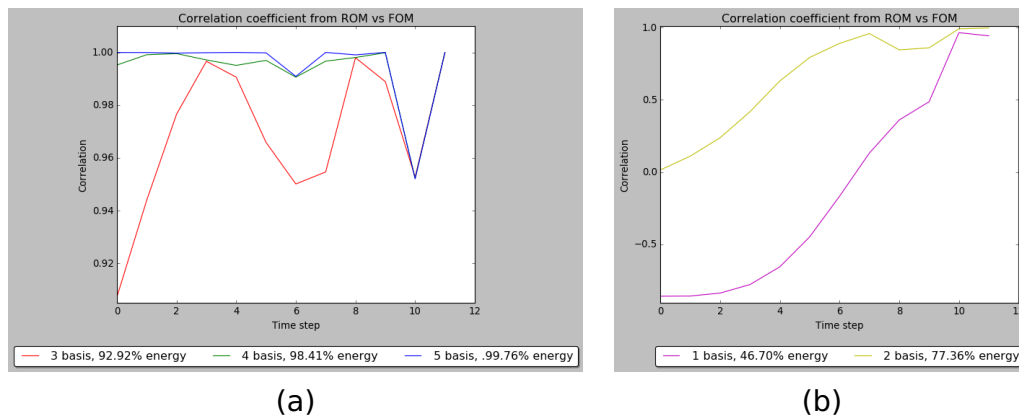


**Figure 6.9:** (a) For 3 or more POD basis functions the ROM and the FOM are strongly correlated. and in (b) the use of 2 POD basis functions shows little correlation for early time steps with vague correlation later in time. A single POD basis function performs even worse at early time, showing inverse correlation from the ROM to the FOM in some parts of the time domain.

In figure 6.10 we can compare the run times of the full order model with the Reduced Order Model. We can see the ROM offers substantial speed up. This

is still true if we were to consider the size of the time stepping. In the full order solutions a time step of  $dt = \frac{0.01}{N_{SUPCV}} = \frac{1}{1000}$  is used for stability reasons. We can see that the difference in run time between the full order and ROM is at least 4 orders of magnitude. The output of the ROM is a new solution for a single time step so even per time step the ROM offers a speed up of an order of magnitude. It is interesting to see the break down of the run times. We expect the SVD to be one of the longest stage of the ROM. We see this becoming more dominate as the degrees of freedom increase. The SVD is order  $O(m^2n + n^3)$  for an  $m$  by  $n$  input matrix. Constructing known coefficients  $\alpha_{known}$  and the ROM weights  $w_i$  both rely on matrix inversion and thus scale order  $O(n^{2.37}) - O(n^3)$ . The Radial basis kernel scales with matrix population, that is  $O(nm)$ . We expect this to be lessen as the degrees of freedom increase. Asymptotically the ROM should scale  $O(n^{2.37}) - O(n^3)$ . The full order results are constructed from a large variety of operations but likely to be dominated by matrix inversions being  $O(N^3)$  where  $N > n$ , since we are reducing the dimensionality. We have a condition that shows for all practical, stable runs is will always be faster than out full order model.

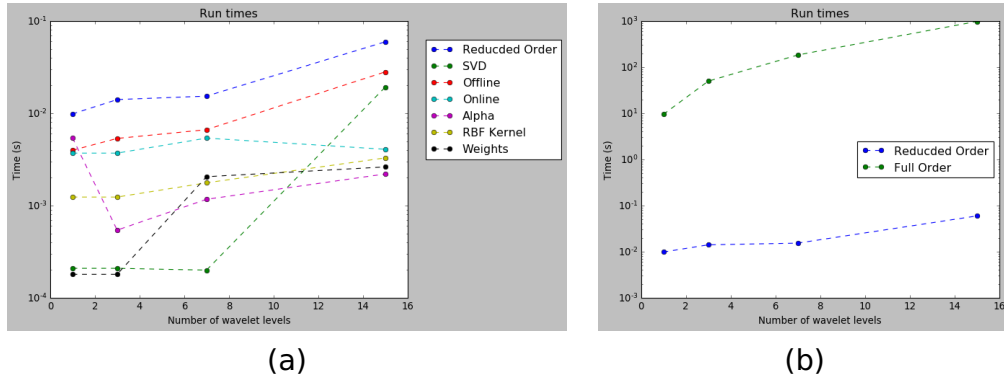


**Figure 6.10:** (a) Run times, in seconds (s), of the Reduced Order Model and its internal calculation phases, (b) The Reduced Order Model run time and the full order run time. You can see orders of magnitude of speed up.

Now we can also look at the same model as figure 6.8 but with two different pre-conditioners:

- A logarithmic pre-conditioner as done in chapters 4 and 5: taking natural logarithm of the snapshot matrix and the the exponential of the ROM solution as a pre and post-conditioning step to the NIROM.
- A deviation from the mean pre-conditioner: taking the derivation from the mean of the snapshot matrix and adding it back later for the ROM solution.

**NIROM result: logarithmic pre-conditioner** In figure 6.11 we see that, everything else being equal, a logarithmic pre-conditioner improves the ROM results substantially. The information captured by the POD basis functions is immediately higher and after the same number used as without the pre-conditioner capturing a similar 99.9% of the energy of the POD basis functions we reduce the error by an order of magnitude for much of the domain.

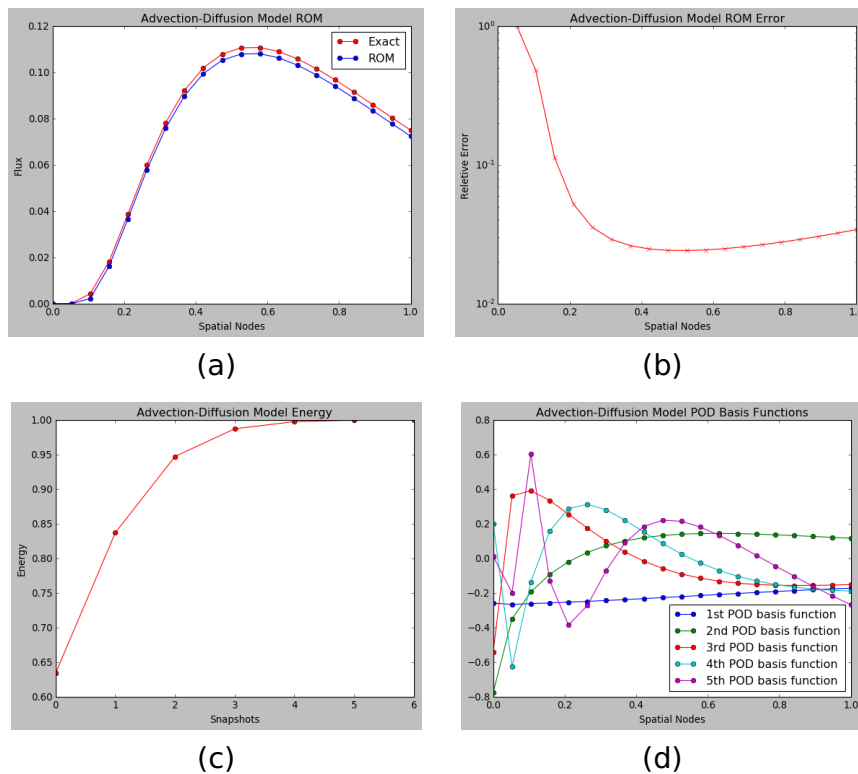


**Figure 6.11:** (a) The NIROM and exact solution, (b) the relative error, (c) the information captured by the POD basis functions and (d) the shape of the POD basis functions for a logarithmic pre-conditioner of the NIROM.

The energy captured by the PDO basis for 3 or more POD basis functions is a couple of percent improved from the case with no pre-conditioner. The correlations in figure 6.12 show a very similar pattern however a bit more variation, some time steps a little better and some worse. This might indicate that with in this case, the logarithmic pre-conditioner benefits the radial basis interpolation but has less effect on the POD basis representation than in earlier chapters.

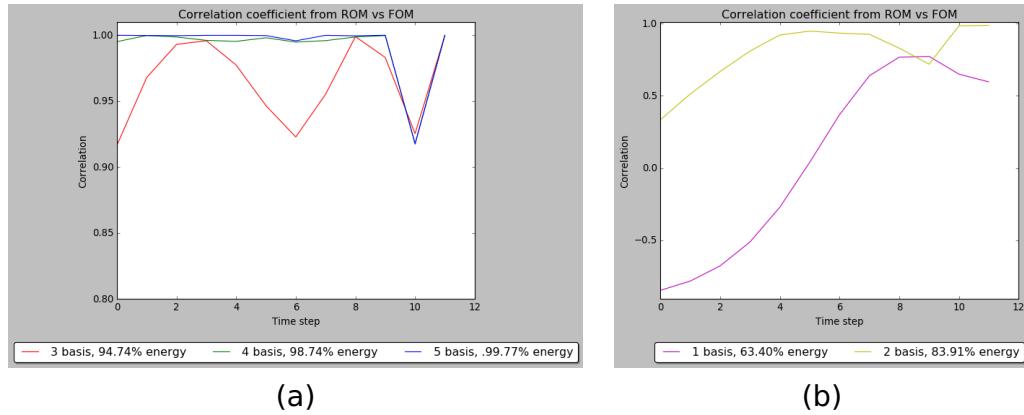


**Figure 6.12:** (a) For 3 or more POD basis functions the ROM and the FOM are strongly correlated. and in (b) the use of 2 POD basis functions shows little correlation for early time steps with vague correlation later in time. A single POD basis function performs even worse at early time, showing inverse correlation from the ROM to the FOM in some parts of the time domain. There is some slight overall improvement with the logarithmic pre-conditioner

**NIROM result: deviation from mean pre-conditioner** In figure 6.13 we see that, again with everything else being equal to the original NIROM, a deviation from the mean pre-conditioner improves the results. The nodes near the left boundary are intentionally exuded from the pre-conditioner as removing the mean should improve the feature capture of the POD basis functions however the noise around the zero values was subsequently perceived as a feature, distorting the initial few nodes. Excluding these nodes from the pre-conditioning and leaving them just as the raw snapshot values resolved this. We see comparable results to the logarithmic pre-conditioner with better results all but the very start of the domain. Using both conditioners in tandem produces similar results but no improvement over using just the deviation from the mean pre-conditioner.

In figure 6.14 we can see correlation is strong for 3 or more POD basis functions are poor for fewer. Interestingly although strong, correlation here is not as strong as the other two cases, with no pre-conditioner and with the logarithmic pre-conditioner. This is odd at face value as the results in figure 6.13 suggest this case is the lowest error. This is explained as the correlation is taken at the training points whereas the ROM results in figure 6.13 are taken at a testing point furthest from the training points.

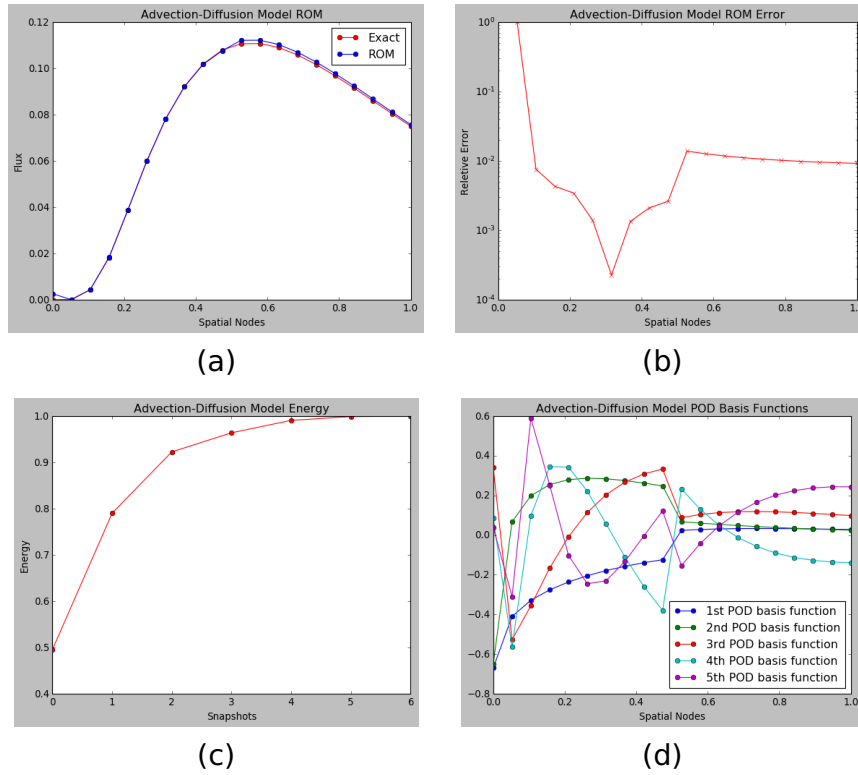


**Figure 6.13:** (a) The NIROM and exact solution, (b) the relative error, (c) the information captured by the POD basis functions and (d) the shape of the POD basis functions with a deviation from the mean as a pre-conditioner.

The speed up offered by the NIROM of this problem should not be overlooked and as we have seen adding pre-conditioners that are informed by the exact physics and shape information of the snapshot data confers significant advantages. Improved overall accuracy from the deviation from the mean pre-conditioner has the most to offer a problem with a wide range of training data as this is why popular use in intrusive ROMs is not surprising. The logarithmic pre-conditioners perform well here also and are suitable anywhere in which exponential shapes are expected in the POD basis functions. Here we have shown that the use of pre-conditioners can be an important consideration in the NIROM as well. It is interesting to note that the POD basis shapes in



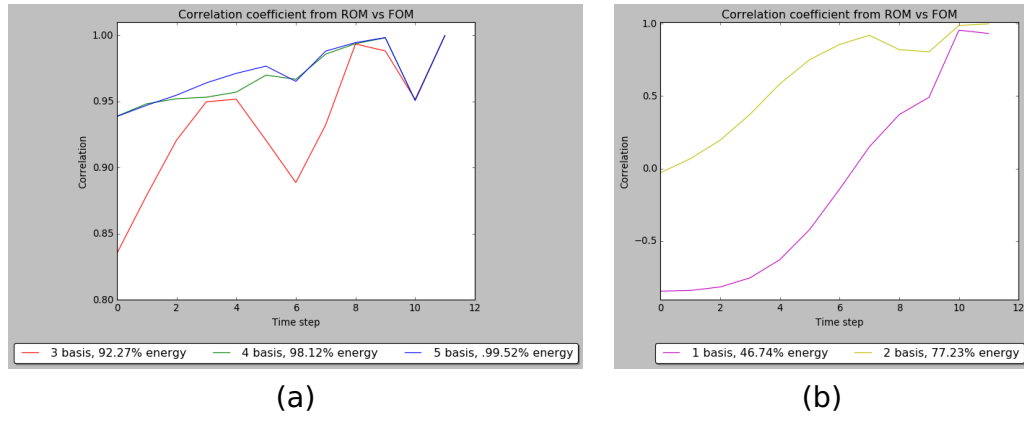


**Figure 6.14:** (a) For 3 or more POD basis functions the ROM and the FOM are strongly correlated. and in (b) the use of 2 POD basis functions shows little correlation for early time steps with vague correlation later in time. A single POD basis function performs even worse at early time, showing inverse correlation from the ROM to the FOM in some parts of the time domain.

figures are in some sense less user-friendly with the use of pre-conditioner, being not as intuitively a representation of the solutions different behaviour.

The use of the Sub-Grid Scale approach for obtaining full order ROM training data adds no additional difficulty beyond the numerical method for the full order model, itself being an additive term to existing schemes, but confers conservativeness to the ROM solutions and an increase in resolution. The Sub-Grid Scale snapshot matrix takes in the order of minutes to construct and the NIROM takes  $\frac{1}{10}$ th of a second.

In the next section we will show the slight subtlety in extending to 2D as the basis will be different, namely a cross product of the basis functions which could be extended to more dimensions or a less didactic choice of mesh. An extension to a non-uniform mesh can be done as in the appendix [135]. The paper [136] provides instruction for the adaptive mesh generation in the research code fluidity for example. Similar concepts are leveraged in [137] and applied to reduced order modelling.

## 6.4 Extension of the Sub-Grid Scale model to 2D

The easiest way to extend to 2D is to use a basis function that is a simple cross product of the basis functions. This can be done as the tensor product of Hilbert spaces forms another Hilbert space [138]. We must also cross multiply the wavelet basis functions with unity, the basis function associated with the course grid scale. This is perhaps not the best approach as it mixes wavelets in the x and y- directions that are different scales however a change of basis is always possible from an existing basis.

Through a Galerkin projection this results in:

$$T_{CV_{i1,i2,k1,k2}}^n = T_{C_{i1,i2}}^n + \sum_{l1=0}^{\mathcal{L}1} \sum_{l2=0}^{\mathcal{L}2} z_w(l1, l2) s_w(k1, l1) s_w(k2, l2) T_{SGS_{i1,i2,jw(k1,l1),jw(k2,l2)}}^n, \quad (6.92)$$

Notice we have started from 0 rather than 1 as in the 1D base. The reason for this is to introduce the cross product of the wavelet basis functions with the unity basis functions associated with the course grid scale, thus

$$s_w(k, l) = 0 \text{ if } l = 0 \quad (6.93)$$

$$\text{otherwise } s_w(k, l) = 2 \left( 2 \left\lfloor \frac{k-1}{2^{\mathcal{L}-l+1}} + 1 \right\rfloor - \left\lfloor \frac{k-1}{2^{\mathcal{L}-l}} + 1 \right\rfloor \right) - 1. \quad (6.94)$$

Also:

$$z_w(i, j) = 0 \text{ if } i = j = 0 \text{ otherwise } z_w(i, j) = 1 \quad (6.95)$$

Expanding the rhs of the discretized equation in 2D in a similar way to the way we did it for 1D in terms of CV basis functions then:

$$\begin{aligned}
T_{C_{i1,i2}}^{n+1} = T_{C_{i1,i2}}^n &+ \sum_{j2=1}^{\mathcal{N}_{2CV}} u1 \frac{\Delta t}{\Delta x1_i} (T_{CV_{i1-1,i2,\mathcal{N}_{1CV},j2}}^n - T_{CV_{i1,i2,\mathcal{N}_{1CV},j2}}^n) / \mathcal{N}_{2CV} \\
&+ \sum_{j1=1}^{\mathcal{N}_{1CV}} u2 \frac{\Delta t}{\Delta x2_i} (T_{CV_{i1,i2-1,j1,\mathcal{N}_{2CV}}}^n - T_{CV_{i1,i2,j1,\mathcal{N}_{2CV}}}^n) / \mathcal{N}_{1CV} \\
&\forall i,
\end{aligned}
\tag{6.96}$$

$$\begin{aligned}
T_{SGS_{i1,i2,j1,j2}}^{n+1} &= T_{SGS_{i1,i2,j1,j2}}^n \\
&+ \sum_{k2=\tilde{m}_L^+(j2)+1}^{m_R^-(j2)} u1 \frac{\Delta t}{\Delta x_{i1,j1}} (T_{CV_{v(i1,j1),i2,m_L^+(j1),k2}}^n - T_{CV_{i1,i2,m_R^+(j1),k2}}^n \\
&\quad - T_{CV_{i1,i2,m_L^-(j1),k2}}^n + T_{CV_{i1,i2,m_R^-(j1),k2}}^n) \\
&+ \sum_{k1=\tilde{m}_L^+(j1)+1}^{m_R^-(j1)} u2 \frac{\Delta t}{\Delta x_{i2,j2}} (T_{CV_{i1,v(i2,j2),k1,m_L^+(j2)}}^n - T_{CV_{i1,i2,k1,m_R^+(j2)}}^n \\
&\quad - T_{CV_{i1,i2,k1,m_L^-(j2)}}^n + T_{CV_{i1,i2,k1,m_R^-(j2)}}^n) \\
&\forall i, j,
\end{aligned}
\tag{6.97}$$

in which the 1 and 2 corresponds to the x- and y-coordinates for the 2D problem.

This pair of equations can form the basis of a sub-grid scale ROM for a more sophisticated range of phenomena than the advection problem in 2D. The method could be projection based as illustrated in the intrusive ROM section of this chapter or employ a NIROM approach. As with the simpler example the sub-grid scale can form a correction to other coarse models. The Sub-Grid Scale model brings in conservation automatically and increases the resolution some via an additive correction to the coarse model, conferring these properties to Reduced Order Models trained or in the intrusive case projected on these Sub-Grid Scale dynamics.

### 6.4.1 2D Full Order Sub-Grid Scale Numerical Results

The figure 6.15 shows the 2D Sub-Grid scale full order model, the 2D equivalent of figure 6.5. Here we have a prolate Gaussian shaped initial profile advected upwards across the plane with an advection speed  $u_y = 5.0, u_x = 0.0$ . There are 14 coarse control volumes used for each 1D axis giving a total of 196. A single wavelet level is used giving 4 sub-grid control volumes in each coarse volume. The size of the time stepping is  $dT = \frac{0.1}{14(1+1)} = \frac{1}{280}$ . A sample set of 7 time steps is stored to represent the time evolution.

The corrections from the Sub-Grid scale approach range in size from 12% to  $-12\%$ . The symmetry here is due to these particular plots only possessing numerical diffusion and no physical diffusion. We can see the corrections improve the results and the prolate Gaussian keeps its shape as it travels across the domain.

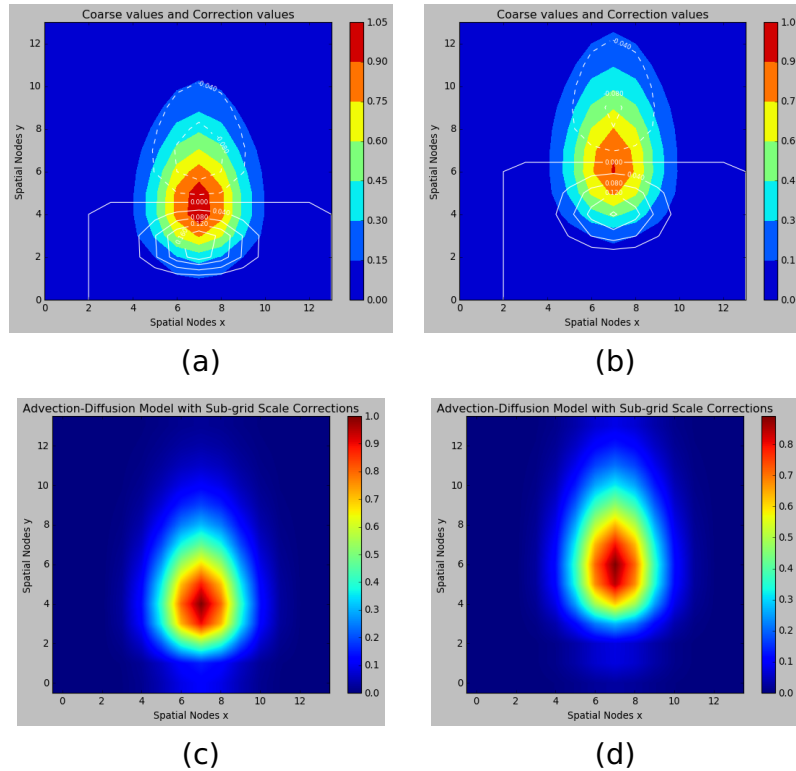


**Figure 6.15:** (a) The coarse control values in coloured contours and sub-grid scale control volumes in white inline contours at  $t_5$ , (b) the coarse control values in coloured contours and sub-grid scale control volumes in white inline contours at sampled time step  $t_8$ , (c) the coarse solution with the sub-grid scale correction at  $t_5$  (d) the coarse solution with the sub-grid scale correction at sampled time step  $t_5$ .

The figure 6.16 shows the maxima, minima and positive mean of the Sub-Grid scale corrections as time steps forward and further shows the symmetry in the problem. We can see the mean correction in the 2D case is small when compared with the 1D case 6.5. This is partly due to the much larger amount of zeros in the 2D the domain. The largest corrections are in the wake of the direction of travel.

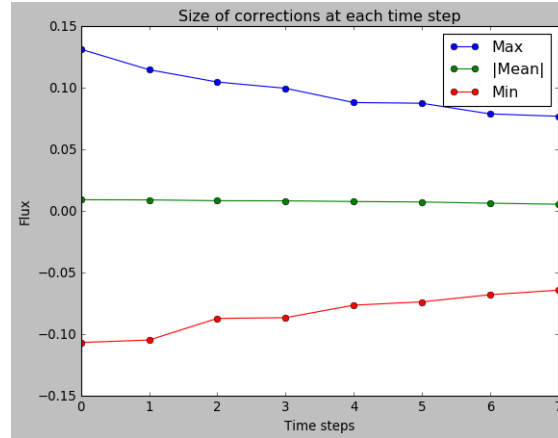


**Figure 6.16:** Size of corrections in Sub-Grid Scale as time evolves take from the 1D profile that forms the peak of the 2D solutions at 8 evenly sampled time steps.

The terms we have considered in this work, advection, diffusion and source functions, when combined can be used to enhance ROMs based on a large class of PDEs. We have also provided a framework for extending this both in terms of a 2D mesh and higher non-linear order derivative terms. The two most pressing tasks left to future work are a computational example and generalising to an unstructured mesh. Solving problem with these kinds of ROM on an adaptive mesh without an expensive re-mapping to non-adaptive reference mesh before constructing the ROM would also be a significant contribution making use of state of the art research codes such as Imperial College's Fluidity [139]. One way of using adaptive mesh techniques with NIROM could be through constructing a super-mesh [140]. Expanding the terms covered until the scheme can handle solving the Navier-Stokes equations or other systems characterised by bifurcations, instabilities and hysteresis, through Sub-Grid Scale version of [141] or likewise other prominent and hard to solve PDEs are obvious pieces of work left for the future.

## 6.4.2 2D Reduced Order Sub-Grid Scale Numerical Results

To extend the NIROM approach as used to a 2D mesh is straightforward due to the method being meshless and data driven. Analogous to the concatenation approach in chapter 5 employed to handle multiple energy groups, a concatenation of the 1D slices of a full 2D solution for each time instance become the ROM snapshots used here. The procedure goes as follows:

---

**Algorithm 6** NIROM for 2D problems - concatenated snapshots

---

- 1: 2D training data for each time step is collected in a series of matrices
  - 2: At each time step the data is then reshaped and stored in a single long vector where each 1D slice that makes up the full 2D solution is concatenated to form a non-physical snapshot for the NIROM to process
  - 3: This vector is fed through the NIROM
  - 4: During post-processing, 2D ROM solution is recovered from a ROM solution of the concatenated data.
- 

chosen so the profile can completely cross the domain,

The following results come from applying this algorithm to construct a NIROM for the Advection-diffusion problem dominated by advection,  $u = 1.0$  with no source or absorption. An initial profile of a prolate Gaussian is positioned centred in the  $x$  direction and near the boundary in  $y$  direction. Time stepping is  $dt = 0.00025$ , with a run time chosen so the profile can completely cross the domain. A total of 400 snapshots sampled evenly from this. An equal number of spatial nodes,  $NSUPCV = 40$  in each axis is used for a total of 1600 spatial degrees of freedom. The 2D Sub-Grid scale numerical scheme is taken as the FOM with a single level of sub-grid scale correction, generating the snapshots. The NIROM is parameterised to investigate new, unseen time steps.

In figure 6.17 we see that even with a challenging point for the ROM to investigate in the training space and the 2D profiles concatenated into a non-physical snapshot, strong agreement between the FOM and the NIROM is achievable. In figure 6.18 we see the shapes of the first few POD basis functions. As in the shielding NIROMS in chapter 5, the concatenation

approach still does not limit the feature recognition although the user may need more degrees of freedom to clearly distinguish feature recognition from noisy basis functions.

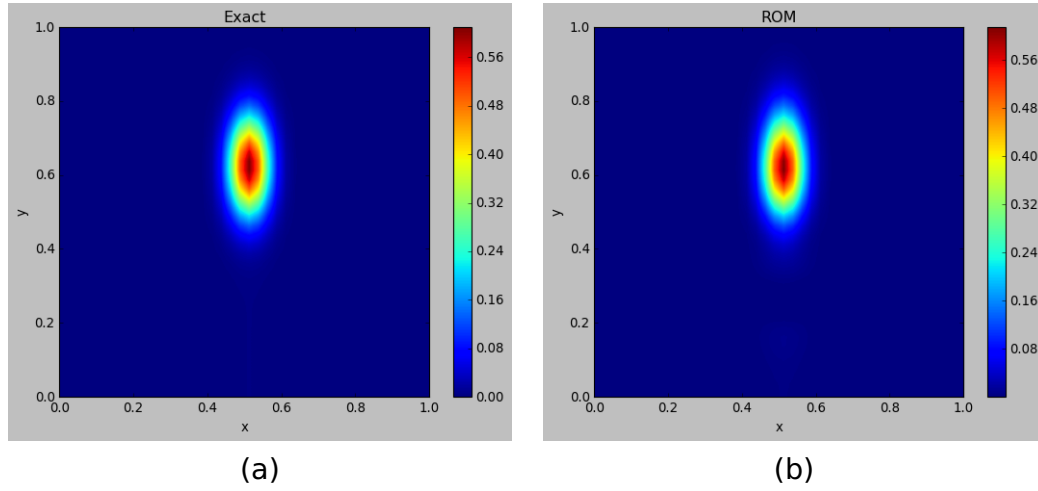


**Figure 6.17:** (a) The reduced order model solution and (b) the exact solution of a 2D Gaussian profile undergoing advection to the right. The point the ROM is investigating is an untrained point as far from the training data as possible, the mean of the 160<sup>th</sup> and 161<sup>th</sup> time step.

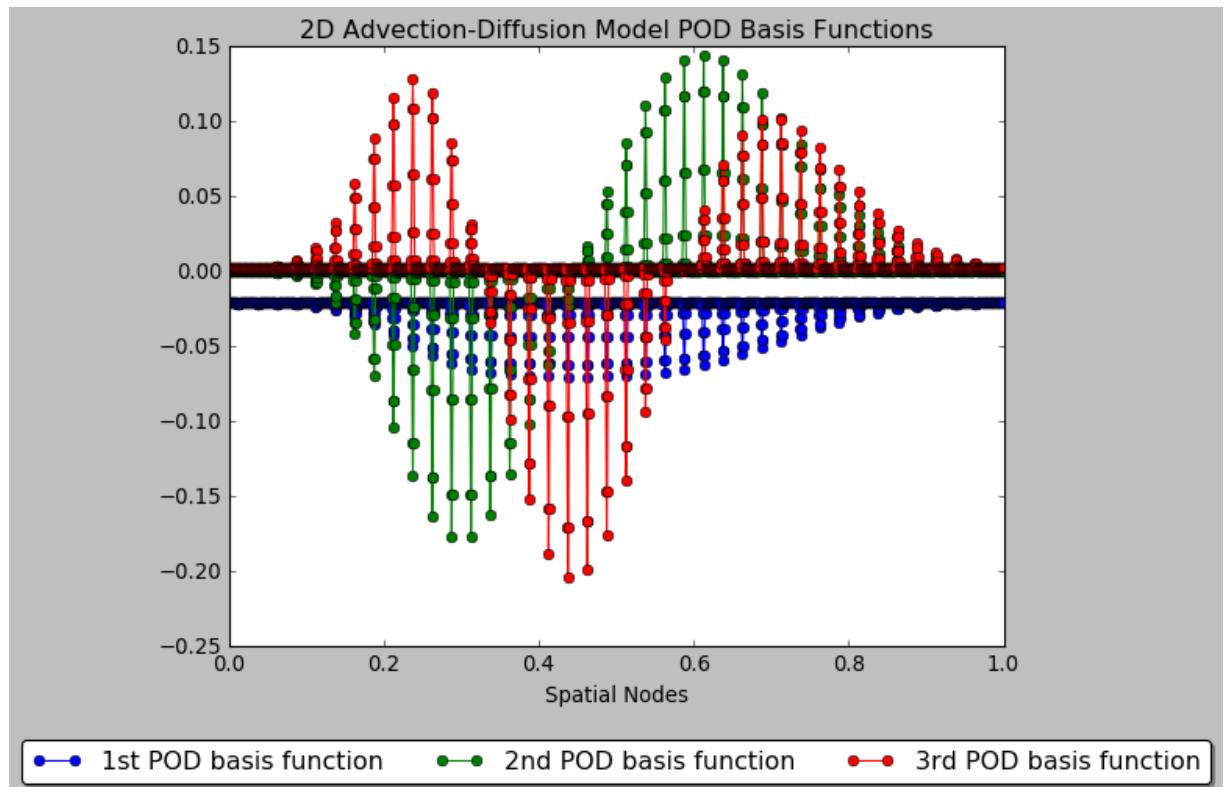


**Figure 6.18:** (The POD basis functions.

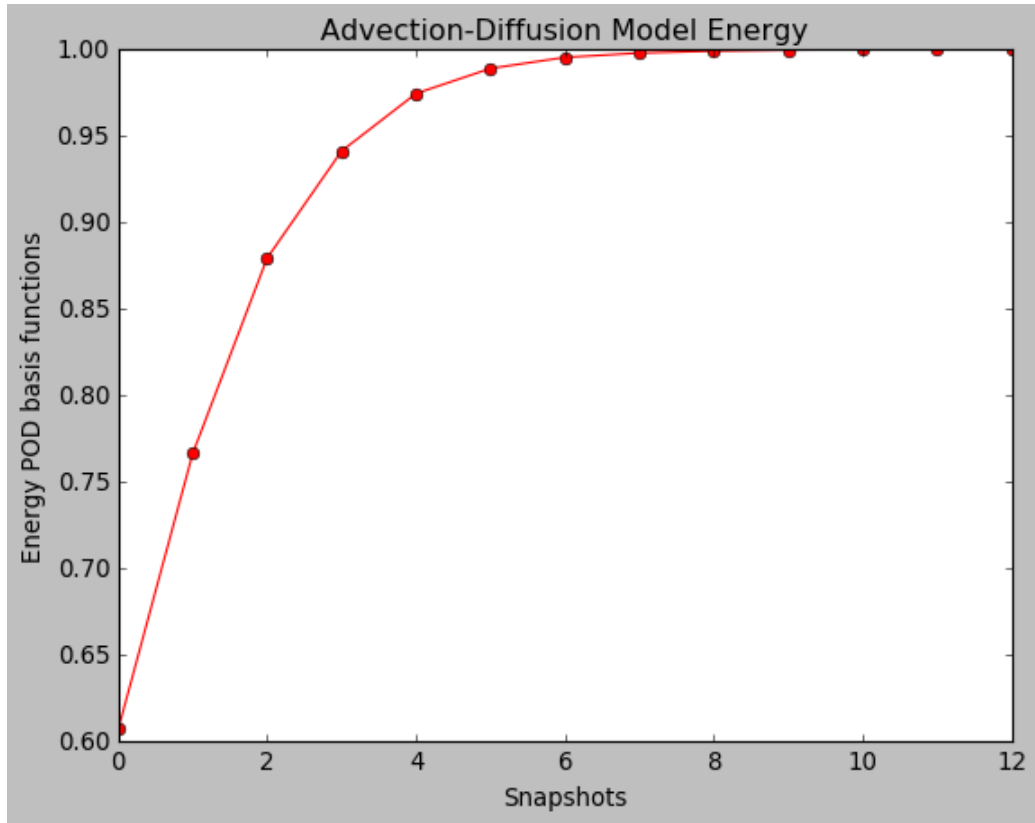


**Figure 6.19:** The energy of the POD basis functions. Only the first 13 out of a possible 100 are shown.

Figure 6.19 informs further the choice of basis functions, with 24 being used in this set of results. The choice of 24 POD basis functions is used throughout these results and gives an energy of 99.86%, capturing enough of the information to adequately represent the ROM for all points in the training space. The shape of radial basis function used is Gaussian with a characteristic length chosen to give smooth results in the centre of the training data points. Gaussian is used as the default in this thesis to keep matrices non-singular, strictly positive-definite and such that any range of smooth ROM solutions are possible between the bed-of-nails case, suitable interpolation and noise.



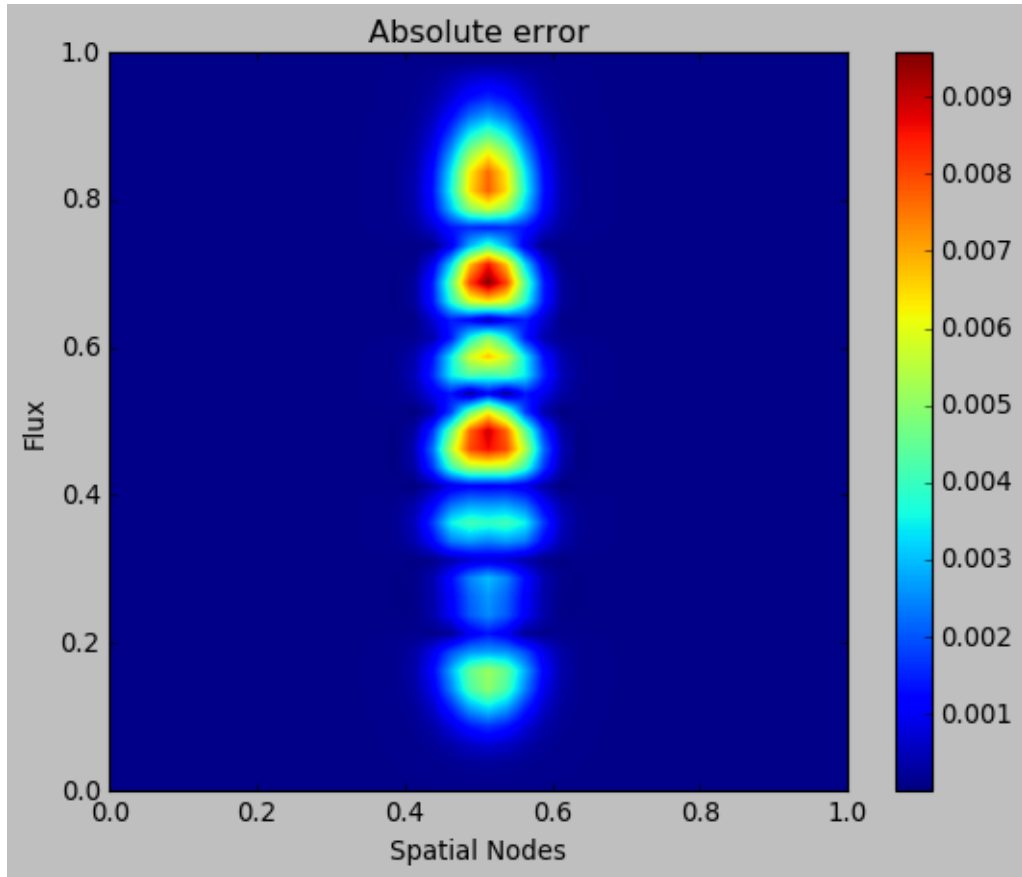


**Figure 6.20:** The error in the ROM solution compared with the exact solution. The ROM uses just 24 POD out of a possible 400.

The figures 6.20 and 6.21 show the performance of the NIROM more clearly. In absolute terms the error does not exceed 2% of the solution at this, worse case point under investigation. The RMS error shows small of variation in the NIROM result of the training time domain with the extremes at the edges due to Gibbs-like phenomena, the maximum error gives an upper bound for the model.

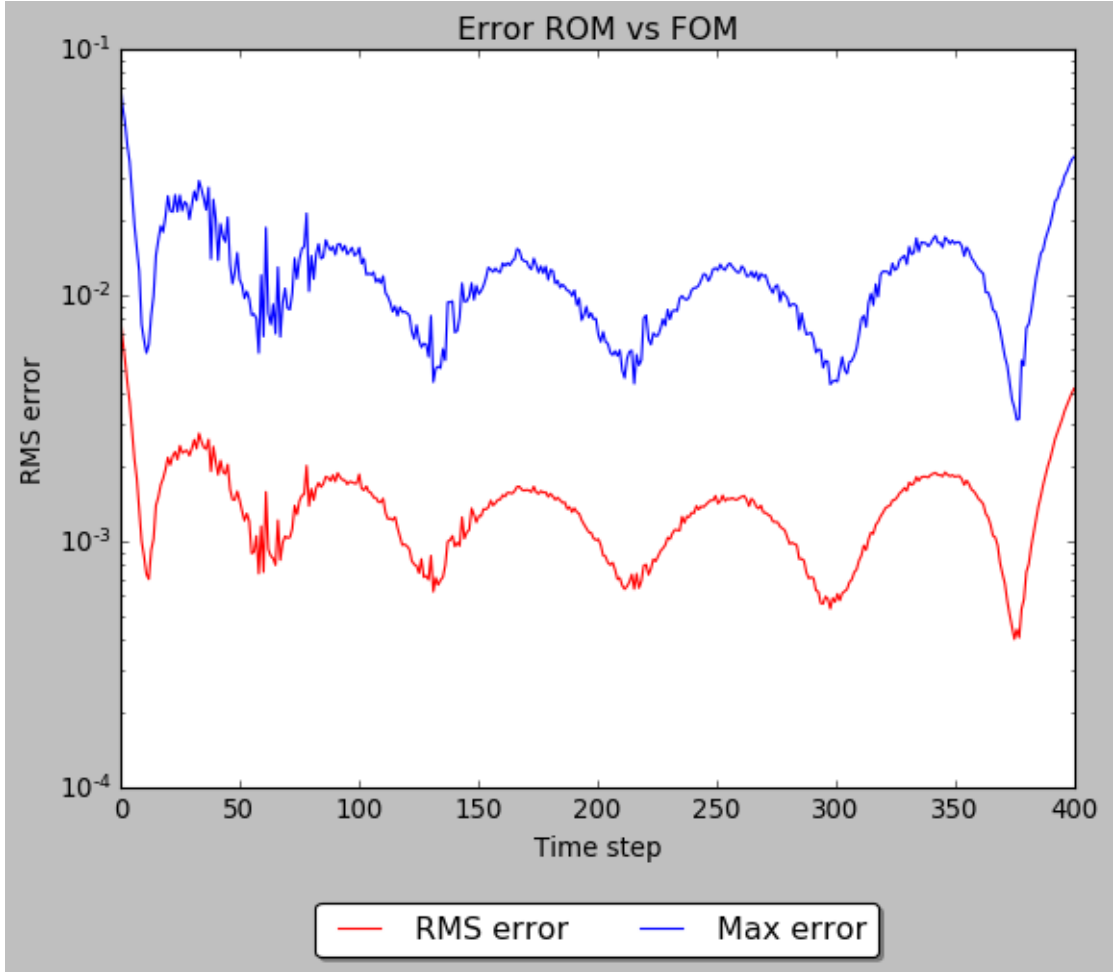


**Figure 6.21:** The RMS error of the ROM along with the maximum relative error both at each time step. The ROM uses just 24 POD out of a possible 400.

Recall we define the correlation coefficient as:

$$r(T_{ROM}, T_{FOM}) = \frac{cov(T_{ROM}, T_{FOM})}{\sigma(T_{ROM})\sigma(T_{FOM})} \quad (6.98)$$

where  $T_{ROM}$  and  $T_{FOM}$  are the solutions to the ROM and FOM respectively.  $\sigma$  is the standard deviation of the solutions and  $cov$  is the covariance defined as:

$$cov(T_{ROM}, T_{FOM}) = \mathbb{E}[(T_{ROM} - \sigma(T_{ROM}))(T_{FOM} - \sigma(T_{FOM}))] \quad (6.99)$$

with  $\mathbb{E}$  being the expected value.

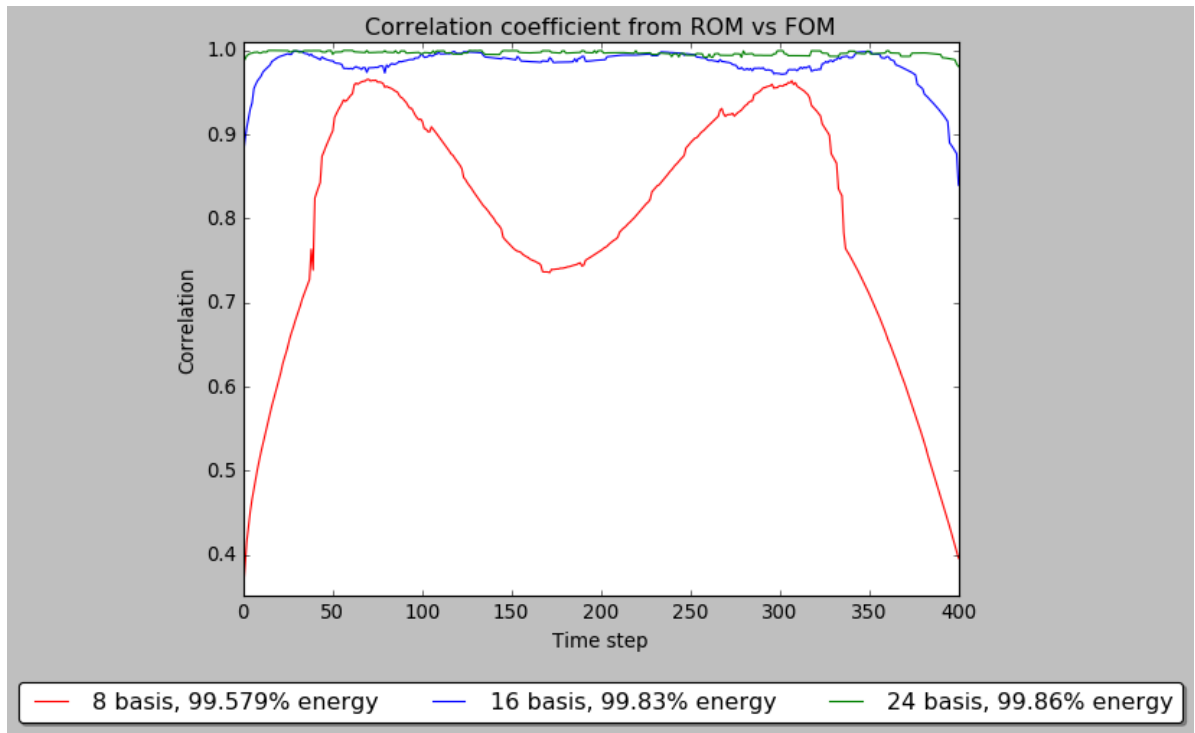


**Figure 6.22:** The value of the correlation coefficient between the ROM and FOM solutions at each time step. Convergence is demonstrated through using 8, 16 and 24 POD basis functions.

In figure 6.22 the normalised correlation between the ROM solutions and the FOM solutions shows a strong, positive correlation. This is strictly positive and close to 1.0 demonstrating a near-linear relation. The Gibbs-like phenomena are decreased significantly as more POD basis functions are used. Using 24 basis functions is only 6% of the total 400 however by this point the correlation shows little variation across the time steps. Taking further numbers of basis functions yields little further improvement.

The total run time for the FOM takes 318s, about 5mins. In terms of speed-up, table 6.1 illustrates run times and shows the big-O complexity of each part of the NIROM. The sub-grid scale NIROM offers a real speed-up, with the ROM taking 3% of the time of the FOM, while bringing in the conservative properties of the sub-grid scale model. Taking the model to 2D offers little difficulty for the NIROM due to its fundamentally meshless nature. The features picked out by the POD basis functions in 2D when trained as concatenated snapshots may eventually break down if the concatenation is pushed to its limit though this is not close to happening with the current setup. The shapes of the POD basis functions are certainly less user friendly in the 2D case so being conservative with the number of basis functions used, the amount of snapshots and the fineness of the mesh is advisable. Even with cautious choice of problem setup the speed-up is significant and the numerical diffusion is removed.

**Table 6.1:** Run times (s)

Stage	Time (s)	Asymptotics in big-O notation
ROM	6.96	$O(n^3)$
Offline	6.80	$O(n^3)$
Online	0.16	$O(n^{1.46})$
SVD	1.56	$O(m^2n + n^3)$
alpha	0.10	$O(n^{2.37}) - O(n^3)$
weights	0.02	$O(n^{2.37}) - O(n^3)$
RBF kernel	5.09	$O(nm)$

# Chapter 7

## Conclusion and Future Work

### 7.1 Conclusions

This research aimed to develop and apply new reduced order model techniques to two areas with relevance to nuclear energy: Shielding and general Advection-diffusion type problems of interest physics of nuclear reactors. In this thesis several novel approaches of the NIROM technique have been introduced and applied to the areas outlined.

In chapter 1 the key contributions are outlined, along with motivating work and a brief foray into the status of the surrounding literature. Most of the applications listed apply a fairly direct POD-Galerkin, intrusive, approach to show applicability in a wide range of fields. The short literature that follows aimed to highlight more sophisticated techniques and give an idea of the considerations a ROM practitioner must make when first approaching a new problem to model. Chapter 2 provides the basic definitions in the fields of Numerical Methods, Reduced Order Modelling, Neutron Diffusion and Transport Theory, and Shielding. Here the algorithm for the NIROM is first presented and a vigorous definition of the POD basis functions is shown along with the Radial basis function interpolation.

Then in chapter 3 the Non-intrusive Reduced Order Model (NIROM) is applied to some preliminary problems based on elementary functions approximating attenuation of flux. We show how we will use the language of convergence and error measures and shape and energy capture of the POD basis functions. Forward coupling is contrasted with using the location of an interface as a

NIROM model parameter. This detailed background of the NIROM approach some of the advantages and limitations of this type of ROM were illustrated provides motivation for the main chapters of work that follow in which two novel contributions were made.

Chapter 4 presents coupling of ROMs to solve complex problems in shielding, recovering the ASPIS benchmark for positive and negative scatter with 1-group interactions. Firstly the physics of scattering is presented to outline the physical model assumptions and provides a place from which the left-right approach scattering could be modified to get an angular framework. The coupling scheme is first introduced along with efforts to control the stability and convergence through successive over-relaxation. The exact solutions for the flux scattering in each material are intruded and coupled to confirm the shape for the ROM coupling and to help calibrate the convergence process. Only 2 POD basis functions were used in the ROM coupling, illustrating a significant reduction. The quality of the results show the accuracy is maintained while scope for CPU cost or the avoidance of a more complex series of experiments is introduced.

Chapter 5 in a similar way presents coupling of ROMs to solve complex problems in shielding, recovering the ASPIS benchmark for positive and negative scatter with 2-group interactions. We see that the coupling is simply extended as the tolerance across the interfaces is now the maximum of a set of different group tolerances. This is a promising area as a library of comparatively simple models can be confidently coupled together to solve a problem of industrial scale and relevance. The work also demonstrates the generalisation to n-group models and the training data could assimilate experimental data with ease.

In chapter 6 the derivation of a Sub-Grid Scale numerical scheme to make the NIROM approach conservative. This is done through testing a finite volume scheme over Haar wavelets and coarse indicator functions for the two scales respectively. Control over conservation laws is a desirable property when modelling a wide range of phenomena. A range of more complex phenomena

are systematically introduced up to the Advection-diffusion equation with source and absorption and a 2D version of the scheme. The full order of this scheme is presented and shows the effectiveness of this approach in controlling conservation. This is along with a NIROM of the 1D that is parameterized in time-stepping and offers very significant speed up with only 7 snapshots of training and just 3 POD basis functions used capturing over 90% of the energy. How this could be done through a POD-Galerkin based projection is also explored.

It can be concluded from these works that widespread applications of ROMs such as prototyping, product development, real-time simulation or shorter design cycles can be extended to larger problems though ROM coupling just as ROM itself may take unfeasible direct numeral simulations into the realm of possibility. Improved real-time simulation for larger problems could also improve control systems, visualisations or optimisation. A typical limitation of ROMs are that they may require more user input to setup and develop than direct numerical approaches thus applications that require multiple runs as recently alluded. This is slightly exasipated by using the techniques developed in this thesis however there are numerous settings which the extra manual set-up is worthwhile. Recall the results from the sub-grid scale model require little work to employ as they can be re-written as a small correction to well known numerical schemes. This is a significant development, yielding control over conservation laws in ROMs. Practitioners should consider that making the most out of these insights only needs a small amount of extra work in the data collection phase.

## 7.2 Future Work

The ROM coupling and control over NIROM conservativeness have been constructed and demonstrated as valid additions to the NIROM approach. Due to the scope of this thesis, there are many natural extensions of this work that have been left for a future time.

### 7.2.1 Extending training and possible applications

Natural extensions to the work presented in this thesis are generalisations to yet higher dimensions. Models with 2-group and n-group coupled shielding with 2D,3D or angular more complex spatial and group scattering physics would be partially interesting to study, building of the elementary exponential in-shield models in previous chapters 4 and 5.

The most pressing work is to sample the training of the NIROMs in a more intelligent manor and a necessary step if the methods developed in this thesis are to be applied to thermal-hydraulics or n-group shielding problems. This could be done through latin hyper-cube sampling, [142],[120]. Adaptive meshing is highly desirable. Overcoming spatial inconsistencies between the POD basis functions and spatial nodes introduced attempting to use an adaptive mesh would greatly expand the scope of what is possible [137]. Taking this approach to wider ranged of phenomena could develop a ROM model for a full reactor core. This work suggests this is possible and would be a significant achievement.

Outside of nuclear applications fields such as urban wind flow, human comfort studies and pollution models would be interesting research topics to apply the NIROM coupling and conservativeness. If paired with fluid-structure interaction, medical applications could be interesting. Addition of these techniques and optimisation of the solvers and code involved in a commercial or well used research code could lower any barriers to use and promote ROM practices.



### 7.2.2 Additional directions

Integrating other emerging techniques poses many interesting questions, warranting study. Neural networks could be introduced in a variety of ways, for example to replace or supplement the radial basis interpolation with a set of ROM coefficients learned from training on a few iterations of the conventional NIROM approach. This could lead to many different choices of architecture and domain decomposition [143]. Multigrid methods should be considered beyond what has been done here with the sub-grid scale model. The deviation of the sub-grid scale numerical scheme for the advection-diffusion equation could be applied to other PDEs of interest conferring the same benefits of conservative ROM solutions to new problems. The important question here is asking which method is best to obtain ROM coefficients for a particular problem.

The reduced space itself is also an area that could be developed. A variational auto-encoder could be used in place of POD. This would improve the accuracy of the method at the cost of ROM solutions no longer existing in a reduced linear subspace. While POD is the best linear subspace in a  $L_2$  sense, a non-linear space that maintains the most important variance with a smaller error introduced may be desirable. This has been demonstrated in [144] for similar dynamics as the diffusion approximation of the transport equation.

Assimilating experimental data and more sophisticated models into the ROM coupling approach present in this thesis could yield a cutting edge shielding tool. If the condition number of the interpolation kernel was tracked an adaptive choice of characteristic length may be possible when ROM is used in an iterative scheme.

## 7.3 Appendices

### 7.3.1 Linear Algebra

Linear algebra is a powerful, well understood tool that underlines much of mathematics. It deals with concepts such as matrices, linear transformations and many important spaces. A decent elementary text for Linear Algebra is [145], a full history is [146] and [147] is a more advanced text. It is important for a few key reasons:

- It is fundamental for most presentations of geometry, lines, planes, spaces etc...
- The problems we are interested in can make use of established tools like algebra and calculus with mathematical vigour and that comes from an axiomised system.
- Linear algebra gives you intuitive mini-spreadsheets for your equations.

The axioms and definitions in this appendix elaborates and serves a reference to many underlining concepts used in this thesis.

#### Vector space and field axioms

A vector space  $V$  is a set that is closed under finite vector addition and scalar multiplication. This is equivalent to saying linear combinations of elements of the set  $V$  are themselves elements of  $V$ . A vector space can be axiomised as follows:

For all elements  $X, Y, Z$  in  $V$  and any scalars  $a, b$  in  $F$

1. Commutativity:  $X + Y = Y + X$ .
2. Associativity of vector addition:  $(X + Y) + Z = X + (Y + Z)$ .
3. Additive identity: For all  $X$ ,  $0 + X = X + 0 = X$ .

4. Existence of additive inverse: For any  $X$ , there exists  $a - X$  such that  $X + (-X) = 0$ .
5. Associativity of scalar multiplication:  $a(bX) = (ab)X$ .
6. Distributivity of scalar sums:  $(a + b)X = aX + bX$ .
7. Distributivity of vector sums  $(X + Y) = aX + bY$ .
8. Scalar multiplication identity:  $1X = X$ .

where elements  $a, b, c$  in  $F$  obey the field axioms:

1. associativity  $(a + b) + c = a + (b + c)$   $(ab)c = a(bc)$
2. commutativity  $a + b = b + a$   $ab = ba$
3. distributivity  $a(b + c) = ab + ac$   $(a + b)c = ac + bc$
4. identity  $a + 0 = a = 0 + a$   $a \cdot 1 = a = 1 \cdot a$
5. inverses  $a + (-a) = 0 = (-a) + a$   $aa^{-1} = 1 = a^{-1}a$  if  $a \neq 0$

Elements of a field are referred to as scalars and elements of a vector space are referred to as vectors.

### Example

The complex, rational and real numbers are examples of a field. The Euclidean vectors representing physical forces are an example of a vector space.

### Vector Basis

A consequence of the axiom of choice is that every vector space has a vector basis.

The axiom of choice states: Given any collection of bins, each containing at least one object, it is possible to make a selection of exactly one object from

each bin, even if the collection is infinite.

Set theory is, informally, the study of binary relations of collections of objects. Zermelo–Fraenkel set theory with the axiom of choice is commonly used as the logical and philosophical foundation of mathematics. There are many excellent texts available on the subject.

A vector basis of a vector space  $V$  is defined as a subset  $v_1, \dots, v_n$  of vectors in  $V$  that are linearly independent and span  $V$ .

Vectors  $f_1, f_2, \dots, f_n$  that cannot be expressed in the form  $a_1 f_1 + a_2 f_2 + \dots + a_n f_n = 0$  with  $a_1, a_2, \dots$  constants which are not all zero are said to be linearly independent.

The span is the set of linear combination of all elements of the vector space ie)  $\{av_1 + bv_2 : a, b \in F\}$ .

An Orthonormal basis,  $e_i$ , is a basis on an inner product space  $V$  that has unit size and orthogonal elements.

For vectors  $x, y, z \in V$  an inner product space is a vector space with a function  $\langle \cdot, \cdot \rangle \rightarrow F$  called the inner product that satisfies:

1. Linearity in the first argument  $a\langle x, y \rangle = \langle ax, y \rangle, \langle x + y, z \rangle = \langle x, z \rangle + \langle y, z \rangle$
2. Conjugate symmetry or Hermitian symmetry  $\langle x, y \rangle = \overline{\langle y, x \rangle}$
3. Positive-definite  $\langle x, x \rangle \geq 0, x \neq 0$ .

### Hilbert–Schmidt norm and Hilbert space

The Hilbert–Schmidt norm is the norm of the bounded operator  $A$  in Hilbert space  $H$  is:

$$\|A\|_{HS}^2 = \sum_i \|Ae_i\|^2 \quad (7.1)$$

The condition for  $A$  to be bounded is that there exists some  $M$  such that for all  $x$   $\|Ax\| \leq M\|x\|$ .

A Hilbert space is an inner product space with an inner product defined in a way that lets length and angle to be measured and complete in the sense that limits behave in a way calculus can be employed. Formally a Hilbert

space is a complete metric space.

A metric space has an inner product acting as the norm  $\|x\| = \langle x, x \rangle$  such that a distance function:  $d(x, y) = \|x - y\| = \sqrt{\langle x - y, x - y \rangle}$  obeys the triangle inequality.

The triangle inequality states that:

$$d(x, z) \leq d(x, y) + d(y, z) \quad (7.2)$$

.

Completeness means that a Cauchy sequence of elements converges with respect to this norm. A Cauchy sequence has the property that given any small positive distance, all but a finite number of elements of the sequence are less than that given distance from each other. This is necessary for the limits that define calculus to be valid.

### 7.3.2 The Error function

The analytical solution to the equations that describe Fick's law of diffusion rely on a non-elementary function  $erf(x, t)$  called the Error function [134].

For real or complex value  $z$  we have that:

$$erf(z) = \frac{2}{\sqrt{\pi}} \int_0^z e^{-p^2} dp \quad (7.3)$$

Note that the variable  $z$  is contained in the limit of integration. A property of the function is that  $erf(-z) = -erf(z)$ , that is the Error function is an odd function, following from the integrand being even.

### 7.3.3 Notes on coding languages and tools

This work is made possible through fantastic open source tools such as: the languages Python and FORTRAN [148],[149], visualisation of data with matplotlib [150], matrices and arrays in numpy [151], numerical schemes from SciPy [152].

### 7.3.4 Odd and even functions

We make use of the property of odd and even functions and the integration in the sub-grid scale model chapter. Let  $f$  be some real valued function. Then for all  $x$  if:

$$f(x) - f(-x) = 0 \quad (7.4)$$

we call  $f$  and Even function and if:

$$f(x) + f(-x) = 0 \quad (7.5)$$

we call  $f$  and Odd function [153],[154]. The names come from the whether the power functions  $f(x) = x^n$  have even or odd integers  $n$ .

Form functions of the same parity, that is two odd functions for example, the sum or difference will not change the parity.

The sum different party functions, an even and odd function is neither even or odd, unless one of the functions is equal to zero over the given domain.

For differentialable, continuous functions:

- The derivative of an even function is odd.
- The derivative of an odd function is even.
- The integral of an odd function over a symmetric domain, from  $[a, -a]$ , is zero.
- The integral of an even function over a symmetric domain, from  $[a, -a]$  is double in integral of the function from  $[0, a]$

### 7.3.5 Condition number

The condition number of a problem is a measure of how much an output of a function depends on small changes to the input. A high condition number in a function is said to be ill-conditioned. This has particular relevance to

Radial basis interpolation as the choice of characteristic or shape parameter determines not only error in interpolation but the solvability. The specific constraint in the solvability of the RBF interpolation is called conditional positive definiteness:

$$\lambda \|w\|_2 \leq w^T K w \quad (7.6)$$

where  $w \in \mathbb{R}$ ,  $\lambda$  is a positive constant and  $K$  is the kernel matrix for the RBF interpolation. The equation:

$$\|K^{-1}\| \leq \lambda^{-1} \quad (7.7)$$

holds in the spectral norm, that is the norm induced by  $L - 2 \max \frac{\|Kx\|_2}{\|x\|_2}$ . There follows a kind of uncertainty relation between error and solvability proved in [155].

### 7.3.6 Intrusive reduced order models

So far the Reduced Order Models, ROMs, we have discussed derive their ROM coefficients using the Non-Intrusive Reduced Order Model, NIROM, approach in which the ROM coefficients are found using radial basis approximation. Unlike the rest of the work in this thesis the majority work with ROMs use a form of intrusive technique though data driven approaches are gaining recent traction [47]. The intrusive class of ROMs relies on projection of the dynamics of a PDE onto the POD basis functions such that the evolution of the coefficients of the POD basis function is the variable that changes instead of the problems state variables: in our advection problem  $T(t)$  is the state variable. In the paper [78] we can gain understanding of how an intrusive ROM is put together for the Navier-stokes equations with insight into handling the non-linear terms of the PDEs. The paper [55] is part of a series of papers seminal for the intrusive approach in fluid dynamics and beyond, also providing a practical procedure concisely and in the abstract that we can follow.

It is within this framework of separating the governing equations into linear and non-linear operations an intrusive ROM for the sub-grid scale numerical scheme can be constructed. The advection equation is initially chosen so that the additional considerations in projecting non-linear dynamic onto POD basis functions can be ignored. The numerical scheme derived in the sub-grid scale section can directly yield conservative ROM solutions using an intrusive ROM.

Generally a non-linear system of governing PDEs in the form:

$$\frac{dT(t)}{dt} = LT(t) + N(T(t)) \quad (7.8)$$

where some variable  $T(t)$  evolving in time  $t$  according to linear and non-linear operations  $L$  and  $N$ . PDEs will have some associated boundary conditions and initial conditions.



The intrusive ROM relies on the projection of the dynamics onto the POD basis functions. This takes the form:

$$\frac{d\alpha(t)}{dt} = \Phi_r^T L \Phi_r \alpha(t) + \Phi_r^T N(\Phi_r \alpha(t)) \quad (7.9)$$

where  $\Phi_r$  is a truncated set of POD basis functions and  $\alpha$  is the coefficients of the ROM. As with the NIROM the intrusive ROM is reconstructed from linear combinations of POD basis functions:

$$\hat{T}(t; \hat{p}) = \sum_{i=1}^r \alpha_i(\hat{p}) \Phi_i(t) \quad (7.10)$$

where  $\alpha(t)$  now arises from solving (7.9) instead of radial basis interpolations and  $\hat{p}$  is the parameterization of the governing equations. The first contribution of this chapter is thus to replace the general operators  $L$  and  $N$  with the specific ones that follow from the sub-grid scale derivation. The linearity depends on if the advection speed is a function of time or a constant and for the sake of simplicity it is assumed constant. Thus the operators are:  $N = 0$  and  $L = -u \frac{d}{dx}$  for a general advection equation and this linearity allows a strait forward projection of the POD basis functions onto the discretized sub-grid scale dynamics all be it with two intrusive ROMs coupled though the shared indexing. The POD basis functions therefore could be formed hierarchically or as two distinct snapshot matrices.

The projection in the case where just a single POD basis functions is enough too capture the dynamics for our advection equation problem would take the form:

$$\frac{d\alpha(t)}{dt} + u\alpha(t) \frac{d\Phi(x)}{dx} = 0 \quad (7.11)$$

as the inner product  $\langle \Phi, \Phi \rangle = 1$  when one POD basis function is used. This equation for the ROM coefficients comes from substituting the reconstructed form of the solutions (7.10), and then taking the inner product of the equation with respect to the POD basis functions. For a truncated series of POD basis functions we would have

$$\frac{d\alpha(t)}{dt} + u\Phi_r^T \left( \frac{d\Phi_1(x)}{dx}, \frac{d\Phi_2(x)}{dx}, \dots, \frac{d\Phi_r(x)}{dx} \right) \alpha(t) = 0 \quad (7.12)$$

In the intrusive approach the terms  $G = \Phi_r^T \left( \frac{d\Phi_1(x)}{dx}, \frac{d\Phi_2(x)}{dx}, \dots, \frac{d\Phi_r(x)}{dx} \right)$  can be pre-computed in an offline stage before solving the new PDE for  $\alpha$ . The online stage would solve new PDE for  $\alpha$  for some parameter not included in the training data: this could be yet untrained time steps or different values of  $u$  than in the training data. Unlike this NIROM this requires solving a new PDE for each new what-if analysis with a new parameter. The equation (7.12) can be solving with the numerical scheme derived in this chapter encapsulated by the discretized equations (6.46) with the operator  $L$  acting on  $\alpha$ . We have

$$\alpha_{C_i}^{n+1} = \alpha_{C_i}^n + uG \frac{\Delta t}{\Delta x_i} (\alpha_{CV_{i-1}, \mathcal{N}_{CV}}^n - \alpha_{CV_{i, \mathcal{N}_{CV}}}^n) \quad (7.13)$$

for the coarse scale and the sub-grid scale takes a similar form and are subject to initial conditions

$$\alpha_{C_i}(t = 0) = (T(t = 0), \Phi_{C_i}). \quad (7.14)$$

This is now everything needed to obtain the ROM intrusively using the coefficients from 7.13 and the combination 7.10. Recall that the addition of nonlinear dynamics can extend the cost of calculation inner products. In the initial review of the relevant literature techniques such as DEIM are referenced are solutions to this problem.

It may be desirable to precondition the snapshots matrix in some way. For example taking the deviation from the mean of the snapshots modifies the snapshot matrix as follows

$$\tilde{\mathbb{X}} = \mathbb{X} - \bar{\mathbb{X}} \quad (7.15)$$

A correction of  $+\bar{T}$ , the mean of variable  $T$  to the linear combination 7.10 is then needed along with a modified initial condition  $\alpha_{C_i}(t = 0) = (T(t = 0 - \bar{T}), \tilde{\Phi}_{C_i})$ . This modification may help the POD basis functions pick out more features in the data and is partially suited to snapshots in an ensemble that cover multiple variables.

This method of projection had been chosen for illustration and in general is not always the most desirable approach. The paper [156] contrasts Galerkin non-linear ROMs with least-squares Petrov–Galerkin non-linear ROMs and gives the theoretical background. Broadly we have that, Galerkin is continuous-time optimal in that the PDE has a continuous residual that is the best in a  $l_2$ -norm sense and Petrov–Galerkin discrete-optimal being discrete-optimal. Ease of use is a key consideration and many choices in the field of ROMs are strongly problem-dependent.

With this framework for constructing intrusive ROMs we can get ROM solutions that are both detailed and conservative in nature.

# Bibliography

- [1] D. Xiao, *Non-intrusive reduced order models and their applications*. PhD thesis, 02 2016.
- [2] Georg-Johann. <https://creativecommons.org/licenses/by-sa/3.0>. CC BY-SA 3.0 via Wikimedia Commons, Accessed: June 2021.
- [3] oec nea, "Sinbad abstract nea-1517/95 winfrith iron 88 benchmark (aspis)." <https://www.oecd-neo.org/science/wprs/shielding/sinbad/as88-abs.htm>, 1997. Accessed:2021-06-09.
- [4] D. L. Broder, A. P. Kondrashov, A. A. Kutuzov, V. A. Naumov, Y. A. Sergeev, and A. V. Turusov, "The use of multigroup methods in biological shielding calculations," *The Soviet Journal of Atomic Energy*, vol. 12, pp. 139–150, Aug 1962.
- [5] B. Lindley, J. Hosking, P. Smith, D. Powney, B. Tollit, T. Newton, R. Perry, T. Ware, and P. Smith, "Current status of the reactor physics code wims and recent developments," *Annals of Nuclear Energy*, vol. 102, pp. 148–157, 04 2017.
- [6] A. D. Fokker, "Fokker, A.D.: Die mittlere Energie rotierender elektrischer Dipole im Strahlungsfeld. Ann. Physik 43, 810-820," Mar. 2006.
- [7] D. A. der Wissenschaften zu Berlin., *Sitzungsberichte der Königlich Preussischen Akademie der Wissenschaften zu Berlin.*, vol. Jan-Mai 1882. Berlin :Deutsche Akademie der Wissenschaften zu Berlin,, 1882. <https://www.biodiversitylibrary.org/bibliography/42231>.
- [8] F. Black and M. Scholes, "The pricing of options and corporate liabilities,"

*Journal of Political Economy*, vol. 81, no. 3, pp. 637–654, 1973.

- [9] L. D. Landau and E. M. Lifshits, *Fluid Mechanics*. Course of Theoretical Physics, London, England: Pergamon Press, 2 ed., 1969.
- [10] Y. Cao, J. Zhu, Z. Luo, and I. Navon, “Reduced-order modeling of the upper tropical pacific ocean model using proper orthogonal decomposition,” *Computers Mathematics with Applications*, vol. 52, no. 8, pp. 1373 – 1386, 2006. Variational Data Assimilation and Optimal Control.
- [11] IEA, “Nuclear power, ie, paris.” <https://www.iea.org/reports/nuclear-power>. Accessed:2021-06-17.
- [12] A. Cho, “The little reactors that could,” *Science*, vol. 363, no. 6429, pp. 806–809, 2019.
- [13] A. Buchan, A. Calloo, M. Goffin, S. Dargaville, F. Fang, C. Pain, and I. Navon, “A pod reduced order model for resolving angular direction in neutron/photon transport problems,” *Journal of Computational Physics*, vol. 296, pp. 138 – 157, 2015.
- [14] M. L. Adams, “Reactor analysis methods. 6. angular dependence of the fast flux in reactor lattices,” *Transactions of the American Nuclear Society*, vol. 84, pp. 212–214, 2001.
- [15] L. Soucasse, A. G. Buchan, S. Dargaville, and C. C. Pain, “An angular reduced order model for radiative transfer in non grey media,” *Journal of Quantitative Spectroscopy and Radiative Transfer*, vol. 229, pp. 23–32, 2019.
- [16] A. Buchan, S. Jewer, and I. Navon, “A reduced order model for the fast predictions of reactivity and neutron distributions within reactor cores,” *International Conference on Computational Experimental Engineering and Sciences*, vol. 22, pp. 179–179, 01 2019.

- [17] A. Sartori, A. Cammi, L. Luzzi, and G. Rozza, "A multi-physics reduced order model for the analysis of lead fast reactor single channel," *Annals of Nuclear Energy*, vol. 87, pp. 198 – 208, 2016.
- [18] A. Manzoni, F. Salmoiraghi, and L. Heltai, "Reduced basis isogeometric methods (rb-iga) for the real-time simulation of potential flows about parametrized naca airfoils," *Computer Methods in Applied Mechanics and Engineering*, vol. 284, pp. 1147 – 1180, 2015. Isogeometric Analysis Special Issue.
- [19] J. A. Burns and B. B. King, "A reduced basis approach to the design of low-order feedback controllers for nonlinear continuous systems," *Journal of Vibration and Control*, vol. 4, no. 3, pp. 297–323, 1998.
- [20] P. Benner, R. Herzog, N. Lang, I. Riedel, and J. Saak, "Comparison of model order reduction methods for optimal sensor placement for thermo-elastic models," *Engineering Optimization*, vol. 0, no. 0, pp. 1–19, 2018.
- [21] P. Rosenzweig, A. Kater, and T. Meurer, "Model predictive control of piezo-actuated structures using reduced order models," *Control Engineering Practice*, vol. 80, pp. 83 – 93, 2018.
- [22] R. Filomeno Coelho, P. Breitenkopf, and C. Knopf-Lenoir, "Model reduction for multidisciplinary optimization - application to a 2D wing," *Structural and Multidisciplinary Optimization*, vol. 37, pp. 29–48, Dec. 2008.
- [23] C. Szczyglowski, C. Howcroft, S. Neild, B. Titurus, J. Jiang, J. Cooper, and E. Coetzee, "Strut-braced wing modelling with a reduced order beam model," in *5th Aircraft Structural Design Conference*, (United Kingdom), Royal Aeronautical Society, Oct. 2016. 5th Aircraft Structural Design Conference ; Conference date: 04-10-2016 Through 06-10-2016.
- [24] O. San and J. Borggaard, "Principal interval decomposition framework for pod reduced-order modeling of convective boussinesq flows,"

- [25] O. San and J. Borggaard, "Basis selection and closure for pod models of convection dominated boussinesq flows," 07 2014.
- [26] F. Fang, C. C. Pain, I. M. Navon, M. D. Piggott, G. J. Gorman, P. A. Allison, and A. J. H. Goddard, "Reduced-order modelling of an adaptive mesh ocean model," *International Journal for Numerical Methods in Fluids*, vol. 59, no. 8, pp. 827–851, 2009.
- [27] N. Ardjmandpour, C. Pain, F. Fang, A. Buchan, J. Singer, M. Player, X. Xu, I. Navon, and J. Carter, "Reduced order borehole induction modelling," *International Journal of Computational Fluid Dynamics*, vol. 28, no. 3-4, pp. 140–157, 2014.
- [28] M. Esmaeili, M. Ahmadi, and A. Kazemi, "A generalized deim technique for model order reduction of porous media simulations in reservoir optimizations," *Journal of Computational Physics*, vol. 422, p. 109769, 2020.
- [29] Z. Alghareeb, "Optimal reservoir management using adaptive reduced-order models," 07 2015.
- [30] J. Chen, Y. Li, and X. Hu, "A two-grid method for the phase-field model of photonic band gap optimization," *Computers Mathematics with Applications*, vol. 96, pp. 44–54, 2021.
- [31] E. Shlizerman, E. Ding, M. Williams, and J. Kutz, "The proper orthogonal decomposition for dimensionality reduction in mode-locked lasers and optical systems," *International Journal of Optics*, vol. 2012, 05 2012.
- [32] M.-C. Cheng, "Quantum element method for quantum eigenvalue problems derived from projection-based model order reduction," *AIP Advances*, vol. 10, no. 11, p. 115305, 2020.

- [33] S. Singh, A. Bazaz, and S. Nahvi, "Reduced order modeling of large power grid model with pod-deim," *Journal of Physics: Conference Series*, vol. 1478, p. 012003, 04 2020.
- [34] A. Thakallapelli, S. Ghosh, and S. Kamalasadan, "Sensorless real-time reduced order model-based adaptive maximum power tracking pitch controller for grid connected wind turbines," *Electric Power Systems Research*, vol. 194, p. 107115, 2021.
- [35] F. Fang, T. Zhang, D. Pavlidis, C. Pain, A. Buchan, and I. Navon, "Reduced order modelling of an unstructured mesh air pollution model and application in 2d/3d urban street canyons," *Atmospheric Environment*, vol. 96, pp. 96–106, 2014.
- [36] D. Xiao, F. Fang, J. Zheng, C. Pain, and I. Navon, "Machine learning-based rapid response tools for regional air pollution modelling," *Atmospheric Environment*, vol. 199, pp. 463–473, 2019.
- [37] G. H. Chang and Y. Modarres-Sadeghi, "A reduced order model for fluid-structure interaction of thin shell structures conveying fluid for physiological applications," in *APS Division of Fluid Dynamics Meeting Abstracts*, APS Meeting Abstracts, p. A24.007, Nov. 2015.
- [38] C. M. Colciago and S. Deparis, "Reduced order models for fluid-structure interaction problems with applications in haemodynamics," 2018.
- [39] E. Noether, "Invariant variation problems," *Transport Theory and Statistical Physics*, vol. 1, pp. 186–207, Jan. 1971.
- [40] D. Xiao, F. Fang, C. Pain, and I. Navon, "A parameterized non-intrusive reduced order model and error analysis for general time-dependent nonlinear partial differential equations and its applications," *Computer Methods in Applied Mechanics and Engineering*, vol. 317, pp. 868 – 889, 2017.



- [41] U. Baur, P. Benner, and L. Feng, "Model order reduction for linear and nonlinear systems: A system-theoretic perspective," *Archives of Computational Methods in Engineering*, vol. 21, pp. 331–358, 2014.
- [42] W. Schilders, *Introduction to Model Order Reduction*, pp. 3–32. Berlin, Heidelberg: Springer Berlin Heidelberg, 2008.
- [43] P. Benner, S. Gugercin, and K. Willcox, "A survey of projection-based model reduction methods for parametric dynamical systems," *SIAM review*, vol. 57, no. 4, pp. 483–531, 2015.
- [44] C. Prud'homme, D. V. Rovas, K. Veroy, L. Machiels, Y. Maday, A. T. Patera, and G. Turinici, "Reliable real-time solution of parametrized partial differential equations: Reduced-basis output bound methods," *Journal of Fluids Engineering-transactions of The Asme*, vol. 124, pp. 70–80, 2002.
- [45] G. Rozza, D. B. P. Huynh, and A. T. Patera, "Reduced basis approximation and a posteriori error estimation for affinely parametrized elliptic coercive partial differential equations," *Archives of Computational Methods in Engineering*, vol. 15, pp. 229–275, 2007.
- [46] K. Veroy, "Reduced-basis methods applied to problems in elasticity : analysis and applications," 2003.
- [47] P. Wu, J. Sun, X. Chang, W. Zhang, R. Arcucci, Y. Guo, and C. C. Pain, "Data-driven reduced order model with temporal convolutional neural network," *Computer Methods in Applied Mechanics and Engineering*, vol. 360, p. 112766, Mar. 2020.
- [48] M. Barrault, Y. Maday, N. C. Nguyen, and A. T. Patera, "An 'empirical interpolation' method: application to efficient reduced-basis discretization of partial differential equations," *Comptes Rendus Mathematique*, vol. 339, no. 9, pp. 667–672, 2004.

- [49] F. Fang, C. Pain, I. Navon, M. Piggott, G. Gorman, P. Allison, and A. Goddard, "Reduced-order modelling of an adaptive mesh ocean model," *International journal for numerical methods in fluids*, vol. 59, no. 8, pp. 827–851, 2009.
- [50] S. L. Brunton and J. N. Kutz, *Data-Driven Science and Engineering: Machine Learning, Dynamical Systems, and Control*. Cambridge University Press, 2019.
- [51] J. Hesthaven, G. Rozza, and B. Stamm, *Certified Reduced Basis Methods for Parametrized Partial Differential Equations*. 01 2016.
- [52] A. Patera and G. Rozza, "Reduced basis approximation and a posteriori error estimation for parametrized partial differential equations," 09 2010.
- [53] L. Sirovich, "Turbulence and the dynamics of coherent structures. i. coherent structures," *Quarterly of Applied Mathematics*, vol. 45, pp. 561–571, 1987.
- [54] L. Sirovich, "Turbulence and the dynamics of coherent structures. ii. symmetries and transformations," *Quarterly of Applied Mathematics*, vol. 45, pp. 573–582, 1987.
- [55] L. Sirovich, "Turbulence and the dynamics of coherent structures. iii. dynamics and scaling," *Quarterly of Applied Mathematics*, vol. 45, pp. 583–590, 1987.
- [56] K. Fukunaga, *Introduction to statistical pattern recognition*. Elsevier, 2013.
- [57] I. T. Jolliffe and J. Cadima, "Principal component analysis: a review and recent developments," *Philosophical Transactions of the Royal Society A: Mathematical, Physical and Engineering Sciences*, vol. 374, no. 2065, p. 20150202, 2016.

- [58] D. Crommelin and A. Majda, "Strategies for model reduction: Comparing different optimal bases," *Journal of the Atmospheric Sciences*, vol. 61, no. 17, pp. 2206–2217, 2004.
- [59] G. Golub and W. Kahan, "Calculating the singular values and pseudo-inverse of a matrix," *Journal of the Society for Industrial and Applied Mathematics: Series B, Numerical Analysis*, vol. 2, no. 2, pp. 205–224, 1965.
- [60] R. Ștefănescu, A. Sandu, and I. Navon, "Pod/deim reduced-order strategies for efficient four dimensional variational data assimilation," *Journal of Computational Physics*, vol. 295, pp. 569 – 595, 2015.
- [61] M. Schlegel and B. R. Noack, "On long-term boundedness of galerkin models," *Journal of Fluid Mechanics*, vol. 765, p. 325–352, 2015.
- [62] N. C. Nguyen and J. Peraire, "An efficient reduced-order modeling approach for non-linear parametrized partial differential equations," *International Journal for Numerical Methods in Engineering*, vol. 76, no. 1, pp. 27–55, 2008.
- [63] J. K. White et al., *A trajectory piecewise-linear approach to model order reduction of nonlinear dynamical systems*. PhD thesis, Massachusetts Institute of Technology, 2003.
- [64] L. P. Franca and S. L. Frey, "Stabilized finite element methods: II. the incompressible navier-stokes equations," *Computer Methods in Applied Mechanics and Engineering*, vol. 99, no. 2, pp. 209 – 233, 1992.
- [65] F. Fang, C. Pain, I. Navon, A. Elsheikh, J. Du, and D. Xiao, "Non-linear petrov–galerkin methods for reduced order hyperbolic equations and discontinuous finite element methods," *Journal of Computational Physics*, vol. 234, pp. 540 – 559, 2013.
- [66] D. Xiao, F. Fang, J. Du, C. C. Pain, I. M. Navon, A. G. Buchan,

- A. H. ElSheikh, and G. Hu, "Non-linear Petrov-Galerkin methods for reduced order modelling of the Navier-Stokes equations using a mixed finite element pair," *Computer Methods in Applied Mechanics and Engineering*, vol. 255, pp. 147–157, Mar. 2013.
- [67] O. San and T. Iliescu, "A stabilized proper orthogonal decomposition reduced-order model for large scale quasigeostrophic ocean circulation," *Advances in Computational Mathematics*, vol. 41, pp. 1289–1319, 2015.
- [68] A. HAY, J. T. BORGGGAARD, and D. PELLETIER, "Local improvements to reduced-order models using sensitivity analysis of the proper orthogonal decomposition," *Journal of Fluid Mechanics*, vol. 629, p. 41–72, 2009.
- [69] S. Sirisup and G. Karniadakis, "A spectral viscosity method for correcting the long-term behavior of pod models," *Journal of Computational Physics*, vol. 194, no. 1, pp. 92–116, 2004.
- [70] A. Cammilleri, F. Guéniat, J. Carlier, L. R. Pastur, E. Mémin, F. Lusseyran, and G. Artana, "POD-Spectral Decomposition for Fluid Flow Analysis and Model Reduction," *Theoretical and Computational Fluid Dynamics*, vol. 27, pp. 787–815, Feb. 2013.
- [71] B. Bond and L. Daniel, "Guaranteed stable projection-based model reduction for indefinite and unstable linear systems," pp. 728–735, 11 2008.
- [72] F. Sabetghadam and A. Jafarpour, "regularization of the pod-galerkin dynamical systems of the kuramoto–sivashinsky equation," *Applied Mathematics and Computation*, vol. 218, no. 10, pp. 6012–6026, 2012.
- [73] I. Tezaur and M. Barone, "On the stability and convergence of a galerkin reduced order model (rom) of compressible flow with solid wall and far-field boundary treatment," *International Journal for Numerical Methods*

*in Engineering*, vol. 83, pp. 1345 – 1375, 09 2010.

- [74] M. Barrault, Y. Maday, N. C. Nguyen, and A. T. Patera, “An ‘empirical interpolation’ method: application to efficient reduced-basis discretization of partial differential equations,” *Comptes Rendus Mathematique*, vol. 339, no. 9, pp. 667–672, 2004.
- [75] S. Chaturantabut and D. C. Sorensen, “Nonlinear model reduction via discrete empirical interpolation,” *SIAM J. Sci. Comput.*, vol. 32, pp. 2737–2764, 2010.
- [76] J. Du, F. Fang, C. Pain, I. Navon, J. Zhu, and D. Ham, “Pod reduced-order unstructured mesh modeling applied to 2d and 3d fluid flow,” *Computers Mathematics with Applications*, vol. 65, no. 3, pp. 362 – 379, 2013. Efficient Numerical Methods for Scientific Applications.
- [77] D. Xiao, F. Fang, A. Buchan, C. Pain, I. Navon, J. Du, and G. Hu, “Non-linear model reduction for the navier–stokes equations using residual deim method,” *Journal of Computational Physics*, vol. 263, pp. 1–18, 2014.
- [78] K. Carlberg, C. Farhat, J. Cortial, and D. Amsallem, “The gnat method for nonlinear model reduction: Effective implementation and application to computational fluid dynamics and turbulent flows,” *J. Comput. Physics*, vol. 242, pp. 623–647, 2013.
- [79] R. Jiang and L. J. Durlofsky, “Implementation and detailed assessment of a gnat reduced-order model for subsurface flow simulation,” *Journal of Computational Physics*, vol. 379, pp. 192–213, 2019.
- [80] D. Xiao, P. Yang, F. Fang, J. Xiang, C. Pain, and I. Navon, “Non-intrusive reduced order modelling of fluid–structure interactions,” *Computer Methods in Applied Mechanics and Engineering*, vol. 303, pp. 35 – 54, 2016.

- [81] D. Xiao, F. Fang, A. Buchan, C. Pain, I. Navon, and A. Muggeridge, "Non-intrusive reduced order modelling of the navier–stokes equations," *Computer Methods in Applied Mechanics and Engineering*, vol. 293, pp. 522–541, 2015.
- [82] W. J. Kostorz, A. H. Muggeridge, and M. D. Jackson, "An efficient and robust method for parameterized nonintrusive reduced-order modeling," *International Journal for Numerical Methods in Engineering*, vol. 121, no. 20, pp. 4674–4688, 2020.
- [83] W. J. Kostorz, A. H. Muggeridge, and M. D. Jackson, "Non-intrusive reduced order modeling: Geometrical framework, high-order models, and a priori analysis of applicability," *International Journal for Numerical Methods in Engineering*, vol. 122, no. 10, pp. 2545–2565, 2021.
- [84] M. Xiao, P. Breiẗkopf, R. Coelho, C. Knopf-Lenoir, M. Sidorkiewicz, and P. Villon, "Model reduction by cpod and kriging," *IntJStruc Multidisc Optim*, vol. 41, pp. 555–574, 01 2009.
- [85] M. Abbaszadeh, M. Dehghan, and I. Navon, "A proper orthogonal decomposition variational multiscale meshless interpolating element free galerkin method for incompressible magnetohydrodynamics flow: A proper orthogonal decomposition variational multiscale meshless interpolating element free galerkin method for incompressible magnetohydrodynamics f," *International Journal for Numerical Methods in Fluids*, vol. 92, 04 2020.
- [86] S. Sargsyan, S. Brunton, and J. Kutz, "Online interpolation point refinement for reduced-order models using a genetic algorithm," *ArXiv*, vol. abs/1607.07702, 2018.
- [87] S. Ahmed, O. San, D. Bistrian, and I. Navon, "Sampling and resolution characteristics in reduced order models of shallow water equations: intrusive vs non-intrusive," 10 2019.

- [88] M. Raissi, P. Perdikaris, and G. E. Karniadakis, "Physics informed deep learning (part ii): Data-driven discovery of nonlinear partial differential equations," 2017.
- [89] E. Krause, *The Millennium-Problem of Fluid Mechanics – The Solution of the Navier-Stokes Equations*, pp. 317–341. Berlin, Heidelberg: Springer Berlin Heidelberg, 2014.
- [90] A. Tasri and A. Susilawati, "Accuracy of compact-stencil interpolation algorithms for unstructured mesh finite volume solver," *Heliyon*, vol. 7, no. 4, p. e06875, 2021.
- [91] C. J. Cotter, D. A. Ham, and C. C. Pain, "A mixed discontinuous/continuous finite element pair for shallow-water ocean modelling," *Ocean Modelling*, vol. 26, no. 1, pp. 86–90, 2009.
- [92] J. R. Percival, D. Pavlidis, Z. Xie, J. L. Gomes, M. Sakai, Y. Shigeto, H. Takahashi, O. K. Matar, and C. C. Pain, "Control volume finite element modelling of segregation of sand and granular flows in fluidized beds," *International Journal of Multiphase Flow*, vol. 67, pp. 191–199, 2014. A Collection of Papers in Honor of Professor G. Hewitt on the Occasion of his 80th Birthday.
- [93] N. Metropolis and S. Ulam, "The monte carlo method," *Journal of the American Statistical Association*, vol. 44, no. 247, pp. 335–341, 1949. PMID: 18139350.
- [94] B. Kirk, "Overview of monte carlo radiation transport codes," *Radiation Measurements*, vol. 45, no. 10, pp. 1318–1322, 2010. PROCEEDINGS OF THE 11TH SYMPOSIUM ON NEUTRON AND ION DOSIMETRY.
- [95] S. D. Richards, C. M. Baker, A. J. Bird, P. Cowan, N. Davies, G. P. Dobson, T. C. Fry, A. Kyrieleis, and P. N. Smith, "Monk and mcbend: Current status and recent developments," *Annals of Nuclear Energy*, vol. 82, pp. 63–73, 2015. Joint International Conference on Supercomputing in

Nuclear Applications and Monte Carlo 2013, SNA + MC 2013. Pluri- and Trans-disciplinarity, Towards New Modeling and Numerical Simulation Paradigms.

- [96] C. Ding, R. R. Deokar, Y. Ding, G. Li, X. Cui, K. K. Tamma, and S. P. Bordas, "Model order reduction accelerated monte carlo stochastic isogeometric method for the analysis of structures with high-dimensional and independent material uncertainties," *Computer Methods in Applied Mechanics and Engineering*, vol. 349, pp. 266–284, 2019.
- [97] M. Abbaszadeh, M. Bayat, M. Dehghan, and M. I. Azis, "Investigation of generalized couette hydromagnetic flow of two-step exothermic chemical reaction in a channel via the direct meshless local petrov–galerkin method," *Engineering Analysis with Boundary Elements*, vol. 125, pp. 178–189, 2021.
- [98] P. Kerfriden, O. Gouy, T. Rabczuk, and S. Bordas, "A partitioned model order reduction approach to rationalise computational expenses in nonlinear fracture mechanics," *Computer Methods in Applied Mechanics and Engineering*, vol. 256, pp. 169–188, 2013.
- [99] Y. Wang, W. Bangerth, and J. Ragusa, "Three-dimensional h-adaptivity for the multigroup neutron diffusion equations," *Progress in Nuclear Energy*, vol. 51, no. 3, pp. 543–555, 2009.
- [100] R. Barrett, M. Berry, T. F. Chan, J. Demmel, J. Donato, J. Dongarra, V. Eijkhout, R. Pozo, C. Romine, and H. V. der Vorst, *Templates for the Solution of Linear Systems: Building Blocks for Iterative Methods, 2nd Edition*. Philadelphia, PA: SIAM, 1994.
- [101] G. ROZZA, *AN INTRODUCTION TO REDUCED BASIS METHOD FOR PARAMETRIZED PDEs*, pp. 508–519.
- [102] W. Chen, J. Hesthaven, B. Junqiang, Z. Yang, and Y. Tihao, "A greedy non-intrusive reduced order model for fluid dynamics," *AIAA Journal*,



vol. 56, pp. 4927–4943, 2018.

- [103] G. Berkooz, P. Holmes, and J. L. Lumley, “The proper orthogonal decomposition in the analysis of turbulent flows,” *Annual Review of Fluid Mechanics*, vol. 25, pp. 539–575, Jan. 1993.
- [104] E. W. Weisstein, “singular value decomposition.” Visited on 13/10/2018.
- [105] I. Jolliffe and Springer-Verlag, *Principal Component Analysis*. Springer Series in Statistics, Springer, 2002.
- [106] R. L. Hardy, “Multiquadric equations of topography and other irregular surfaces,” , vol. 76, pp. 1905–1915, Mar. 1971.
- [107] G. Fasshauer and J. Zhang, “On choosing "optimal" shape parameters for rbf approximation,” *Numerical Algorithms*, vol. 45, pp. 345–368, 08 2007.
- [108] N. Flyer, G. A. Barnett, and L. J. Wicker, “Enhancing finite differences with radial basis functions: Experiments on the navier–stokes equations,” *Journal of Computational Physics*, vol. 316, pp. 39–62, 2016.
- [109] Y.-H. Wang, M. Xie, and Y. Ma, “Neutron discrete velocity boltzmann equation and its finite volume lattice boltzmann scheme,” *Communications in Computational Physics*, vol. 25, 01 2019.
- [110] E. E. Lewis and W. F. Miller, “Computational methods of neutron transport,”
- [111] G. Barton, “The mathematics of diffusion 2nd edn,” *Physics Bulletin*, vol. 26, pp. 500–501, nov 1975.
- [112] J. Philibert, “One and a half century of diffusion: Fick, einstein before

and beyond,” 2006.

- [113] L. H. J.J. Duderstadt, *Nuclear Reactor Analysis*. John Wiley Sons USA, 1976.
- [114] G. Espinosa-Paredes, J. B. Morales-Sandoval, R. Vázquez-Rodríguez, and E.-G. Espinosa-Martínez, “Constitutive laws for the neutron density current,” *Annals of Nuclear Energy*, vol. 35, no. 10, pp. 1963 – 1967, 2008.
- [115] E. Isaacson and H. B. Keller, *Analysis of Numerical Methods*. Dover Books on Mathematics, New York: Dover Publications, 1994.
- [116] D. E. Knuth, *The art of computer programming, volume 2 (3rd ed.): seminumerical algorithms*. Boston, MA, USA: Addison-Wesley Longman Publishing Co., Inc., 1997.
- [117] B. Fornberg, T. Driscoll, G. Wright, and R. Charles, “Observations on the behavior of radial basis function approximations near boundaries,” *Computers Mathematics with Applications*, vol. 43, no. 3, pp. 473–490, 2002.
- [118] S. Dargaville, A. Buchan, R. Smedley-Stevenson, P. Smith, and C. Pain, “Scalable angular adaptivity for boltzmann transport,” *Journal of Computational Physics*, vol. 406, p. 109124, 11 2019.
- [119] S. A. Sarra, “Multiquadric radial basis function approximation methods for the numerical solution of partial differential equations,” 2009.
- [120] D. Xiao, F. Fang, C. Pain, and I. Navon, “Towards non-intrusive reduced order 3d free surface flow modelling,” *Ocean Engineering*, vol. 140, pp. 155–168, 2017.
- [121] M. Raissi and G. E. Karniadakis, “Hidden physics models: Machine learning of nonlinear partial differential equations,” *Journal of*

*Computational Physics*, vol. 357, pp. 125–141, 2018.

- [122] P. Schoeffler, *Dissipation, dispersion and stability of numerical schemes for advection and diffusion*. SMHI, 1982.
- [123] M. H. Holmes, ed., *Advection Equation*, pp. 127–154. New York, NY: Springer New York, 2007.
- [124] A. Haar, “Zur Theorie der orthogonalen Funktionensysteme,” *Mathematische Annalen*, vol. 69, no. 3, pp. 331–371, 1910.
- [125] I. Daubechies, *Ten Lectures on Wavelets*. CBMS-NSF Regional Conference Series in Applied Mathematics, Society for Industrial and Applied Mathematics, 1992.
- [126] M. Hedayati, R. Ezzati, and S. Noeiaghdam, “New procedures of a fractional order model of novel coronavirus (covid-19) outbreak via wavelets method,” *Axioms*, vol. 10, no. 2, 2021.
- [127] N. Fallah, C. Bailey, M. Cross, and G. Taylor, “Comparison of finite element and finite volume methods application in geometrically nonlinear stress analysis,” *Applied Mathematical Modelling*, vol. 24, no. 7, pp. 439–455, 2000.
- [128] B. Adigun, A. Buchan, A. Adam, S. Dargaville, M. Goffin, and C. Pain, “A haar wavelet method for angularly discretising the boltzmann transport equation,” *Progress in Nuclear Energy*, vol. 108, pp. 295–309, 09 2018.
- [129] P. K. Sweby, “High resolution schemes using flux limiters for hyperbolic conservation laws,” *SIAM Journal on Numerical Analysis*, vol. 21, no. 5, pp. 995–1011, 1984.
- [130] P. Lax and B. Wendroff, “Systems of conservation laws,” *Communications on Pure and Applied Mathematics*, vol. 13, no. 2, pp. 217–237, 1960.

- [131] *Neutron Nuclear Reactions*, ch. 1, pp. 1–32. John Wiley Sons, Ltd, 2007.
- [132] “Relaxation methods in theoretical physics. r. v. southwell, m.a., ll.d, f.r.s. oxford university press, london, 1946. 248 pp. 20s.,” *The Journal of the Royal Aeronautical Society*, vol. 51, no. 434, p. 270–270, 1947.
- [133] S. L. Brunton, J. L. Proctor, and J. N. Kutz, “Sparse identification of nonlinear dynamics with control (sindyc)\*\*slb acknowledges support from the u.s. air force center of excellence on nature inspired flight technologies and ideas (fa9550-14-1-0398). jlp thanks bill and melinda gates for their active support of the institute of disease modeling and their sponsorship through the global good fund. jnk acknowledges support from the u.s. air force office of scientific research (fa9550-09-0174).,” *IFAC-PapersOnLine*, vol. 49, no. 18, pp. 710–715, 2016. 10th IFAC Symposium on Nonlinear Control Systems NOLCOS 2016.
- [134] A. Sexton, “Abramowitz and stegun – a resource for mathematical document analysis,” vol. 7362, 07 2012.
- [135] H. Versteeg and W. Malalasekera, *An Introduction to Computational Fluid Dynamics: The Finite Volume Method*. Pearson Education Limited, 2007.
- [136] D. R. Davies, C. R. Wilson, and S. C. Kramer, “Fluidity: A fully unstructured anisotropic adaptive mesh computational modeling framework for geodynamics,” *Geochemistry, Geophysics, Geosystems*, vol. 12, no. 6, 2011.
- [137] K. Carlberg, “Adaptive h-refinement for reduced-order models,” *International Journal for Numerical Methods in Engineering*, vol. 102, no. 5, pp. 1192–1210, 2015.
- [138] J. Szűcs and J. Weidmann, *Linear Operators in Hilbert Spaces*. Graduate Texts in Mathematics, Springer New York, 2012.

- [139] D. R. Davies, C. R. Wilson, S. C. Kramer, M. D. Piggott, G. Le Voci, and G. S. Collins, "Fluidity: A New Adaptive, Unstructured Mesh Geodynamics Model," in *EGU General Assembly Conference Abstracts*, EGU General Assembly Conference Abstracts, p. 5364, May 2010.
- [140] P. Farrell, M. Piggott, C. Pain, G. Gorman, and C. Wilson, "Conservative interpolation between unstructured meshes via supermesh construction," *Computer Methods in Applied Mechanics and Engineering*, vol. 198, no. 33, pp. 2632–2642, 2009.
- [141] E. Bender, "Numerical heat transfer and fluid flow. von s. v. patankar. hemisphere publishing corporation, washington – new york – london. mcgraw hill book company, new york 1980. 1. aufl., 197 s., 76 abb., geb., dm 71,90," *Chemie Ingenieur Technik*, vol. 53, no. 3, pp. 225–225, 1981.
- [142] R. L. Iman, J. M. Davenport, and D. K. Zeigler, "Latin hypercube sampling (program user's guide). [lhc, in fortran],"
- [143] T. Phillips, C. Heaney, B. Tollit, P. Smith, and C. Pain, "Reduced-order modelling with domain decomposition applied to multi-group neutron transport," *Energies*, 2021.
- [144] T. Phillips, C. Heaney, P. Smith, and C. Pain, "An autoencoder-based reduced-order model for eigenvalue problems with application to neutron diffusion," 08 2020.
- [145] H. Anton, *Elementary Linear Algebra*. John Wiley & Sons, 2010.
- [146] D. Fearnley-Sander, "Hermann grassmann and the creation of linear algebra," *The American Mathematical Monthly*, vol. 86, no. 10, pp. 809–817, 1979.
- [147] K. Hoffman and R. Kunze, *Linear Algebra 2Nd Ed*. Prentice-Hall Of India Pvt. Limited, 1971.

- [148] G. Van Rossum and F. L. Drake Jr, *Python reference manual*. Centrum voor Wiskunde en Informatica Amsterdam, 1995.
- [149] I. John Backus, "High-performance parallel programming language." <https://fortran-lang.org>, 1952. Accessed:2021-06-09.
- [150] J. D. Hunter, "Matplotlib: A 2d graphics environment," *Computing in Science & Engineering*, vol. 9, no. 3, pp. 90–95, 2007.
- [151] C. R. Harris, K. J. Millman, S. J. van der Walt, R. Gommers, P. Virtanen, D. Cournapeau, E. Wieser, J. Taylor, S. Berg, N. J. Smith, R. Kern, M. Picus, S. Hoyer, M. H. van Kerkwijk, M. Brett, A. Haldane, J. F. del Río, M. Wiebe, P. Peterson, P. Gérard-Marchant, K. Sheppard, T. Reddy, W. Weckesser, H. Abbasi, C. Gohlke, and T. E. Oliphant, "Array programming with NumPy," *Nature*, vol. 585, pp. 357–362, Sept. 2020.
- [152] P. Virtanen, R. Gommers, T. E. Oliphant, M. Haberland, T. Reddy, D. Cournapeau, E. Burovski, P. Peterson, W. Weckesser, J. Bright, S. J. van der Walt, M. Brett, J. Wilson, K. J. Millman, N. Mayorov, A. R. J. Nelson, E. Jones, R. Kern, E. Larson, C. J. Carey, İ. Polat, Y. Feng, E. W. Moore, J. VanderPlas, D. Laxalde, J. Perktold, R. Cimrman, I. Henriksen, E. A. Quintero, C. R. Harris, A. M. Archibald, A. H. Ribeiro, F. Pedregosa, P. van Mulbregt, and SciPy 1.0 Contributors, "SciPy 1.0: Fundamental Algorithms for Scientific Computing in Python," *Nature Methods*, vol. 17, pp. 261–272, 2020.
- [153] L. Euler, "'problematis traiectionarum reciprocarum solutio" (1729). euler archive - all works. 5.," 1729.
- [154] J. Stewart, *Calculus*. Available 2010 Titles Enhanced Web Assign Series, Cengage Learning, 2007.
- [155] R. Schaback, "Error estimates and condition numbers for radial basis function interpolation," *Adv. Comput. Math*, vol. 3, pp. 251–264, 1994.

- [156] K. Carlberg, M. Barone, and H. Antil, “Galerkin v. least-squares petrov-galerkin projection in nonlinear model reduction,” *J. Comput. Phys.*, vol. 330, p. 693–734, Feb. 2017.